LRP 824/06 October 2006

Stability and toroidal rotation properties of highly shaped plasmas in the TCV tokamak

A. Scarabosio

ISSN 0458-5895

Abstract

Magnetohydrodynamic (MHD) instabilities and plasma rotation have various impacts on particle and thermal transport in toroidal plasmas. MHD instabilities degrade the confinement, limit the maximum achievable plasma pressure, and can lead to plasma disruptions. Plasma rotation is observed to have beneficial effects on global instabilities and improve confinement through the reduction of turbulent transport. Plasma rotation and stability are strongly coupled, influencing each other in a complicated fashion. The *Tokamak à Configuration Variable* (TCV), unique in its plasma shaping capabilities, is equipped with a flexible auxiliary heating system (ECRH) and several diagnostics allowing us to study the effect of the plasma shape on stability in a wide range of scenarios. TCV also provides for measurements of carbon toroidal velocity in the absence of external momentum input, an experimental condition poorly studied in the past but of major interest for an accurate prediction of the toroidal rotation in future large experiments.

The work presented in this thesis may be divided into two parts. In the first part, we focus on plasma instabilities appearing in three different TCV scenarios. These instabilities limit the achievable maximum pressure and current density. New features and previously unnoticed dependencies are shown. In the second part of this thesis, we experimentally study the plasma rotation properties and their relation with the plasma parameters and MHD activity. The new insight on spontaneous rotation may help in constructing a complete model of plasma rotation in tokamaks.

During the initial plasma current rise, edge MHD instabilities are commonly observed in most tokamaks when the edge safety factor q_a approaches low rational values. These instabilities may lead to plasma disruptions and can effectively limit the edge safety factor to $q_a > 3$, which is above the well-known operational limit $q_a \geq 2$. We report on a detailed analysis of the MHD modes leading to disruptions and show experimental evidence of the key role of mode coupling. The beneficial effect of plasma shaping on current rise experiments was early noted in the TCV operation. In this thesis we characterise the effect of the plasma shape on the instability, showing how plasma elongation and triangularity (positive and negative) act as stabilising factors. The complex shape dependence of such MHD modes is interpreted on the basis of the theory of coupled tearing modes. Three

stabilising mechanisms linked with plasma shaping are shown to be important for TCV and likely to other tokamaks.

Sawteeth, which are central relaxation oscillations common to most tokamak scenarios, also have a significant effect on central plasma parameters. In highly elongated TCV discharges heated with far off-axis ECRH, the sawtooth oscillations are observed to disappear and to be replaced by a continuous MHD mode resonant on the $q = 1$ surface. The combination of a flat current profile and small $q = 1$ radius determines the change in the plasma stability, which we study using ideal and resistive MHD models.

Plasmas with internal transport barriers (ITBs) are routinely produced in TCV using high power ECRH and current drive. A variety of MHD activity is observed during these discharges including classical $m/n = 3/1$ and neoclassical $m/n = 2/1$ tearing modes, and more exotic $q = 2$ pseudo-sawteeth central relaxations. Disruptive modes are observed in ITB plasmas with strong reverse magnetic shear. In general, the MHD instabilities limit the maximum achievable plasma pressure. The experimental β-limit in this scenario is observed to depend strongly on the peaking of the electron pressure profile, in agreement with the ideal MHD theory.

The properties of the toroidal carbon impurity rotation in Ohmic limited L-mode plasmas are studied in detail in stationary conditions. The dependence and scaling of the toroidal velocity with plasma parameters, such as the plasma current and density, are highlighted, as well as the effect of the sawtooth activity on the rotation profile. We show that the toroidal rotation in TCV is generally directed in the counter-current or electron diamagnetic drift direction. We also compare the experimental results with the neoclassical prediction for stationary toroidal rotation in absence of external momentum input.

Angular momentum relaxations are observed in TCV Ohmic plasmas. Large magnetic islands cause strong losses of angular momentum, flattening the rotation profile. Once the MHD mode has disappeared, the stationary angular velocity profile is restored over a typical time scale, 100–200 ms, providing experimental evidence of the spontaneous torque spinning the plasma column.

We show that we can reproduce the phenomena of “toroidal spin-up” and rotation inversion observed in TCV Ohmic plasmas with a phenomenological momentum transport model. We infer transport coefficients, such as the momentum diffusivity, and compare them with theoretical predictions.

Keywords: plasma physics, tokamak, magnetohydrodynamics, plasma instabilities, plasma spontaneous rotation.

Résumé

Les instabilités magnétohydrodynamique (MHD) et la rotation du plasma ont des impacts divers sur le transport des particules ainsi que sur le transport thermique dans les plasmas toroïdaux. Les instabilités MHD dégradent le confinement, limitent le maximum de pression de plasma réalisable et peuvent mener à la disruption du plasma. On observe que la rotation du plasma a des effets bénéfiques sur les instabilités globales et améliore le confinement en réduisant le transport turbulent. La rotation du plasma et sa stabilité sont également fortement couplées, s'influençant réciproquement de manière complexe. Le *Tokamak à Configuration Variable* (TCV), unique dans sa capacité á créer des plasmas de formes très diverses, est équipé d'un système de chauffage additionnel (ECRH) flexible et d'un faisceau de diagnostiques nous permettant d'étudier l'effet de la forme du plasma sur sa stabilité dans un éventail de scénarios. TCV fournit également des mesures de la vitesse toroïdale du carbone en l'absence d'injection externe de moment, une condition expérimentale peu étudiée dans le passé mais d'intérêt essentiel pour une prévision précise de la rotation toroïdale dans les futures grandes expériences.

Cette thèse peut être divisée en deux parties. Dans la première partie, nous nous sommes concentrés sur les instabilités du plasma apparaissant dans trois scénarios différents de TCV. Telles instabilités limitent le maximum de courant et densité réalisable. Dans la deuxième partie, nous avons étudiés expérimentalement les propriétés de la rotation du plasma et leur relation avec les paramétres du plasma et l'activité MHD.

Pendant la rampe de courant plasma initiale, des instabilités MHD localisées au bord sont généralement observées dans la plupart des tokamaks quand le facteur de sécurité au bord q_a s'approche des valeurs rationnelles basses. Ces instabilités peuvent mener à la disruption du plasma et peuvent effectivement limiter le facteur de sécurité à $q_a > 3$, valeur supérieure à la limite opérationnelle bien connue $q_a \geq 2$. Dans TCV, des balayages systématiques de la forme du plasma ont démontré la possibilité d'éviter de tels types de disruption en façonnant suffisamment le plasma avant d'atteindre des valeurs critiques de q_a. A la fois l'élongation et la triangularité (positive et négative) du plasma agissent en tant que facteur stabilisant. L'évidence expérimentale montre clairement l'importance du couplage de modes. La dépendance complexe de la forme de tels modes MHD est interprétée sur la base de la théorie des modes de déchirement couplés. La déstabilisation

d'un large îlot magnétique $m/n = 2/1$ dans des plasmas quasi-circulaires s'avére être due à l'effet du couplage de mode toroïdal. On montre que trois mécanismes stabilisants, liés à la forme du plasma, sont importants dans le cas de TCV.

Les instabilité dents de scie, qui sont des oscillations de relaxation centrales communes à la plupart des scénarios de tokamak, ont un effet significatif sur les paramètres centraux du plasma. Dans des décharges fortement allongées de TCV, avec injection ECRH fortement hors-axe, les oscillations de dent de scie disparaissent et sont remplacées par un mode MHD continu résonnant sur la surface $q = 1$. La combinaison d'un profil de courant plat et d'un petit rayon $q = 1$ déterminent le changement de comportement des dents de scie. Dans de telles conditions expérimentales, la stabilisation du mode kink interne, dont on pense qu'il est responsable des oscillations de dent de scie, est prédit de manière consistante par les théories de la MHD idéale et résistive.

Des plasmas avec des barrières de transport internes (ITB) sont obtenus de manière routinière dans TCV en utilisant le chauffage ECRH et de la génération de courant haute puissance. On observe une grande diversité d'activité MHD pendant ces décharges comprenant des modes classiques $m/n = 3/1$, des modes de déchirement néoclassiques $m/n = 2/1$, et de plus exotiques pseudo dents de scie $q = 2$. Des modes disruptifs sont observés dans des plasmas ITB avec une fort inversion du cisaillement magnetique. Généralement les instabilités MHD limitent le maximum de pression de plasma réalisable. On observe que la limite de β diminue avec le piquage du profil de pression électronique, en accord avec théorie MHD idéale.

Les propriétés de la rotation toroïdale d'impuretés de carbone dans des plasmas limités ohmiques en mode L sont étudiées en détail dans des conditions stationnaires. La dépendance et la loi d'échelle de la vitesse toroïdale avec les paramètres du plasma, tels que le courant du plasma et la densité, sont dèmontres, aussi bien que l'effet de l'activité des dents de scie sur le profil de rotation. On montre que la rotation toroïdale est généralement dirigée dans la direction opposée au courant du plasma c'est-á-dire paralléle à la direction diamagnétique de dérive des électrons. La comparaison avec les prédictions néoclassiques montre que la rotation du plasma dans TCV est principalement générée par les champs électriques radiaux, avec une contribution négligeable des champs électriques toroïdaux.

On observe des relaxations de moment angulaire dans les plasmas ohmiques de TCV. De grands îlots magnétiques causent de fortes pertes de moment angulaire, aplatissant le profil de rotation et freinant le plasma jusqu'au blocage du mode. Une fois que le mode MHD a disparu, le profil stationnaire de la vitesse angulaire est rétablit aprés un temps typique de 100–200 ms, fournissant une évidence expérimentale du couple faisant tourner la colonne de plasma.

Une inversion de la rotation toroïdale centrale est observée dans les plasmas ohmiques à haut courant au-dessus d'un certain seuil de densité. Cette inversion de rotation est bien reproductible et reversible. Un modèle phénoménologique de transport de moment a été développé pour interpréter les caractéristiques du transport de moment angulaire dans les plasmas ohmiques de TCV. Les coefficients de transports comme la diffusivité et la vitesse convective sont déduits et comparés

aux prévisions théoriques.

Mots-clés: physique des plasmas, tokamak, magnétohydrodynamique, instabilités des plasmas, rotation du plasma.

Contents

Abstract i

Résumé iii

I Overview 1

1 Introduction 3
1.1 Nuclear Fusion . . . 3
1.1.1 Nuclear Fusion: a possible source of energy for the future . 3
1.1.2 Nuclear Fusion: the physical process . . . 5
1.2 Principle of a nuclear fusion power plant . . . 6
1.3 Plasmas and methods of confinement . . . 8
1.3.1 Magnetic confinement . . . 9
1.3.2 The tokamak concept . . . 10
1.4 Plasma heating . . . 13
1.5 Motivations and structure of the manuscript . . . 16
1.5.1 Motivations . . . 16
1.5.2 Outline of the thesis . . . 16

2 MHD instabilities and equilibrium 19
2.1 Magnetohydrodynamics theory . . . 19
2.2 Magnetohydrodynamic equilibrium of a tokamak plasma . . . 20
2.3 Magnetohydrodynamic stability . . . 23
2.3.1 Ideal instabilities: the internal kink mode . . . 24
2.3.2 Resistive Instabilities . . . 25

3 The TCV experiment 29
3.1 The Tokamak à Configuration Variable . . . 29
3.1.1 Electron cyclotron heating system . . . 33
3.2 TCV diagnostics . . . 34
3.2.1 Far-infrared interferometer (FIR) . . . 34
3.2.2 Thomson scattering diagnostic (TS) . . . 35
3.2.3 Soft X-ray emission measurements . . . 36

3.2.4 Fast edge magnetic perturbation measurements (Mirnov system) . . . 38
3.2.5 CXRS measurements of impurity temperature and rotation velocity . . . 39
3.2.5.a Effects of the neutral beam (DNBI) on toroidal rotation . . . 41
3.3 Equilibrium reconstruction . . . 43

II Plasma instabilities in TCV **45**

4 Analysis of MHD fluctuations **47**
4.1 Perturbation of the magnetic field . . . 47
4.1.1 Flux coordinate, magnetic field lines and decomposition into modes . . . 48
4.2 Numerical techniques for the MHD mode analysis . . . 50
4.2.1 Temporal analysis . . . 50
4.2.2 Spatial analysis and mode numbers . . . 52
4.2.2.a Toroidal analysis . . . 52
4.2.2.b Poloidal analysis . . . 54
4.2.2.c Spatiotemporal mode structure from bi-orthogonal analysis . . . 56
4.3 Perturbations in approximate flux surface quantities . . . 58
4.3.1 Soft X-ray perturbed emissivity . . . 59
4.4 Modelling of magnetic islands . . . 60
4.4.1 Perturbation current density and reconstruction of the magnetic field . . . 60
4.4.2 Comparison with the edge magnetic signal . . . 63
4.4.3 Magnetic island width . . . 65
4.5 Concluding remarks . . . 67

5 Plasma shape stabilisation of current rise MHD instabilities **69**
5.1 Introduction to plasma instabilities during current rise . . . 69
5.2 MHD activity during current rise in TCV . . . 71
5.2.1 Current rise disruption in $q_a = 3$ quasi-circular plasmas . . . 72
5.3 Discussion and interpretation . . . 75
5.3.1 Evidence and role of the $m/n = 3/1$ and $m/n = 2/1$ mode coupling . . . 76
5.4 Avoidance of the $q = 3$ current rise disruption by means of plasma shaping . . . 77
5.5 The 2/1 tearing modes stability of TCV shaped plasmas . . . 78
5.5.1 Toroidal destabilisation of the tearing mode . . . 80
5.5.2 Plasma shape stabilisation of tearing modes . . . 82
5.6 Concluding remarks . . . 83

6 Disappearance of the sawtooth oscillations with far off-axis ECRH at high elongation **85**
6.1 Introduction to sawteeth 85
6.2 Experiments with far off-axis ECRH and sawteeth disappearance . . 87
6.3 The disappearance of sawteeth: n_e and l_i thresholds 90
6.3.1 High current plasmas ($I_p \geq$ 350 kA, $q_{95} \leq$ 4.5, $r_{\rm inv} \geq$ 8 cm) . 90
6.4 MHD modes analysis 91
6.4.1 Evolution of the q=1 position. 94
6.5 Comparison with sawtooth models 95
6.5.1 Sawtooth crash triggering conditions in the Porcelli model . 96
6.5.2 Analysis of the ideal internal kink stability with KINX 98
6.5.3 Comparison with the Porcelli model using PRETOR simulations 100
6.6 Concluding remarks 102

7 MHD activity in EC-heated TCV plasmas with eITBs **105**
7.1 Introduction to electron internal transport barriers 105
7.2 An ideal MHD result: infernal modes in reverse shear scenario . . . 108
7.3 MHD mode in improved central electron confinement scenario . . . 109
7.3.1 Tearing modes in ICEC plasmas 109
7.3.2 Pseudo sawteeth in ICEC plasmas 111
7.4 MHD activity in fully non-inductive reverse shear scenario 115
7.5 Summary, further discussions and conclusions 116

III Toroidal plasma rotation and momentum transport **119**

8 Introduction to plasma rotation **121**
8.1 Motivations 121
8.2 Aims and objectives of the TCV rotation studies 122

9 Stationary toroidal plasma rotation in TCV **125**
9.1 Introduction 125
9.2 Experimental results 126
9.2.1 Plasma current effects on TCV toroidal rotation profiles . . . 126
9.2.2 Edge toroidal rotation measurements 132
9.2.3 Basic scaling law for the TCV toroidal rotation 133
9.2.4 Rotation profiles with plasma triangularity 135
9.3 Comparison with neoclassical predictions 136
9.3.1 Toroidal electric field contribution to impurity toroidal rotation 136
9.3.2 Radial electric field and diamagnetic contributions to toroidal rotation 138
9.3.3 Comparison of experimental and theoretical stationary toroidal velocity profiles 140
9.4 Summary and conclusions 143

10 Angular momentum transport in TCV L-mode plasmas **147**
10.1 Observations of momentum transport phenomena 147
10.1.1 Ion momentum losses with large MHD activity 147
10.1.1.a Discussion and interpretation of the observations . 149
10.1.2 Plasma toroidal spin-up following large MHD event 151
10.1.3 Core toroidal rotation inversion at high I_p and n_e 152
10.2 Phenomenological modelling of momentum transport 153
10.2.1 Momentum transport modelling: equations and methodology 153
10.2.1.a External momentum source and boundary conditions 156
10.2.1.b The effect of the sawteeth 156
10.2.1.c Implementation, tests and method of comparison . 156
10.2.2 Modelling of the toroidal plasma spin up and core rotation inversion 158
10.2.2.a Simulations of the toroidal spin-up 159
10.2.2.b Simulation of the core rotation inversion 160
10.3 Final remarks and conclusions 161

Conclusion **165**

Bibliography **169**

Remerciements **179**

Part I

Overview

Chapter 1

Introduction

This chapter is, as the title says, introductory to the context and subject of this thesis. We briefly introduce the basic concepts of nuclear fusion reactions and nuclear fusion power plants. Nuclear fusion reactions may be achieved in high temperature plasmas. We focus here on magnetic plasma confinement methods.

1.1 Nuclear Fusion

1.1.1 Nuclear Fusion: a possible source of energy for the future

Finding a safe, reliable, economic and environmentally compatible source of primary energy is certainly crucial for the future development of mankind. Despite the relevance of the topic, no commonly accepted strategies have been found yet on the energy sources needed to sustain the world economic growth. It is a fact that, sooner or later, we will have to replace the power obtained by burning oil (about 40% of the total energy produced every day [1]) and other fossil materials by other means. Surprisingly, we will not have to wait on the end of the oil resources (4 or 5 decades according to recent estimations [2]) before we face the risk of an energy shortage. The reader may also question whether it is a good idea to burn all the oil, producing tons and tons of greenhouse gases which may alter the climate.

Since 1985 we have been consuming more oil than what is actually discovered. According to several experts we will soon reach the point where the oil demand exceeds the oil production, the so-called "oil production peak". More precisely, the relevant question is: do we have an idea of when the decline of the production will begin, not for conjunctural reasons, because a war has damaged a pipeline here, or because there is a transient little recession there, but for structural reasons, because there is not enough oil left underground to satisfy the demand? The

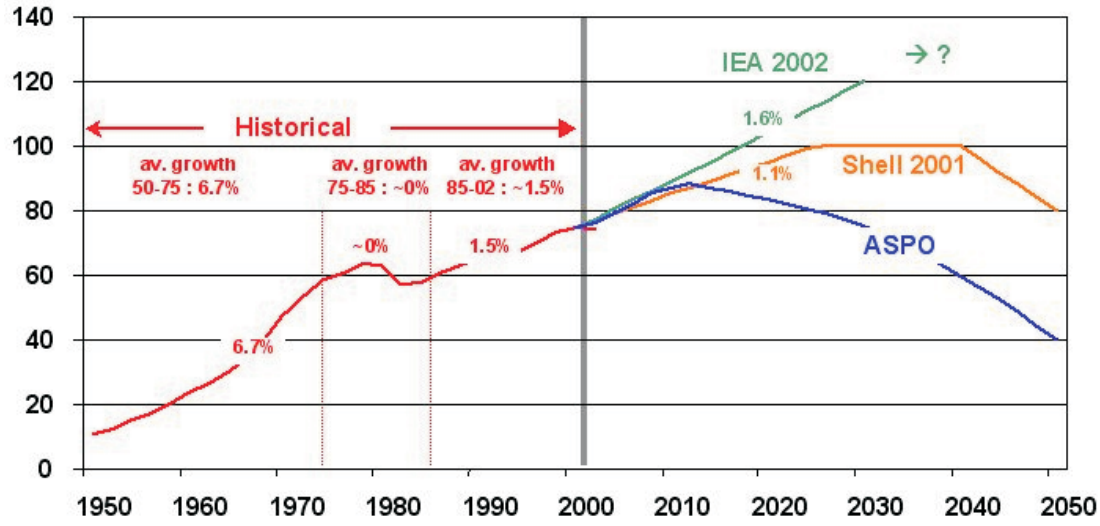

Figure 1.1: *World oil production in million barrels per day. Up to 2002, the red curve indicates the real production. Afterwards we show various predictions according to various sources. ASPO, the Association for the Study of Peak Oil, gathers retired oil geologists and various experts still professionally active. It organises an annual meeting to discuss the remaining ultimate reserves (for up-to-date information, the reader may refer to the web site [2]). The ASPO curve represents their prediction of the maximum possible oil production for the future. The Shell (the worldwide known oil company) curve predicts the beginning of the peak production (actually a plateau) around 2025, which is also the approximate date mentioned in the 2003 annual report of Total (another oil company). The IEA (International Energy Agency) curve refers to a prediction of oil demand, not production. One can see that the IEA predicted demand is larger than the shown production predictions*

"production peak" topic is the ground for large discussions between experts. To summarise, pessimists see the peak within 5 to 10 years from today, whereas in the more optimistic views, it will occur within 20 to 30 years [3], as illustrated in figure 1.1.

This suggests the urgency of a large worldwide effort in finding new technologies and strategies to fulfil our needs of energy in the medium-long term. Nowadays the existing technologies that may replace the oil as a energy source, based on nuclear reactions, solar or wind energy, do not satisfy all the requirements mentioned above, i.e. safety, reliability, economical advantages and environmental compatibility. In this context the thermonuclear fusion power has the potential to offer a practically inexhaustible and inherently safe source of energy. It also has the advantage of producing neither greenhouse gases nor long-lived radioactive wastes. This thesis represents a small contribution to the effort undertaken by the international scientific community toward the development of nuclear fusion as a commercial source of energy for the future.

1.1.2 Nuclear Fusion: the physical process

We call nuclear fusion the process in which two nuclei collide and combine or fuse to make a larger atom. If the two starting nuclei are lighter than iron, the fusion process releases a large amount of energy as in the reactions:

$$ {}_1H^1 + {}_1H^1 \rightarrow {}_1D^2 + e^+ + \nu_e \quad (1.1) $$
$$ {}_1D^2 + {}_1H^1 \rightarrow {}_2He^3 + \gamma \quad (1.2) $$

where hydrogen (H) or deuterium (D) fuses to form larger nuclei as helium (He). These reactions involve the electro-weak interactions and they have therefore very small cross-section (i.e. they are not very likely to happen). They are very common in the core of the stars since the most abundant fuel is hydrogen, on earth however they should be replaced by other reactions involving the heavier hydrogen isotopes deuterium and tritium (T):

$$ {}_1D^2 + {}_1D^2 \rightarrow {}_2He^3(0.817\ \text{MeV}) + {}_0n^1(2.45\ \text{MeV}) \quad (1.3) $$
$$ {}_1D^2 + {}_1D^2 \rightarrow {}_1T^3(1.01\ \text{MeV}) + {}_1H^1(3.02\ \text{MeV}) \quad (1.4) $$
$$ {}_1D^2 + {}_1T^3 \rightarrow {}_2He^4(3.50\ \text{MeV}) + {}_0n^1(14.1\ \text{MeV}) \quad (1.5) $$
$$ {}_1D^2 + {}_2He^3 \rightarrow {}_2He^4(3.67\ \text{MeV}) + {}_1H^1(14.7\ \text{MeV}) \quad (1.6) $$

where the quantities between parentheses are the final state kinetic energies in the reaction rest frame.

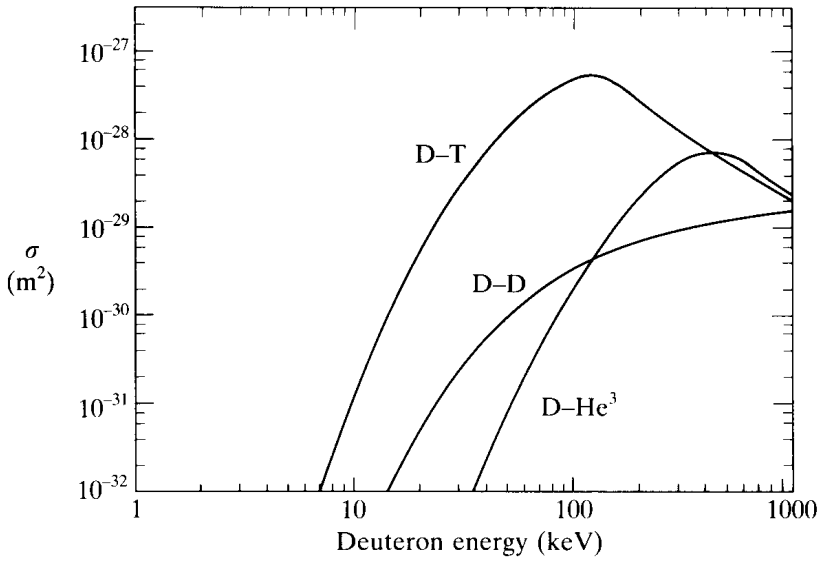

Figure 1.2: *Cross-section for the fusion reactions $D-T$, $D-D$, and $D-He^3$. For the $D-D$ reaction, the sum of the cross-sections of both reactions 1.3 and 1.4 is given [4].*

Among these fuelling elements only tritium is naturally radioactive (with a half life of 12.3 years) and it hence is not freely available in nature. Thus the $D-D$ or $D-He$ reactions would be preferable, because there is no need to produce and manage any radioactive element. Unfortunately these reactions have cross-sections comparable to the $D-T$ reaction only at high temperatures, as can be seen from figure 1.2. Therefore, at least in the beginning, the $D-T$ reaction is advised as the best candidate for a future nuclear fusion reactor.

Tritium can be produced from lithium (Li) using the neutron induced fission reactions:

$$ {}_3Li^7 + {}_0n^1 \rightarrow {}_2He^4 + {}_1T^3 + {}_0n^1 + 2.5 \text{ MeV} \quad (1.7) $$

$$ {}_3Li^6 + {}_0n^1 \rightarrow {}_2He^4 + {}_1T^3 + 4.8 \text{ MeV}. \quad (1.8) $$

The relative abundances of the two lithium isotopes Li^6 and Li^7 are 7.4% and 92.6% respectively. Lithium can be found in abundance in the earth's crust, and also dissolved in the sea water. If all the world's electricity were to be provided by fusion, known total reserves would last for at least a million years [5]. Thus, nuclear fusion promises to be a practically inexhaustible source of energy.

1.2 Principle of a nuclear fusion power plant

We call *beam-target fusion* the process in which the energy to initiate the reaction comes from accelerating one of the nuclei, whereas *beam-beam fusion* is the process in which both nuclei are accelerated. If the required energy is distributed in random incoherent fashion, the fuel atoms are completely ionised and form a plasma in so-called near thermal equilibrium. In this case one speaks of *thermonuclear fusion*.

One possible strategy for a fusion power plant is to produce and control a large volume of $D-T$ plasma at high temperature. In the ideal case, the temperature of the D and T combustibles is maintained by the energy transfer of the 3.5 MeV α-particle (${}_2He^4$) created in the fusion reaction (equation 1.5), therefore additional heating is unnecessary. If the α-particles are sufficiently well confined they can transfer their energy via collisions. This condition is called *plasma ignition*. However confining the α-particles is more difficult than confining the bulk plasma, mainly because of their energy and mass. This issue is still to be addressed for an optimal fusion reactor. The emitted neutrons may instead leave the plasma without further interaction and should be absorbed in the blankets surrounding the reactor vessel. The heat is then carried away by a suitable coolant and provides the power output for the power generation.

Finally the requirements for fusion power plants are given by power balance considerations. We can define the rate of fusion reactions ν as

$$ \nu = \int_V n_D n_T < \sigma_{D-T} \mathrm{v} >_\mathrm{v} \, \mathrm{dV} \quad (1.9) $$

with n_D, n_T being the deuterium and tritium density, v the particle velocity, and $<>_{\mathrm{v}}$ denoting the average over the velocity distribution function. The heating power P_α generated by the α-particles slowing down is given by ν multiplied by the kinetic energy E_α given off by a single fusion reaction:

$$P_\alpha = \nu E_\alpha. \tag{1.10}$$

In the same way, one can define the fusion power P_{fusion} as the rate of fusion reactions multiplied by the emitted neutron kinetic energy E_{fusion}:

$$P_{\mathrm{fusion}} = \nu E_{\mathrm{fusion}}. \tag{1.11}$$

The energy loss can be expressed by the ratio of the total plasma energy content $W = \int 3nTdV$ (where T is the temperature and n the total particle density) and the energy confinement time τ_E,

$$P_{\mathrm{loss}} = \frac{W}{\tau_E} = \frac{\int (n_e T_e + n_D T_D + n_T T_T) dV}{\tau_E}. \tag{1.12}$$

The power balance for a not yet ignited plasma in a steady state yields:

$$P_\alpha + P_{\mathrm{external}} = P_{\mathrm{loss}} \tag{1.13}$$

where P_{external} is the external power required to sustain the plasma.

Let us now replace P_{external} by P_{fusion}/Q where Q is the gain factor. The Lawson criterion requires $P_{\mathrm{fusion}} > Q(P_{\mathrm{loss}} - P_{\mathrm{external}})$. Using equations 1.10 and 1.11 we obtain therefore:

$$P_{\mathrm{fusion}} \left(\frac{E_\alpha}{E_{\mathrm{fusion}}} + \frac{1}{Q} \right) > \frac{W}{\tau_E}. \tag{1.14}$$

Assuming a uniform $50\%-50\%$ deuterium-tritium plasma ($n_D = n_T = n/2$) the rate of fusion reactions (equation 1.9) becomes:

$$\nu = \frac{n^2}{4} V < \sigma_{D-T} v >_{\mathrm{v}} . \tag{1.15}$$

With the further assumption of constant and equal temperatures ($W = 3nVT$), and using equations 1.10 and 1.12, one finally obtains:

$$n\tau_E > \frac{12}{E_{\mathrm{fusion}} \left(\frac{E_\alpha}{E_{\mathrm{fusion}}} + \frac{1}{Q} \right)} \frac{T}{< \sigma_{D-T} v >_{\mathrm{v}}}. \tag{1.16}$$

Assuming that τ_E does not depend on the temperature, at ignition ($Q = \infty$) the r.h.s. of equation 1.16 has a wide minimum close to T = 30 keV. Taking into account the τ_E dependency on the temperature, it turns out that the ignition temperature is likely to be somewhat lower. Using the approximated fusion rate $< \sigma_{D-T} v >_{\mathrm{v}} = 1.1 \cdot 10^{-24} T^2 \mathrm{m^3 s^{-1}}$ (T in KeV) we finally obtain a convenient condition for the ignition in terms of the triple product:

$$nT\tau_E > 3 \cdot 10^{21} \mathrm{m^{-3} keV\ s} \tag{1.17}$$

The value of $nT\tau_E$ obtained in fusion reaction experiments has improved by five orders of magnitude over the past 35 years and is on the verge of reactor conditions (see figure 1.3).

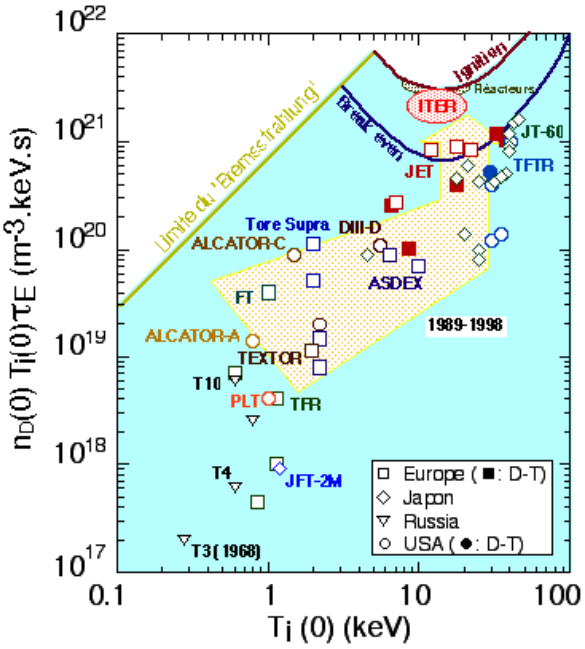

Figure 1.3: *Progress of the triple product $nT\tau_E$ obtained by several experiments worldwide. The condition for an ignited plasma is shown in red.*

1.3 Plasmas and methods of confinement

Any gas at high temperature is partially or totally ionised and over a wide range of conditions constitutes a new state of the matter called plasma: a (globally) electrically neutral system showing dominant collective behaviour. In a plasma at the temperature required for fusion reactions the atoms are fully ionised. In a fusion reactor the highly energetic charged particles must be kept clear from the vessel wall containing the plasma to avoid damage to the reactor. Achieving a good confinement is also necessary to minimise the plasma thermal energy loss, in order to self-sustain the plasma (ignition condition) or at least minimise the external power input. Most common confinement methods are:

Gravitational confinement. To confine the plasma one could use the gravitational interaction. However the mass needed to confine the fuel well enough to satisfy Lawson criterion is so large that gravitational confinement is only possible in stars. Even if the more reactive deuterium fuel was used, a mass about the size of the Moon would be needed.

Magnetic confinement. Since plasmas are very good electrical conductors, magnetic fields can also be used to confine fusion fuel. A variety of magnetic configurations can be used, in linear devices such as magnetic mirrors and toroidal devices, such as tokamaks (see section 1.3.2).

Inertial confinement. It consists in applying a rapid pulse of energy to a small volume of fusion fuel, causing it to “implode” and heat simultaneously, reach-

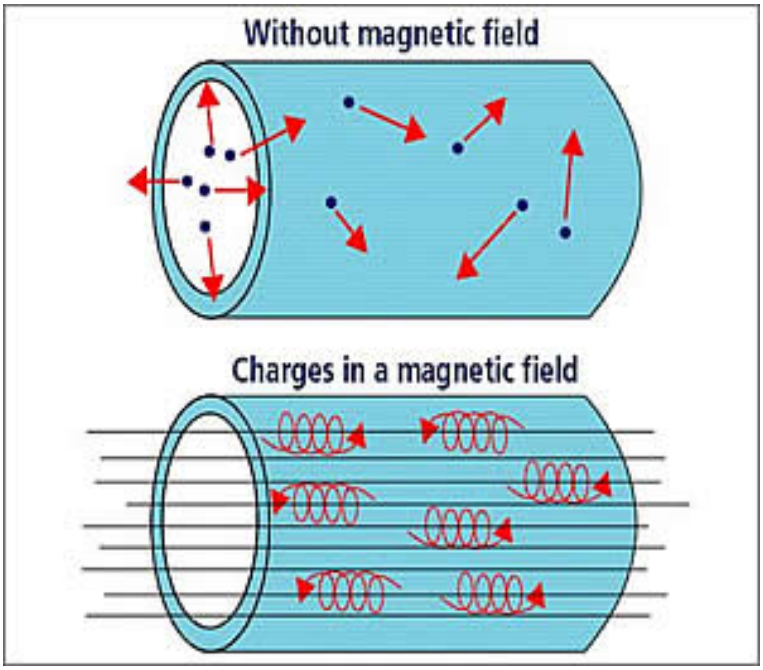

Figure 1.4: *Principle of the magnetic confinement: the motion of a charged particle in a magnetic field is restricted to a circle and, in first approximation, it is bound to follow a magnetic field line.*

ing very high pressure and temperature. This will significantly increase the fusion reaction rate, and a large fraction of the fuel can be burned before it dissipates. To achieve these extreme conditions, the initially cold fuel must be explosively compressed. Inertial confinement is used in the hydrogen bomb, where X-rays created by a fission bomb are used as reaction driver. There are also attempts of using inertial confinement in a "controlled" nuclear fusion reaction, where a laser, ion, or electron beam is used as a driver.

Other confinement principles, such as muon-catalysed fusion, Farnsworth-Hirsch fusor (inertial electrostatic confinement), and bubble fusion have also been investigated.

1.3.1 Magnetic confinement

Owing to the Lorentz force, a magnetic field can tie a charged particle by inducing a helical trajectory around a single field line. The motion of a particle of mass m_s and charge q_s in the plane perpendicular to the field line is restricted to a circle of radius:

$$r_{L,s} = \frac{m_s v_\perp}{q_s B} \tag{1.18}$$

where $r_{L,s}$ is the so-called Larmor radius, B is the magnetic field, and $v_\perp$ is the particle velocity in the plane perpendicular to B. On the contrary there is no restriction to the motion along the field lines. This is the basis of magnetic confinement as depicted in figure 1.4.

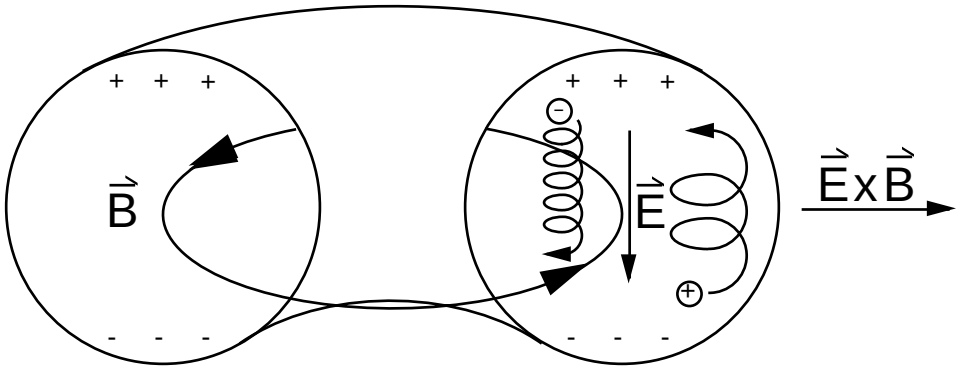

Figure 1.5: *Particle drift motions in a pure toroidal magnetic field. The inhomogeneous field leads to a separation of the charges. The resulting electric field combined with the toroidal field causes an outward expulsion of the plasma particles.*

The general motion of a charged particle in an electromagnetic field is more complex and an analytical solution of the motion equations can not in general be found. However, in the case of a slowly (in time and space) varying magnetic field the perpendicular motion may be described as the sum of an helical (Larmor) gyromotion and perpendicular drifts. A systematic treatment can be found in reference [6].

1.3.2 The tokamak concept

Open magnetic field line configurations can not be used to constrain a plasma. The simplest configuration with closed field lines is a torus. Let us define a cylindrical coordinate system (R, Z, ϕ), with the origin at the torus centre, as for instance in figure 1.8.

A purely toroidal magnetic field $\vec{B}$ is however found not to be homogeneous. In fact, it varies with the radial distance according to $1/R$. The magnetic field line curvature and the gradient of the field amplitude lead to a vertical drift in opposite directions for electrons and ions (see figure 1.5). The consequent charge separation develops a vertical electric field $\vec{E}$ and an $\vec{E} \times \vec{B}$ drift, which eventually brings the whole plasma toward the outer wall. This process is fast ($\sim 1\ \mu$s) and no good confinement can therefore be achieved with a pure toroidal field geometry.

The solution consists in adding a poloidal component to the magnetic field which twists the field lines into an helical structure. The particles, (approximately) following the field lines, will now drift partly toward the edge and partly toward the centre of the torus, averaging out the net vertical drift and therefore avoiding the creation of the vertical electric field.

The helical field lines can eventually wind endlessly around the torus defining a surface. The generated magnetic structure thus consists of nested magnetic surfaces also called flux surfaces. Flux surfaces provide a barrier to charged particles,

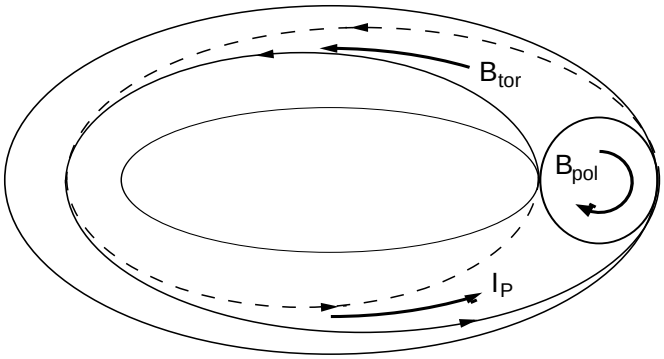

Figure 1.6: *A field line on a q=2 magnetic surface. One can see that the magnetic field line closes up on itself after 2 toroidal rotations.*

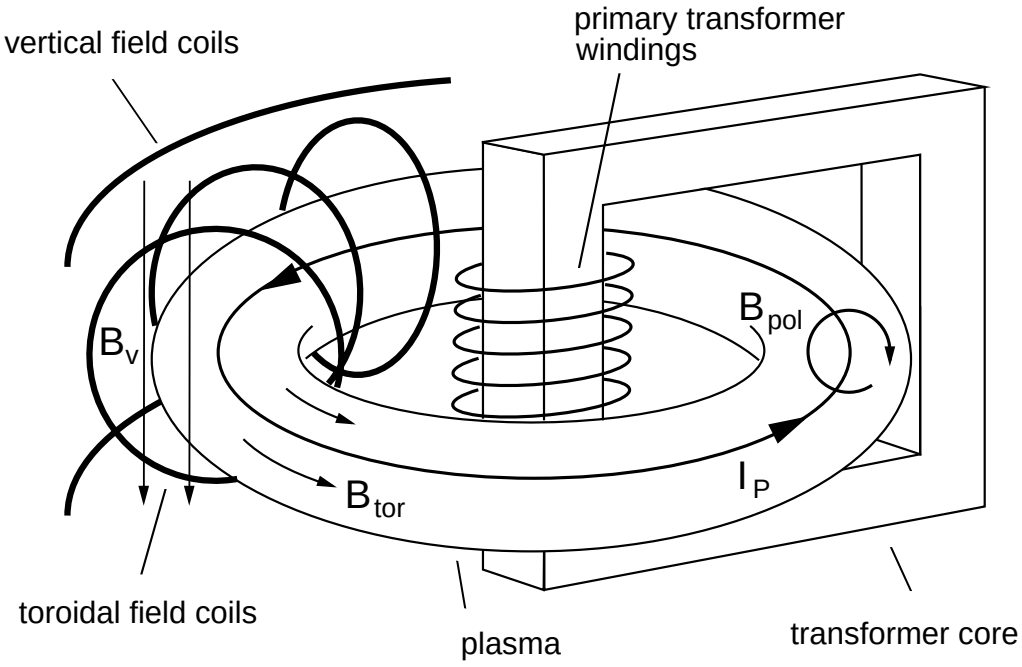

Figure 1.7: *The tokamak magnetic confinement uses three magnetic fields: the toroidal field B_ϕ, the poloidal field B_θ, and the vertical field B_v (for plasma control). The poloidal field B_θ is generated by the internal plasma electric current, which is inductively generated by the central solenoid.*

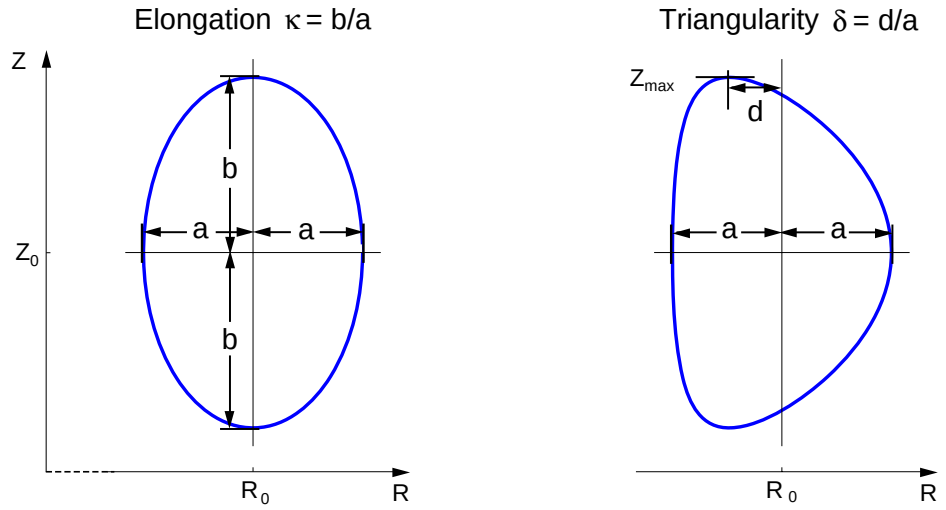

Figure 1.8: *Definition of the elongation κ (left), and the triangularity δ, (right) for a plasma with minor radius a.*

assuming that there are no collisions. The twist of the field line on each surface is characterised by the safety factor q,

$$q = \frac{\Delta\phi}{2\pi} \tag{1.19}$$

where $\Delta\phi$ represents the variation in the toroidal angle after a full poloidal turn of the field line. If $q = m/n$ with m and n being integers, the magnetic field line closes up on itself after m toroidal and n poloidal rotations. A field line with q=2 is illustrated in figure 1.6. We will see that rational surfaces (flux surfaces characterised by a rational value of the parameter q) play an important role in plasma stability.

At the plasma centre the magnetic field is purely toroidal and defines the so-called magnetic axis. Owing to the $1/R$ dependence of the toroidal magnetic field, we can define the High Field Side, HFS, (where $B > B_0$) and the Low Field Side, LFS, (where $B < B_0$) of the torus, with respect to the magnetic axis (B_0 is the magnetic field on the magnetic axis).

One method to produce poloidal magnetic field and magnetic surfaces is to induce an electric current flowing into the plasma, as in the so-called *tokamaks*, the Russian acronym for "Toroidalnaja Kamera Magnitnymi Katushkami" (figure 1.7). An excellent guide on the tokamak concepts, physics, present and past experiments can be found in reference [4].

The plasma current is usually induced by a transformer action in which the central solenoid acts as the primary coil and the plasma column as a secondary winding (see figure 1.7). The toroidal geometry and the plasma pressure act as an outward radial force (similarly to a bladder) which tends to expand the plasma column. This force can be balanced by the $\vec{j} \times \vec{B}_v$ force generated with an external vertical magnetic field $\vec{B}_v$ generated and the plasma current $\vec{j}$.

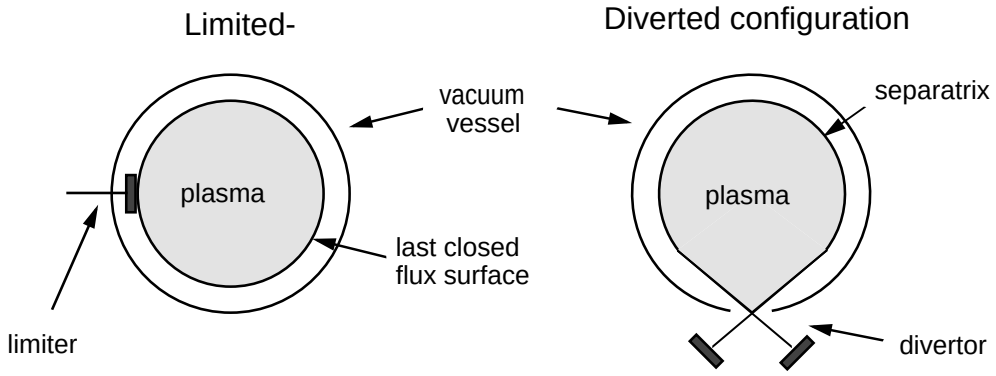

Figure 1.9: *Separation of the plasma from a vessel wall using a limiter (left) or a divertor (right) configuration.*

It has been shown that the plasma shape influences the stability and transport properties of the plasma. To characterise different plasma shapes we can use the elongation κ and the triangularity δ parameters, which are shown in figure 1.8.

To separate the plasma from the vessel wall, two main configurations can be employed, as shown in figure 1.9. In the limiter configuration the plasma outer boundary is defined using a material limiter, whereas in the divertor configuration the magnetic field structure is appositely modified to produce a magnetic divertor.

Tokamak devices have the advantage of retaining the toroidal symmetry (axisymmetry $\Longleftrightarrow \partial/\partial\phi = 0$) and are therefore essentially two-dimensional systems. On the other hand, the necessity of inducing the plasma current allows only for pulsed operation, therefore reducing the efficiency as a fusion power plant. Recently, techniques to drive the current by other means (such as plasma waves or ions beams) have been developed and successfully applied, opening the route toward continuous tokamak operation.

Other magnetic configurations can be conceived, in which the poloidal magnetic field is produced by an external magnetic coil. Such configurations, as in stellarators, are non-axisymmetric and in general much more complex, but have the advantage of an intrinsic continuous operation.

At the present date the highest $nT\tau_E$ triple product values have been achieved in tokamaks devices, which have therefore been chosen as the leading technology for the foreseen future fusion reaction experiment (ITER) and the experimental nuclear power plant (DEMO).

1.4 Plasma heating

Several methods to heat the plasma can be used to reach the required fusion temperature (of hundreds of millions K):

- Ohmic heating. Due to the intrinsic plasma resistivity η, the toroidal plasma

current $\vec{j}$ heats the plasma. The Ohmic power density is given by

$$P_\Omega = \eta j^2 = \vec{E} \cdot \vec{j}. \tag{1.20}$$

The plasma resistivity decreases with increasing electron temperatures as $T_e^{-3/2}$. Therefore the current density increases with the applied ohmic power (and loop voltage) but is limited by stability requirements which impose a maximum P_Ω. The achievable temperature increases with the toroidal magnetic field. However, the magnetic fields generated by today's superconducting magnets are not sufficient to obtain the temperatures required for fusion. Supplementary heating methods are therefore necessary.

- Neutral beam injection. It consists in the injection of beams of fast neutral particles. Hydrogen or deuterium atoms with typical energy of 50–100 keV are frequently used. They can penetrate the interior of the plasma, since they are not influenced by the magnetic field, and are ionised by colliding with the plasma electrons and ions, or by charge exchange reaction. Once ionised, they are confined by the magnetic field and release their energy and momentum through collisions with the other particles.

- Plasma wave heating. It consists in the excitation of electromagnetic waves into the plasma. In addition to collisional absorption (thermalisation), a variety of resonant interactions is possible with different plasma waves allowing for several heating schemes. For an efficient coupling and absorption, the plasma wave must be excited and able to propagate to the resonant region (or resonant layer). Here the wave frequency approaches resonant frequencies such as the ion or electron cyclotron frequencies,

$$\omega_{ci} = \frac{q_i B}{m_i} \tag{1.21}$$

$$\omega_{ce} = \frac{eB}{m_e} \tag{1.22}$$

or other hybrid frequencies and their higher harmonics.

In tokamaks ion cyclotron frequencies are typically in the MHz range while electron cyclotron frequencies are approximately 1000 times higher (ranging up to 200 GHz). The electron cyclotron resonance heating (ECRH) has the advantage that the plasma wave can propagate in vacuum, therefore allowing for the antenna to be located far from the plasma boundary. Moreover due to the B-dependence of the resonance frequency and the properties of the resonance layer ERCH techniques permit to have a highly localised absorption, and to modify the electron temperature and current profile by directly heating the electrons.

The wave polarisation can also be adapted to optimise the coupling with the plasma. For a wave which propagates perpendicular to the magnetic field ($\vec{k} \perp \vec{B}$) two independent modes exist: the ordinary mode (O-mode), where

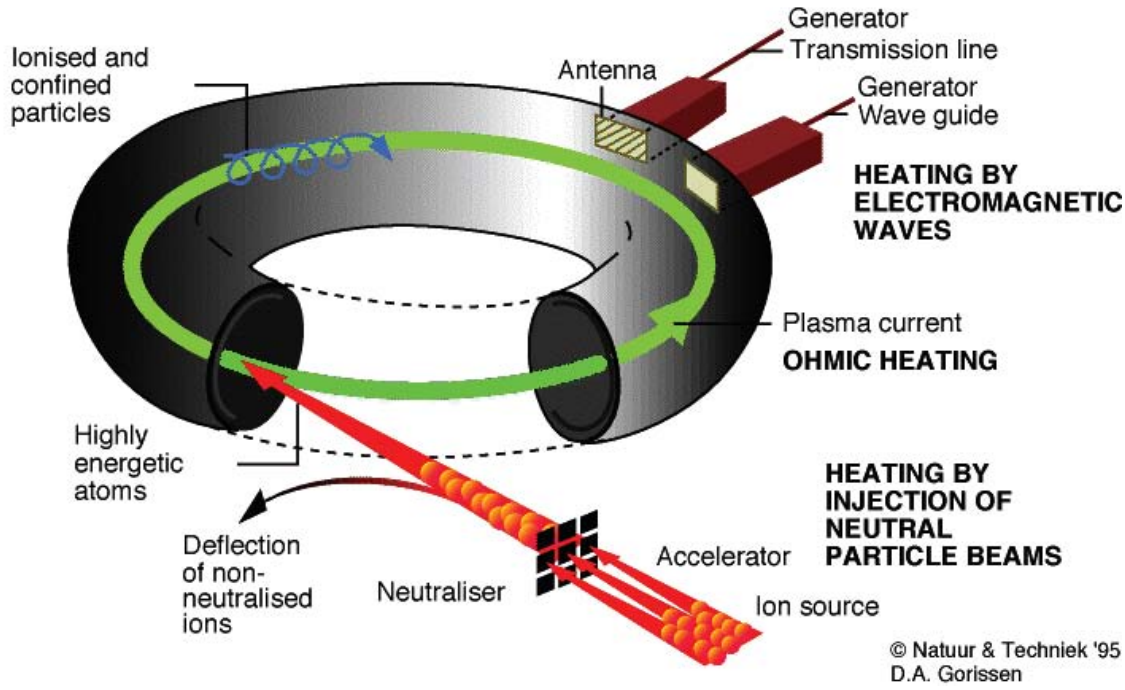

Figure 1.10: *Main heating techniques of a tokamak plasma: ohmic, neutral beam injection, and electromagnetic waves absorption.*

the incident wave electric field is parallel to the background magnetic field, and the extraordinary mode (X-mode), where the incident wave electric field is perpendicular to $\vec{B}$.

The propagation of these waves (with frequency ω) can be described by their refractive index N,

$$N_O^2 = 1 - (\omega_{pe}/\omega)^2 \tag{1.23}$$

$$N_X^2 = (1 - (\omega_{pe}/\omega)^2 - \omega_{ce}/\omega)\frac{1 - (\omega_{pe}/\omega)^2 + \omega_{ce}/\omega}{1 - (\omega_{pe}/\omega)^2 - (\omega_{ce}/\omega)^2} \tag{1.24}$$

where $\omega_{pe} = (e^2 n_e/\epsilon_0 m_e)^{1/2}$ is the plasma frequency. If the refractive index is zero (or imaginary) the wave is evanescent, and is reflected. The locus where the refractive index reaches zero is called *cut-off* region. The non-collisional absorption is maximal when N tends to infinity, the so-called *resonance* condition.

The O-mode exhibits a resonance when temperature effects are included in the calculation of the wave dispersion. Unfortunately its absorption is relatively weak, therefore limiting the heating efficiency. The X-mode has in general a better absorption, but the cut-off frequency depends on the magnetic field. The wave can therefore be reflected (depending on plasma conditions) before reaching the resonance region. On the contrary for the O-mode

the cut-off ($\omega_{co} = \omega_{pe}$) does not depend on the magnetic field but limits the accessibility at high density.

1.5 Motivations and structure of the manuscript

1.5.1 Motivations

This thesis addresses some aspects of plasma stability and confinement. If focuses on the effect of plasma shaping upon (mainly) current driven modes and on the instabilities observed in TCV advanced scenarios with very large and localised pressure gradients. Through an analysis and interpretation of the measurements, the instabilities and the conditions leading to their occurrence can be characterised. A comparison with the existing theories will then lead to a deeper understanding of the physics involved.

When they do not lead to discharge disruption, plasma instabilities increase the radial transport of particle energy and momentum, lowering the confinement time and the achievable pressure (for a given input power) and thus the triple product (equation 1.17). This can be compensated by building larger machines but also leads to higher costs. Avoiding or controlling instabilities is therefore desirable as it may lead to a more economical fusion reactor. In particular, controlling instabilities through plasma shaping is highly desirable because it has a relatively low cost compared to other means. The TCV tokamak is well suited to study the shape effects on MagnetoHydroDynamic (MHD) stability given its flexible design and control system. The powerful heating system allows for the attainment of high temperatures and pressures. More importantly, it provides a local power deposition which allows tailoring the pressure and current profiles and to test and improve the plasma stability. The first part of this thesis is dedicated to the experimental study of the plasma instabilities.

It has been recently recognised that another means of improving and modifying the plasma stability and confinement is through plasma rotation. Recent diagnostics improvements in the TCV tokamak allows us to study and characterise the plasma rotation without an external momentum input: this condition is unusual in today's large tokamaks but will be common in future experiments such as ITER. It is thus important to study what is sometimes called "spontaneous rotation". This is the aim of the second part of this thesis.

1.5.2 Outline of the thesis

The manuscript is divided into three parts. In the introductory part, after a brief overview on nuclear fusion and tokamak concepts given in this chapter, we will describe the TCV experiment and some of the diagnostics (chapter 2). In chapter 3 the most relevant (to this thesis) elements of plasma theory are highlighted.

The second part of this thesis is dedicated to the study of plasma instabilities. In chapter 4 the analysis methods and the models used for the interpretation of

experimental data are described. Then we present original results on the effect of plasma shaping on MHD modes (chapter 5), the stabilisation of the well-known sawtooth instability with appropriate shape (chapter 6), and current control and the MHD modes in plasmas with electron transport barriers respectively (chapter 7).

The third part is devoted to plasma rotation studies. After a short introduction on the subject in chapter 8, we describe in detail the stationary rotation profiles in the Ohmic limited L-mode scenario (chapter 9). The main features of momentum transport phenomena observed in the TCV tokamak are described in chapter 10, and analysed with a phenomenological model to get insight into the physical processes involved. Finally, conclusions are drawn on the presented work and proposals for future work outlined (chapter 11).

Chapter 2

MHD instabilities and equilibrium

In this chapter we discuss some theoretical aspects of MHD stability theory in tokamaks. Various instabilities caused by current and density gradients are introduced.

2.1 Magnetohydrodynamics theory

A plasma can be modelled as an ionised gas consisting of both charged and neutral particles. A complete statistical description of plasma dynamics involves an equation for the distribution function (the so-called Boltzmann equation) for each particle specie (electron, ions, impurities, etc.), coupled with the Maxwell equations for the macroscopic $\vec{E}$ and $\vec{B}$ fields. However, solving such a system of equations is in general rather complicated, and simpler models have been developed for practical applications. Fortunately, a thermonuclear plasma can be considered, in general, as quasi-neutral,

$$\sum_i eZ_s n_s \approx 0 \tag{2.1}$$

where Z_s and n_s are the charge and the density of the s particle specie. In this sense, a plasma may also be modelled as a single, neutral, conducting fluid. An external magnetic field can influence the motion of such a fluid, and the theory describing this motion is called magnetohydrodynamic (MHD) theory. A complete derivation and mathematical description of the MHD theory can be found in many textbooks [6, 7, 4]. We will introduce here only the main concepts needed to understand the following.

To describe the resistive MHD fluid, besides the Maxwell equations, we need to take into account also the mass conservation and force balance, as well as the

generalised Ohm's law

$$\nabla \times \vec{B} = \mu_0 \vec{j} \tag{2.2}$$

$$\nabla \times \vec{E} = -\frac{\partial \vec{B}}{\partial t} \tag{2.3}$$

$$\nabla \cdot \vec{B} = 0 \tag{2.4}$$

$$\frac{\partial \rho}{\partial t} = -\nabla \cdot (\rho \vec{v}) \tag{2.5}$$

$$\rho \left(\frac{\partial \vec{v}}{\partial t} + (v \cdot \vec{\nabla}) \vec{v} \right) = \vec{j} \times \vec{B} - \nabla \cdot P \tag{2.6}$$

$$\vec{E} + \vec{v} \times \vec{B} = \eta \vec{j} \tag{2.7}$$

where $\vec{v}$ is the fluid velocity, μ_0 the vacuum magnetic permeability, $\rho = \sum_s m_s n_s$ the mass density with m_s the mass of the particle specie s, η the electrical resistivity, j the electrical current, and P the pressure tensor. We also neglect the displacement current in the Maxwell equation 2.3. This set of single-fluid equations (equations 2.3–2.7) is still incomplete. Closure requires in fact assumptions concerning the pressure tensor P. We choose to complete the set of equations by assuming an isotropic pressure tensor $P = Ip$ and an adiabatic behaviour,

$$\frac{\partial p}{\partial t} + \vec{v} \cdot \nabla p = -\gamma p \nabla \cdot \vec{v} \tag{2.8}$$

with $\gamma = 5/3$ being the ratio of the specific heat.

By taking the curl of equation 2.7 one finds an equation governing the evolution of the magnetic field,

$$\frac{\partial \vec{B}}{\partial t} = \nabla \times \left(\vec{v} \times \vec{B} \right) + \frac{\eta}{\mu_0} \triangle \vec{B}. \tag{2.9}$$

The first term at the right hand side describes the variation of the magnetic field due to the convection of the field moving with the plasma. The second term gives the variation of the magnetic field by diffusion driven by gradients, and with a diffusion coefficient η/μ_0. In the case of a perfectly conducting plasma ($\eta = 0$) the magnetic flux through any surface moving with the plasma remains constant. This means that the magnetic flux is "frozen" into this fluid and forced to move with it. In this case the MHD theory is called ideal MHD theory.

2.2 Magnetohydrodynamic equilibrium of a tokamak plasma

In a stationary plasma ($\partial/\partial t = 0$) with the assumption of zero fluid velocity, $\vec{v} = 0$, the force balance equation 2.7 is written as

$$\nabla p = \vec{j} \times \vec{B}. \tag{2.10}$$

A scalar multiplication of equation 2.10 with $\vec{B}$ yields $\vec{B} \cdot \nabla p = 0$. Thus, there are no pressure gradients along the magnetic field lines. The magnetic field lines lay on the nested surfaces of constant pressure which coincides with the magnetic flux surfaces (see section 1.3). Similarly, a scalar multiplication of equation 2.10 with $\vec{j}$ yields $\vec{j} \cdot \nabla p = 0$, implying that currents only flow tangential to flux surface. Owing to $\nabla \cdot \vec{B} = 0$ the poloidal magnetic flux defined as,

$$\psi_{\rm pol} = \int_{A_{\rm pol}} \vec{B} \cdot d\vec{A} \tag{2.11}$$

and the toroidal magnetic flux,

$$\psi_{\rm tor} = \int_{A_{\rm tor}} \vec{B} \cdot d\vec{A} \tag{2.12}$$

with $A_{\rm pol}$ and $A_{\rm tor}$ being arbitrary poloidal and toroidal cross-sections of a flux surface, are both constant on magnetic flux surfaces. The introduction of ψ_{pol} and $\psi_{\rm tor}$ allows us to rewrite the definition of the safety factor (equation 1.19) as,

$$q = \frac{d\psi_{\rm tor}}{d\psi_{\rm pol}}. \tag{2.13}$$

This definition, valid for a general toroidal configuration, is used across this thesis, with no cylindrical approximation. The cylindrical coordinates (R, ϕ, Z) are well suited to describe a toroidal asymmetric equilibrium. The toroidal vector unit is $\hat{e}_\phi = R\nabla\phi$. Owing to the ignorable ϕ coordinate, the magnetic field in the axisymmetric case can be written as,

$$\vec{B} = \nabla \times (A_\phi \hat{e}_\phi) + B_\phi \hat{e}_\phi = \nabla \times \psi \nabla\phi + B_\phi \hat{e}_\phi. \tag{2.14}$$

where we have defined the stream function, $\psi = RA_\phi$. By replacing $\vec{B}$ in equation 2.11 with its expression in equation 2.14, we recognise that $\psi_{pol} = 2\pi\psi$. We can express the component of the magnetic field in cylindrical coordinate as,

$$B_R = -\frac{1}{R}\frac{\partial\psi}{\partial R} \tag{2.15}$$

$$B_Z = \frac{1}{R}\frac{\partial\psi}{\partial Z} \tag{2.16}$$

Now using equation 2.14 and the Ampere's law into the force balance equation 2.10 we obtain a scalar equation for the equilibrium of an axisymmetric system, the so called *Grad-Shafranov* equation:

$$R\frac{\partial}{\partial R}\left(\frac{1}{R}\frac{\partial\psi}{\partial R}\right) + \frac{\partial^2\psi}{\partial R^2} = -\mu_0 R^2 p'(\psi) - I(\psi)I'(\psi) \tag{2.17}$$

where $I(\psi) = RB_\phi$ and $p' = \partial p/\partial\psi$. Equation 2.17 was derived under the assumption $\vec{v} = 0$ but it remains a good approximation if $\vec{v} \ll \vec{v}_s$ with $\vec{v}_s$ the plasma sound velocity, a condition well satisfied for the TCV plasmas (chapter 9). The

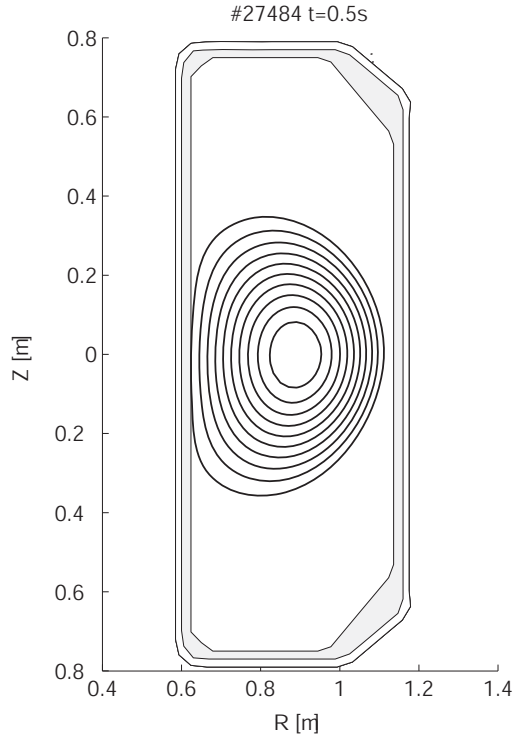

Figure 2.1: *Equilibrium nested flux surfaces of a real TCV plasma calculated by solving the Grad-Shafranov equation.*

Grad-Shafranov equation is a non-linear elliptical differential equation, and must in general be solved numerically. From the solution of equation 2.17, a displacement of the centre of the flux surfaces $\Delta(\psi)$ in the direction of the major axis R with respect to the outermost flux surface can be derived. The displacement of the magnetic axis is called Shafranov-shift Δ_0. This shift causes a closer packing of the magnetic surfaces at the LFS of the torus (figure 2.1).

An important equilibrium parameter is the magnetic shear,

$$s(\rho) = \frac{\rho}{q}\frac{dq}{d\rho} \tag{2.18}$$

where $\rho = \sqrt{\frac{\psi-\psi_0}{\psi_a-\psi_0}}$ is the normalised radial coordinate. ψ_0 and ψ_a are calculated respectively on the magnetic axis and the plasma boundary.

To define the efficiency of confinement, the averaged plasma pressure $< p >$ is divided by the strength of the magnetic field defining the dimensionless parameter:

$$\beta = \frac{< p >}{\langle B^2/2\mu_0 \rangle}. \tag{2.19}$$

β strongly influences the behaviour of the plasma stabilities, as we will discuss below.

Table 2.1: *Examples of instabilities relevant for TCV plasmas.*

Driven by:	**Ideal**	**Resistive**
current gradient	Kink mode	Tearing mode
pressure gradient	Ballooning mode	
both gradients	Internal kink ($m = 1$) mode	

A similar figure of merit can be written in terms of the flux surface averaged poloidal magnetic field B_p only,

$$\beta_p = \frac{< p >}{\langle B_p^2 / 2\mu_0 \rangle} \tag{2.20}$$

It can be shown [6, 8] that β_p is related to the diamagnetic properties of the plasma. If $\beta_p < 1$ the plasma is paramagnetic because the toroidal field is larger than in vacuum, if $\beta_p > 1$ the plasma is diamagnetic and the toroidal field is smaller than in vacuum.

2.3 Magnetohydrodynamic stability

MHD theory has proven to provide a satisfactory description of plasma equilibrium as well as instabilities with relatively low frequencies. In the MHD model, the main destabilising forces in a tokamak are due to the gradients of the plasma current density and pressure, which contain the free energy of the plasma. MHD instabilities can be divided into *ideal modes*, which do not depend critically on the plasma resistivity, and *resistive modes* which depend on the finite resistivity of the plasma. A second frequent characterisation of instabilities is based on whether the mode structure requires any motion of the plasma vacuum boundary (external modes) or not (internal modes). In a helical magnetic field, each mode can be characterised by its m and n mode numbers. In this case, m stands for the number of wavelengths of the modes on the poloidal circumference, and n for the number on the toroidal circumference. It may be seen that a geometrical resonance occurs at the magnetic surface where $q = m/n$.

The magnetic shear is the main stabilising factor against geometrically resonant perturbations in closed magnetic configurations. Magnetic field line bending and plasma compression oppose to the perturbations, and thus help to stabilise the magnetic configuration. Typical instabilities and their main source of free energy are given in table 2.1.

In the following, only the MHD modes relevant for this thesis will be discussed. The experimental observation of these modes and the analysis of their structure and occurrence will be given in the second part of this thesis. A complete review, derivation and discussion of the MHD modes may be found in [7, 6].

2.3.1 Ideal instabilities: the internal kink mode

To describe the stability of ideal MHD modes the concept of potential energy δW is used. The following energy principle may be formulated [6]: a plasma is stable if the potential energy $\delta W(\vec{\xi})$ of the plasma and the magnetic field is positive for any physically allowable perturbation $\vec{\xi}$.

For low-β plasmas, the main destabilising factor is the radial gradient in the parallel current. Since they minimise the field line bending, small mode numbers are the most unstable. They are often referred to as *kink modes*.

For a circular, low-β plasma in the straight tokamak approximation, without a conducting wall, the potential energy for a perturbation with a radial displacement $\xi(r)e^{i(m\theta-n\phi)}$ is,

$$\begin{aligned}\delta W &= \frac{2\pi B_0^2}{\mu_0 R_0}\left(\int_0^a \left[r\left(\frac{d\xi}{dr}\right)^2 + (m^2-1)\xi^2\right]\left(\frac{n}{m}-\frac{1}{q}\right)^2 rdr + \right. \\ &\left. \left[\frac{2}{q_a}\left(\frac{n}{m}-\frac{1}{q_a}\right) + (1+m)\left(\frac{n}{m}-\frac{1}{q_a}\right)^2\right] a^2\xi_a^2\right). \qquad (2.21)\end{aligned}$$

The role of ξ_a and the sign of $n/m-1/q_a$ in equation 2.21 lead to different stability properties of internal and external modes.

Since in first approximation the perturbation of an internal kink mode does not affect the plasma boundary ξ_a, the second term on the R.H.S. of equation 2.21 can be neglected. For $m > 1$ the remaining integral is always positive, and the internal mode is generally stable. It can be shown that the $m = 1$ mode on the $q = 1$ surface is marginally stable, and pressure effects need to be included in δW. It was shown by *Bussac et al.* [9] that for simple current profiles toroidal effects such as the coupling to the $m \pm 1$ sidebands stabilise the internal kink mode up to $\beta_{p,1} \approx 0.3$. Here, the poloidal beta is defined as,

$$\beta_{p,1} = \frac{< p >_1 - p(r_1)}{B_p(r_1)^2/(2\mu_0)} \qquad (2.22)$$

where $<>_1$ denotes a volume average inside the $q = 1$ surface, and r_1 the radial position of the $q = 1$ surface. However, the shaping of the poloidal plasma cross-section can largely modify the critical value of $\beta_{p,1}$. Shaping effects will be discussed in chapter 6.

The internal kink mode can generally be avoided by maintaining $q_0 > 1$ (the suffix $_0$ indicates values on the magnetic axis). Although these profiles are MHD stable, operating Ohmically heated plasmas at $q_0 > 1$ is experimentally rather complicated, owing to the conductivity dependence on the temperature, $\sigma \propto T_e^{3/2}$, which leads to a peaking of the current profile. In TCV $q_0 > 1$ may be maintained by applying strong EC current drive (see chapter 7).

For high-β plasmas pressure terms have to be taken into account in δW. For sufficiently large β, internal kink modes with $m > 1$ can be destabilised. These modes are sometimes referred to as *infernal modes*. In TCV, infernal modes are

held responsible for disruptions and rapid collapses in plasmas with extremely high and localised pressure gradients (see chapter 7 and [10]).

Even if a movement of the plasma boundary is allowed, modes with a resonant surface inside the plasma, $m/n < q_a$, result in the low-β approximation in a positive energy functional (equation 2.21), and are always stable. Since q increases outside the plasma, modes with resonant surfaces outside the plasma, $m/n > q_a$, can be unstable. In particular, plasmas with $m > 1$ and current profiles with large current gradients close to the edge are unstable. In this case the current has to be sufficiently peaked in the centre. For example in the case of the so-called *Shafranov profiles* [11],

$$j(r) = \begin{cases} j_0 & \textit{for } r < r_0, \\ 0 & \textit{for } r_0 < r < a \end{cases} \tag{2.23}$$

the stability requirement is

$$q_a > [q_0] + 1 \tag{2.24}$$

where $[q_0]$ represents the integer part of q_0. This imposes an upper limit to the total current $I_p \propto 1/q_a$, which depends on the central current density $j_0 \propto 1/q_0$.

A profile independent current limit is imposed by the external $m = 1$ mode. For a rigid displacement, $\xi = \text{const.}$, the integral term on the R.H.S. of equation 2.21 vanishes. The resulting potential energy is,

$$\delta W = \frac{4\pi^2 B_0^2}{\mu_0 R_0} n \left(n - \frac{1}{q_a} \right) a^2 \xi_a^2, \tag{2.25}$$

which depends solely on the total current, and not on the profiles.

The most restrictive stability requirement is found for $n = 1$, and leads to the well-known *Kruskal-Shafranov limit*, $q_a > 1$. In practice, the internal kink prevents the central safety factor from significantly decreasing below 1. In agreement with equation 2.24, the appearance of a $2/1$ kink-mode imposes the operational current limit, $q_a \geq 2$. As we will see in chapter 5, owing to the toroidal coupling between the external kink and internal resistive modes [12] (see section 2.3.2), this current limit becomes even more stringent in case of circular plasmas, effectively imposing the limit, $q_a \geq 3$. Fortunately, this limit can be overcome by proper plasma shaping during the plasma current rise. It is however possible to suppress the external kink mode by moving an ideal conducting wall sufficiently close to the plasma boundary.

2.3.2 Resistive Instabilities

When the finite resistivity of the plasma is taken into account, the ideal constraint of the flux frozen with the plasma fluid is broken. The magnetic field lines may diffuse through the plasma, and new states with lower potential energy become accessible. In particular the magnetic structure is allowed to change topology by *breaking and reconnecting* the magnetic field lines. These magneto-fluid motions are very common in tokamak plasmas, and lead to the formation of the so-called

magnetic islands. Rapid reconnection can only occur in the vicinity of a magnetic surface, where the perturbation is resonant and produces the magnetic island configuration.

It is convenient to discuss the magnetic field line geometry in the *helical coordinate system* ($\hat{e}_\rho$, $\hat{e}_\zeta$, $\hat{e}_\eta$), where $\hat{e}_\eta$ has the same helicity of the magnetic field on the resonant surface, $\hat{e}_\rho$ is perpendicular to the magnetic flux surface, and $\hat{e}_\zeta$ is perpendicular to both directions. When the perturbation has a single helicity (m, n) there still exists an ignorable coordinate, the helical coordinate η.

In the cylindrical approximation the radial flux coordinate ρ can be replaced with the minor radius r. The equilibrium field close to the resonant magnetic surface can be written as:

$$B_{\mathrm{eq}} = B_\eta = -\left(B_\theta \frac{q}{q'}\right)_s (r - r_s) \tag{2.26}$$

where r_s is the radial position of the resonant surface s, and $'$ denotes derivative with respect to r. A perturbation current along the field line causes a radial perturbation of the magnetic field. Supposing a single harmonic we can write,

$$B_r = \hat{B}_r \sin(m\zeta) \tag{2.27}$$

with $m\zeta = m\theta - n\phi$. The superposition of the equilibrium and the radial perturbation fields reveals the new topology [6].

A differential equation for the field line in the (r, ζ) plane is:

$$-\left(B_\theta \frac{q'}{q}\right)(r - r_s)dr = r_s \hat{B}_r \sin(m\zeta)d\zeta. \tag{2.28}$$

By integration we obtain the field line equation:

$$(r - r_s)^2 = \frac{w^2}{8}(1 - \cos(m\zeta)) \tag{2.29}$$

where we have defined the island width w as

$$w = 4r_s\sqrt{\frac{\hat{B}_r}{mB_\theta s}}. \tag{2.30}$$

Figure 2.2 illustrates the magnetic island geometry. Inside the island, the magnetic field lines lay on a set of helical magnetic surfaces with the magnetic centre indicated as the O-point. The magnetic surface that bounds the island is called separatrix. Two separatrices meet at the X-point.

Taking into account the field perturbation $\vec{B}_1$ and the velocity perturbation $\vec{v}_1$, equation 2.9 can be written in the following form:

$$\frac{\partial \vec{B}_1}{\partial t} = (\nabla \vec{B})\vec{v}_1 + \frac{\eta}{\mu_0}\triangle \vec{B}_1 \tag{2.31}$$

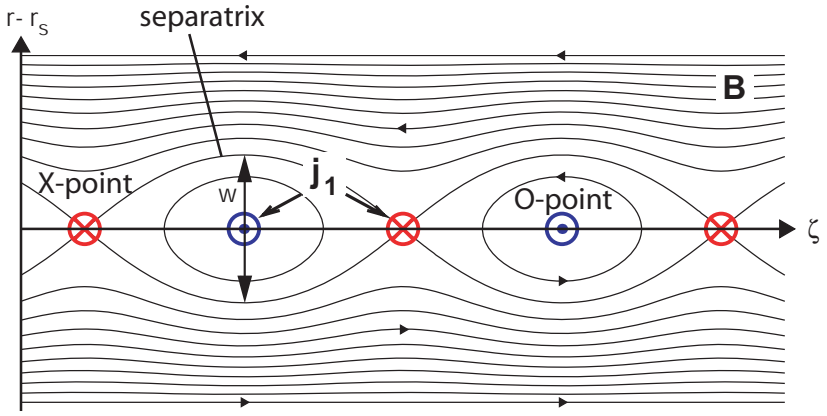

Figure 2.2: *Sketch of the magnetic island resulting from a radial perturbation of the magnetic field. The graphical definition of the island width is shown.*

or, expressed in flux coordinates for the radial component,

$$\gamma\psi + B'_\theta \left(\frac{m - nq}{m} v_{r,1} \right) = \frac{\eta}{\mu_0} \triangle\psi \tag{2.32}$$

where γ is the growth rate. The second term in the L.H.S disappears on the rational surface, and the term on the R.H.S. dominates despite the assumption of small resistivity. The integration of equation 2.32, and the matching of the perturbation between the resistive layer and the "ideal" layer outside the separatrix, allows us to describe the growth of the island:

$$\frac{dw}{dt} \approx \frac{\eta}{2\mu_0} \frac{\Delta'}{d} w \tag{2.33}$$

where we define Δ' as the jump of the logarithmic derivative of the radial field across the resistive layer,

$$\Delta' = \frac{B'_{r,1}(r_s + d/2) - B'_{r,1}(r_s - d/2)}{B_{r,1}(r_s)} \tag{2.34}$$

with d the width of the resistive layer. From equation 2.33 we see that Δ' determines whether the mode is stable ($\Delta' < 0$) or unstable ($\Delta' > 0$).

However, the linear theory used to derive equation 2.33 can not explain the experimental observation of modes with saturated amplitudes. Therefore nonlinear effects have to be considered. It was shown by Rutherford [13] that once the island grows as large as the resistive layer a force arises that opposes to the plasma flow reducing the growth of the mode.

Taking into account modifications of the equilibrium current profile as well as the island current profile leads to a quasi-linear decreasing of the driving term [14]. The island width evolves according to,

$$\frac{dw}{dt} = 1.66 \frac{\eta}{\mu_0} (\Delta' - \alpha w) \tag{2.35}$$

with α being a factor that depends on plasma local parameters.

In high-β plasmas various effects, such as the so-called bootstrap drive due to perturbations of the bootstrap current, modify the stability of the tearing mode, referred to as *neoclassical tearing mode* (NTM) in this regime. The growth of NTMs is described by the generalised Rutherford equation [15]:

$$\frac{\tau_R}{r_s}\frac{dw}{dt} = r_s\Delta' + r_s\beta_p a_{\rm BS}\frac{w}{w^2 + w_d^2(\nu_e)} \tag{2.36}$$

where τ_R is the resistive time on the resonant surface. The first term on the R. H. S. is the drive of a convectional tearing from the equilibrium current profile. The second term describes the destabilising effect of the perturbed bootstrap current $j_{\rm BS}$, being $a_{\rm BS} = a_2 L_q j_{\rm BS} B_{\rm pol}/p$, with $L_q = q/q'$ the scale length of the safety factor profile, and a_2 a numerical factor. The factor w_d gives a threshold island width below which the flattening of the pressure profile, and thus the loss of bootstrap current, is reduced.

An interesting property of NTMs is that they can grow even if $\Delta' < 0$. The growth however requires a minimum island size, a so-called *seed island*. Such an island can be created by MHD activities such as sawtooth oscillations.

NTMs cause a serious limitation to the achievable plasma pressure and must thus be avoided or suppressed.

Chapter 3

The TCV experiment

This chapter briefly describes the main features of the Tokamak à Configuration Variable (TCV), such as the plasma shaping and electron cyclotron resonant heating systems, and the main plasma diagnostics used in this thesis. The plasma equilibrium reconstruction, which is at the basis for the interpretation of the plasma parameter measurements, is also introduced.

3.1 The Tokamak à Configuration Variable

The *Tokamak à Configuration Variable* (TCV) at the Centre de Recherches en Physique des Plasmas (CRPP) is a medium size tokamak with a standard aspect ratio $1/\epsilon = R_0/a \backsimeq 3.5$, with R_0 and a being respectively the major and minor radius of the toroidal vacuum vessel. The main TCV parameters can be found in Table 3.1. TCV has been explicitly designed to allow the maximal flexibility in producing different plasma shapes and configurations, its aim being the study of the effects of plasma shaping on confinement and stability.

The flexibility in plasma shaping is achieved by 16 independently controlled poloidal field coils which are mounted outside the vacuum vessel (coils E1-8 and F1-8 in figure 3.1). In particular, the operation at high plasma elongation requires a good control of the vertical plasma position, which is achieved by a combination of passive elements and active feedback control. The toroidally continuous, highly conducting vessel wall acts as a passive shell allowing eddy currents which oppose changes in the equilibrium.

TCV also features a powerful and flexible Electron Cyclotron Resonance Heating (ECRH) system, which is optimal to study plasmas with electron temperature much larger than the ion temperature: $T_e \gg T_i$.

As much as 90% of the internal surface of the stainless steel vacuum vessel is covered with 24 mm thick graphite tiles, designed to withstand the large power

Table 3.1: *Main parameters of the TCV machine.*

Parameter	Symbol	Value
Major radius	R_0	0.88 m
Minor radius	a	0.25 m
Aspect ratio	$1/\epsilon$	≈ 3.5
Vacuum vessel elongation	κ_{TCV}	2.9
Vacuum vessel resistance	Ω_{TCV}	45 mΩ
Toroidal field on axis	B_0	$\leq$ 1.54 T
Plasma current	I_p	$\leq$ 1.2 MA
Loop voltage	V_{loop}	$\leq$ 10 V
Additional heating power (ECH)	$P_{\mathrm{ECRH,X2}}$	2.8 MW
	$P_{\mathrm{ECRH,X3}}$	1.4 MW
Discharge duration		$<$ 4 s

Table 3.2: *Typical parameters in Ohmic and ECRH TCV plasmas. The* $_0$ *suffix indicates values at the plasma centre.*

Parameter	Symbol	Value
Central electron density	n_{e0}	1–20 $\cdot$ 10^{1}9 m$-$3
Central electron temperature	T_{e0}	$\leq$ 1 keV (Ohmic)
		$\leq$ 10 keV (ECRH)
Central ion temperature	T_{i0}	$\leq$ 1 keV (Ohmic)
		$\leq$ 0.5 keV (ECRH)
Electron cyclotron frequency	$f_{\mathrm{ce}} = eB/(2\pi m_e)$	$\approx$ 41 GHz
Elongation at the edge	κ_a	1–2.82
Triangularity at the edge	δ_a	(-0.8)–(+0.9)

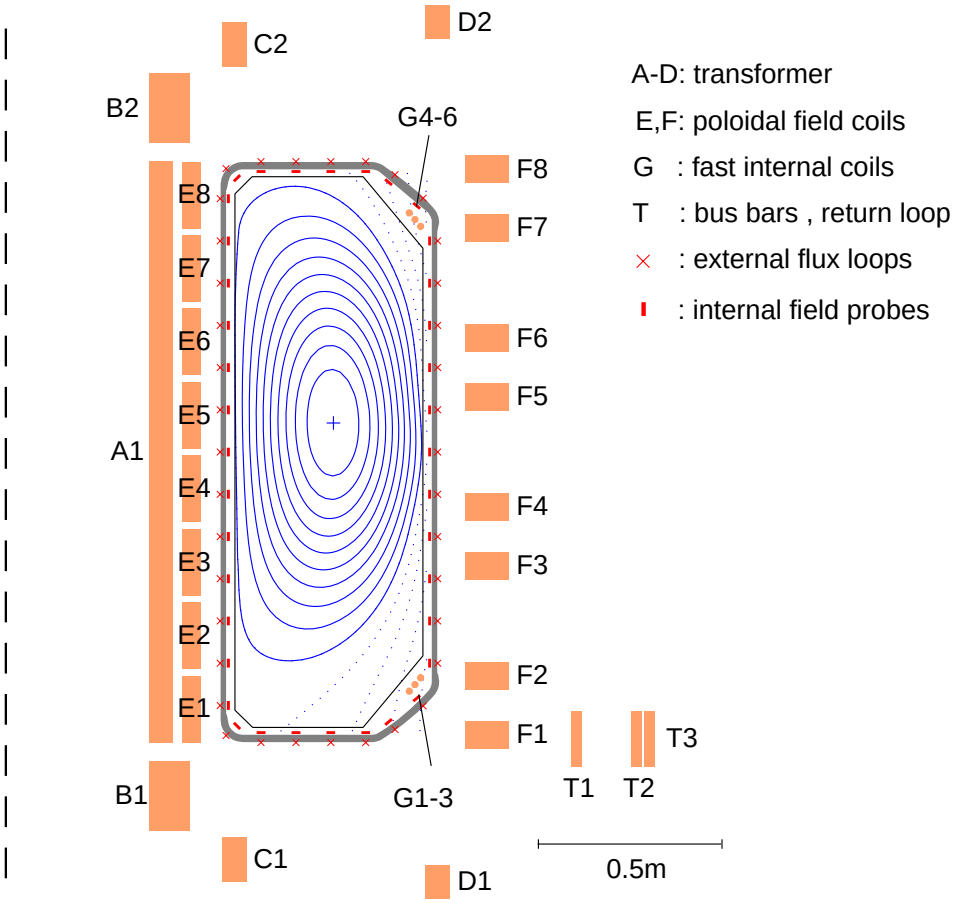

Figure 3.1: *Coil configuration showing the transformer windings (A,B,C,D), the poloidal field coils (E,F) and the fast internal coils (G). The magnetic configuration is measured with external flux loops (x) and internal poloidal field coils.*

fluxes (in particular during the ERCH) and minimize plasma contamination by metallic impurities. As a consequence, carbon is the main impurity in TCV plasmas.

The TCV flexibility allows us to obtain different plasma shapes and configurations (see figure 3.2), not only from one discharge to another, but during a single discharge. TCV has produced a wide range of limited and diverted plasmas. Low (L-mode) and High (H-mode) confinement plasmas are routinely produced in both limited and diverted configurations with purely Ohmic or Electron Cyclotron (EC) heating (see Table 3.2). More recently, plasmas with internal transport barriers have been produced using the Electron Cyclotron Current Drive (ECCD) capabilities of the ECRH system. Plasma currents up to 1 MA have been attained in the Ohmic regime, and purely wave currents up to 210 kA have been driven with EC waves.

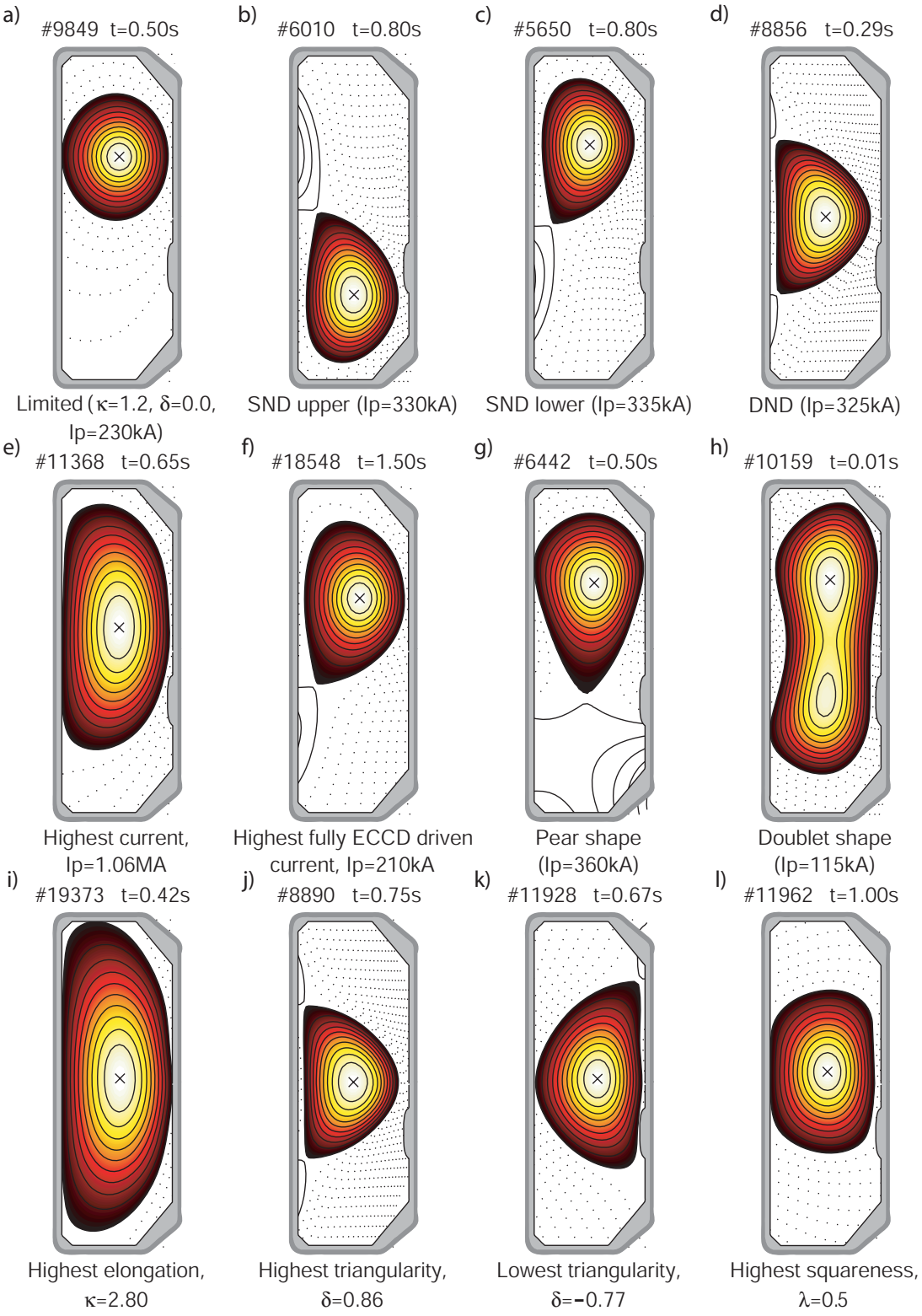

Figure 3.2: *TCV shapes*

3.1.1 Electron cyclotron heating system

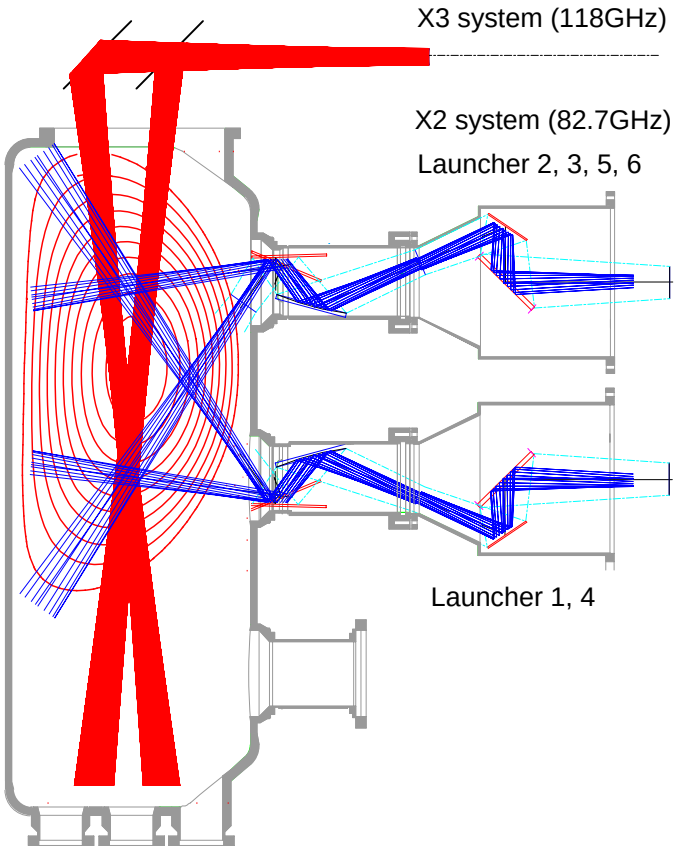

Figure 3.3: *Poloidal view of the TCV ECRH system*

The EC system consists of six 82.7 GHz gyrotrons coupled in two clusters for heating at the second harmonic of the electron cyclotron resonance, and a cluster of three 118 GHz gyrotrons for heating at the third harmonic.

The nominal power of each 82.7 GHz gyrotron is 0.5 MW, resulting in a total of 3 MW of nominal heating power at the second harmonic ($\sim$ 2.7 MW is delivered to the plasma) with a maximum pulse length of 2 s. The electromagnetic power is transmitted through high efficiency corrugated wave guides connected to a launcher. There are two second harmonic launchers on the equatorial ports (1, 4 with reference to figure 3.3) and four on the upper lateral ports (2, 3, 5, 6).

Each launcher has two degrees of freedom, one in the poloidal direction, and one in the toroidal direction. The poloidal injection angle may be varied by means of a steerable mirror during the discharge, which allows us to change the power deposition location. The toroidal angle may be varied in between discharges to allow for different parallel wave vectors which change the amount and/or the direction of the current drive. The polarisation of each beam can be adjusted to couple to the extraordinary "X" mode ($\vec{E} \perp \vec{B}$) or the ordinary "O" mode ($\vec{E} // \vec{B}$).

Since the absorption in the second harmonic X-mode is better than in the second harmonic O-mode, the polarisation of the beams is usually set to X-mode. In the following we will refer to the X-mode as X2, in case of heating at the second harmonic, and as X3 for heating at the third harmonic.

The cut-off density (see section 1.4) for the X2 wave is $n_e \sim 4{\cdot}10^{19}\mathrm{m}^{-3}$. In order to extend the accessible density up to $n_e \sim 1.1{\cdot}10^{20}\mathrm{m}^{-3}$, the 118 GHz gyrotrons for X3 heating were recently added. A common launcher for the 118 GHz gyrotrons is located at the top of the vessel to maximise the path of the microwave beam along the resonance surface in the plasma, and thus maximise the absorption. Each gyrotron provides 0.46 MW and a total of 1.4 MW of heating power with a maximum pulse length of 2 s. The injection of the heating beam from the the low or high field side with respect to the resonance is determined by the position of a steerable mirror. Since the absorption efficiency is extremely sensitive to the angle of injection, especially at low power, a feedback system is required to maintain the optimal angle during the discharge [16].

3.2 TCV diagnostics

TCV is equipped with a comprehensive set of diagnostics, most of them offering a complete coverage of the highly elongated vacuum vessel. Standard diagnostics in TCV include the Thomson Scattering (TS) system, for measuring the electron temperature and density profiles, a multichannel far-infrared (FIR) interferometer measuring the line-integrated electron density, and several multichannel systems for plasma radiation measurement: a soft X-ray (X-TOMO) tomographic system, a multi-wire soft X-ray proportional detector (MPX), various foil bolometers and a diode bolometric system, and several HFS and LFS EC radiometers.

The magnetic equilibrium is reconstructed using several sets of flux loops and magnetic probes. A fast magnetic fluctuation diagnostic allows the monitoring of MHD activity. TCV was recently equipped with a diagnostic neutral beam injector (DNBI) and a Charge eXchange Resonance Spectroscopy (CXRS) system, their combined use allows us to obtain temperature and bulk velocity profiles of light impurities.

In the following, only the diagnostics providing the measurements relevant to this thesis work will be described.

3.2.1 Far-infrared interferometer (FIR)

The far-infrared interferometer measures the line-integrated density. It exploits the fundamental dependence of the refractive index on the plasma density.

In the high frequency limit ($\omega \gg \omega_{pe}, \omega_{ce}$), the phase difference $\Delta\phi$ between two laser beams, one travelling through the plasma and one travelling through air, is proportional to the electron density integrated along the path of the beam,

$$\Delta\phi = \frac{\lambda e^2}{4\pi c^2 \epsilon_0 m_e} \int n_e(l) dl \tag{3.1}$$

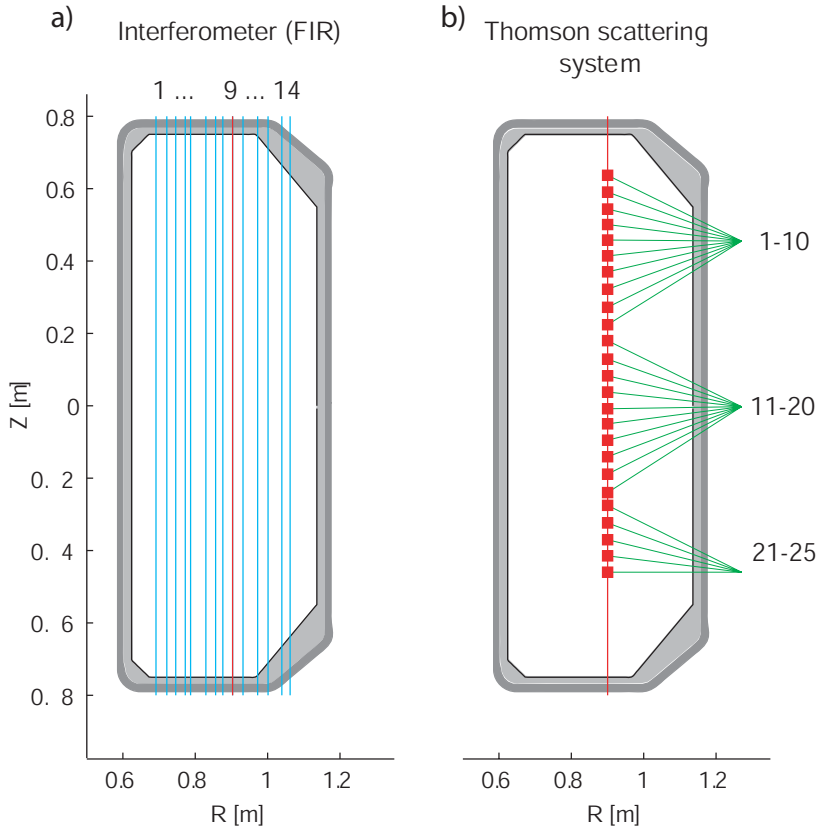

Figure 3.4: *Poloidal section of TCV with: a) 14 vertical chords of the FIR diagnostic. The red chord (#9) provides the measurement of the central density; b) 25 viewing chords of the Thomson scattering diagnostic. The dots mark the volume from which the scattered light is collected.*

where λ is the laser wavelength, and the line-integrated density $\bar{n}_e$ is given by,

$$\bar{n}_e = \frac{1}{L} \int n_e(l) dl. \tag{3.2}$$

where L is the length of the observation chord.

In TCV the FIR measures $\bar{n}_e$ along 14 vertical chords (figure 3.4) and is equipped with a 214.5 μm wavelength laser. This diagnostic is of fundamental importance for the density control during TCV operation. A feedback loop controls the injection of the neutral gas by comparing the measured central density (from the FIR chord $\#9$ at R=0.9 m) with the density required by the operator.

3.2.2 Thomson scattering diagnostic (TS)

The TS diagnostic is based on the spectral analysis of the light scattered by free electrons in the plasma. If the wave vector k_i of the input wave is sufficiently large,

yielding $k_i\lambda_D \gg 1$ (with Λ_D being the Debye length), particle correlations can be neglected, and the scattered power is the incoherent sum of powers from single electrons. The scattered field from a single electron moving with a velocity $\vec{v}_e$ has a frequency,

$$\omega_s = \omega_i + \left(\vec{k}_s - \vec{k}_i \cdot \vec{v}_e\right) \tag{3.3}$$

which is actually the Doppler shifted frequency with respect to the input wave of frequency ω_i. In the non-relativistic approximation and for a monochromatic incident wave, the frequency spectrum for a fixed scattering geometry is directly proportional to the one-dimensional velocity distribution in the direction along $\vec{k} = \vec{k}_s - \vec{k}_i$. Assuming a Maxwellian electron distribution, the electron temperature can be obtained from the width of the measured spectrum. The intensity of the scattered light is proportional to the electron density. Thus, density measurements can be obtained by integrating the signal over the width of the spectrum.

The TS system on TCV uses three lasers which operate at a pulse rate of 20 Hz. The beams are combined to form a closely spaced fan within a poloidal plane. From the side of the detection optics this fan appears as a single beam (see figure 3.4b)). Using alternate triggering of the lasers, higher sampling rates (60 Hz) can be obtained. Twenty-five viewing chords are distributed on three horizontal ports. The scattered light is analysed with filter polychromators with three or four spectral channels, which have been optimised for temperatures in the range 50 eV – 20 keV. The TS diagnostic is calibrated against Raman scattering from molecular nitrogen. The electron density measurement is cross-checked by comparing the line-integrated data to those obtained from the FIR interferometer.

3.2.3 Soft X-ray emission measurements

The soft X-ray emission of a plasma originates from the ion-electron and electron-impurity Bremsstrahlung, as well as from recombination radiation.

The Bremsstrahlung spectrum essentially depends on the density, temperature and impurity content. For a Maxwellian electron distribution of temperature T_e, and ions of charge Z, the continuous Bremsstrahlung spectrum is,

$$\frac{dN}{dE_X} \propto Z^2 n_e n_Z \frac{g_{\text{ff}} e^{-E_X/T_e}}{E_X\sqrt{T_e}} \tag{3.4}$$

with N being the number of emitted photons of an energy E_X, n the specie density, and g_{ff} the Maxwell-averaged Gaunt factor.

The calculation of the electron-impurity-ion recombination radiation requires detailed knowledge of the atomic structure of the impurity ion and usually dominates 3.4.

The TCV soft X-ray tomographic system consists of 10 linear detector arrays, each equipped with strips of 20 silicon diodes, and 47 μm thick beryllium absorption foils in front of each array. The arrays are distributed in 9 ports of a single poloidal sector to give full poloidal coverage (figure 3.5a)). The resulting 200 lines of sight are used to perform a tomographic reconstruction of the 2D emissivity for

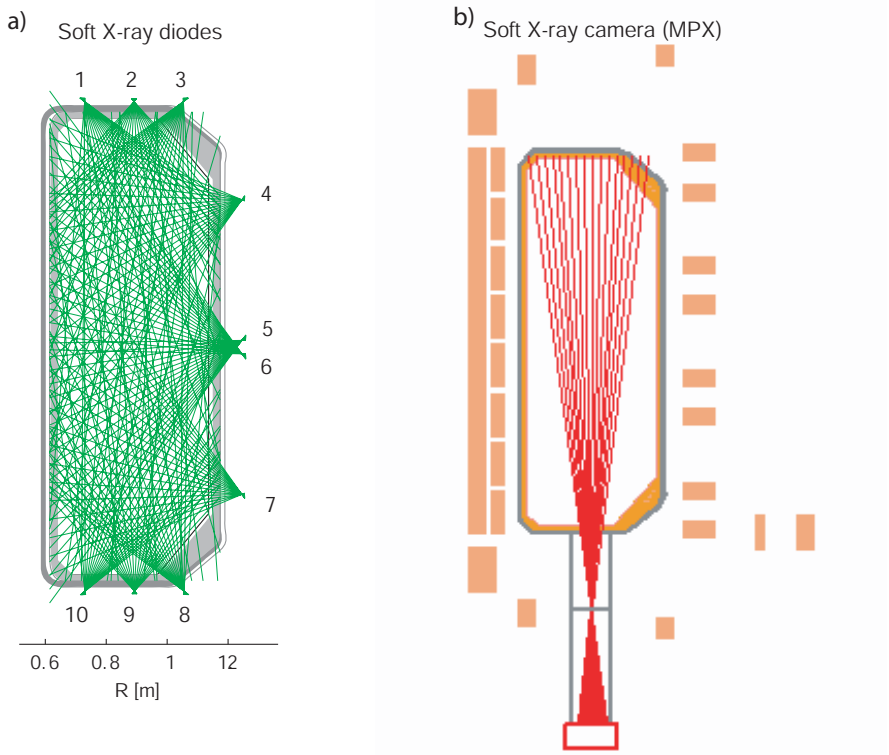

Figure 3.5: *View of the experimental setup of the TCV soft X-ray tomography system.*

virtually all possible plasma configuration on TCV, resulting in a spatial resolution of 3-4 cm and an acquisition rate up to 80 kHz [17].

A compact 64 channel Multiwire Proportional X-ray (MPX) detector is installed on a helium filled slot-hole camera and views the plasma through two beryllium windows (in total 100 μm thick). It measures soft X-ray emission in the 1–30 keV range with a radial resolution of about 8 mm. An additional 308 μm thick aluminium foil may be used to observe higher energy photons.

The MPX detector consists of a plane of parallel anode wires placed between two cathode plates. The anode plane has 64 independent sensitive wires. A constant negative voltage is applied to the cathodes. Each sensitive wire collects the electrons arising from photo-ionisation, and produces a continuous output current proportional to the incident x-ray intensity. The sensitive wires are connected to amplifiers.

Since the X-ray emissivity has a strong dependence on the electron temperature, density, and impurity mixture, the X-ray signals are very sensitive to the presence of MHD instabilities. In particular they allow the determination of the sawtooth inversion radius and the identification of the poloidal mode structure of the helical perturbations [17]. In particular, the high spatial resolution of the MPX camera allows the detection of the small scale structure of the perturbations. The soft X-ray diagnostics mainly measure parameters from the plasma centre,

and therefore provide complementary information to the magnetic measurements, which are described in the next section.

3.2.4 Fast edge magnetic perturbation measurements (Mirnov system)

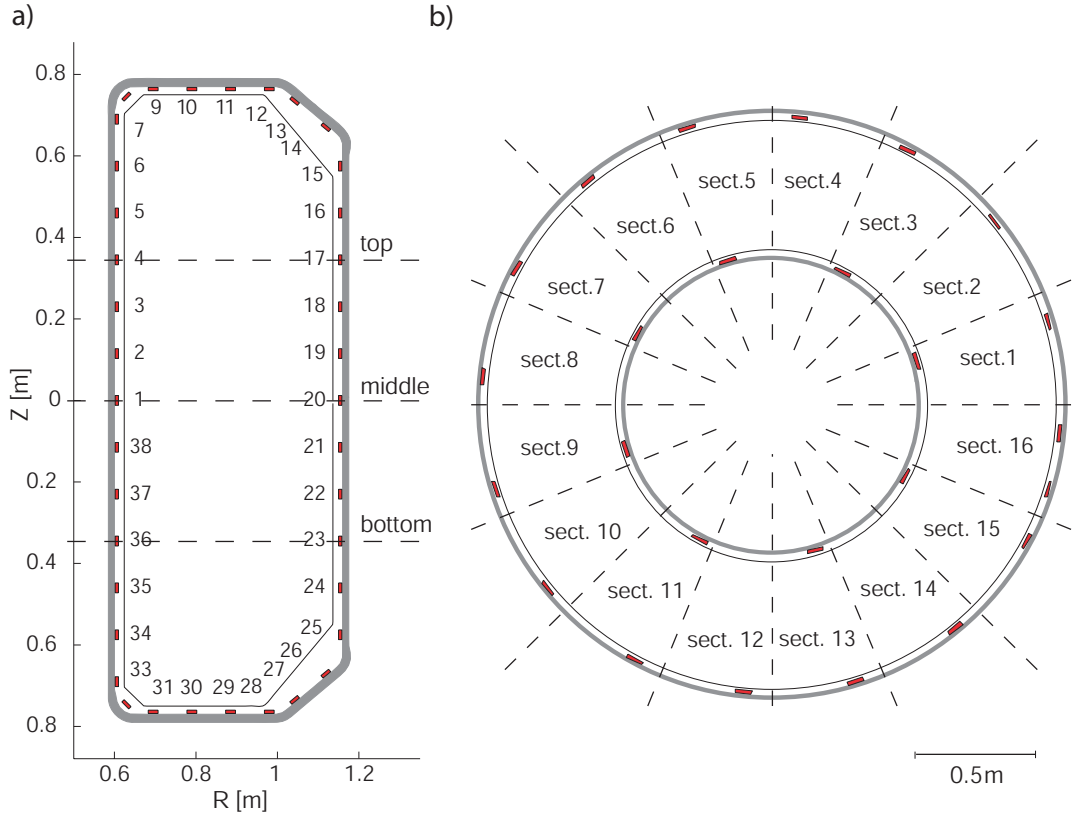

Figure 3.6: *Arrangement of the TCV magnetic probes in poloidal and toroidal arrays. (a): the 38 probes of each poloidal array are numbered clockwise starting on the equatorial mid-plane on the high field side of the vessel. The poloidal locations of the six toroidal arrays are indicated by the dashed lines. (b): full toroidal arrays consisting of 17 and 8 probes are located respectively on the LFS and HFS.*

Magnetic pick-up coils measure the time derivative of the magnetic flux, which induces the voltage,

$$U_p = -\frac{\partial}{\partial t}\int_{\text{probe}} \vec{B} d\vec{A}. \tag{3.5}$$

with A being the surface perpendicular to the main probe axis. Assuming that the variations of the magnetic field within the probe volume are small, the measurement gives the time derivative of the magnetic field along the axis of the probe. Since $(\vec{\nabla} \times \delta\vec{B})_r = 0$ in the absence of a radial current density, the poloidal perturbation field outside the plasma, δB_θ, is larger than the toroidal perturbation field,

δB_ϕ, typically by one order of magnitude. An alignment of the probes along the poloidal direction is therefore well suited for the analysis of the magnetic fluctuations.

The magnetic probes are arranged in different toroidal and poloidal arrays for optimal coverage. There are 6 toroidal arrays: 3 on the HFS with 8 equally spaced probes for each array, and 3 on the LFS with 16 equally spaced probes for each array (figure 3.6b). The three pairs of toroidal arrays are located at different vertical positions, respectively –35, 0 and +35 cm (figure 3.6a). Furthermore, the array on the LFS is complemented by an additional (17th) probe in sector 16, thus increasing the resolution of toroidal mode numbers up to n=16. Arrays located at two different vertical positions can not be simultaneously acquired.

There are 4 poloidal arrays with 38 magnetic probes each, located in sectors 3, 7, 11 and 15. They are toroidally separated by 90°. The probes are evenly distributed around the poloidal circumference as shown in figure 3.6a). The poloidal position is numbered clockwise starting on the equatorial mid-plane of the HFS of the vessel. Note that these probes are neither poloidally equidistant nor equally oriented with respect to the poloidal magnetic field. The inhomogeneities in the probe geometry has to be carefully taken into account in the interpretation of the MHD mode structure, as described in the next chapter. Currently, only one poloidal array is used for fast measurements.

The magnetic probes are mounted on the inside of the vacuum vessel, and they are protected from the plasma by graphite tiles. The use of poloidal field measurements for real-time control requires an absolute calibration with an uncertainty less than 1%. The probes are calibrated using the well-defined magnetic field of a Helmholtz coil in the range 100 Hz – 100kHz. The analog signals are amplified in two stages: close to the tokamak, and after the long transmission line in the acquisition room.

3.2.5 CXRS measurements of impurity temperature and rotation velocity

The first wall of TCV being almost completely covered by carbon tiles, carbon constitutes the main impurity in TCV deuterium discharges. The impurity temperature and toroidal velocity are measured by Charge eXchange Recombination Spectroscopy, analysing the fully ionised carbon (CVI) H-like 529.1 nm emission line induced by the DNBI [18, 19]. The experimental setup is shown schematically in figure 3.7 (the convention on the directions of the plasma current and toroidal field is also shown).

The CXRS diagnostic is arranged with 8 horizontal viewing chords crossing the neutral beam. The observation points, corresponding to the intersection between the diagnostic chords and the neutral beam, are located at the midplane of the vacuum vessel, covering the LFS profile from R=0.885 m to R=1.065 m. They have 2.5 cm radial resolution (figure 3.8), with a 1 cm uncertainty mainly due to the radial extent of the emitting volumes.

During plasma discharges, the DNBI power is modulated in a sequence of

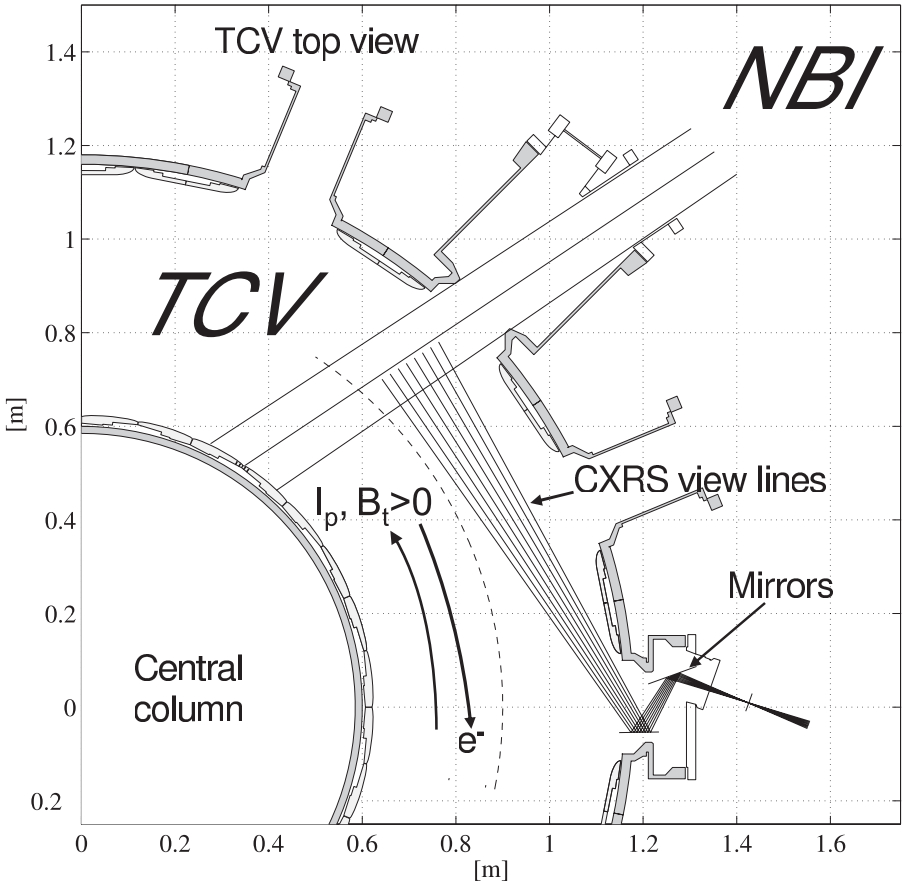

Figure 3.7: *Experimental setup of the CXRS system.*

pulses, in order to trace the background spectrum due to passive charge exchange (CX) emission. The CXRS temporal resolution is synchronised to the beam duty cycle, and is usually set to 90 (45) ms, depending on the level of the active signal. During the duty cycle, the CCD camera is exposed to the plasma emitted light in three 30 (15) ms time windows. This results in three CX spectra: two without the neutral beam, and one with the beam switched on. The 30 (15) ms 'integration time' has been chosen to collect enough statistics. This time is generally longer than the sawtooth oscillation period of Ohmic TCV discharges (2–12 ms); each CX spectrum is therefore averaged over several sawtooth cycles.

A typical emission spectrum and intensity, acquired on the CCD detector during a beam pulse, are shown in figure 3.9. Once the passive background is subtracted from the NBI-enhanced spectrum, the resulting active component is fitted with a single or multiple Gaussian model, taking into account the spectrometer instrumental function. The carbon temperature and toroidal velocity can be deduced from the spectral line broadening and Doppler shift.

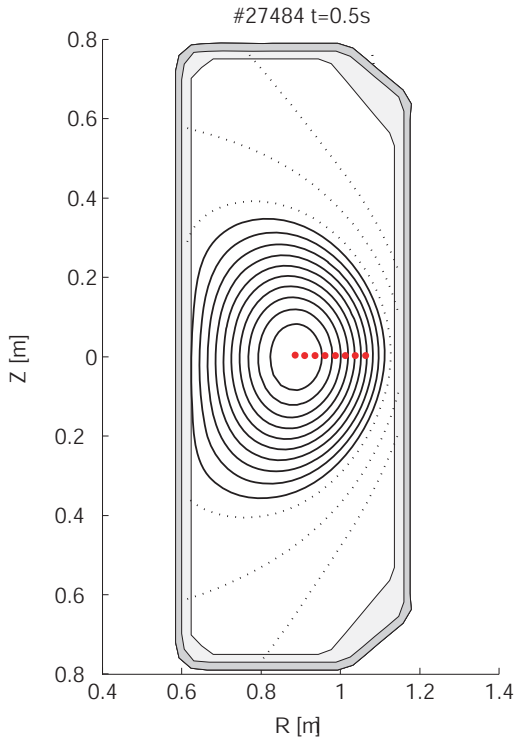

Figure 3.8: *Experimental view points of the CXRS system. Toward the plasma edge, the compression of the magnetic surfaces reduces the spatial resolution.*

3.2.5.a Effects of the neutral beam (DNBI) on toroidal rotation

In part III of this thesis we study the toroidal rotation of Ohmic L-mode plasmas. To this aim, it is important to study a possible beam effect on the plasma rotation.

The neutral beam is injected at an angle of 11.25° with respect to the radial direction (see figure 3.7), and is composed of different hydrogen species with different energies: H (50 keV), H_2 (25 keV) and H_3 (16.6 keV). The total injected power (up to 80 kW modulated in 30 ms pulses) is relatively small compared to the TCV Ohmic power (0.25–1 MW) [18]. Most significantly, the calculated absorbed power is only a fraction of the injected power, ranging from 20% at $\langle n_e \rangle >= 1 \cdot 10^{19}$ m^{-3} to 78% at $\langle n_e \rangle = 6 \cdot 10^{19}$ m^{-3}.

Considering a deuterium plasma with carbon impurities only and a beam pulse length of 30 ms, the estimated beam induced rotation is positive (co-current directed) and smaller or close to 1 km/s [19], which is negligible compared to the typically observed experimental values. Experiments using 180 ms long DNBI power pulses have demonstrated the existence of a beam effect on plasma rotation (figure 3.10).

The plasma rotation is monitored by measuring the frequency of the sawtooth precursors oscillations visible on the soft X-ray signals. As expected with a co-current DNBI beam (figure 3.7), the natural counter-current rotation of the plasma

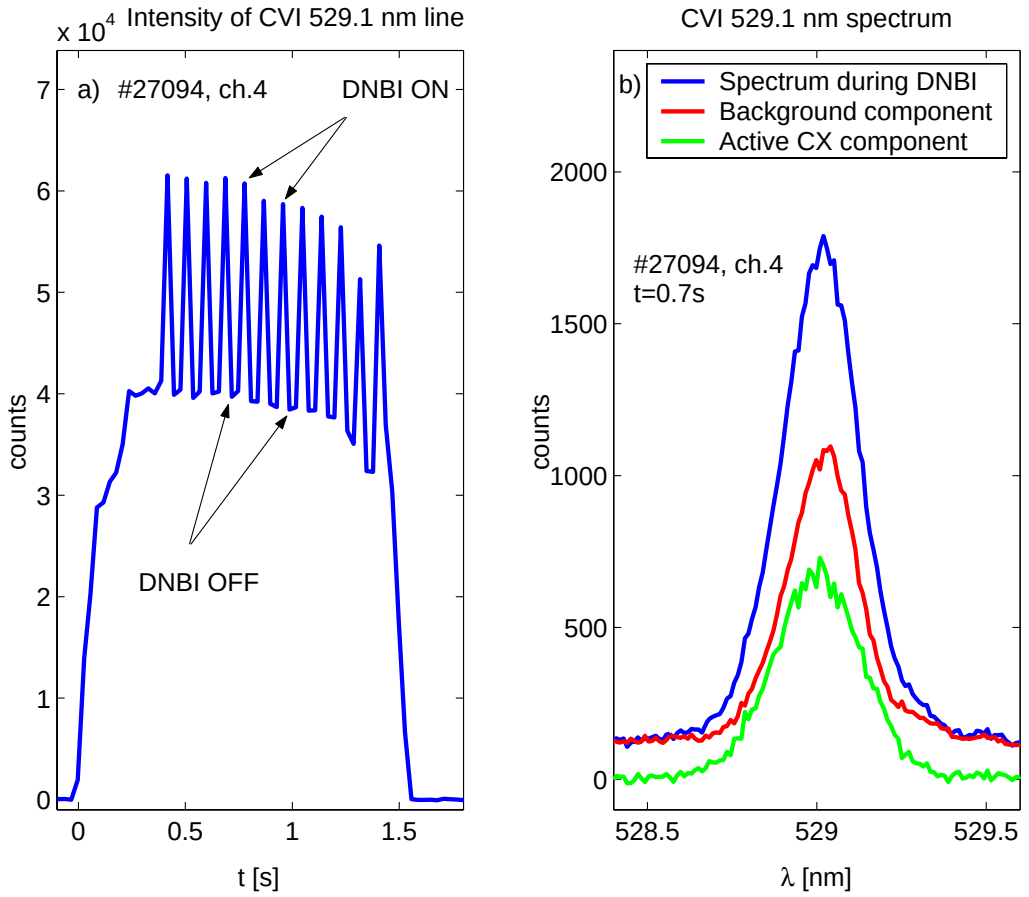

Figure 3.9: *Typical intensity evolution (a) and spectrum (b) of the observed CVI 529.1 nm line. The intensity peaks correspond to acquisition times during DNBI pulses (a). The CX spectrum induced by the neutral beam (active spectrum) is shown in (b). The background component is interpolated from the nearest beam-off phases.*

(see chapter 9) is reduced when the beam is switched on, resulting in a modulation of the frequency of the sawtooth precursor oscillations. The amplitude of the modulation is approximately of 1 kHz, which corresponds to $\sim$ 6–7 km/s.

In order to extrapolate the effect of the shorter 30 ms pulses usually applied on TCV, we fit the modulated sawtoooth precursor oscillation frequency with exponential functions of decaying time τ (see figure 3.10),

$$\omega_{\mathrm{ON}}(t) = \omega_f + \Delta\omega e^{-t/\tau_{\mathrm{ON}}} \quad (3.6)$$

$$\omega_{\mathrm{OFF}}(t) = \omega_f - \Delta\omega e^{-t/\tau_{\mathrm{OFF}}} \quad (3.7)$$

where ω_f and $\Delta\omega$ are the final frequency and amplitude of the modulation. The suffix ON (OFF) indicates time windows with the beam switched on (off). The fit yields $\tau_{\mathrm{ON}} \sim \tau_{\mathrm{OFF}} \sim$ 60–90 ms.

Therefore the induced beam velocity for a $\Delta t = 30$ ms pulse is $\simeq$ 1–2 km/s, which is slightly higher than the one calculated from the beam attenuation. It should be noted, however, that the measured induced velocity is taken at the

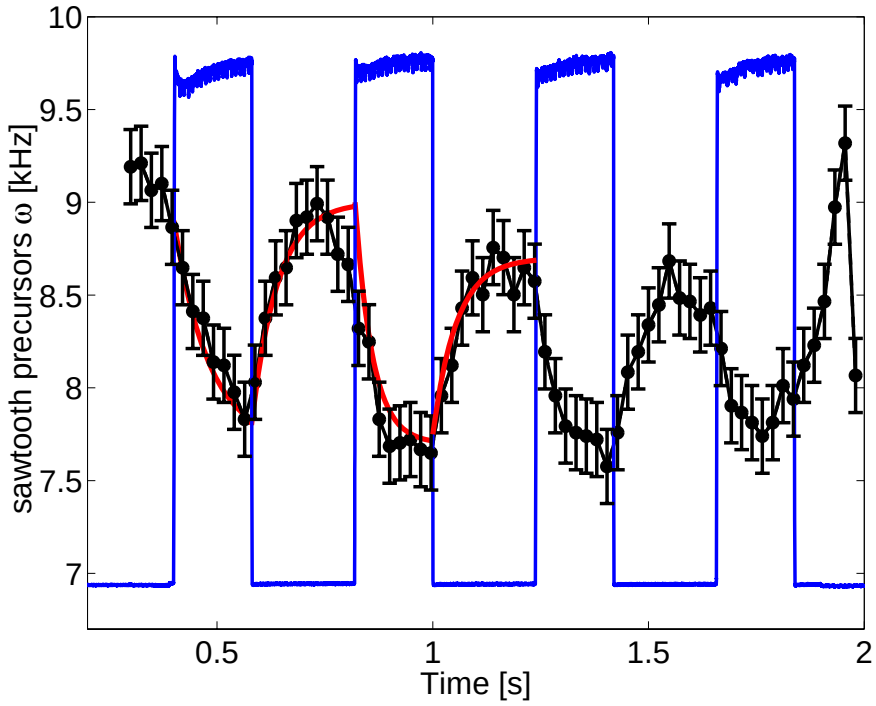

Figure 3.10: *Frequency of the sawtooth precursor oscillations (black dots) ω modulated by long (180 ms) NBI pulses at maximum power (in blue). The frequency is fitted with an exponential function of decaying time τ ∼60-90 ms (in red).*

plasma centre where the beam power absorption is maximum (and thus the local induced rotation), while the theoretical induced velocity is averaged over the plasma volume.

No other external momentum source is applied to TCV plasmas. Counting rate, wavelength calibration and background substraction represent the main sources of error in velocity measurements. The wavelength calibration is obtained from a reference Ne spectrum, acquired after each TCV discharge, to compensate for effects of thermal and mechanical drifts. The total uncertainty on the measured toroidal velocity is 5 km/s at the plasma edge (where the carbon density is low) and 2 km/s at the core (where beam attenuation becomes significant).

3.3 Equilibrium reconstruction

To find a tokamak equilibrium reconstruction, one has to solve the Grad-Shafranov equation,

$$R\frac{\partial}{\partial R}\left(\frac{1}{R}\frac{\partial \psi}{\partial R}\right)+\frac{\partial^2 \psi}{\partial R^2}=-\mu_0 R^2 p'(\psi)-I(\psi)I'(\psi) \tag{3.8}$$

where ψ is the poloidal stream function, $p(\psi)$ the plasma pressure and I is equal to RB_ϕ. The $'$ sign denotes differentiation with respect to ψ. The arbitrary source functions $p'(\psi)$ and $I'(\psi)I(\psi)$, are chosen to reproduce the measurements as ac-

curately as possible. However, the problem is ill posed, since $p'(\psi)$ and $I(\psi)$ are functions of ψ, whose spatial dependence is not known until equation (3.8) is solved. Consequently, an iterative scheme has to be employed.

The TCV equilibria are reconstructed using the Grad-Shafranov solver LIUQE [20]. The standard reconstruction, calculated immediately after each discharge, uses the magnetic measurements from the flux loops, the poloidal field probes shown in figure 3.1, and measurements from a diamagnetic loop to constrain the plasma pressure. If available, additional measurements may improve considerably the accuracy of the reconstruction. Some examples are: the Thomson and CXRS pressure profiles, inversion surface of sawteeth obtained from tomographic reconstruction from the soft X-ray and/or some internal measurement of the poloidal magnetic field in order to constrain the current density profile.

In LIUQE, the source functions are expanded into a series of pre-defined base functions,

$$p' = \sum_{n=0}^{N_p} a_n U_n(\psi) \tag{3.9}$$

$$II' = \sum_{n=0}^{N_T} b_n U_n(\psi) \tag{3.10}$$

where a_n and b_n are constants to be determined. The base functions U_n are defined as functions of the normalised poloidal flux $\phi = (\psi - \psi_a)/(\psi_0 - \psi_a)$, yielding $\phi = 0$ at the edge and $\phi = 1$ on axis,

$$U_0 = 1 \tag{3.11}$$

$$U_1 = \phi \tag{3.12}$$

$$U_2 = 1 - (2\phi - 1)^2 \tag{3.13}$$

$$U_3 = \left[1 - (2\phi - 1)^2\right](2\phi - 1). \tag{3.14}$$

The optimal number and combination of source functions depend on the properties of the analysed equilibria and on the available measurements. An estimate of the accuracy of the reconstruction can be obtained by comparing the flux surfaces with measured plasma parameters such as the soft X-ray emissivity, temperature or density, which are assumed to be constant on flux surfaces.

If the position of an MHD mode is determined with an independent measurement, it may also be compared with the position of the resonant $q = m/n$ rational surface (see section 4.1.1) given by the equilibrium reconstruction. It is usually found that the accuracy of the reconstruction degrades in the plasma core, toward the magnetic axis.

Part II

Plasma instabilities in TCV

Chapter 4

Analysis of MHD fluctuations

This chapter describes the main techniques for the analysis of plasma long wavelength (macro) instabilities. It is shown how the main mode characteristics are extracted from perturbations of plasma quantities. Such quantities include the magnetic field and the soft X-ray emission. In particular the poloidal and radial structure of the perturbations is compared with the analytical and numerical models of magnetic islands. From the comparison, island widths and radial positions can be obtained.

Macro or MHD instabilities have long wavelengths, typically of the order of the plasma size. Such instabilities perturb the equilibrium magnetic field. These perturbations usually extend to the plasma edge, where they can be detected with magnetic pick-up coils. Owing to the rotation of the plasma they are usually observed as fluctuations in the laboratory reference frame. The perturbation of the magnetic surfaces also affects other quantities, such as the temperature, density or soft X-ray emissivity and can therefore be observed with corresponding diagnostics which provide a sufficient temporal and spatial resolution.

4.1 Perturbation of the magnetic field

The magnetic probes measure the temporal variations of the poloidal magnetic fields, δB. Since the typical frequencies of MHD instabilities are in the kHz range and higher, they can be easily separated from the slower changes of the equilibrium magnetic field.

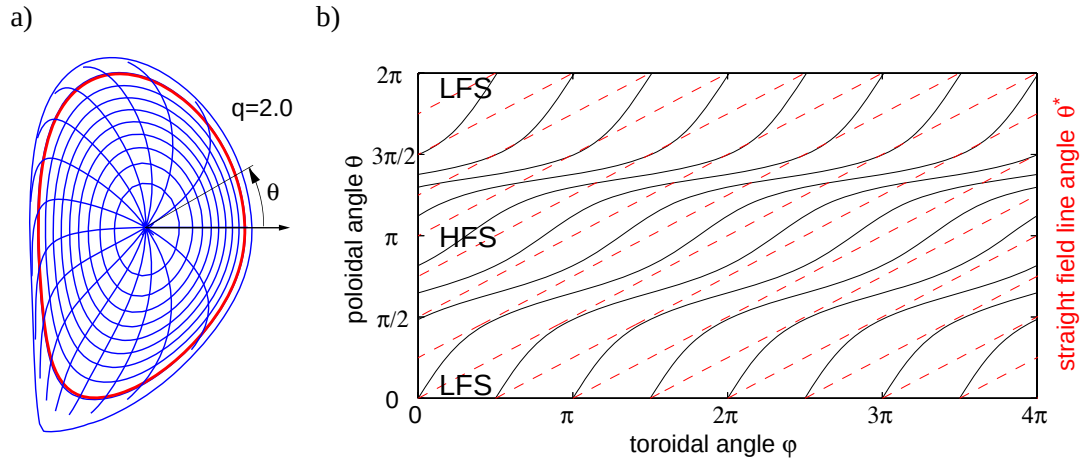

Figure 4.1: *Magnetic field line geometry of a diverted discharge (q_{95}=2.5). a) The flux contours in the poloidal plane show the plasma shape. The geometry of the field lines on the flux surfaces is represented by the contours of the straight field line coordinate θ^*, indicating the advance of field lines in the poloidal direction for equal toroidal lengths. b) The field lines of the q=2 flux surface are shown in the unfolded $\theta-\phi$ plane (solid line). Replacing the polar angle θ by θ^* results in a straight magnetic field line representation (dashed).*

4.1.1 Flux coordinate, magnetic field lines and decomposition into modes

The geometry of the magnetic perturbations is strongly linked to the geometry of the equilibrium field. It is thus important to study in detail the field line geometry in a general tokamak equilibrium.

The magnetic field lines of the equilibrium field lay on nested flux surfaces (section 1.3.2) with toroidal topology, which are usually described by the coordinates φ and θ. Owing to the $1/R$ decay of the toroidal field, the angle of a field line with respect to the toroidal direction is generally smaller on the high-field-side (HFS) than on the low-field-side (LFS). Hence the local pitch angle of the field line,

$$\frac{d\theta}{d\varphi} = \frac{\vec{B}\cdot\vec{\nabla}\theta}{\vec{B}\cdot\vec{\nabla}\varphi} \tag{4.1}$$

is not constant on a flux surface. The pitch angle also decreases at the top and bottom of elongated plasmas as well as in the vicinity of an X-point, where it approaches zero. The field line geometry of a diverted plasma is shown in figure 4.1.

In order to exclude the effect of toroidicity and shaping the local pitch angle can be made a flux function with a change of coordinates which allows the magnetic field to be expressed in terms of a flux representation:

$$\vec{B} = 1/2\pi \left(\vec{\nabla}\Psi_p \times \vec{\nabla}\varphi + \vec{\nabla}\Psi_t \times \vec{\nabla}\theta^* \right). \tag{4.2}$$

By recalling the definition of the safety factor (equation 1.19) it can be seen by a direct calculation that the local pitch angle is now constant on a flux surface and equal to $1/q(r)$. The so-called straight-field-line coordinate function $\theta^*(\theta, \psi)$ can be obtained by multiplying the representation of an axisymmetric magnetic field, $\vec{B} = I(\psi)\vec{\nabla}\varphi + \vec{\nabla}\psi \times \vec{\nabla}\varphi$, with $\vec{\nabla}\theta^*$ and substituting into equation 4.1 results in,

$$\underbrace{\vec{\nabla}\psi \times \vec{\nabla}\varphi \cdot \vec{\nabla}\theta}_{J} \cdot \frac{\partial\theta^*}{\partial\theta} = \frac{I(\psi)}{qR^2} \,. \tag{4.3}$$

The mixed product of $\vec{\nabla}\psi$, $\vec{\nabla}\varphi$ and $\vec{\nabla}\theta$ on the left hand side of equation 4.3 can be identified as the Jacobian J of the transformation of the toroidal coordinates (ψ, θ, φ) into cylindrical coordinates (R,φ,Z). It can be simplified by using toroidal symmetry and the identity of the toroidal coordinate [21],

$$J = \begin{vmatrix} \partial\psi/\partial R & 0 & \partial\psi/\partial Z \\ 0 & 1 & 0 \\ -Z/r^2 & 0 & (R-R_0)/r^2 \end{vmatrix} = \frac{\partial\psi}{\partial R}\frac{(R-R_0)}{r^2} + \frac{\partial\psi}{\partial Z}\frac{Z}{r^2} \tag{4.4}$$

with $r^2 = Z^2 + (R - R_0)^2$. Equation 4.3 can be integrated over θ,

$$\theta^*(\theta) = \frac{I(\psi)}{q(\psi)} \int_0^\theta \frac{d\theta}{R^2 \mathrm{J}} + C \tag{4.5}$$

where the constant C can be determined by normalising $\theta^*(2\pi)$ to 2π. Since in flux coordinates (Ψ, θ^*, ϕ) the magnetic field lines are straight lines in the $\theta^* - \varphi$ plane, flux coordinates are sometimes called "straight field-line coordinates".

We will see, in the next sections, the importance of the straight field-line coordinates and of θ^*.

To extract coherent modes, the fluctuation measurements can be decomposed into spatial Fourier components. The measurements are conveniently expanded in the toroidal and (straight field-line) poloidal angles:

$$\delta B(\vec{x}, t) = \sum_{m,n} \delta\hat{B}_{m,n}(\psi) \cos(\vec{k} \cdot \vec{x} - \Phi_{m,n}(t)) = \sum_{m,n} \delta\hat{B}_{m,n} \cos(m\theta^* - n\varphi - \Phi_{m,n}(t)). \tag{4.6}$$

Because of the toroidal symmetry each toroidal mode $\Sigma_m \delta\hat{B}_{m,n} \cos(m\theta^* - \Phi_{m,n}(t))$ is linearly independent and the expansion in φ is well justified. However, toroidicity and plasma shaping couples several poloidal harmonics which are resonant on different flux surfaces $q = m/n$. Mode coupling is often observed in tokamak experiments and plays an important role in plasma stability as we will see in more details later in this chapter and in chapter 5. A single helicity mode with amplitude $\hat{B}_{m,n}$ is often called an m/n mode with m and n the poloidal and toroidal mode numbers respectively.

The phase $\Phi_{m,n}$ of the m/n mode generally varies with time,

$$\Phi_{m,n}(t) = \omega_{m,n}t + \chi_{m,n} = \vec{k}_{m,n}\vec{v}t + \chi_{m,n} = \left(\frac{m}{r}v_{\theta^*} - \frac{n}{R}v_{\varphi}\right)t + \chi_{m,n} \tag{4.7}$$

where $\chi_{m,n}$ is a constant phase angle and $\vec{v}$ is the phase velocity of the magnetic perturbation with respect to the probes and generally depends on the local $\vec{E} \times \vec{B}$ and diamagnetic flows around the resonant surface.

4.2 Numerical techniques for the MHD mode analysis

Various numerical techniques are used to analyse fast magnetic fluctuations and to extract information concerning the temporal evolution and spatial structure of coherent modes.

Most of the methods presented in this section are standard and were already integrated in the tools for the analysis of high frequency fluctuations available in TCV. A few original contributions were added during this thesis as highlighted in the following. These methods can also be applied to other fluctuation measurements. In the following an arbitrary fluctuation $s(\vec{x}, t)$ is analysed.

4.2.1 Temporal analysis

The standard approach to the analysis of an oscillating signal is the Fourier transform, which links the representation of a function in the time and frequency domains,

$$S(\omega) = \int_{-\infty}^{\infty} s(t)e^{i\omega t}dt. \tag{4.8}$$

In an experiment a function $s(t)$ is recorded at time $t = t_k$, with $k = 0, ..., N-1$ at a finite sampling rate $f_s = 1/\Delta t$ over a finite time interval $N\Delta t$, therefore leading to N discrete samples $s(t_k)$. The discrete form of the Fourier transform (equation 4.8) is

$$S(f_n) = \Delta t \sum_{k=0}^{N-1} s(t_k)e^{2\pi kn/N} \tag{4.9}$$

with $f_n = n/(N\Delta t)$. Equation 4.9 is periodic in n which is usually varied from $-N/2$ to $N/2$ and corresponds to a spectral resolution up to the Nyquist frequency $f_c = 1/(2\Delta t)$. If the signal $s(t_k)$ consists of purely real numbers, the Fourier coefficients of positive and corresponding negative frequencies are complex conjugates, $S(-f_n) = S^*(f_n)$. The original data set can be reconstructed from the Fourier coefficients using the discrete form of the inverse Fourier transform,

$$s(t_k) = \frac{1}{N\Delta t} \sum_{n=-N/2}^{N/2} S(f_n)e^{-2\pi kn/N}. \tag{4.10}$$

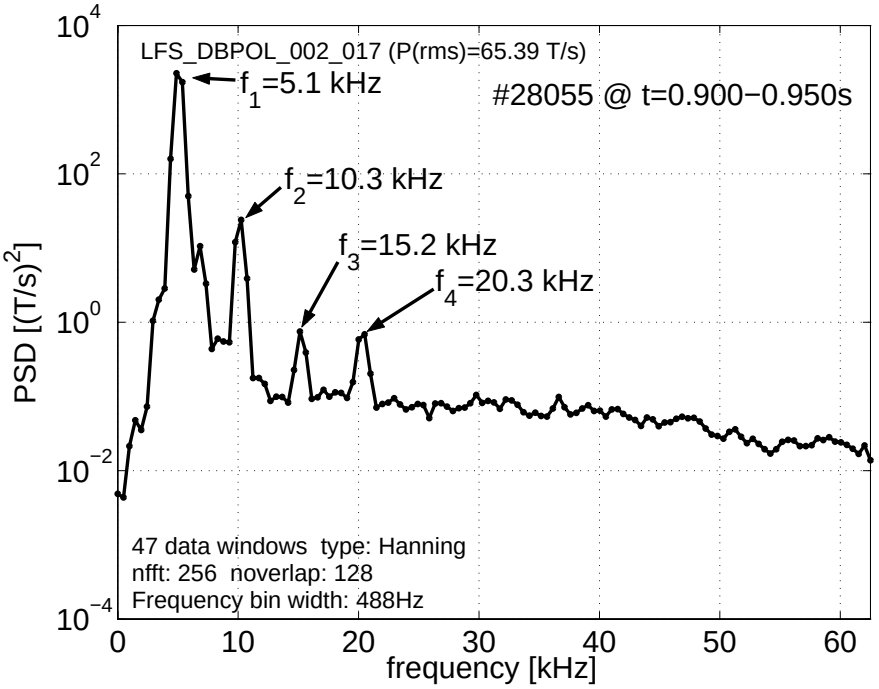

Figure 4.2: *Estimates of the power spectral density of an edge magnetic probe for a discharge where a strong mode at 5.1 kHz was present . Several harmonics are also clearly visible.*

An estimate of the continuous power spectrum $P(f)$ can be obtained from the Fourier coefficients $S(f_n) = S_n$ and is defined at $N/2 + 1$ positive frequencies as,

$$P(0) = \frac{1}{(N\Delta t)^2}|S_0|^2 \,, \tag{4.11}$$

$$P(f_n) = \frac{1}{(N\Delta t)^2}\left[|S_n|^2 + |S_{-n}|^2\right] \,, \tag{4.12}$$

$$P(f_c) = \frac{1}{(N\Delta t)^2}|S_{N/2}|^2 \,. \tag{4.13}$$

The normalisation used in equation 4.11 ensures that the sum over the $N/2+1$ values of $P(f_n)$ is equal to the mean squared amplitude of the function $s(t)$. The value $P(f_n)$ is an estimate of the average power over a narrow window centred on f_n. It is well known that, due to the finite length of the sampled time, this technique leads to a significant leakage of signal power on the adjacent frequency bins and thus to a broadening of the power spectrum [22]. The power estimation also suffers from a large variance [22]. By partitioning the original data set in K segments with an overlapping in the data points of one half of their length and then averaging each power estimate for the f_n frequencies, the deviation can be reduced. The spectral leakage can be partially cured using the data windowing technique [22, 23].

The actual power spectral density (PSD) of the magnetic data is the result of several contributions:

- The power spectra of the physical perturbations in the magnetic signal. In general, it is composed of a background signal with a wide frequency range that slowly decreases with f_n, plus sharp peaks corresponding to the frequency of coherent modes. The background spectrum is related to the magnetic plasma turbulence.
- Electronic noise and spurious pick-up of the electrical signals.
- Numerical noise and power spectral leakage as described above.

In figure 4.2 we compare the PSD from a magnetic probe during an Ohmic shot where a strong MHD mode was present. Several harmonics of the main frequency, f_1, can be observed.

4.2.2 Spatial analysis and mode numbers

The Fourier coefficients at the mode frequency can be used to determine the mode structure and thus identify the mode numbers. The analysis of the toroidal structure is simplified by the toroidal symmetry of a tokamak plasma, which allows a straightforward Fourier decomposition into toroidal mode components. The poloidal mode identification is more complex with toroidicity and poloidal shaping affecting the structure of the perturbation. Varying the setup of the detectors, such as the orientation and distance of the magnetic probes with respect to the plasma, can also affect the measured poloidal structure of a mode.

As it was shown in section 4.2.1, the amplitude of the complex Fourier coefficient allows the estimation of the spectral density, revealing the frequency f_* of a distinct mode. In addition to the measurement of the signal power, the Fourier coefficient at the mode frequency $Y_* = Y(f_*)$ also yields a phase angle $\Phi_* = \arctan(\Im(Y_*)/\Re(Y_*))$, which represents the phase of the mode $\Delta\Phi(\theta, \phi, t) = \vec{k} \cdot \vec{x} = m\theta - n\phi - \Phi_{m,n}$ (compare the real part of the equation 4.10 and equation 4.6). Figure 4.3 shows the phases of the magnetic fluctuation measurements at $f_* = 5.1$ kHz as they were recorded with the toroidal array of the LFS (a) and poloidal probe array in sector 3 (b). The phase variation of the Fourier coefficient Y_* along the toroidal and poloidal direction can then be analysed (spectral analysis) to extract the mode numbers m and n.

4.2.2.a Toroidal analysis

Owing to the toroidal symmetry of the plasma and of the toroidal probe array, the phase difference $\Delta\Phi$ between probes of the toroidal array increases linearly with the toroidal angle ϕ of the probes. A linear fit of the type $\Delta\Phi = n\phi + \phi_0$ is thus sufficient to determine the toroidal mode number n. In figure 4.3(a) an n=1 structure is easily identified.

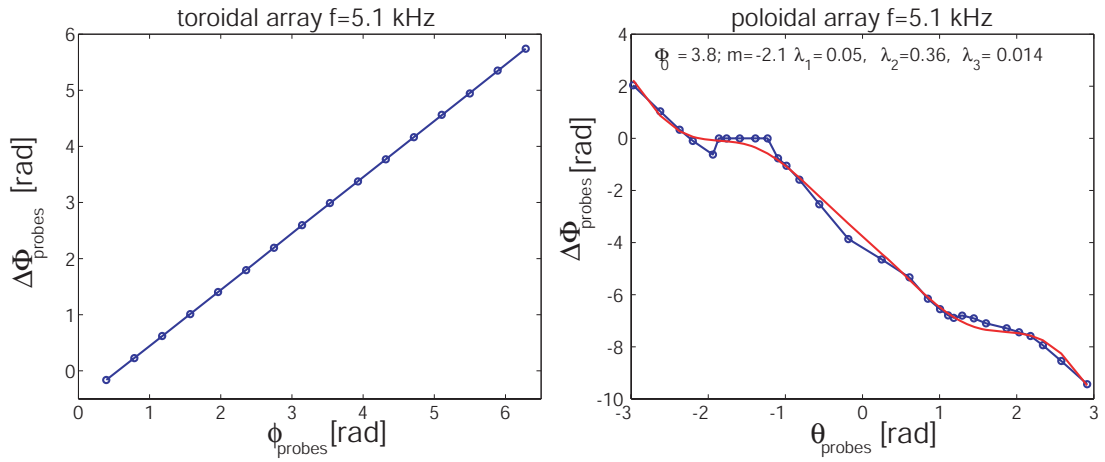

Figure 4.3: *Phase of the Fourier coefficient at f_*=5.1 kHz as a function of the toroidal (a) and poloidal (b) angle for a quasi-circular plasma ($\kappa = 1.12$ and $\delta = 0$). Following the phase of the toroidal and poloidal ($\theta = 0°$ on the HFS) direction reveals the toroidal and poloidal mode number n=1 and m=2 respectively. The best-fit result with equation 4.17 is also shown (red) confirming the evaluation of the poloidal mode number m.*

The advantage of this spectral analysis is its close relation to the decomposition of the signals into modes. To do so, it uses standard routines such as the Fast Fourier Transform (FFT). However, its application is restricted to modes whose oscillation frequency remains constant over the analysed time interval. Since this time interval needs to be of a certain length to allow for a sufficient frequency resolution, the present analysis has limited applicability.

Signals which are measured with complete toroidal arrays of equidistant detectors, such as the toroidal arrays of magnetic probes on the TCV HFS and LFS (section 3.2.4), can be directly decomposed into Fourier components of the Fourier transform between ϕ and k ($= n/R$) space. The periodic boundary conditions lead to discrete modes characterised by their mode numbers n. The measurements $s(t_k, \phi_l)$, taken at $l = 1, ..., N$ toroidal locations, can be decomposed for any sampled time t_k yielding cosine and sine components for toroidal mode numbers $n = 0, 1, ..., N/2$,

$$c_n(t_k) = \frac{2}{N} \sum_{l=1}^{N} s(t_k, \phi_l) \cos(n\phi_l), \tag{4.14}$$

$$z_n(t_k) = \frac{2}{N} \sum_{l=1}^{N} s(t_k, \phi_l) \sin(n\phi_l). \tag{4.15}$$

The Fourier components of the measurements can also be expressed by mode amplitudes $A_n(t_k) = \sqrt{c_n(t_k)^2 + z_n(t_k)^2}$ and corresponding phases $\Phi_n(t_k) = \arctan(z_n/c_n)$,

$$s(t_k, \phi_l) = \frac{A_0(t_k)}{2} + \sum_{l=1}^{N/2} A_n(t_k) \cos(n\phi_l - \Phi_n(t_k)). \tag{4.16}$$

In contrast to the spectral analysis, the toroidal mode analysis does not impose any time behaviour and allows the measurement of the toroidal component A_n with varying frequency. A_n thus characterises the amplitude of an MHD mode with the toroidal mode number n and can be used, for example, to measure the growth rate or the saturation level of a specific mode (equation 4.34 in section 4.4.3). Owing to the axisymmetric geometry of the tokamak plasma, each toroidal component of the instabilities is linearly independent, but it may contain simultaneously several poloidal harmonics. The temporal derivative of the phase $\Phi_n(t_k)$ allows the determination of the instantaneous frequency and the direction of propagation of the mode.

4.2.2.b Poloidal analysis

The identification of the poloidal mode number m from a poloidal probe array is more complex. As can be seen from figure 4.3(b) the slope of the phase varies with the poloidal position θ of the probes in plasmas with quasi-circular cross-section, and such variation becomes even more evident in highly shaped plasmas. The poloidal mode number can be obtained, in principle, by counting the multiples of 2π of the phase shift along the entire poloidal circumference. However, this operation can be complicated by a fast changing phase of modes with high poloidal number and/or by the low signal amplitude caused by large distances between the resonant surface and the magnetic probes (see section 3.2.4). In this case some modelling for the phase-shift between probes $\Delta\Phi(\theta)$ is needed.

Under the assumption of field-aligned current perturbations localised around a particular rational surface $q = m/n$ (see section 4.4) the phase of the perturbed magnetic field is constant on a field line and changes poloidally proportionally to θ^*. The constant phase of the perturbation along a single field line was first experimentally verified on the ASDEX tokamak [24]. Thus the phase variation $\Delta\Phi$ in the magnetic probe signal along the poloidal direction for an m-mode is $\Delta\Phi(\theta) = m\theta^*(\theta)$. The function $\theta^*(\theta)$ can be computed from equation (4.5) using the equilibrium reconstruction from the LIUQE code. However, the use of an analytical expression of θ^* allows us for a faster determination of the poloidal mode number m. The function $\theta^*(\theta)$ was first derived in the large aspect ratio limit for circular plasma by Merezhkin [25] and then generalised for shaped plasmas in [26]. It may be expressed as,

$$\theta^*(\theta) = \theta - \lambda_1 \sin(\theta) + \lambda_2 \sin(2\theta) - \lambda_3 \sin(3\theta) + O(\epsilon^4) \quad (4.17)$$

$$\lambda_1 = \Delta' + \epsilon \quad (4.18)$$

$$\lambda_2 = \frac{\epsilon_a r \kappa'}{2} \quad (4.19)$$

$$\lambda_3 = \frac{\epsilon_a r^2 \delta'}{3a} \quad (4.20)$$

where Δ is the Shafranov shift, $\epsilon = r/R$ is the local inverse aspect ratio with r and R the minor and major radius respectively. Here $\kappa(r)$ and $\delta(r)$ are, respectively, the local elongation and triangularity. The sign $'$ denotes the derivative with respect to the minor radius r. This method, implemented during this thesis, allows an accurate extraction of the main poloidal number m by comparing the experimental phase-shift with equation (4.17). An example of the use of this method (though redundant in this case) is shown in figure 4.3(b). The modelling of the phase-shit with equation (4.17) becomes critical in the case that a small number of probes is available for the analysis or when the amplitude of the mode is below the noise level on several probes. An example of the determination of m in such case is shown in figure 4.4.

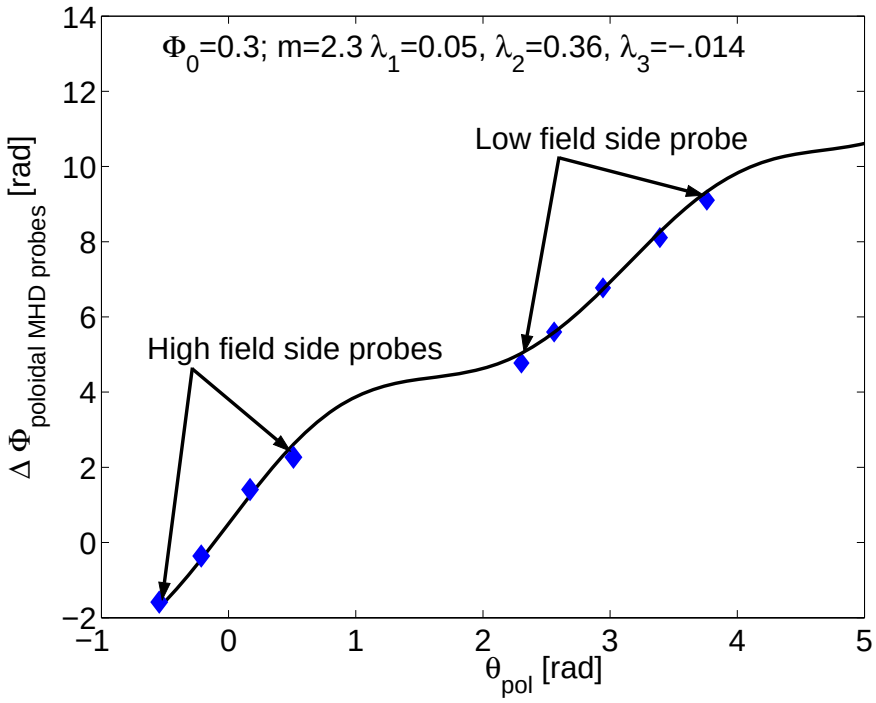

Figure 4.4: *Phase-shift analysis of an incomplete poloidal probe array. The best-fit result with equation 4.17 allows to connect the probes on the LFS to those on HFS and recognise an $m = 2$ mode number.*

Eddy currents in the wall and the abrupt change of probe orientation close to the vessel corner may add further complications and even allow for a reversal of

the phase change [27]. A more detailed model which includes eddy currents and geometrical details of the probe system is required in these cases. It turns out, however, that for most applications in TCV, equation 4.17 allows for a sufficiently accurate determination of the poloidal mode number.

The determination of the mode structure (in particular the poloidal mode structure) can be, in some cases, considerably improved by applying another technique on the row magnetic data, the so-called bi-orthogonal decomposition.

4.2.2.c Spatiotemporal mode structure from bi-orthogonal analysis

Another method for the analysis of spatiotemporal signals is bi-orthogonal decomposition (BD), which is formally identical to the singular value decomposition (SVD) in numerical linear algebra. Unlike Fourier techniques it is a multivariate analysis handling several dimensions at the same time. The bi-orthogonal decomposition separates the coherent signal structures and their temporal evolutions from the incoherent part. The measurements $s(x_i, t_j)$ taken at M locations x_i and sampled at N times t_j can be constructed from $K = \min(M, N)$ pairs of spatial eigenvectors $\zeta_k(x_i)$ and temporal eigenvectors $\psi_k(t_j)$,

$$s(x_i, t_j) = A_k \sum_{k=1}^{K} \zeta_k(x_i)\psi_k(t_j). \tag{4.21}$$

The spatial eigenvectors $\zeta_k(x_i)$ are also called topos, whereas the temporal eigenvectors $\psi_k(t_j)$ are called chronos. Topos and chronos are mutually orthogonal. The eigenvalues, or weights A_k, are positive or equal to zero and it is conventional to sort out the pairs of bi-orthogonal components in order of decreasing weights. This allows the representation of the original signal with a limited number of pairs of components (often from two to four pairs depending on the application) with good accuracy. The total signal energy $E = \Sigma_i \Sigma_j s^2(x_i, t_j)$, is equal to the sum of the squared weights,

$$E = \sum_{k=1}^{K} A_k^2. \tag{4.22}$$

The relative energy stored in each pair of eigenvectors (ζ_k, ψ_k) can be expressed with the dimensionless energy,

$$p_k = A_k^2 / E \tag{4.23}$$

and thus quantifies the importance of an eigenvector. A physical interpretation of the bi-orthogonal decomposition is the projection of the data on an orthogonal basis which de-correlates both the time and the space series. In contrast to spectral analysis, the BD does not assume a constant frequency throughout the analysed time interval and allows the identification of an arbitrary temporal evolution. Neither does it make any assumption about the spatial structure, such as the toroidal mode analysis, which requires pure Fourier components. The basis of the expansion is automatically generated to adapt best to the coherent structures

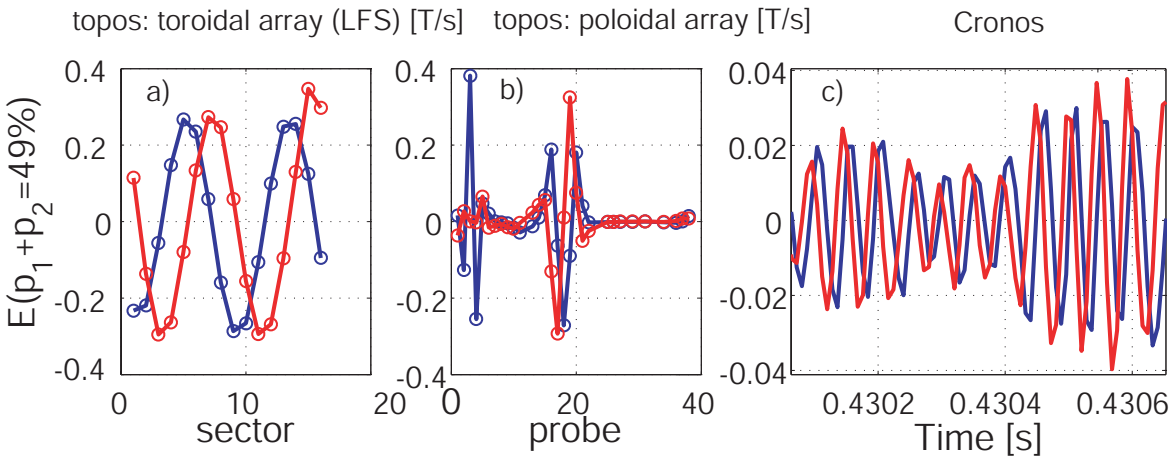

Figure 4.5: *Two principal eigenvectors of the bi-orthogonal decomposition of the edge magnetic signal from a low $q_a \sim 2.5$ discharge (#21402). The spatial structure (topos) is separated in the toroidal a) and b) poloidal contributions. The temporal behaviour (chronos) is shown in figure c). Note the $\pi/2$ phase shift between the degenerate eigenvectors. The sinusoidal toroidal structure reveals an n=2 mode number while the poloidal structure requires a dedicated phase analysis (see figure 4.6).*

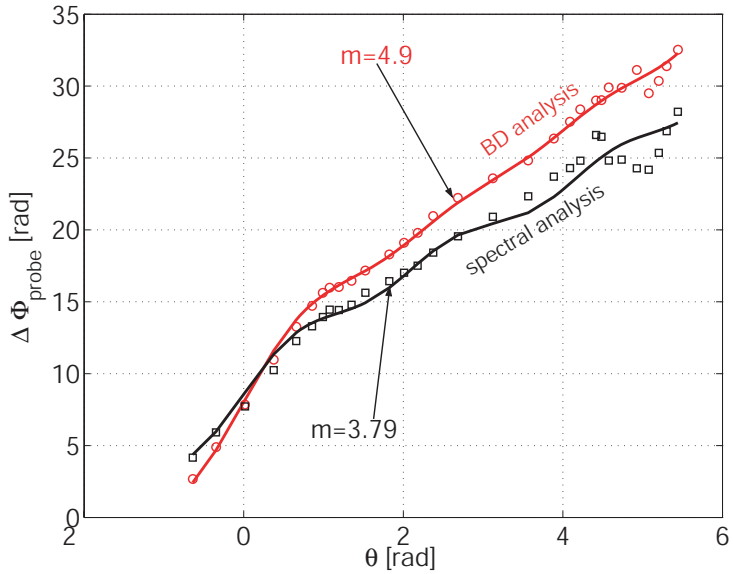

Figure 4.6: *Phase analysis of the poloidal structure from the BD decomposition in figure 4.5b (red dots) and from spectral analysis (black squares). The best-fit of the phase variation from BD reveals an m=5 poloidal mode number and allows the identification of the mode in discharge #21402 as a rotating 5/2 mode. The spectral analysis leads to an underestimation of the poloidal mode number.*

in the signals, that become thus more evident. The BD has the property that the truncated sum over ordered eigenvectors is the best approximation of the original data s, in the least-square sense. Other properties of the bi-orthogonal decomposition as well as some of its applications have been discussed in detail, for example, in references [28, 21].

An interesting case is the presence of two similar, non-negligible weights $A_{k_1} = A_{k_2}$. This degeneracy can usually be ascribed to the existence of a spatiotemporal symmetry, $s(t, x - x_0) = s(t + t_0, x)$, such as a rotating mode where $x_0 = vt_0$, with v the phase velocity of the mode. In this case the phases of ζ_{k_1} and ζ_{k_2} as well as of ψ_{k_1} and ψ_{k_2} are shifted by $\pi/2$. A time variation of the frequency and amplitude of the mode only shows up in the chronos and not in the topos. Coupled modes, which have identical frequencies but different wave vectors (for example modes with the same frequency and n number but different poloidal numbers), are not separated and appear in one pair of the bi-orthogonal components.

In figure 4.5 the possibilities of the bi-orthogonal decomposition are illustrated for magnetic measurements from the toroidal and poloidal arrays, for a single mode very close to the plasma edge. The two principal eigenvectors, which comprises 49% of the total signal energy, are degenerate and describe a rotating mode. The toroidal and poloidal parts of the two main topos, which are shown separately in (a) and (b), respectively, as well as the corresponding chronos (c), show a typical phase shift of $\pi/2$. The toroidal part of the topos reveals an n=2 structure whereas the poloidal part is very difficult to interpret and requires additional analysis. The poloidal mode number can be inferred by treating the two degenerate eigenvectors as the sine and cosine part of a Fourier expansion. The phase and amplitude of the rotating mode can thus be obtained. The toroidal and poloidal mode numbers can then be extracted by fitting the phase shift as described earlier in this section. In figure 4.6, we show the phase of the probes along the poloidal direction extracted from the BD (circles) and spectral analysis (squares) together with the best fit of the phase variation model described the section 4.2.2.b. From the type of discharge it is recognised that the poloidal number of the mode is m=5 (see figure 5.7 in chapter 5). It can be seen that the BD analysis allows a good estimation of the number m whereas, in this case, the spectral analysis significantly underestimates the mode number, enlightening the ability of the BD analysis in reducing the noise while extracting only the coherent part from the signals.

4.3 Perturbations in approximate flux surface quantities

The presence of MHD modes perturbs all plasma parameters, such as the temperature, density and soft X-ray emissivity. While magnetic measurements are usually limited to the plasma edge, additional internal perturbation measurements are often needed to *detect and identify MHD modes in the plasma centre*.

The TCV photo-diode soft X-ray detection system allows a tomographical reconstruction of the 2D emissivity (see section 3.2.3) and the recognition of MHD

modes [17]. This method, although also used in this thesis, is often limited by its spatial and temporal resolution. The MPX camera (section 3.2.3), with its high spatial resolution and high sampling rate constitutes a very good tool for MHD studies.

4.3.1 Soft X-ray perturbed emissivity

The MPX camera views cover the plasma cross-section at one toroidal position from below the torus. The structure of the perturbation may be detected due to the mode rotation. A spectral analysis of the complete set of the 64 channels allows the visualisation of the radial mode structure.

An example of an FFT analysis of the sawtooth precursor oscillations in the soft X-ray channels is shown in figure 4.7. The mode amplitude presents two off-axis peaks symmetrically placed with respect to the magnetic axis. The perturbations at the HFS of the torus are out-of-phase with respect to the perturbations at the LFS and a jump of π can be clearly seen at the position of the magnetic axis, in correspondence with the minimum amplitude of the perturbations. Such a structure, commonly observed in tokamaks, is usually interpreted as an m=1 mode [29].

In particular, the peaks of the perturbation correspond to the maximum displacement of the magnetic axis and the frequency doubling observed in the most central channels may be regarded as the signature of a rigid hot core displacement which passes through the view line of the central channel twice per period. Such a displacement can be produced by an ideal kink motion, that conserves the magnetic topology, or by a $m/n = 1/1$ magnetic island [30]. No flattening in the emissivity profile or phase jump are observed in both sides of the torus which may indicate the presence of a magnetic island [30]. However, the signatures of magnetic islands are more easily observed with local, non-line integrated, measurements such as ECE temperature measurements [30, 31].

Another example of a mode observed with the MPX camera is shown in figure 4.8. The fluctuation amplitude now shows a more complex structure. There are several maxima and several minima of the perturbation amplitude. The amplitude minima correspond to phase changes (of about π). The two off-axis amplitude maxima at $R \sim$ 80 cm and $R \sim$ 97 cm show in-phase perturbations, whereas the on-axis maximum at $R \sim$ 88 cm corresponds to out-of-phase oscillations. Such symmetric structure with respect to the magnetic axis reveals an even poloidal mode number. Note that, simultaneously, the magnetic signal reveals an m/n=2/1 mode at the edge rotating at the same frequency. Cross-correlation techniques between the edge magnetic signals and the MPX channels identify a common origin of the observed perturbations, thus allowing us to interpret the radial mode structure in figure 4.7 as a m=2 mode. On the HFS a secondary outer peak is observed at $R \sim$ 75 cm. It has the opposite phase with respect to the primary peak, as is also visible on the raw time traces. Such a behaviour is expected for a magnetic island which induces a flat density and temperature profile inside the separatrix [30, 31, 32]. However, similar features are not observed in all cases, nor are observed on the LFS channels. A few obvious reasons for the inconsistency between

HFS and LFS are:

- The effect of the integration of the signals along the view line may destroy local features (such as phase jump) especially on the high field side where the magnetic surfaces are more densely packed.
- Asymmetries in the perturbed temperature and density have been observed in many tokamaks and complicate further the interpretation of the measurements.
- Coupling with outer modes plus the effect of the integration may distort the radial structure of the perturbation.
- The temperature and density profiles inside the magnetic island are not flat, but may present a peak on the O-point [33, 32]. A peaked pressure profile inside the separatrix is likely to lead to a perturbation with peak amplitude on the position of the resonance surface r_s. This occurs as a consequence of the different temperatures between the X-point and the O-point of the island.

A proper interpretation of the perturbed soft X-ray signal requires detailed modelling of the magnetic island geometry, a prescription for the pressure profile inside and outside the island separatrix, and the complete geometry of SXR diagnostic. Although SXR signal modelling constitutes an interesting task, it is however outside the scope of this thesis.

4.4 Modelling of magnetic islands

So far we have mainly analysed the phase of the fluctuation along the toroidal and poloidal direction in order to extract the mode numbers and thus the resonant rational surface. A complete characterisation of the mode structure requires, however, an analysis of the amplitude as well. Field-aligned current perturbations lead to the formation of magnetic island around rational surfaces. Such current perturbations may be modelled and the resulting magnetic fluctuation can be calculated and compared with experimental edge magnetic signals.

4.4.1 Perturbation current density and reconstruction of the magnetic field

Modelling of the edge magnetic fluctuations from a magnetic island was successfully applied on ASDEX Upgrade [21]. On TCV, a similar method was implemented by Reimerdes [23] and used for the interpretation of the Mirnov measurements. We briefly describe this method and we show some applications in case of the simultaneous presence of multiple poloidal harmonics (coupled modes) which allows us to reveal modes not observed by other means. This type of analysis has been extensively used during this thesis (see chapters 5 and 7).

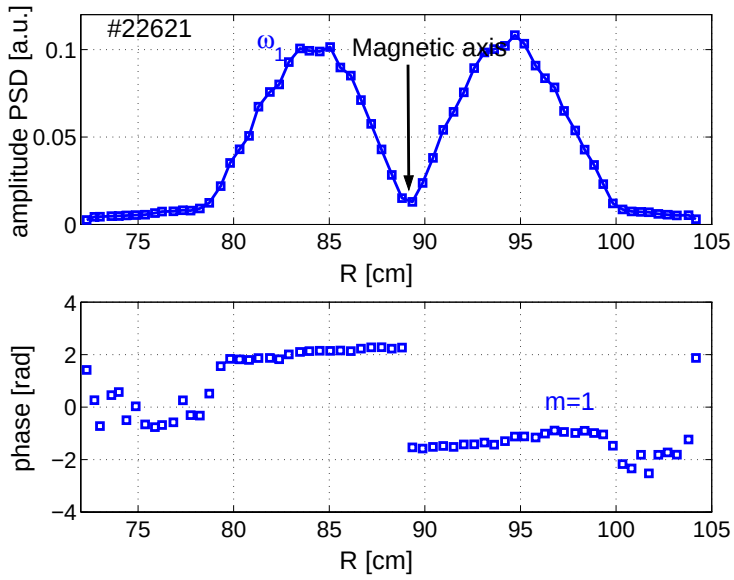

Figure 4.7: *Radial mode structure of the perturbed soft X-ray emissivity by a* $m/n = 1/1$ *mode. The radial position is given by the intersection of the flux surface tangent to the viewing chord with the mid-plane of the discharge cross-section at the level of the magnetic axis.*

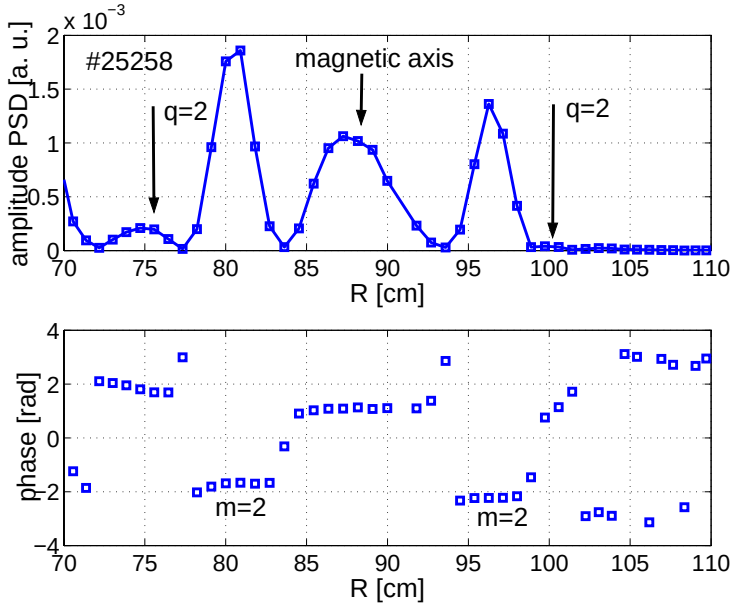

Figure 4.8: *Radial mode structure of the perturbed soft X-ray emissivity by a* $m/n = 2/1$ *mode.*

The model is based on the assumption that the perturbation currents flow along the equilibrium magnetic field lines and are localised on resonant flux surfaces. The model neglects the response of the plasma. These currents do not produce any charge accumulation (divergence-free) and do not change the plasma equilibrium. Using the straight field line coordinate (ψ, θ^*, ϕ) (equation 4.5), the perturbation current in the direction of the magnetic field can be decomposed into Fourier components with toroidal and poloidal mode numbers n and m,

$$\delta\vec{j} = \sum_{m,n} C_{m,n}(\psi)\cos(m\theta^* - n\phi)\hat{b}. \tag{4.24}$$

If the requirements of a divergence free current perturbation ($\vec{\nabla}\cdot\delta\vec{j} = 0$) is applied on each Fourier component (cylindrical approximation) equation 4.24 leads to the resonance condition [21],

$$m\vec{B}\cdot\vec{\nabla}\theta^* - n\vec{B}\cdot\vec{\nabla}\phi = 0 \tag{4.25}$$

which can be fulfilled at a resonant surface with the safety factor $q = m/n = d\phi/d\theta^*$ for a perturbation with the corresponding mode number (m, n).

In the limit of the model, the perturbation current is a sheet current flowing on this resonant surface. In order to transform the current density $j(\Psi)$ into a sheet current density j_A, it is assumed that current flows in an infinitesimally narrow flux tube of width dr which corresponds to a flux,

$$d\Psi = \frac{j(\Psi)}{j_A}dr. \tag{4.26}$$

With $d\Psi = RB_\theta dr$ the sheet current density can be identified as,

$$j_A = \frac{j(\Psi)}{RB_\theta}. \tag{4.27}$$

Even though the current, which flows in a flux tube, is constant on a flux surface, the sheet current density varies like $1/RB_\theta$ and it follows that,

$$\vec{j_A} \propto \frac{1}{RB_\theta}\sin(m\theta^* - n\phi)\hat{b}. \tag{4.28}$$

In order to reconstruct the poloidal component of the perturbed field only the toroidal component of the perturbation current density needs to be taken into account. With $I = RB_\phi \approx const.$, the toroidal perturbation current density is proportional to,

$$j_{A,\phi} \approx \frac{1}{R^2B_\theta}\sin(m\theta^* - n\phi). \tag{4.29}$$

Note that the coefficient in front of the sinusoidal function in equation 4.29 depends on the poloidal angle but not on the toroidal angle. Thus, a poloidal variation of the mode amplitude is expected whereas along the toroidal direction the mode amplitude remains constant as observed in the experiments.

Toroidal eddy currents on the vacuum vessel may strongly influence the amplitude and the phase of the perturbations and must thus be taken into account. The problem is discretised and the resonant flux surface and the conducting vacuum vessel are divided into toroidal current filaments. The eddy current in each of the toroidal filaments of the vacuum vessel can be obtained from the response induced by the magnetic flux generated by all the other filaments [23]. The contributions from the eddy currents and the current flowing on the resonant surfaces filaments can then be linearly added to calculate the perturbation in the poloidal field at the probe location B_m,

$$B_m = B_s + B_v \tag{4.30}$$

where B_s is the contribution from the resonant surface and B_v the contribution from the vacuum vessel.

The response of the vessel depends on the frequency f of the mode. It has been calculated that for $f < 10$ Hz the eddy current in the wall can be neglected whereas for $f > 1$ kHz the resistivity of the wall can be neglected and the field amplitude doubles at the wall on the LFS with respect to the no-wall case [23].

4.4.2 Comparison with the edge magnetic signal

When a single mode, arising from one resonant surface, is observed it can usually be identified with the methods described in section 4.2. In [23] it was also shown that the island model (section 4.4) agrees well with the experimental mode structure of single modes. The analysis becomes, however, more complicated when two or more modes are present at the same time. If the modes are coupled and have the same toroidal mode number they rotate at the same frequency and it is impossible to separate their structure with the spectral or BD analysis. The poloidal harmonics mix up together and may give rise to strongly distorted poloidal structure, whereas the phase of the fluctuation is dominated by the mode resonant on the outermost flux surface. Only modelling of both the phase and amplitude allows the identification of the different modes that contribute to the observed structure $b_j = b(x_j)$. The modelled structure of an m/n-mode $B_{m,n}(x_j)$, or the linear combination of several modes $\sum_{k=1}^{K} a_k B_{m_k,n_k}(x_j)$, is fitted to the data by the least square method by choosing K coefficients a_k to minimise the χ^2 [23]. Then, assuming that all the measurements have the same standard deviation and that the model is correct, the standard deviation of the measurements can be calculated,

$$\sigma^2 = \sum_{j=1}^{N} \left(b_j - B(x_j)\right)^2 / N. \tag{4.31}$$

The parameter $\sigma_n = \sigma/\max(b_j)$ can also be used as an estimator of the fit quality.

In figure 4.9 we show three examples of mode identification with single and multiple coupled modes. In the first example (from the top), a single modelled

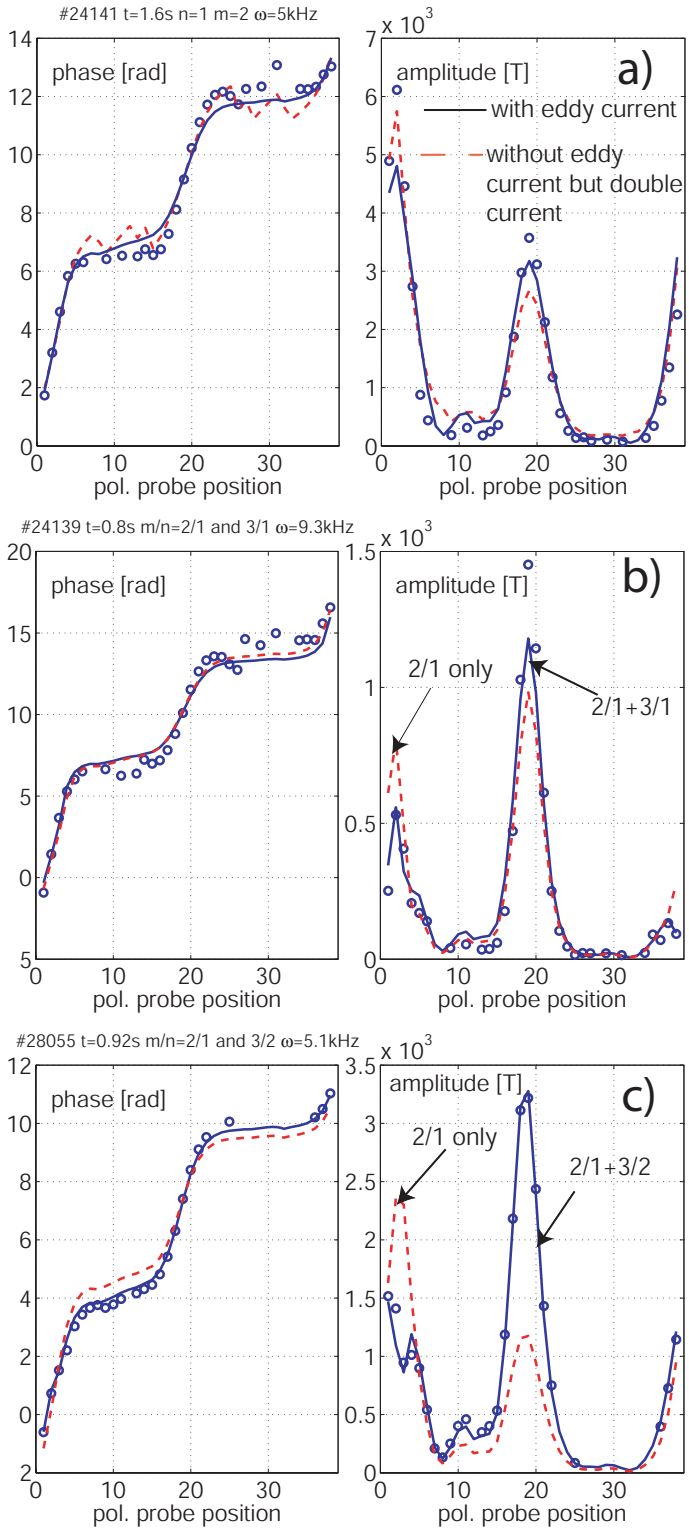

Figure 4.9: *Comparisons of the mode poloidal structure with the magnetic island model. a) Case of a single rotating* $m/n = 2/1$ *mode, b) coupled* $2/1 + 3/1$ *modes and c) coupled* $2/1 + 3/2$ *modes.*

$m/n = 2/1$ mode reproduces well the phase as well as the amplitude of the observed mode rotating at 5 kHz (blue solid line). The dashed line in figure 4.9a) represent the same mode simulation without the inclusion of the eddy currents on the wall. The parameter σ_n is almost identical for the two cases, $\sigma_n = 8\%$ but the current on the q=2 rational surface is doubled in the case of no induced eddy current compared to the case of the complete simulation with the inclusion of the eddy current. This difference in the flux surface current has important consequences because it determines a large difference in the inferred magnetic island width (see section 4.4.3). It turns out that the eddy currents are essential for a realistic estimation of the island width.

The second case shows the simulation of two coupled modes, an $m/n = 3/1$, clearly visible on the edge magnetic signal, coupled with an $m/n = 2/1$ mode, independently observed in the SXR signal. While the mode coupling effect is very weak on the phase behaviour (compare solid and dashed lines in figure 4.9b), the linear combination of the $B_{3/1}$ and $B_{2/1}$ allows a better simulation of the mode amplitude. With only the $3/1$ mode, $\sigma_{n,3/1} = 11\%$ while with inclusion of both modes $\sigma_{n,3/1+2/1} = 5\%$. Attempting to model the experiment with other combinations of coupled modes (e.g. $m/n = 2/1$+$m/n = 3/2$) results in a much worse comparison. This example demonstrates how this method may improve the analysis of coupled modes as also observed in ASDEX upgrade [21]. Note that in TCV, the mode coupling between modes with m and $m + 1$ poloidal numbers appears to increase the mode amplitude on the LFS of the torus. This type of poloidal asymmetry is understood on the basis of a phase locking at the LFS (e.g. island X-points both at the LFS) as predicted by mode coupling due to toroidicity [12].

A stronger effect of the mode coupling is given in figure 4.9c). The observed phase reveals a dominant $m = 2$ (figure 4.9-3a) but the amplitude shows a strong poloidal asymmetry, typical of coupled modes. The simulation with a $2/1$ mode results in an unsatisfactory comparison with $\sigma_{n,2/1} = 20\%$.

It is interesting to note that other harmonics are observed in the power spectrum of the magnetic signal (see figure 4.2) that can be identified as the harmonics $m/n = 2/1$, $4/2$ and $6/3$. However, it can be shown that the inclusion of these harmonics in the mode simulation does not improve the comparison. Neither does the SXR signal reveal the presence of other modes. Nevertheless the island model with coupled $2/1$ and $3/2$ harmonics agrees well with the observed mode structure ($\sigma_{n,2/1+3/2} = 3\%$), revealing an $m/n = 3/2$ mode that could not be seen otherwise.

4.4.3 Magnetic island width

The full island geometry and thus the island width can be reconstructed using the model elucidated in section 4.4.2 by calculating the magnetic perturbation in the whole plasma. The superposition of the helical perturbation flux ψ_1^* and the equilibrium flux ψ_0^* then reveals the geometry of the magnetic island. Note that this linear treatment is not self-consistent but it allows us to capture the main island features [21, 23]. The equilibrium and perturbed helical fluxes are given by,

$$\psi_0^* = \psi_{pol,0} - \frac{1}{q_s}\psi_{tor,0} \tag{4.32}$$

$$\psi_1^* \ (x_p) = M_{ps} I_s \cdot \frac{\sqrt{B_\phi^2 + B_\theta^2}}{B_\phi} \tag{4.33}$$

where M_{ps} is the mutual inductance between the toroidal filaments at the location x_p (where the flux ψ_1^* is calculated) and x_s. An example of the reconstructed island

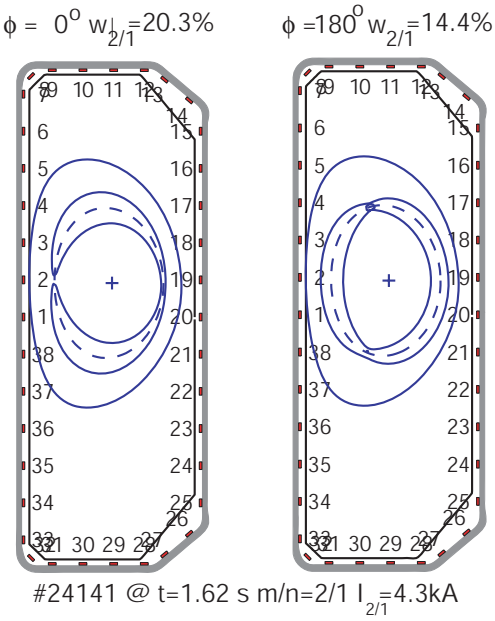

Figure 4.10: *Island geometry of the discharge #24141 (at t=1.62 s) at two different toroidal locations.*

geometry is plotted in figure 4.10 at different toroidal locations separated by $\pi/2$. The average island width is about 6 cm. This island width may be compared with the one given by the cylindrical approximation in equation 2.30. Owing to multipolar field decay, the signal at the edge is attenuated with respect to the value at the resonant surface by a factor $1/r^{m+1}$. Taking this into account, the island width w as function of the detected magnetic signal can be written as [23],

$$w = \sqrt{\frac{(8b/r_s)^{m+1} B_{\theta,m,n}}{\epsilon_s n B_{\phi,0} s_s}} r_s \tag{4.34}$$

with b the radial position of the vacuum vessel. The uncertainty of this method is mainly due to the assumption of cylindrical geometry, vacuum-like magnetic field

decay, and the errors on the different parameters in equation 4.34, in particular the shear s_s is not known accurately. This formula gives, for the same discharge in figure 4.10, a value for the island width of 6-7 cm (see figure 7.5 b) in good agreement with the more complete island model. However a larger discrepancy is often found.

4.5 Concluding remarks

Several numerical methods have been presented to extract the coherent mode structure from fluctuation measurements, separating their temporal and spatial behaviours. The MHD analysis in TCV relies mostly on edge magnetic probes and line-integrated soft X-ray emissivity measurements. Local fluctuation measurement of the plasma core, such as from ECE measurements, would, perhaps, greatly help in extracting and interpreting the structure of the instabilities observed in TCV plasmas. Most of the methods presented here are part of the standard data analysis tools available at TCV. New features have been added during this thesis, such as coherence analysis between edge and core fluctuations and modelling of the phase of the magnetic fluctuations which allows a fast and reliable analysis of the poloidal mode number. This is however out of the scope of the present work.

Chapter 5

Plasma shape stabilisation of current rise MHD instabilities

This chapter describes a potentially disruptive plasma instability, typically occurring in tokamaks during the early current rise phase of plasma formation, as well as how to reduce or suppress this instability using plasma cross section shaping. The perturbations in plasma parameters before disruption are characterised and the main unstable modes identified. In TCV, plasma shaping is observed to completely stabilise this disruptive mode and is regularly used for safe current ramp-up. Coupling between modes is found to play a major role in the destabilisation of the disruptive mode, as suggested by theoretical models. Three stabilising mechanisms, related with plasma shape, are discussed and shown to be relevant in TCV plasmas with edge safety factor close to 3.

5.1 Introduction to plasma instabilities during current rise

The abrupt termination of plasma discharge, often called plasma disruption, is of major concern in present day and future tokamak fusion experiments. A disruption causes high heat and mechanical stresses to the structures surrounding the plasma column (the vessel wall, the divertor, the magnetic coils, the diagnostics, etc.). In large devices, such as fusion reactors, these stresses may provoke serious damage and therefore need to be avoided or mitigated. Understanding the dynamics leading to plasma disruption, and looking for mechanisms to avoid it, is an important part of today's research in fusion science.

It is generally agreed that large, growing magnetic islands can cause plasma disruption by inducing ergodization of the field line, followed by a rapid loss of

confinement (thermal quench), and eventually by plasma current decay [34]. The Tearing Mode (TM) instability is believed to be responsible for the formation of the magnetic islands observed in tokamaks. In low-β regime (classical TM), the TM stability mainly depends on the current density profile [35]. Stationary current profiles in ohmic plasmas are typically peaked owing to the strong coupling with the electron temperature through plasma resistivity. During the current rise phase, the current profile can be different from its fully relaxed (stationary) shape. In fact, if the current rise time is shorter than the current redistribution time, the current profile can be flat or hollow in the centre with possibly large gradients toward the edge (skin effect) [36]. Such profiles may be unstable with respect to surface kink modes, localised on magnetic surfaces just outside the minor radius, and to tearing modes. In general, large gradients in the current profile destabilise the tearing modes.

MHD instabilities are often observed in tokamaks during the plasma current rise phase [34, 37]. The MHD activity is sharply correlated with the edge safety factor q_a. These modes appear as bursts of magnetic activity localised at the plasma edge, where surface kink modes are expected, and generally disappear as q_a drops below the rational value. The magnetic perturbation shows n=1 and $m = q_a$ mode numbers, typically associated with low q (q=5, 4, 3, 5/2, 2) rational surfaces. However under certain conditions such modes are accompanied by other instabilities, typically m=2 modes, which grow in amplitude, lock to the external wall, and finally lead to plasma disruption.

In large shaped tokamaks, such as JET, it is usually sufficient to decrease the current ramp rate in order to peak up the current profile, keep the MHD activity at a reasonable level, and avoid disruptions. In circular tokamaks, such as in the Tore Supra tokamak, obtaining stable discharges with $q_a < 3$ is complicated by the presence of large MHD modes appearing during the current rise phase [38]. The generation of an ergodic divertor was reported to improve the plasma stability allowing stable discharges with $q_a = 2.5$. Coupling between modes is believed to play a major role in driving large MHD modes that cause disruptions [38].

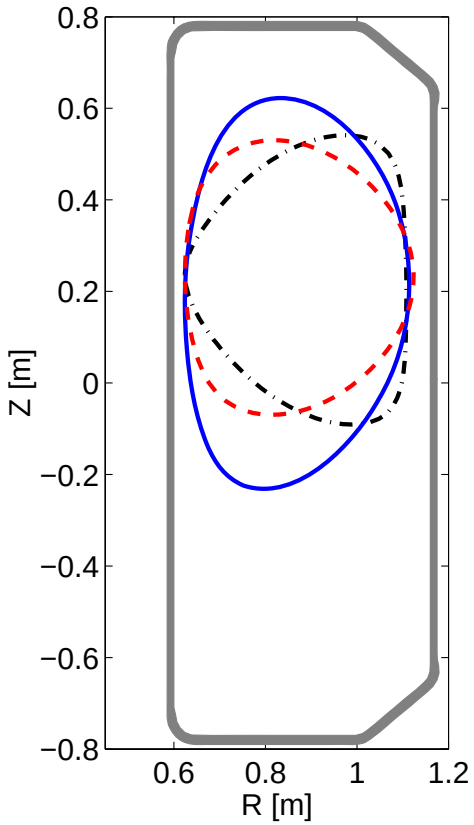

Figure 5.1: *Different TCV plasma shapes: quasi-circular (#21400, dashed red line), moderately shaped with negative triangularity (#21402, black dashed-dotted line), and medium-high elongated plasma (#21399, blue solid line)*

In smaller tokamaks, partly because of the vicinity of rational surfaces, and

party because of lower temperatures, the mode coupling is expected to be effective even for low amplitude modes [12].

In this context, plasmas can be divided in three categories according to their shape: *strongly shaped* ($\kappa > 1.7$, $\delta > 0.3$ or $\delta < -0.4$), *moderately shaped* ($1.7 > \kappa > 1.4$ and $-0.5 < \delta < -0.3$ or $0.3 > \delta > 0.2$) and *quasi-circular plasmas* ($\kappa < 1.4$, $-0.3 < \delta < 0.2$). Some examples of TCV plasma shapes used in this study are shown in figure 5.1.

In TCV, the plasma current of quasi-circular plasmas is limited by disruptions at $q_a \sim 3$. Suitable control of the plasma shape is required during current rise to find a stable path to discharges with safety factor below 3.

The work in this chapter describes an original analysis of the MHD modes responsible for disruptions during current rise at $q_a \sim 3$ in Ohmic TCV plasmas. We also report experimental evidence of the important role played by mode coupling on TM stability. In particular, we show experimental evidence of the tearing mode and external kink mode coupling, which is predicted to be responsible of the large growth of the m/n=2/1 TM by Fitzpatrick [39]. We then attempt to get new insight on the "operational" knowledge of the beneficial effect of plasma shaping in current rise experiments. We characterise the effect of shaping on the observed instabilities, and suggest an interpretation on the basis of the available theoretical models.

5.2 MHD activity during current rise in TCV

The standard initial current rise rate in TCV is rather high (dI_p/dt = 2 MA/s), and accurate monitoring of plasma parameters during the rapid development of the disruptive mode is not possible. A set of experiments with slower current rise has therefore been performed to study specifically the pre-disruption mode activity.

In a typical experiment, the plasma shape is kept constant while the current is raised by increasing the loop voltage. As a consequence, the edge safety factor decreases in time. To explore the effect of plasma shaping, the elongation is varied on a shot-to-shot basis from 1.1 to 1.8, and the triangularity from –0.5 to +0.4. In TCV, increasing the plasma density is found to enlarge the current density profile, and thus to influence the stability of current driven modes. For this reason, the gas valve is pre-programmed to maintain a constant electron density at a value of about $\bar{n}_e$= 2.5·10^{19} m^{-3}.

However, due to the strong dependence between the plasma current and the ionisation rate, the density is also increasing during the current rise. Nevertheless, the density variation is kept within 10% during the relevant part of the current ramp, between q_a = 4 and q_a = 3. Such a small variation is believed to only slightly modify the current profile and the plasma stability properties. Note that a sufficiently slow current ramp up is an essential condition for these experiments, since it allows:

- the production of quasi-stationary current profiles, thus reducing the skin effect.

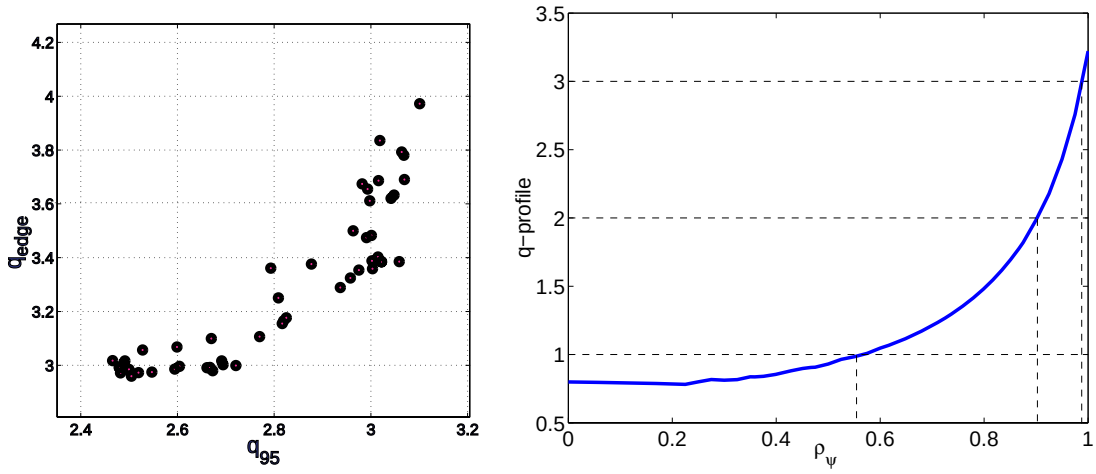

Figure 5.2: *Left: Values of q_a and q_{95} at the first appearance of MHD activity for a set of TCV discharges. The q=3 surface is located inside the plasma very close the edge. Right: LIUQE reconstruction of the q profile at t=0.367 s, approximately at the time of modes appearance (discharge #21400, κ=1.32, δ=0.2).*

- the delay of the disruption time, allowing for a better time resolution at which the phenomena are observed.

In fact, the time scale of the current rise, $\tau_{I_p} = I_p/(dI_p/dt) \sim 500$ ms, is longer than the current diffusion time, $\tau_\eta \sim 100$ ms, calculated from the experimental profiles, and the current can relax close to its stationary profile. The current profile has therefore a standard peaked shape in the majority of the discharges, as suggested by the presence of sawtooth oscillations visible on the soft X-ray plasma emission. The sawtooth oscillations are closely related with the presence of the $q = 1$ flux surface in the plasma, and their occurrence indicates a current profile peaked on-axis with a central safety factor smaller than 1.

Moreover, numerical simulations using the fixed boundary transport code PRETOR support the hypothesis of stationary current profile [40]. The PRETOR code simulates the plasma discharge with and without the inclusion of the current diffusion equation. The simulations show that significant transient modifications of the current profile are induced for current rise rates larger than 1 MA/s, whereas the experimental value does not exceed 0.5 MA/s.

The condition of quasi-stationary current profile considerably simplifies the interpretation of the experimental results. It allows us to neglect any transient phenomena, and justifies the use of the current profile from the equilibrium reconstruction (such as the profile from the LIUQE code).

5.2.1 Current rise disruption in $q_a = 3$ quasi-circular plasmas

The first detectable MHD activity normally appears when the $q = 3$ magnetic surface enters the last 5% of the poloidal magnetic flux, equivalent to $q_{95} < 3$ (see figure 5.2). An example of the evolution of a disruptive discharge is shown in

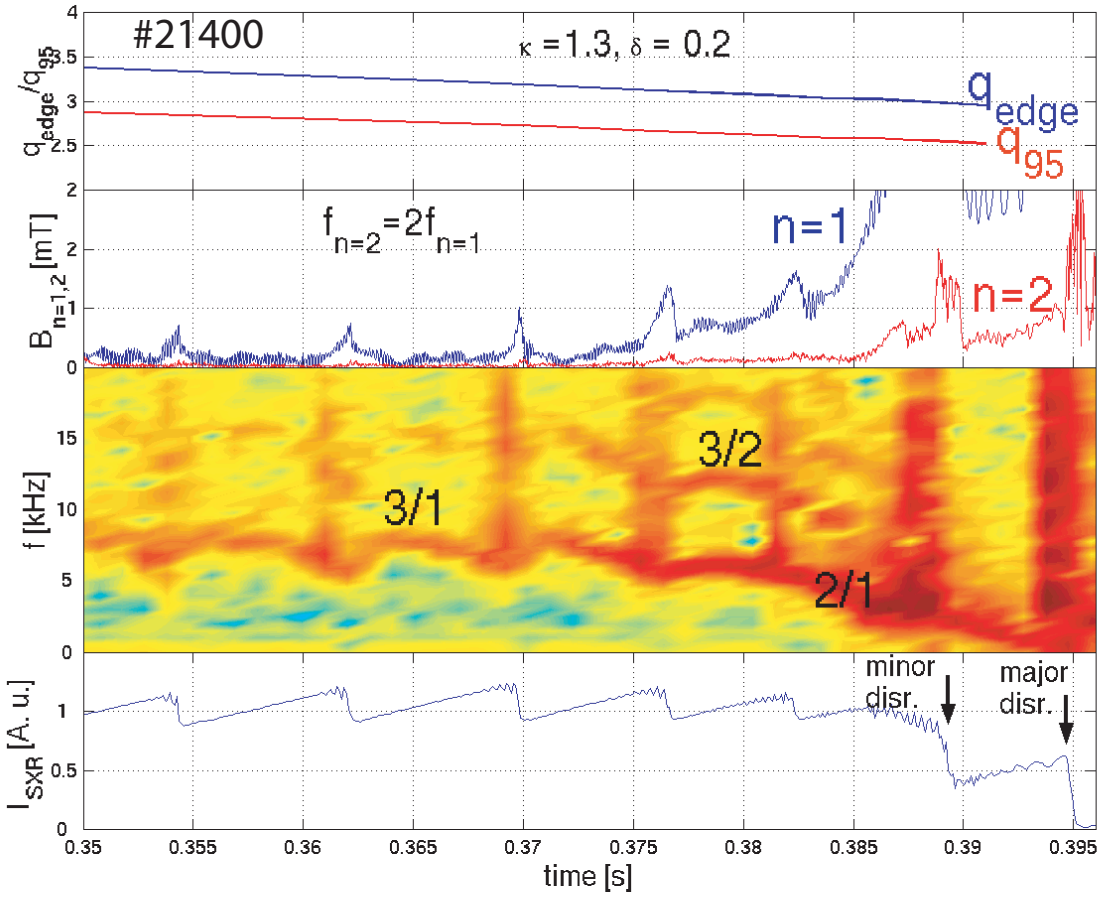

Figure 5.3: *Disruptive instability during current rise at $q_a \sim 3$ in weakly shaped plasma ($\kappa = 1.3$, $\delta = 0.2$). From top to bottom, q_a and q_{95}, the amplitude of the $n = 1$ and $n = 2$ toroidal components of the magnetic perturbation, the spectrogram of the magnetic signal (with indication of the mode numbers m/n), and the central soft X-ray emissivity are shown.*

figure 5.3. Owing to the mutual interaction of modes resonant on several rational surfaces, and to the influence of the external conductive wall, the evolution of the disruptive instability is rather complex.

We focus here on the pre-disruption MHD activity, which can be divided in four stages:

1. An MHD mode of dominant toroidal number $n = 1$ typically starts when the $q = 3$ rational surface approaches the edge region (from the inside, t = 0.355 s in fig. 5.3). The mode rotates in the electron diamagnetic drift direction with a frequency in the range 5–15 kHz and has a dominant $m = 3$ poloidal number). The mode amplitude and frequency are modulated by the sawtooth crashes.

2. If the current ramp up continues, the mode amplitude increases changing the dominant poloidal number from $m = 3$ to $m = 2$. The mode frequency

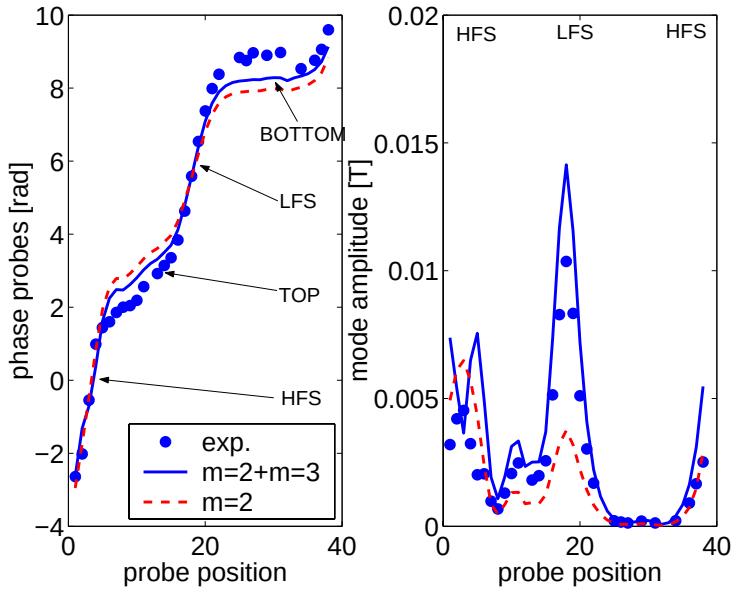

Figure 5.4: *Comparison of the poloidal magnetic structure from SVD analysis of the pre-disruption mode and magnetic island model. The magnetic probes are numbered clockwise from the LFS to the HFS. Good agreement is obtained using two poloidal harmonics $m = 2$ and $m = 3$, resonant on $q = 2$ and $q = 1.5$ respectively, thus identifying the $m/n = 2/1$ and $m/n = 3/2$ as coupled tearing modes.*

decreases.

3. When the amplitude mode is in the range $A_{n=1}$ = 0.5–2 mT, an $m/n = 3/2$ mode is triggered. The mode frequency keeps decreasing. Note that $\omega_{n=2} = 2\ \omega_{n=1}$, corresponding to perturbations which are locked in phase and toroidally rotating at the same speed.

4. One or more minor disruptions, associated with a fast growth of the n=1 and $n = 2$ components, precede the major disruption. Right before the disruption, the mode is still rotating at a frequency of about 1 kHz.

The coupled $2/1$ and $3/2$ perturbations, which can be identified as tearing modes (see figure 5.4), are mainly responsible for current rise disruption in TCV. Note that the maximum island widths evaluated in cylindrical approximation [7] are of typically 7 and 5 cm respectively for the $2/1$ and $3/2$ mode. Although these values are probably overestimated, considering that the resonant surfaces are only 3–4 cm apart, they suggest island overlapping and consequent field stochastisation over a large portion of the plasma cross section. Moreover the presence of the $1/1$ (sawtooth) and $3/1$ components may possibly extend the stochastic region up to the plasma limiter, leading to the loss of confinement visible from the soft X-ray emissivity collapses. The discharge terminates with a rapid current decay accompanied by spikes on the loop voltage signal.

5.3 Discussion and interpretation

The "current rise disruption" in TCV shows several of the most common disruption features in tokamak devices. For instance, the simultaneous presence of coupled toroidal (n = 1 and n =2) and poloidal (m = 1 sawtooth, m = 2, m = 3) harmonics is common to pre-disruption MHD activity as in the "density limit disruption" and "low-q disruption", described in detail in references [34, 37]. We note that the destabilisation of the $3/2$ TM in presence of large $2/1$ TM was also observed in other tokamaks [36], and has been the object of theoretical investigation involving nonlinear effects. Reference [41], for example, invokes the modification of the current profile due to the presence of $2/1$ and $1/1$ islands. By enhancing the radial thermal transport, the modes decrease the thermal conductivity, and flatten the electron temperature and current profile within the $1/1$ and $2/1$ magnetic islands. Since the total current is kept constant (unlike the total plasma energy content) by a loop voltage feed-back, the local current gradients in the region between the q = 1 and q = 2 surfaces increase and destabilise the tearing mode on the $q = 3/2$ surface. Another well-known non-linear mechanism thought to be responsible for mode destabilisation is the so called 'three-wave coupling' described for example in [42], which may also contribute to the destabilisation of the $3/2$ mode.

Mode rotation braking is often observed in tokamaks . It is generally attributed to the eddy currents on the surrounding metallic walls that generate an electromagnetic braking torque eventually leading to mode locking [43]. The theoretical temporal variation of the mode frequency scales strongly with the island width w, such that $d\omega/dt \sim -w^4$. While the mode is locking, the stabilising contribution of the eddy currents is lost and the mode amplitude increases. Before the first minor disruption the mode frequency decreases whereas the amplitude grows, as shown in figure 5.3, which is in qualitative agreement with the theoretical predictions. However this type of braking mechanism, which always reduces the mode frequency, can not explain the frequency modulation during the sawtooth activity (t $<$ 0.375 s). In fact, right after a sawtooth crash, the mode frequency increases whereas the n = 1 mode amplitude decreases, reaching a minimum after about 2 ms (t $>$ 0.370 s and after). Afterwards, the mode amplitude starts increasing again and the mode frequency decreases while approaching the next sawtooth crash. This behaviour may be attributed to the effect of plasma inertia, as first observed in the FTU tokamak [44]. The plasma inertia in fact contributes to the island frequency evolution with a term proportional to the time derivative of the island size $d\omega/dt \sim -(dw/dt)/w$ [45]. The sawtooth activity modulates the n = 1 mode amplitude which, in turn, modulates the mode frequency owing to the conservation of angular momentum [45].

The peculiarity of the current rise disruption is, perhaps, the early stage of the instability, where the interaction of the $3/1$ and $2/1$ modes plays an important role in the discharge evolution. In TCV, it is clearly observed that a $3/1$ mode precedes the fast growth of the $2/1$ tearing mode (t = 0.370 s in figure 5.3). Such a surface mode is believed to be reminiscent of the ideal external kink, which tends to be unstable when a low order rational surface approaches the plasma

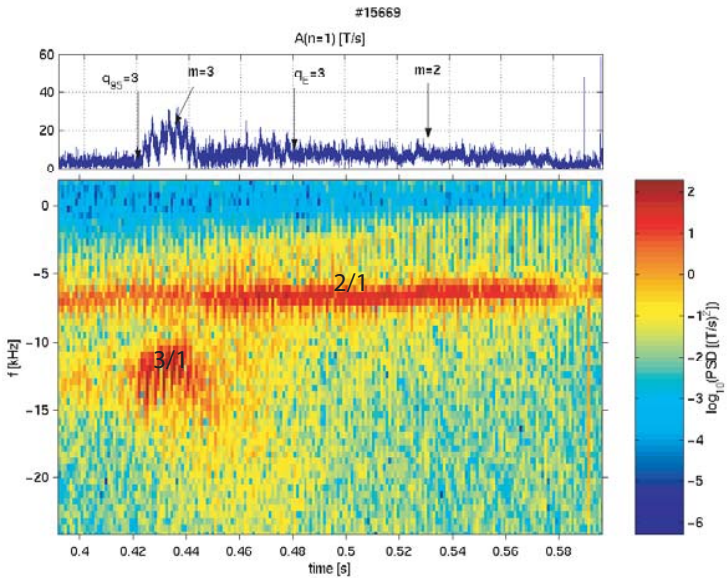

Figure 5.5: *Uncoupled* $3/1$ *and* $2/1$ *modes in non disruptive current ramp up discharge. The* $3/1$ *mode is destabilised at* $q_{95} = 3$*, saturates while rotating at 12–13 kHz, and finally disappears after about 30 ms. The* $2/1$ *mode rotates at 7 kHz, saturates at small amplitudes and disappears at t=0.58 s.*

edge [34]. Although this instability alone, involving only the plasma surface, is rather harmless (see also section 5.4), it is nevertheless able to couple to the $q = 2$ surface and destabilise the $m = 2$ magnetic island.

In the following we aim to enlighten the major mechanisms involved in the modes destabilisation and to show how it can be avoided. We will focus on the role of mode coupling and plasma shaping on the $2/1$ TM stability. In this context we present experimental evidence of the important role of mode coupling in driving large islands, which lead to plasma disruption.

5.3.1 Evidence and role of the $m/n = 3/1$ and $m/n = 2/1$ mode coupling

A signature of the strong interaction of perturbations resonant on different rational surfaces is the frequency locking. Owing to the electromagnetic force, two coupled modes tend to rotate at the same frequency independently of their initial natural frequency [12]. The mode natural frequency depends on the equilibrium $\vec{E} \times \vec{B}$ and diamagnetic flows. The FFT analysis of the n =1 component of the disruption precursors clearly shows a single frequency $\omega(t)$, while the dominant poloidal mode number continuously changes from $m = 3$ to $m = 2$, indicating that the modes located on $q = 2$ and $q = 3$ surfaces are locked (see figure 5.3).

This is to be compared to the evolution of discharges where mode coupling and disruption do not occur despite the small shaping. In these cases the $m/n = 3/1$ and $m/n = 2/1$ modes may coexist but remain uncoupled, rotating at different

frequency while remaining at small amplitude. An example is shown in figure 5.5, where the $m/n = 2/1$ mode saturates at small amplitude and eventually disappears without causing any disruption. It can be noted that the $3/1$ mode is temporarily destabilised (top plot in figure 5.5), as often observed in similar experiments with $q_{95} < 3$ [34]. The $3/1$ mode rotates at about 12 kHz, and the $2/1$ mode at 7 kHz, thus they are uncoupled. Before the $q = 3$ surface leaves the plasma (at t=0.48 s), the $3/1$ mode vanishes while the $2/1$ mode persists at small amplitude. Clearly, the mode coupling between the internal modes and the external surface mode is a key element of the dynamic in this type of disruptions.

5.4 Avoidance of the $q = 3$ current rise disruption by means of plasma shaping

The beneficial effect of plasma shaping in suppressing the MHD activity and disruption was noticed early in TCV operation. During the initial current rise phase, a sufficient plasma elongation and/or plasma triangularity allows for a safe crossing of the $q = 3$ rational surface through the plasma boundary. The effect of plasma shaping is schematised in figure 5.6, where the $\kappa - \delta$ space can be divided in disruptive and non-disruptive regions.

Almost all quasi-circular plasmas disrupt when the edge safety factor decreases below 3 (section 5.2). However in a few cases where only uncoupled modes are present (as shown in figure 5.5), the current ramp up may be continued without disrupting the discharge.

In moderately shaped plasmas, the magnetic signal shows transient bursts of MHD activity not leading to plasma disruption. The $m/n = 3/2$ mode is stable, and no mode coupling is observed. Figure 5.7 shows the MHD activity of a moderately shaped discharge with $\kappa = 1.25$ and $\delta = -0.4$. It can be seen that, at the crossing of the $q_a = 3$ surface, the magnetic signal of a $3/1$ mode increases (and the frequency abruptly decreases), the $2/1$ mode remains stable, and the current rise can be continued without difficulties. We also observe that instabilities with dominant mode numbers $m/n = 4/1$, $3/1$ and $5/2$ are detected when the $q_a = 4$, 3 and 2.5 surfaces are respectively crossed, confirming that an external kink mode is strongly destabilised when a low order rational surface approaches the plasma boundary.

Notably, both positive and negative values of triangularity improve the MHD stability and help avoiding plasma disruptions. A similar beneficial effect of the triangularity on the stability of the internal kink mode, responsible for sawtooth oscillations, has also been noticed [10, 46].

In the same way, and independently of triangularity, plasma elongation is also able to reduce and suppress the MHD activity already at small values of κ. It is found that at an elongation $\kappa \sim 1.35$, the maximum mode amplitude decreases abruptly (see figure 5.6), and disruptions can be avoided.

Finally, in strongly shaped plasmas the MHD activity remains below the detectable level and, remarkably, even the $3/1$ surface mode (also called external kink mode) does not appear.

To summarise, plasma shape appears to act primarily on the stability of the tearing modes (mainly $2/1$ and $3/2$) and, at large values of elongation and triangularity, on the external kink mode stability.

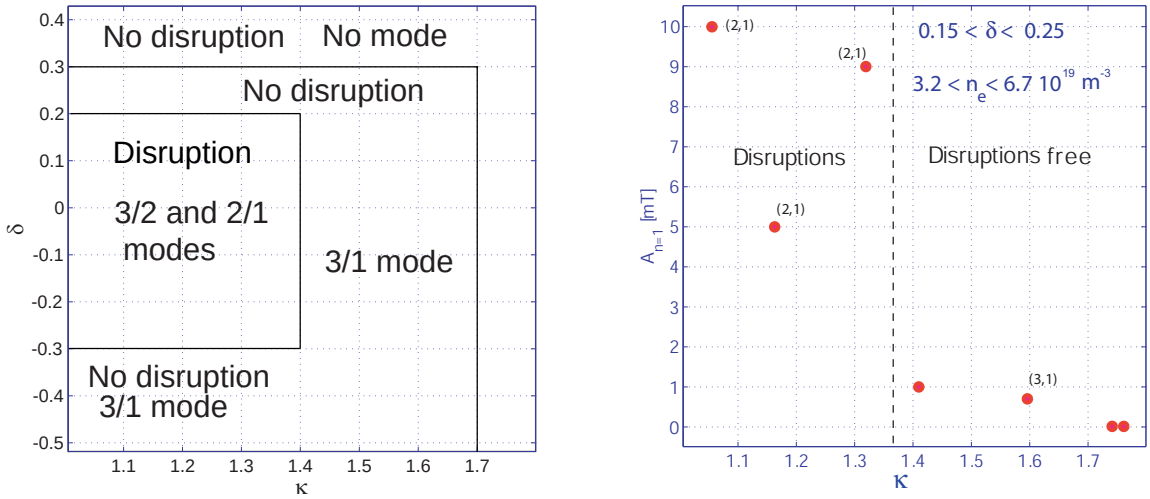

Figure 5.6: *Left: disruption events in the $\kappa - \delta$ plane. The dominant mode numbers are also indicated. Right: maximum mode amplitude as a function of the plasma elongation κ. Large elongation values strongly reduce the risk of disruptions during current rise by stabilising the $m/n = 2/1$ tearing mode.*

Several factors are expected to influence the stability of shaped plasmas and possibly explain the experimental observations. Firstly, the equilibrium current profile may be modified by the plasma shape, especially in the region close to the plasma edge. Secondly, the MHD stability is expected to be strongly influenced by the mode coupling due to the shaped plasma cross-section [12]. Thirdly, the conducting wall stabilisation, due to the wall eddy currents, is expected to become important for strongly shaped plasmas with large cross-sections. In fact, because of the radial multipolar magnetic field decay, the conducting-wall effect depends on the plasma-wall distance. Given the geometry of the TCV vacuum vessel, the averaged distance between the plasma boundary and the metallic wall significantly varies with the plasma shape. We will consider these three factors in section 5.5.2. We now discuss the stability of the $2/1$ tearing mode in a toroidal plasma

5.5 The 2/1 tearing modes stability of TCV shaped plasmas

According to the cylindrical linear resistive MHD theory of low-β plasmas, the criterion for the stability of a tearing mode is given by [35],

$$\Delta' \equiv \lim_{\delta \to 0} \frac{1}{\Psi(r_s)} \left[\frac{d\Psi}{dr}(r_s + \delta) - \frac{d\Psi}{dr}(r_s - \delta) \right] < 0 \tag{5.1}$$

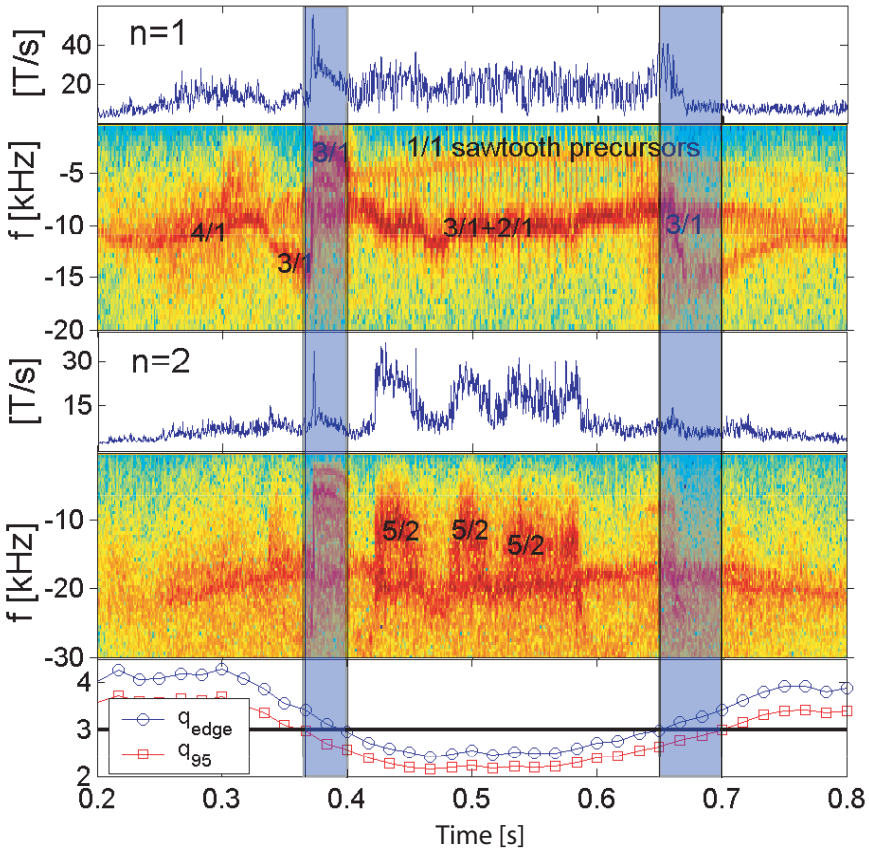

Figure 5.7: *Current ramp up experiment (#21402) at negative triangularity (–0.4). Amplitude and spectrogram of the $n = 1$ and $n = 2$ toroidal components of the magnetic perturbation are shown. Negative frequencies correspond to mode rotation in the electron diamagnetic drift direction). The temporal evolution of the safety factors at the edge and at 95% of the poloidal flux shows the crossing of the $q = 3$ surface through the plasma boundary.*

with $\Psi = rB_r$ and r_s is the radius of the resonant surface. In a cylindrical circular plasma each poloidal harmonic m is decoupled from the others, and the tearing stability depends only on the radial derivative of the perturbed flux calculated on the resonant surface with $q = m/n$. In a toroidal plasma, however, the poloidal harmonics are coupled by the geometry. To the lowest order, the harmonic m drives, through toroidicity, the poloidal sidebands $m \pm 1$ resonant on other flux surfaces. These sidebands couple back to produce corrections to the original cylindrical tearing mode [12]. As shown earlier, in the initial phase of the current rise disruption, the coupling between the $q = 2$ and $q = 3$ rational surfaces is crucial for the subsequent growth of the instability.

We shall see that the theory of coupled tearing modes predicts under certain conditions a destabilising effect on resonant interacting modes.

5.5.1 Toroidal destabilisation of the tearing mode

The dispersion relation of two coupled rotating tearing modes has in general two complex solutions for the eigenvalue ω. Let ω_1 and ω_2 be the 'natural' real (rotation) frequencies of the tearing modes at the $q = 2$ and $q = 3$ surfaces respectively. The interaction between the modes is maximised when the modes are resonant at the same frequency $\omega_1 \sim \omega_2$. Note that this condition is well satisfied in the described experiments since the $2/1$ and $3/1$ perturbations exhibit the same rotation frequency when the disruption occurs (section 5.2). It has been shown in reference [47] that under these conditions the inner mode may become more unstable than in absence of resonant coupling (see also chapter 2). In fact, according to the linear resistive theory, when the $q = 3$ surface is close to the edge, the complex mode frequencies (eigenvalues) can be expressed as [12, 47]:

$$\omega = \omega_2 + i\frac{E_{22}}{\tau_2} \tag{5.2}$$

$$\omega = \omega_2 + i\frac{1}{\tau_1}\left[E_{11} - \frac{E_{12}^2}{E_{22}}\right] \tag{5.3}$$

where τ_1 and τ_2 are respectively the 'visco-resistive' reconnection times at the $q = 2$ and $q = 3$ surface, and $\tau_1 \gg \tau_2$. The diagonal matrix elements E_{ii}, obtained by solving the ideal MHD equations, correspond in the cylindrical limit to the tearing mode stability index $E_{ii} = r_{s_i}\Delta'_i$. The off-diagonal coupling coefficient E_{12} typically increases with the inverse aspect ratio and with decreasing distance between the coupled surfaces (note that in the high magnetic shear edge region the rational surfaces get closer to each other). A positive imaginary part of ω corresponds to an unstable mode. Equation 5.3 suggests that in presence of mode coupling strong destabilising occurs when $E_{22} \to 0^-$. Thus, under certain conditions, even a cylindrically stable $2/1$ mode may be destabilised by mode coupling.

To check if this toroidal destabilising mechanism is relevant in the TCV ramp-up scenario, we calculate the coefficients E_{ij} using numerical codes with the inclusion of the experimental equilibrium from magnetic measurements. The outer region resistive stability code PEST3 [48] is, in principle, able to calculate the complete matrix $\mathbf{E}$ for an arbitrary number of rational surfaces and arbitrary toroidal geometry. Unfortunately due to the vicinity of the q=3 surface to the plasma edge the numerical scheme does not converge and the results are unreliable. We therefore limit the use of PEST3 to the calculation of Δ' for the $2/1$ mode alone while the tearing stability factor of the $3/1$ mode $E_{22} = r_{s_2}\Delta'_2$ is computed with the cylindrical code DELTAPCYL.

An example of such a calculation is shown in figure 5.8 for a quasi-circular plasma (#21400, see section 5.2 and figure 5.3). It can be seen that $\Delta'_{m=2}$ is always negative, indicating an intrinsic stability of the $2/1$ tearing mode. Owing to the vicinity of the $q = 3$ surface to the plasma boundary, $\Delta'_{m=3}$ will strongly depend on the free or fixed boundary conditions (b.c.) employed in the calculation. On the contrary the effect of the conducting wall on the more internal $m = 2$ mode is small, therefore we only show $\Delta'_{m=2}$ calculated with free b.c..

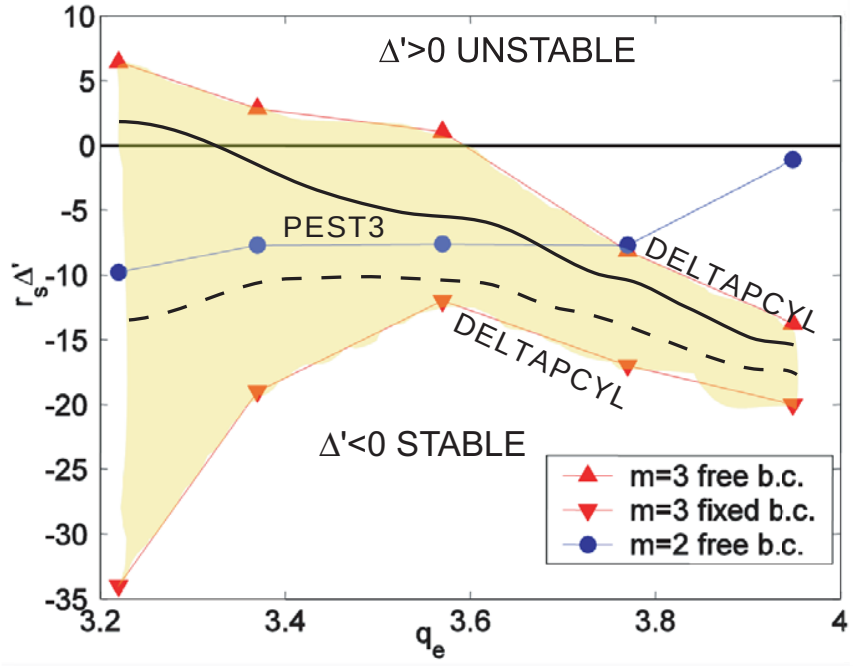

Figure 5.8: *Tearing stability diagram for $m = 2$ mode (blue circles) and $m = 3$ modes with free (red upward triangles) and fixed (red downward triangles) b.c. for a "low shaping" case ($\kappa \simeq 1.3$ and $\delta \simeq 0.2$). The shadowed region represents realistic estimations of the stability index. Negative (positive) Δ' values correspond to stable (unstable) modes. The solid black line represents a possible path in the tearing stability diagram during a TCV ramp up experiment of a quasi-circular plasma leading to $2/1$ mode destabilisation, whereas the dashed line refers to a strongly shaped plasma that remains stable. The experimental equilibria have been obtained from the magnetic measurements of discharge #21400.*

With free (vacuum) b.c., $\Delta'_{m=3}$ evolves during the ramp-up from negative (stable) to positive (unstable) values (when $q_a \lesssim 3.6$). According to equation 5.3, this implies a strong destabilisation of the $2/1$ tearing mode. Despite its cylindrical stability, the $2/1$ mode may in fact abruptly grow. This effect is entirely due to the toroidal coupling.

The presence of a perfectly conducting wall (fixed b.c.) may, however, improve the mode stability. The plasma-wall interaction strongly depends on the distance of the rational surfaces from the wall, and is very effective on the outer mode, stabilising the $3/1$ tearing mode in the range of q_a =3–4. A realistic estimation of the stability index lays, thus, in the region delimited by the free and fixed b.c. curves, and depends on the exact geometry of the plasma and the conducting wall. The boundary of the quasi-circular TCV plasma is on average quite far from the vacuum vessel, and therefore a value of the stability index close to the free b.c.

curve is to be expected.

Toroidal mode coupling may thus explain the destabilisation of a cylindrically stable $2/1$ tearing mode during the plasma current rise in TCV.

5.5.2 Plasma shape stabilisation of tearing modes

There are at least three mechanisms which play a role in the stabilisation of the tearing mode and that depend on plasma shape: the interaction with the *conducting walls*, the *modification of the equilibrium current profile*, and the *coupling* to vacuum rational surfaces. These mechanisms act simultaneously and independently. On the basis of the presented experiments, it is not clear whether one of the three mechanisms is dominant over the others.

As earlier mentioned, the stabilising effect of the *conducting wall* is more effective on strongly shaped plasmas. The average distance between the plasma boundary and the wall decreases at large values of elongation and triangularity. Qualitatively, the coefficient E_{22} in equation 5.2 is expected to have large and negative values, as suggested by the (dashed) "ramp up" path in figure 5.8. As a consequence, according to equation (5.3), the destabilising influence of toroidal mode coupling is reduced, and the growth of a large tearing mode inhibited. The beneficial effect of the conducting wall can also be invoked to explain the observed stabilisation of the external kink mode in strongly shaped TCV plasmas (figure 5.6, section 5.4).

A quantitative realistic modelling of the wall effect requires the implementation of the exact geometry of the TCV vacuum vessel into a numerical outer layer code such as PEST3, and is beyond the scope of this thesis. In future experiments the wall stabilising mechanism could however be experimentally tested using the flexible shape and position control system of the TCV tokamak.

Let us now analyse the stabilising effect related to the *modification of the equilibrium current density profile* by plasma shaping. It is well known that the plasma shape strongly influences the electron temperature profile, which may in turn modify the current profile [49, 50]. In absence of a direct measurement of the current profile, we rely on global current profile peaking indicators, such as the q-profile peaking factor, q_a/q_0, and the normalised internal inductance, $l_{\mathrm{i,norm}}$[51]. Several TCV discharges have been analysed to gain insight on the influence of plasma shape. In figure 5.9 the normalised internal inductance is plotted against the q-profile peaking factor. For a given value of q_a/q_0, a smaller $l_{\mathrm{i,norm}}$ is a sign of broader current profile. We find that the normalised inductance in strongly shaped plasmas is up to 20% lower than in quasi-circular plasmas. In figure 5.9b) we show the Δ' calculations for the two discharges marked with black circles in figure 5.9a). We find that the strongly shaped plasma is stable with respect to the tearing modes, whereas the quasi-circular plasma (with higher $l_{\mathrm{i,norm}}$) is unstable.

Finally, additional *mode coupling* effects due to the shaped plasma cross-section are expected to influence the $2/1$ tearing mode stability. The pure toroidal geometry couples, in the lowest order approximation, to the $m \pm 1$ sideband of the

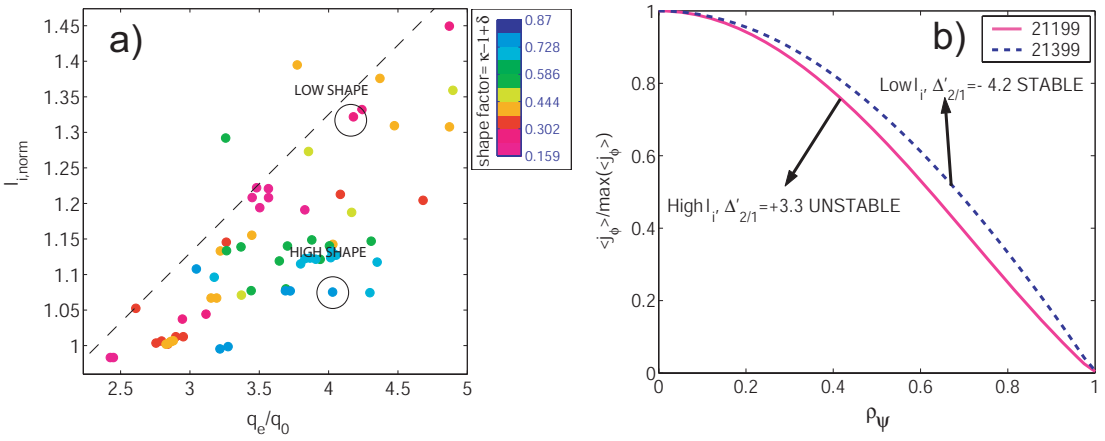

Figure 5.9: *a) Normalised internal inductance plotted against the q_a/q_0 peaking factor for current rise discharges at $q_a \sim 3$. Different plasma shapes are characterised by the shaping factor $s = \kappa - 1 + |\delta|$, and represented with different colours. b) Equilibrium current profiles (from LIUQE) corresponding to the two discharges marked with black circles in a). The solid red line corresponds to the quasi-circular plasma, and the blue dashed line to the strongly shaped plasma.*

principal m poloidal component, resulting in the interaction of the $q = 1$, 2 and 3 rational surfaces, whereas elongation and triangularity couple the $m \pm 2$ and $m \pm 3$ harmonics respectively [12]. The $q = 2$ tearing mode is thus influenced by the $q = 4$ and $q = 5$ resonance surfaces. In limited discharges, the $q = 4$ and $q = 5$ flux surfaces are located in the 2.5 cm thick vacuum that separates the plasma boundary from the conducting wall, and may therefore contribute to the global plasma stability through mode coupling. It has been shown by numerically solving the outer boundary layer equations for coupled modes that both elongation and triangularity can stabilise an unstable $2/1$ tearing mode for plasmas with $q_a < 4$ [12].

5.6 Concluding remarks

- In TCV current rise experiments MHD instabilities appear when the edge safety factor approaches the rational numbers 5, 4, 3 and 2.5. We have analysed, for the first time, the details of this type of disruptions in TCV. We find that the initial instability has dominant mode numbers $m/n = q_a$ and is thus localised at the plasma boundary. This suggests a link with the external kink mode.

- In a quasi-circular plasma the MHD activity often leads to plasma disruption when $q_a \sim 3$. The disruption is preceded by the fast growth of coupled $2/1$ and $3/2$ tearing modes associated with a decreasing of the mode frequency. Experiments with slow current rise rates in presence of sawtooth activity

confirm that the current profile is peaked, close to its quasi-stationary shape. This excludes the role of transient effects, such as the destabilising skin-current effect, on the stability. There are evidences that resonant interaction (mode coupling) between the $3/1$ kink mode and the $2/1$ tearing mode in the initial phase of the MHD activity leads to plasma disruption:

1. disruptions always occur at $q_a \lesssim 3$ in presence of large $2/1$ magnetic islands (figure 5.2);
2. disruptions always occur when the $2/1$ tearing mode coexists with a $3/1$ mode rotating at the same frequency (figure 5.3);
3. disruptions do not usually occur if the $3/1$ and $2/1$ modes do not coexist or coexist but rotate with different frequency (figure 5.5).

- Moderate and strong plasma shaping stabilises the disruptive mode. Both plasma elongation ($\kappa > 1.35$) and positive ($\delta \gtrsim 0.2$) or negative ($\delta \lesssim -0.3$) triangularity prevent the growth of large $2/1$ magnetic islands. For strongly shaped plasma even the surface mode is absent.

- Linear resistive MHD theory of coupled modes successfully predicts the destabilisation of cylindrically stable 2/1 modes by the effect of toroidal coupling. Calculations of the tearing stability index using the TCV experimental data confirm the importance of this destabilising mechanism.

- Three different mechanisms, linked with plasma shaping, are suggested to stabilise the $2/1$ tearing mode:

  1. the effect of the conducting wall (in particular at large elongation);
  2. the modification of the equilibrium current density profile as shown by the small normalised internal inductance of strongly shaped plasmas and tearing stability factor calculations;
  3. the coupling with the $q = 4$ and $q = 5$ resonant surfaces.

Chapter 6

Disappearance of the sawtooth oscillations with far off-axis ECRH at high elongation

In TCV ERCH is used to modify the pressure and current profiles and the plasma shape. For instance, very off-axis heating allows the production of vertically stable, high-elongation discharges at low normalised current. In these discharges, due to the very flat current profile (but still with positive shear), sawtooth oscillations may disappear, replaced by a continuous MHD mode resonant on the $q = 1$ surface. The sawtooth disappearance phenomenon is found to be well predicted by the so-called "Porcelli sawtooth model" based on the linear stability of the internal kink mode.

6.1 Introduction to sawteeth

Sawtooth oscillations, or sawteeth, are periodic relaxations of the central temperature, density and other plasma parameters [4]. First observed in the ST tokamak [52], sawteeth are named after the characteristic signature of the temporal traces of the soft X-ray emission. They present a slow rise of the plasma parameters (ramp-up phase) followed by the onset of $m/n = 1/1$ helical perturbations, or internal kink motions (see chapter 2), localised at the estimated radius of the $q = 1$ surface, causing a rapid drop in the central temperature and density, the so-called sawtooth crash (see figure 6.3). The condition $q_0 < 1$ is necessary but not sufficient for standard sawteeth to occur (see section 2.1). In general, a sufficiently large free energy has to accumulate in the plasma core before an MHD mode may trigger a sawtooth crash. During the crash a reconnection process results in the flattening of the central temperature and density profiles. The corresponding

outward transport and redistribution of energy and particles define an inversion radius $\rho_{\rm inv}$, which separates the central region where energy is lost, from an outer region where the energy is deposited. The inversion radius is expected to be close to the radius of the $q = 1$ surface. The investigation of sawteeth has concentrated on the three consecutive phases of the sawtooth cycle: firstly, on transport of energy and particles as well as current diffusion during the sawtooth ramp, secondly, on the instability triggering the sawtooth crash, and finally, on the relaxation process leading to the rapid outward transport during the sawtooth crash. Important quantities characterising the sawtooth cycle are:

- *The sawtooth amplitude* $A_{\rm saw}$. Combining the measurements of central temperatures, density (or soft X-ray), and inversion radius the total energy lost during a sawtooth crash can be estimated with

$$A_{\rm saw} \equiv \Delta E_c/E_c = \Delta T_e/T_e + \Delta n_p/n_p \tag{6.1}$$

  where the total plasma energy is $E_c = 3/2 N_p \kappa_B (T_e + T_i) V_c$, and the volume $V_c \sim 2\pi R_0 r_{inv}^2$. For simplicity, the variation in the ion temperature is neglected. Frequently, the relative variation of the central soft X-ray emission (corrected for the temperature dependence $\alpha = d(lnI_X)/d(lnT_e)$) is used as an estimate of $A_{\rm saw} \sim \alpha \Delta I_X/I_X$.

- *The sawtooth period* $\tau_{\rm saw}$, the time elapsed between two sawtooth crashes. It has been shown that for Ohmic TCV plasmas the re-heat rate in the sawtooth ramp phase is mainly determined by the heating power density [53],

$$\frac{dE}{dt} \approx p_{\rm in} \tag{6.2}$$

  with $p_{\rm in}$ the central heating power and E the thermal energy. This result is justified by the fact that in the plasma core the radiation and conductive losses are small because of the high temperature and small gradients. For standard, triangular shaped sawteeth, an integration over the sawteeth period and averaging over the core volume yields the relation,

$$\frac{\Delta E_c}{V_c} \approx \langle p_{\rm in} \rangle \tau_{\rm saw} \tag{6.3}$$

  Therefore, $\tau_{\rm saw}$ allows us to estimate the energy lost during a sawtooth crash. In the case of complete flattening of the profiles within $q = 1$ following the sawtooth crash, it can be shown that τ_{saw} is related with the central poloidal beta $\beta_{p,1}$ (also referred to as $\beta_{\rm Bussac}$) attained prior to the sawteeth crash [9]. Roughly it can be said that longer $\tau_{\rm saw}$ corresponds to higher $\beta_{\rm Bussac}$.

- *The collapse time scale* τ_c. It is typically of the order of 100 μs and almost always much shorter than the sawtooth period (from several to hundreds of ms in large tokamaks). The sawtooth collapse is often preceded by a growing m/n=1/1 helical perturbation seen as a sinusoidal oscillation (precursor

oscillations) due to toroidal rotation. The presence of precursors may indicate an instability growing at a rate slower than the plasma rotation period $\gamma < f_{\rm rot}$. The growth of this slow precursor oscillation has been believed to be responsible for the sawtooth crash. Kadomtsev interpreted this precursor as an $m = 1$, $n = 1$ tearing mode growing to invade fully the core encompassed by the island [54]. This picture is in apparent contradiction with the observation of oscillations continuing after the sawtooth crash (successor or postcursor oscillations). Moreover, the rapidity of the sawtooth crash in large tokamaks implies that the relaxation must involve an event faster than the island growth, as indicated by the magnetic signal during the crash [55]. Although many mechanisms for the sawtooth collapse have been proposed there is not yet a commonly accepted model consistent with the large variety of the experimental data.

The interest in sawteeth originated in their impact on central plasma parameters and resulting degradation of confinement. In a fusion reactor the repetitive flattening of central profiles would lead to a reduction of the neutron yield. In recent years, a main concern has arisen from the observation that large sawteeth can generate seed islands particularly on $q = 3/2$ and $q = 2/1$ surfaces and trigger neoclassical tearing modes, which limit the achievable β. Nevertheless, sawteeth can also be beneficial since they can prevent the accumulation of impurities in the plasma centre. A large effort is devoted by the fusion community to the control of sawtooth oscillations and to the understanding of the underlying physics.

6.2 Experiments with far off-axis ECRH and sawteeth disappearance

A means to improve plasma performance is plasma cross-section shaping. Plasma elongation, in particular, allows us to increase the plasma cross-section and achieve higher plasma current ($I_p \propto (1+\kappa^2)/2$) and toroidal beta values than in circular cross-sections with the same minor radius and toroidal magnetic field [56]. Thus, for a desired value of the plasma current, q_a and β_t, it is possible to use smaller devices (smaller major radius) at lower magnetic field with obvious economical advantages. However, stable operation at high elongation is limited by the vertical instability (axisymmetric n = 0 mode) whose growth rate increases with κ and also with the peaking of the current profile. For Ohmic plasmas, this implies operating at low edge safety factor q_a, or, equivalently, at high normalised current $I_N = I_p/aB$. Stable Ohmic operation at $\kappa \sim$ 2.5 requires $I_N >$ 2.25 MA/Tm in TCV [57]. To benefit from high elongation at low and intermediate values of the normalised current, a broadening of the current profile is required.

In TCV, profile broadening can be obtained using off axis ECRH or current drive. Experiments have been performed using localised 2^{nd} harmonic X-modes (X2) to tailor the current profile during the current flat-top, and to stabilise highly elongated discharges ($\kappa \sim$ 2.5) at high safety factor and low current [58, 59, 60].

The current modification relies on the modification of the conductivity profile by radially localised power deposition. Various plasma currents ($280 \leq I_p \leq 430$ kA) and central densities ($(2 \leq n_{e0} \leq 8)\cdot 10^{19}$ m^{-3}, $0.47 \leq n_{e0}/n_{e,\mathrm{cut-offX2}} \leq 1.88$) are explored. The X2 power is deposited in a vertically stable Ohmic plasma, with an intermediate elongation ($\kappa \sim 1.75$). Discharges are preprogrammed with constant quadrupole and hexapole fields and the plasma current is kept constant by feedback control. The profile broadening leads to stronger interaction of the plasma column with the vertical magnetic field and consequently to a higher elongation in a low I_N vertically stable plasma. No direct measurement of current profile is available but three "current indicators" can be used to follow the plasma current evolution.

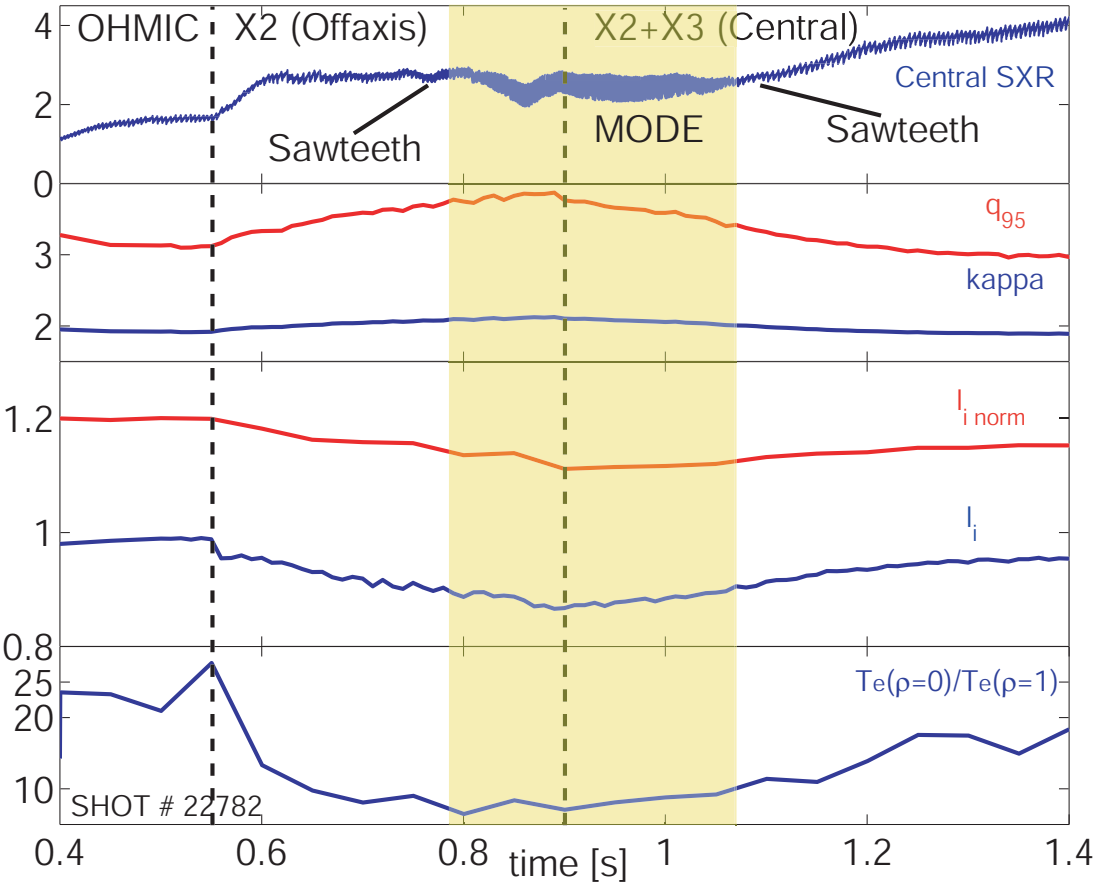

Figure 6.1: *Evolution of the sawtooth activity and current profile indicators in a discharge with X2 off-axis heating phase, and X2 off-axis plus X3 central heating. From top to bottom: central SXR signal, q_{95}, κ, l_i and $l_{\mathrm{i,norm}}$, and central electron temperature/edge electron temperature. The appearance and disappearance (yellow shadowed region) of the sawtooth activity correlates well the current profile broadening.*

First, the elongation results from the interaction between the plasma current

and the current in the shaping coils. When the latter is constant an increasing k indicates a flattening of the current profile [59, 60]. Second, the normalised internal inductance $l_{\mathrm{i,norm}}$ [51], is also a typical (global) indicator of the current profile peakedness that only weakly depends on the plasma shape. Third, as in this scenario the bootstrap contribution is small ($\leq 5\%$) and ECCD is negligible, the electron temperature with its link to the plasma current profile provides useful information on the relative variation of the peaking.

The evolution of the profile indicators is plotted in figure 6.1. During the X2 off-axis power deposition (0.55 < t < 0.9 s), the current profile broadens, increasing the plasma elongation. Since the current is fixed, q_{95} increases. The electron temperature reaches a stationary condition after ∼100 ms (see also soft X-rays), while the plasma current diffuses more slowly, as can be seen from the internal inductance evolution. We are interested in the disappearance of the sawtooth activity observed during the current profile broadening. Under certain conditions, the sawtooth activity is replaced by a continuous MHD mode (shadowed region). The mode structure (see section 6.4) suggests that the $q = 1$ surface, although smaller than its initial size, remains present in the plasma core. The sawtooth disappearance is studied in detail in the following sections.

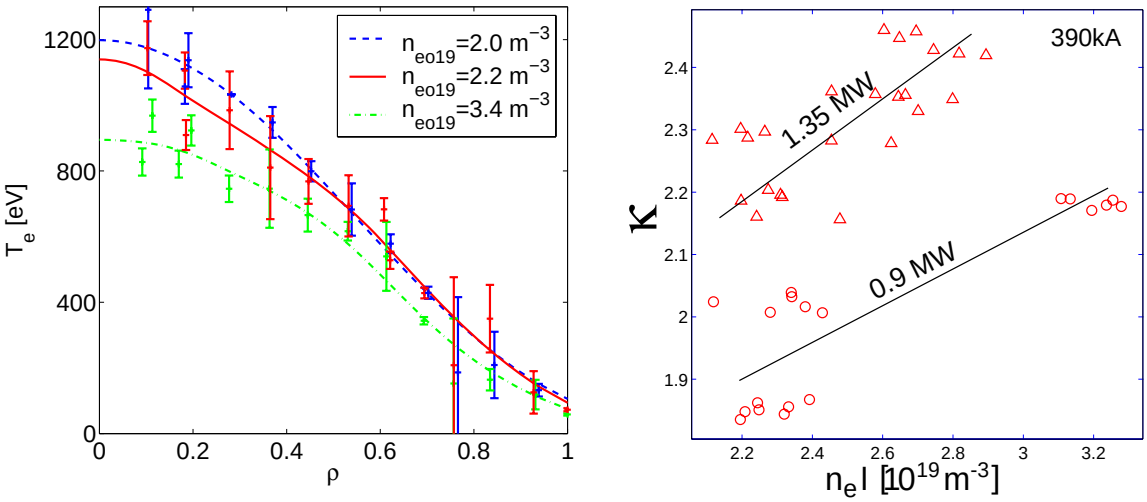

Figure 6.2: *Density effect on the current broadening indicators. Left: a density increase flattens the electron temperature profile in the core (I_p = 300 kA). Right: κ increase with line-averaged density, for a central chord, at constant EC power.*

We empathise again the relation of the disappearance/appearance of sawteeth with the current peaking (right side figure 6.1) as observed in experiments with central third harmonic (X3) heating added to the X2 pre-heated discharges. The X3 power is applied after almost complete relaxation of the current profile (at t= 0.9 s). As a result of the central heating, the electron temperature and current profile peak again as visible from the temporal evolution of the 'current indicators'. The sawtooth crashes reappear after 100–200 ms. This important observation links the current profile evolution to the core MHD activity.

Another important feature of these experiments is related to the plasma density. It is found that the density of the target plasma has a strong influence on the final value of κ and profile broadness. Figure 6.2 shows that higher densities lead to higher κ and broader temperature profiles, as reported and explained in [60]. The plasma density is observed to play an important role in the core MHD activity for this scenario as shown in the next section.

6.3 The disappearance of sawteeth: n_e and l_i thresholds

In these experiments, we distinguish two types of transition to sawtooth-free plasmas. The first occurs in discharges with low plasma current ($<$ 400 kA) with no central MHD activity observed during the sawtooth-free phase. The high resolution ($\sim$ 0.5 cm) MPX camera (see chapter 3.1) allows the detection of a small inversion radius. An example of the evolution of the inversion radius from the chord-integrated signals is shown in figure 6.3, together with the central soft X-ray time trace. The inversion radius decreases from 8.3 cm in Ohmic to 3.3 cm in about 120 ms. For smaller r_{inv} the evaluation becomes inaccurate. The edge safety factor and the elongation continue to increase for more than hundred milliseconds, and the $q = 1$ surface is expected to shrink and eventually disappear explaining the sawtooth disappearance in these lower current plasmas.

The second, more frequent at medium (400 kA) and high ($\sim$ 490 kA) currents, is accompanied by core MHD activity associated with the presence of the $q = 1$ surface (see section 6.4). In the following we focus exclusively on this transition. We first analyse the various phases of the MHD activity. Later, we attempt an interpretation of the sawtooth disappearance on the basis of the MHD theory.

6.3.1 High current plasmas ($I_p \geq$ 350 kA, $q_{95} \leq$ 4.5, $r_{\rm inv} \geq$ 8 cm)

We want to establish the plasma conditions for the disappearance of the sawtooth activity and the appearance of the core MHD mode. If is found that the plasma density and the internal inductance play an important role in triggering the mode. Figure 6.5 shows the paths of discharges with different density and plasma current in the (n_e, l_i) plane during the initial ECRH phase. Together with the requirement of a finite $q = 1$ surface, high density and low internal inductance constitute favourable conditions for the appearance of the central mode that replaces the sawteeth. At sufficiently high plasma density, the sawteeth disappear for $l_i \leq 0.9$ independently of the total current. This circumstance could be related with the shape of the current density profile. Both the low internal inductance and the high density (as shown in figures 6.2 and 6.5) indicate that a very flat current profile is an essential condition for the stabilisation of the sawtooth instability and its replacement by a continuous mode.

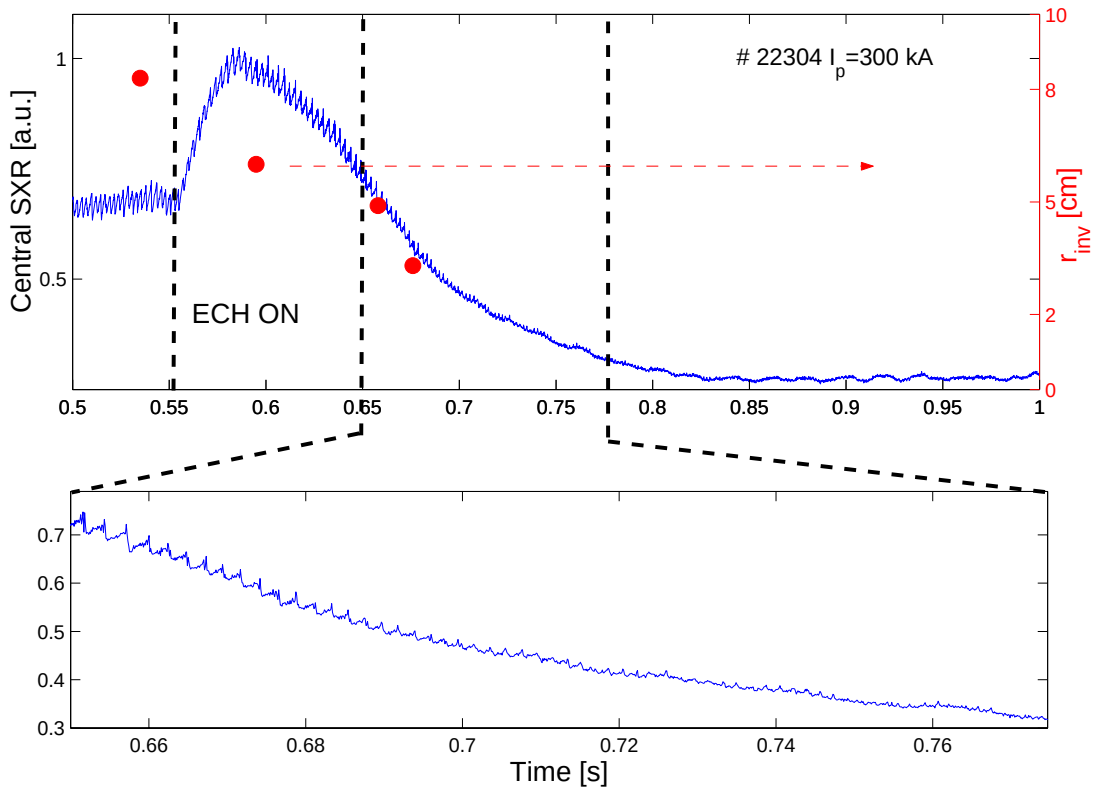

Figure 6.3: *Evolution of soft X-ray emission from the central channel. The sawtooth amplitude decreases below a detectable level about 200 ms after the start of the far off-axis ECRH. The inversion radius decreases accordingly to the evolution of the safety factor q-profile and the $q = 1$ surface is expected to leave the plasma core.*

6.4 MHD modes analysis

In the discharge of figures 6.4 and 6.6 the last visible sawtooth crash happens at t=0.674 s which coincides with the appearance of the continuous mode. The frequency spectra of the magnetic signals shows one or two sharp peaks corresponding to the n =1 and n =2 toroidal Fourier components respectively. The fundamental frequency ω_1 ranges from 2 to 6 kHz (see figure 6.6). The frequency ω_2, of the n =2 component, is $2\omega_1$. The same frequency peaks observed in the magnetics are found in several channels of the MPX detector. A third harmonic may be present with $\omega_3 = 3\omega_1$ and interpreted as the n =3 component of the toroidal spectrum. The relative phases and amplitudes for the three harmonics ω_1, ω_2 and ω_3 can be plotted to visualise the radial mode structure as in figure 6.6. By counting the phase jumps and peaks and comparing the high and low field side structure we can infer that the n =1, 2 and 3 harmonics have dominant poloidal number m =1, 2 and 3 respectively. The three components are resonant on the

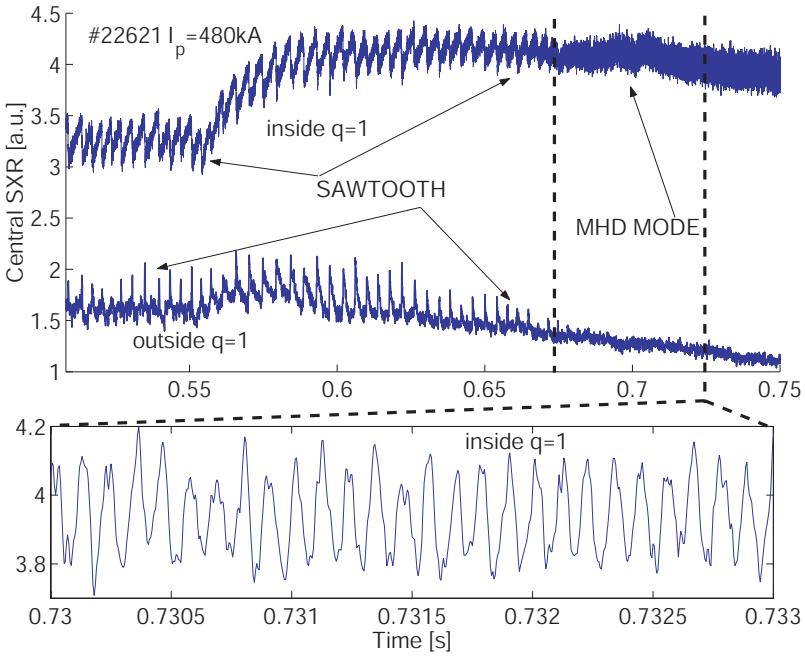

Figure 6.4: *Sawtooth disappearance in high current plasmas. Central soft X-ray signal evolution with off-axis ECRH for I_p = 480 kA. Sawteeth are replaced by continuous MHD activity at t = 0.68 s.*

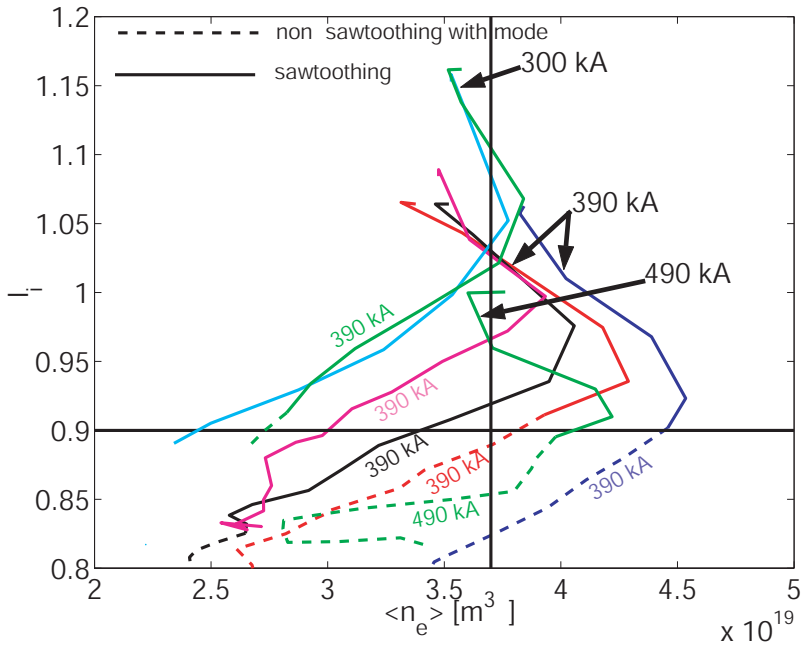

Figure 6.5: *Sawtooth disappearance in high current plasmas. Discharge evolution in the (n_e, l_i) plane for various total currents. Low l_i and high n_e are favourable conditions for the replacement of the sawtooth activity with a continuous MHD mode.*

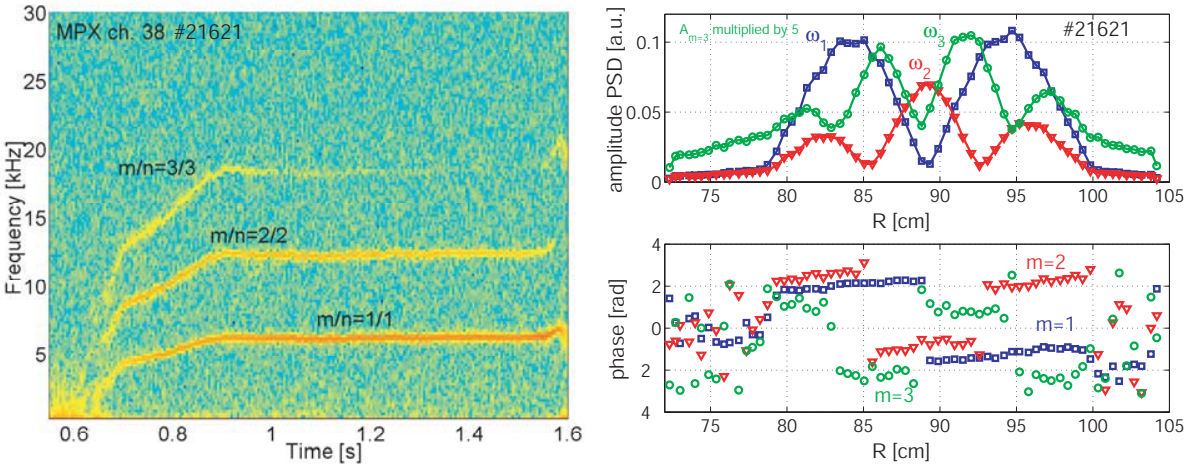

Figure 6.6: *Left: spectrogram of the MPX channel 38. It shows three peak frequencies together with the respective mode numbers identified from the magnetics and soft X-ray emission. Right: the relative amplitude and phase difference in the MPX channels for the three principal Fourier harmonics of the frequency spectra (calculated with [0.70-0.71]s time window)* ω_1*=4.6 kHz,* ω_2*=2*ω_1 *and* ω_3*=3*ω_1*. The poloidal mode numbers* m *=1, 2 and 3 can be inferred for the three harmonics, respectively, from the number of maxima and phase jumps along the plasma radius.*

q =1 flux surface and have similar phase velocity:

$$v_n = \omega_n \frac{R_{q=1}}{n} = \omega_1 R_{q=1} \tag{6.4}$$

The toroidal spectrum of the q =1 mode appears to be rather broad, with important n =1, 2 and 3 components. The broad spectrum may be due to the presence of a relatively high central safety factor q_0, resulting also in a small magnetic shear on q =1, which was observed to broaden the toroidal spectra of the sawtooth instability [55]. This conjecture is supported by the fact that the amplitude of the higher harmonics slowly decreases after t=0.9 s in correspondence with an increase of the magnetic shear (see figure 6.9a) and pressure peaking ($A_{2/2}/A_{1/1}$ from 50% to 20% and $A_{3/3}/A_{1/1}$ from 20% to 0, where $A_{m/n}$ is the amplitude of the mode).

The position of the maximum of the 1/1 component is usually interpreted as the maximum displacement of the hot plasma core due to the kink motion or to a magnetic island. We speculate here, that the off-axis peaks of the 2/2 component correspond to the position of the q =1 surface. These maxima may be expected from the larger density and emissivity of the O-point of the magnetic island with respect to the X-point. Such peak density and temperature profiles inside the magnetic island separatrix have been observed in Textor [33, 32] for the 2/1 island and in many other tokamaks for the 1/1 island (often under the name of "Snake instability"). In section 6.4.1 we will use this conjecture to infer the evolution in the position on the q =1 surface from the radial structure of the mode in figure 6.6. The TCV core MHD activity has some similarities with the well-known Snake instability [61, 62]. For instance, both instabilities are triggered in presence of a

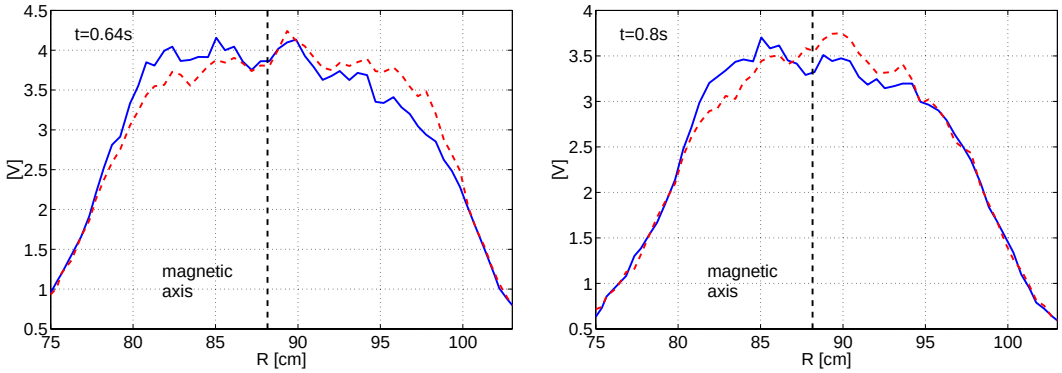

Figure 6.7: *Core displacement during the sawtooth successor oscillations (left) and the continuous oscillation of the central mode all in the same discharge (22621) but at different times. Apart from a slightly more peaked emission profile with the core mode, the two type of perturbations exhibit the same* m *=1 central distortion.*

flattened current profile and both have multiple poloidal harmonics. However, the TCV continuous mode does not show any particular localised emission region (impurity filament) that would be consistent with the present sinusoidal shape of the oscillations in the soft X-ray signal. In this respect, the perturbed emissivity profile has a similar structure to the precursor (successor) oscillations of the sawtooth activity, as shown in figure 6.7. It basically consists of a core displacement, with no evidence of a highly emitting filament or impurity accumulation, and is consistent with the formation of a magnetic island due to an unstable current profile.

6.4.1 Evolution of the q=1 position.

Of great importance to understand the changes of the sawtooth characteristics is the evolution of the q =1 radius. In TCV, $\rho_{q=1}$ can be obtained from the equilibrium reconstruction, radial structure of a MHD mode resonant on q =1 or from the inversion radius of the soft X-ray signals. Figure 6.8a shows the evolution of the q =1 radius obtained combining these techniques. The Ohmic inversion surface can be accurately obtained from the tomographic inversion of the soft X-ray emissivity (figure 6.8b). It corresponds, for this specific case, to an inversion radius $\rho_{\rm inv}$=0.57 (r/a=0.48). The value obtained from the equilibrium reconstruction code LIUQE is somewhat larger, $\rho_{q=1,LIUQE}$=0.62. With the far off-axis ECRH power deposition and the consequent current profile flattening, the q =1 radius decreases as shown by the LIUQE reconstruction (figure 6.8a). Given the reduced sawtooth amplitude and the fast plasma profile evolution, the determination of the inversion surface from tomography is too inaccurate during this transition phase and we therefore rely on the equilibrium reconstruction. Once the core mode is observed, it provides, by means of its radial structure, an alternative measure of the q =1 radius. After the fast shrinking phase (up to about t=0.9 s) the q =1 radius reduces slowly and almost linearly reaching the value $\rho_{q=1} = 0.24$ which corresponds to 5.6 cm. Thus the $q = 1$ surface remains in the plasma during the

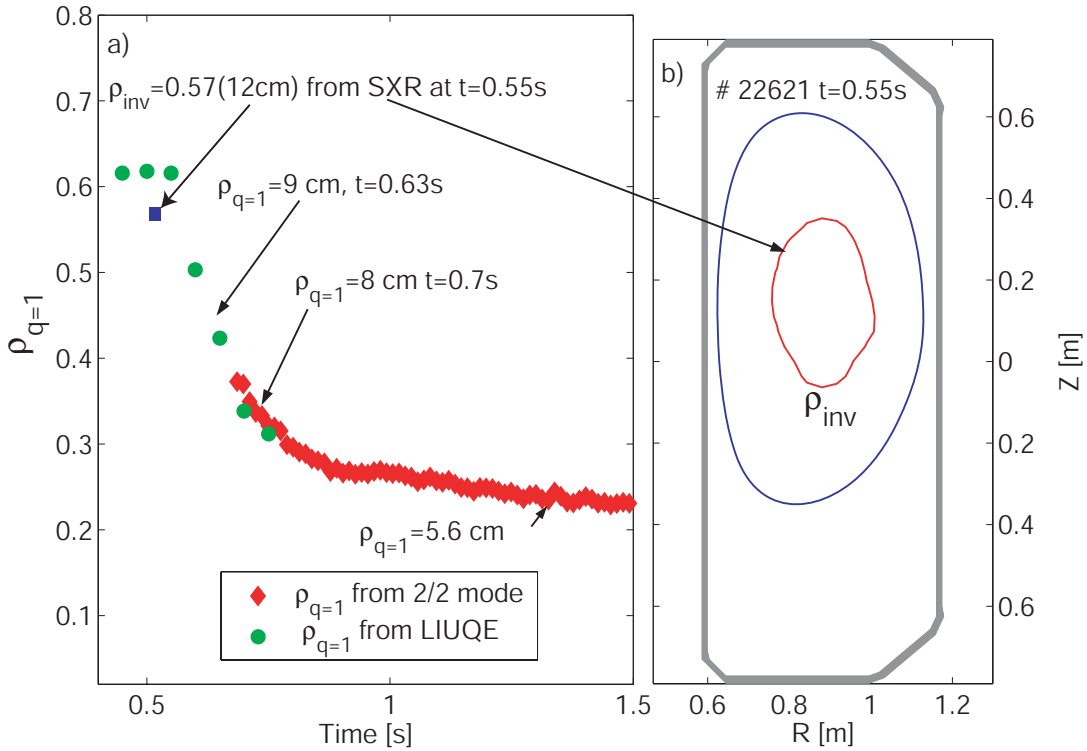

Figure 6.8: *Estimations of the q =1 radius evolution from different techniques. a): evolution of the position of q =1 surface from LIUQE and from the position of the maxima of the 2/2 perturbation in the MHD mode. b): sawtooth inversion surface from the tomography of the soft X-ray emissivity during the Ohmic phase.*

entire of the ECRH phase.

6.5 Comparison with sawtooth models

A complete description of the sawtooth cycle requires a model for the transport inside the q =1 surface, an instability threshold for the onset of the crash and a prescription for the post-crash relaxed profile. In order to explain the sawtooth disappearance we only need to consider the condition for the destabilisation of a mode causing the sawtooth crash. For this purpose we make use of a model developed to predict the sawtooth period in JET and ITER [63] and already successfully applied to Ohmic and ECRH TCV plasmas [64, 65] and NBI plasmas at JET [66]. The model, referred to as Porcelli model [63], has been implemented in the transport code PRETOR [67] by Angioni with some modifications and improvements as described in [65]. The sawtooth crash is triggered by the destabilisation of the internal kink mode, which can be either ideal or non-ideal in nature, depending on the values of the plasma parameters but always evaluated with linear theory. However, the reader may question whether the linear theory is appropriate to treat the

case of the sawtooth disappearance. In fact, the saturated continuous mode in the ECRH phase shows that the internal kink enter the non-linear regime. However, for a certain time, the linear regime should still be relevant and the predictions of the linear theory could nevertheless provide some insight.

The basic features of the Porcelli sawtooth model are presented in the next section. Although in PRETOR are implemented formulas that evaluate the ideal kink mode growth rate, the stability of highly shaped plasmas typical of these experiments is best studied using the full toroidal geometry code KINX [68] (section 6.5.2). Finally, we simulate the evolution of the temperature and current profiles under the effect of the off-axis ECRH using PRETOR in "predictive mode". The transport coefficient is varied in order to match the experimental electron temperature and the experimental sawtooth period $\tau_{\rm saw}$ and inversion radius $\rho_{\rm inv}$.

6.5.1 Sawtooth crash triggering conditions in the Porcelli model

According to reference [63], a sawtooth crash is triggered when an internal kink mode becomes unstable. The kink stability is evaluated using linear MHD theory in the ideal and resistive regime.

Within this framework, an *ideal-like internal kink* triggers the sawtooth crash if its growth cannot be stabilised by the plasma diamagnetic flows, i.e. if,

$$\gamma_{\rm ideal} > 0.5\omega_{i,\rm dia} \tag{6.5}$$

where $\gamma_{\rm ideal}$ is the growth rate of the internal kink and $\omega_{i,dia} = kT_i/L_p eBr_1$ the ion drift frequency with L_p being the pressure scale length, r_1 the radial position of the q =1 surface and B the total magnetic field. The growth rate of the ideal internal kink can be expressed in terms of the normalised potential energy $\delta\hat{W} = -4\delta W/s_1\xi^2\varepsilon_1 RB^2$,

$$\gamma_{\rm ideal} = \frac{-\delta\hat{W}_{\rm MHD}}{\tau_A} \tag{6.6}$$

with $\tau_A = R/{\rm v_A}$ being the Alfvén time, $s_1 = \rho_1(dq/d\rho_1)$ and ε_1 the magnetic shear and inverse aspect ratio on q =1 and ξ the radial displacement. The ideal MHD internal kink potential energy could, in principle, be accurately evaluated using a full geometry ideal MHD code such as KINX. However, a numerical evaluation would be computationally too demanding if employed to simulate the full sawtooth cycle. Therefore analytical formulas are used to evaluate the ideal stability with the form,

$$\delta\hat{W}_{\rm MHD} = \left(\delta\hat{W}_{\rm Bussac} + \delta\hat{W}_{\rm elong}\right) C_\delta \tag{6.7}$$

The terms $\delta\hat{W}_{\rm Bussac}$, first calculated in Ref. [9], takes into account the effect of toroidicity in the large aspect ratio limit of circular cross section while $\delta\hat{W}_{elong}$ includes the destabilising effect of plasma elongation. The additional triangularity factor C_δ give the necessary corrections due to the plasma shape. A well-known

analytical expression for the first term is [9]

$$\delta\hat{W}_{\mathrm{Bussac}} = -\frac{9\pi}{s_1}(l_{i1} - 0.5)\varepsilon_1^2(\beta_{p1}^2 - \beta_{pc}^2) \tag{6.8}$$

where l_{i1} is the internal inductance inside the q =1 surface, $\beta_{p1} = (2\mu_0/B_{p1}^2)(\langle p\rangle_1 - p_1)$ the so-called β_{Bussac} in which $\langle\rangle_1$ denotes volume averaging within the q =1 surface, and $\beta_{pc} = 0.3(1 - 5\bar{r}_1/3\bar{a})$. Therefore, the ideal kink mode (for circular cross-sections) can be destabilised by $\delta\hat{W}_{\mathrm{Bussac}}$ becoming negative once the plasma pressure sufficiently exceeds a critical value. It is interesting to note that for a given q-profile, the ideal internal kink is stable for sufficiently flat pressure profile at a finite value of the q =1 radius. In a shaped plasma, however, the destabilising effect of the elongation may destabilise the ideal internal kink even at $\beta_{p1} = 0$. In addition to the ideal MHD potential energy, fast and trapped particles ion effects can also contribute to the potential energy. In the presently considered TCV experiments, the stabilising effect of fast particles on sawteeth can be neglected. In contrast, the stabilising effect of collisionless thermal trapped ions may be important and its contribution to potential energy, $\delta\hat{W}_{\mathrm{kin}}$, is added to $\delta\hat{W}_{\mathrm{MHD}}$ in equation 6.7. The specific formulas for $\delta\hat{W}_{\mathrm{elong}}$, C_δ and $\delta\hat{W}_{\mathrm{kin}}$, as implemented in PRETOR, can be found in [65]. When the condition 6.5 is satisfied, an internal kink with a step-like radial structure similar to the ideal mode is destabilised. Therefore it will be referred to as the ideal internal kink, even if non-ideal effects have been included.

If the plasma is stable with respect to the ideal mode, the *resistivity* becomes important. When the internal kink potential energy is sufficiently close to zero, the mode dynamics and the linear growth rate are determined by microscopic non-ideal effects in a narrow layer around the q =1 surface where reconnection of magnetic field lines can occur. In this case, the internal kink changes its structure from that of an ideal mode to that of a reconnecting mode and in these condition is referred to as the resistive internal kink. Furthermore, when the internal kink potential energy $\delta\hat{W}$ is positive and larger than a certain threshold, identified in Ref. [63] as basically given by the normalised ion-sound Larmor radius $\hat{\rho}$, the mode structure changes again from that of a global resistive kink to that of a drift-tearing mode [69]. The drift-tearing mode is strongly localised near the q =1 surface and assumed to be too localised to generate an internal collapse as a sawtooth crash. Hence the domain in which the resistive internal kink can be destabilise is given by

$$-\hat{\rho} < -\delta\hat{W}_{\mathrm{MHD}} < 0.5\omega_{i,\mathrm{dia}}\tau_A \tag{6.9}$$

The condition 6.9 defines the *reconnection regime*. When the ion-gyro radius is larger than the resistive layer (i.e. high temperature plasmas), the resistive internal kink in the so-called *semi-collisional ion-kinetic regime* has to be considered [70], which has a different growth rate. A general condition for the resistive mode to be triggered has been proposed [64] which includes the diamagnetic stabilising effects of ions and electrons

$$max(\gamma_\rho, \gamma_\eta) > c_r(\omega_{i,\mathrm{dia}}\omega_{e,\mathrm{dia}})^{1/2} \tag{6.10}$$

where γ_ρ and γ_η are the linear internal kink growth rate in the resistive and ion-kinetic regime respectively and c_r is a numerical coefficient of the order of unity. The resistive growth (γ_ρ or γ_η) essentially depends on the magnetic shear on the q =1 surface, whereas the stabilising diamagnetic effect increases with pressure. Thus, the triggering condition can be rewritten in the form

$$s_1 > s_{1\mathrm{crit},\rho,\eta} \tag{6.11}$$

where s_{1crit}, the critical shear on q =1, is proportional to some power of β_{p1}. The expressions for $s_{1crit\rho,\eta}$, are somewhat different for the two kink regimes but usually give very similar results. The formulas implemented in PRETOR can be found in [65].

An instability condition similar to equation (6.11), involving a critical value of the magnetic shear at q =1, was found in agreement with the experimental observation of stabilisation and onset of sawteeth in TFTR [71]. In particular, it was found that an increased pressure gradient, resulting from an improved core transport, increased the critical shear above the experimental shear value on q =1 stabilising the sawtooth activity. In section 6.5.3, we will see that in TCV off-axis heated discharges, the resistive internal kink may be stabilised by a similar mechanism. However, in TCV, the variation and reduction of the shear on $q = 1$ stabilises the resistive internal kink rather than an increased critical shear.

Since both inequalities (6.9) and (6.11) need to be satisfied for the onset of a resistive internal kink, a crash can be prevented either reaching the condition $s_1 < s_{1crit}$ or the condition $\delta\hat{W}_{\mathrm{MHD}} > \hat{\rho}$. While the latter trigger is found to be the relevant condition for JET NBI-discharges, due to the stabilising effect of the fast ions, the former is found to be consistent with the experimental results in TCV Ohmic and ECRH plasmas at low and moderate elongation. On the contrary, at high elongation, the ideal internal kink was proposed to be responsible for the observed sawtooth behaviour [46, 58]. In the presented ECRH experiments the plasma elongation is fairly high ($\kappa = 2.3 - 2.5$) but the current and pressure profile are rather non-standard, being strongly broadened by the far off-axis ECRH. To determine whether the ideal or the resistive regime of the internal kink mode is relevant, all these competing factors have to be taken carefully into account. We therefore prefer to use the numerical results of the ideal kink stability from the MHD code KINX [68], which are more accurate than the analytical formulas implemented in PRETOR.

6.5.2 Analysis of the ideal internal kink stability with KINX

The internal kink mode stability depends strongly on the plasma shape. The ideal internal kink is predicted to be more stable at large positive and negative triangularities and to be destabilised at large elongation. A detailed discussion of the analytical and numerical results on the effect of plasma shape can be found in reference [72].

Since the growth rate formulas used in PRETOR contain only a simplified description of the shape dependence [65], we use the results of the full toroidal

geometry MHD code KINX. In references [73] and [72] respectively, two formulas are proposed, to fit the numerical results of the mode normalised growth rate, $\gamma_{ideal}\tau_a$, in a wide range of plasma shape, pressure and current profiles,

$$\gamma_1\tau_A = 0.5\epsilon_1(\kappa_1 - 0.5)\left[\beta_{p1} - \left(0.5 - \frac{\epsilon_1}{\epsilon_a}(\kappa_1 - 1.5|\delta_1 + 0.04|)\right)\right]^{(1.23-1.26\epsilon_1)} \quad (6.12)$$

$$\gamma_2\tau_A = 0.44\frac{\epsilon_1\kappa_1}{1+7\epsilon_1 s_1}\left(\beta_{p1} - \beta_{p1}^c\right) \quad (6.13)$$

with $\beta_{p1}^c = 0.9 - (0.6 + 0.1s_1)\kappa_1$ and all plasma parameters evaluated at the $q = 1$ surface. Note the dependence on the elongation (κ_1) and $q = 1$ surface radius ($\epsilon_1 \sim r_1/R$) that increases the growth rate in both cases. According to reference [72] about 300 different equilibria have been used in the fitting procedure, spanning $0.02 < \varepsilon_a < 0.8$, $1 < \kappa_a < 2.8$, $-0.6 < \delta_a < 0.9$, $0.02 < s_1 < 0.75$, and resulting in a $\gamma\tau_A$ variation from 0 to 0.25. The equation 6.12 contains the explicit dependence on plasma triangularity (δ_1) and a stronger dependence on the $q = 1$ radius, while equation 6.13 contains the dependence on the shear (s_1) and is particularly adapted for high elongation, low shear plasmas [72]. The formulas are evaluated using the experimental profiles and the position of the q =1 surface estimated from sawtooth inversion radius and the radial m/n=2/2 mode structure (see section 6.4). In figure 6.9 we show the evolution of the ideal growth rate for a typical case, together with the results of two full numerical KINX simulations in the Ohmic and ECRH phase. Since during the ECRH phase, LIUQE typically gives a central safety factor larger than one, the equilibrium was re-run with a modified current profile which reproduces the experimental value of the q =1 radius but otherwise similar in other parameters. The normalised growth rate ranges from 0. to 0.035 (depending on the model and time) that are, generally speaking, small values. We can see that, in Ohmic, the ideal γ in equations 6.12 and 6.13 have similar trends but different absolute values, larger in both cases than the numerical full simulation. The large difference between the full simulation and the fitting formula is not completely unexpected since such difference was already noted in reference [72] for $\gamma\tau_A$ <0.03.

The analytical formulas are regarded, here, as a useful tool to understand the trends in ideal stability changes due to the additional off-axis heating. The off-axis ECRH changes the ideal kink stability in a rather unexpected way. In fact, despite the increased destabilising plasma elongation (see equation 6.13), the growth rate sharply decreases. This is mainly due to the reduction of the q =1 radius reflected in the ϵ_1 factor while β_{p1} remains constant during this phase (see figure 6.9a). The small increases in γ at t=0.9 s well correlates with the increase of β_{p1} (consequence of a slow density peaking) and the magnetic shear s_1.

For a more accurate analysis of the ideal kink stability we rely on the results from the full numerical simulations. In the ECRH phase we obtain a very low value of the growth rate, of the order of $\gamma_{\rm ideal}\tau_A \sim 10^{-3}$ to be compared to the stabilising contributions from the trapped ions $\delta\hat{W}_{\rm kin}$ [63] and diamagnetic effect $0.5\omega_{i,{\rm dia}}\tau_A$

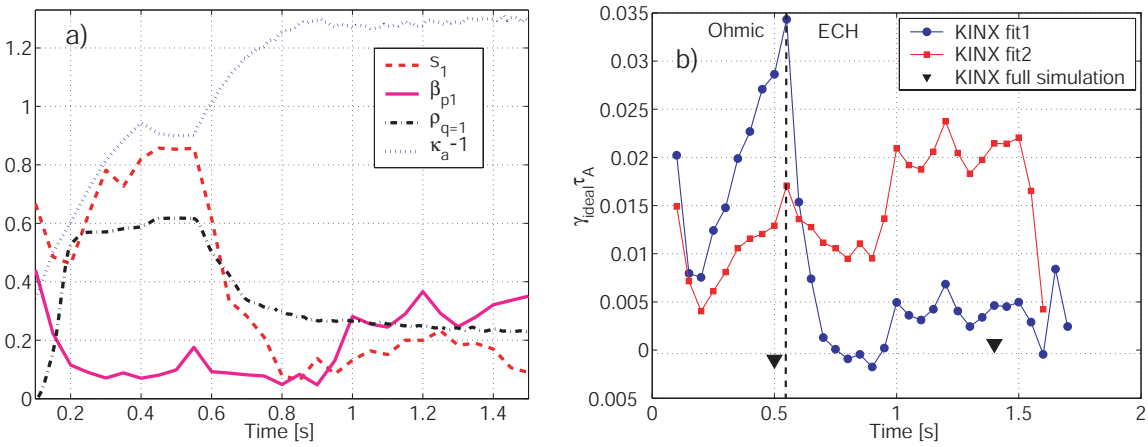

Figure 6.9: *Ideal kink stability evolution of an off-axis heated high elongation discharge (#22621) from KINX code. a) Magnetic shear s_1 (red dashed line), Bussac beta β_{p1} (full magenta), q =1 radius $\rho_{q=1}$ (black dashed dotted), edge elongation κ_a (blue dotted) used in the evaluation of $\gamma_1\tau_A$ and $\gamma_2\tau_A$. b): Evaluation of the normalised ideal growth rate from equations 6.12 (fit 1, blue dots) and 6.13 (fit 2, red squares) and full numerical simulation with KINX (black triangles).*

(see equation 6.5). The term $\delta\hat{W}_{\rm kin}$, explicitly evaluated from equation [65],

$$\delta\hat{W}_{kin} = 0.6 c_p \frac{\epsilon_1^{1/2}\beta_{i0}}{s_1}, \quad c_p = \frac{5}{2}\int_0^1 dx\, x^{3/2} p_i(x)/p_i(x=0), \tag{6.14}$$

with $x = r/r_1$, is typically of the order of $4\cdot10^{-3}$ in Ohmic and of 0.02 in the ECRH phase. The larger value in ECRH is mainly due to the $1/s_1$ dependence of $\delta\hat{W}_{\rm kin}$. The diamagnetic contribution to the rotation stabilisation is $0.5\ \omega_{i,\rm dia} \sim 0.003$ in both cases. We have then, for Ohmic plasmas, $\gamma\tau_A = \delta\hat{W}_{MHD} + \delta\hat{W}_{\rm kin} = 0.003 - 0.031 \geq 0.5\ \omega_{i,\rm dia}$ while in ECH $\delta\hat{W}_{MHD} + \delta\hat{W}_{kin} \leq 0$.

In the far off-axis heated discharges, the linear ideal kink is thus suggested to be stabilised by either diamagnetic effects or trapped ions. This is unexpected because of the large elongation. The present analysis shows, however, that the small radius of the q=1 surface has a strong stabilising effect finally reducing the growth rate of the mode.

6.5.3 Comparison with the Porcelli model using PRETOR simulations

As seen in the previous section, despite the high elongation reached in the ECRH phase, the linear ideal internal kink is likely to be stabilised by non-ideal effects. This is mainly due to the very flat current profile and reduced q =1 radius. Similarly, the condition for the ideal trigger (equation 6.5) is never satisfied in PRETOR simulations of these discharges. The ideal internal kink mode is stable for any $\rho_{q=1}$ value, even without taking into account the (dominant) stabilising kinetic contribution $\delta\hat{W}_{kin}$. The sawtooth trigger is given by satisfying the condition 6.11. It

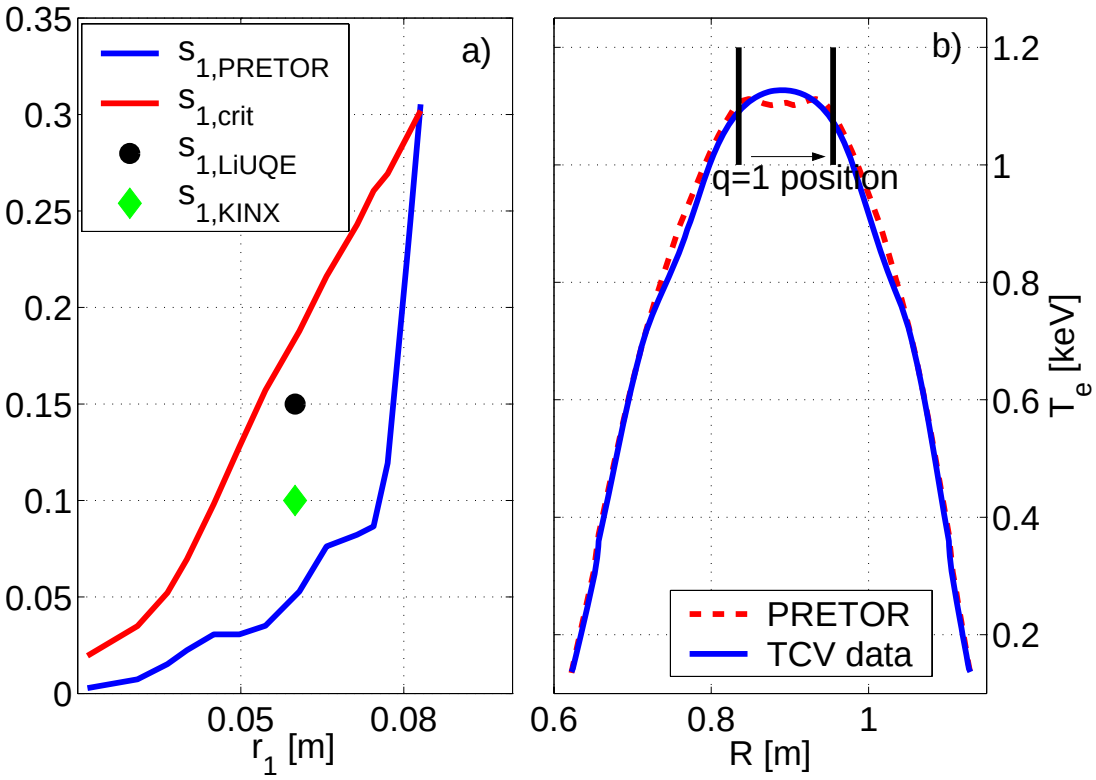

Figure 6.10: *PRETOR-ST simulation of off-axis ECH heated discharge #22621. a): s_1 and $s_{1,crit}$ during the sawtooth cycle showing the complete resistive kink stabilisation since $s_{1,EXP.} < s_{1,crit}$. b): comparison of the experimental and PRETOR-ST electron temperature profile.*

must be said that previous applications of the Porcelli model to TCV Ohmic and ECRH discharges [64, 74] reached the same conclusion, namely that the appropriate trigger in TCV plasma conditions was the resistive or the ion-kinetic trigger.

For a correct evaluation of s_1 and s_{crit}, the simulated profiles must agree, within the errors, with the experimental profiles in the region close to q =1. In particular, it is important to match the experimental density and temperature profiles. The density can be automatically matched by switching off the particle transport equation and fix the density profile to the experimental one. The plasma shape, total current and Z_{eff} are also taken directly from the experiment. The temperature profile is self-consistently simulated using the Ohmic and the additional heating using the ray tracing code TORAY [75]. The simulated electron temperature profile outside q =1 is then matched to the experimental profile by changing the transport coefficients. The sawtooth model contains the free parameter c_r, which is arbitrarily fixed to the value needed to simulate the sawtooth period during the Ohmic phase. The temperature and current profiles are allowed evolve until a sawtooth crash is eventually triggered, and the relevant parameters are monitored during the sawtooth cycle. In figure 6.10b, we compare the experimental and

the PRETOR electron temperature profiles when the q =1 radius matches well the experimental value of 5.6±0.5 cm. The agreement is satisfactory and gives confidence on the evaluation of the critical and magnetic shear that can be compared with the experimental estimations of s_1. The evolution of $s_{1,\mathrm{PRETOR}}$ and $s_{1\mathrm{crit}}$ during the sawtooth cycle is shown in figure 6.10a. The sawtooth trigger condition, $s_1 > s_{1,crit}$, is satisfied when the q =1 radius > 8 cm, corresponding to a sawtooth period of about 10 ms. Below this radius the internal kink is stable. Also the shear calculated with the LIUQE and KINX code are smaller than s_1. We conclude therefore that the stationary current profile is so strongly flattened by the off-axis ECH that the local value of the shear on q =1 is lower than the critical shear. Notably, at the time of the transition to sawtooth-free regime (t=0.68 s in figure 6.8), the estimated q =1 radius is 8-9 cm and agrees quite well with simulated value. However, it remains to explain why the electron temperature and current profiles do not continue to evolve up to a sawtooth crash as occurring in the simulations. We suggest that under the effect of the ERCH, the internal kink enters in the non-linear regime or, perhaps is inhibited by an other instability such as the tearing mode. The linear growth rate is, in fact, reduced and non-linear effects may become important. Moreover, a magnetic island on q=1 is often observed in plasmas with flat q-profiles (Snake instability). The transition to a non-linear saturated state may explain the disappearance of the sawtooth activity.

6.6 Concluding remarks

- Vertically stable discharges with $\kappa \sim 2.5$ at low and medium I_N are obtained in TCV using very off-axis ERCH. The vertical stability at large elongation is essentially obtained by current profile broadening that increases the current density at the edge. Correspondingly the sawtooth activity disappears. At low current ($I_p < 380$ kA) the sawteeth disappear because the q =1 surface shrinks due to the reduction of the central current density. At high current, in the early phase of current broadening, the sawtooth activity is replaced by a continuous MHD activity with multiple m/n=1 harmonics, that persist in stationary conditions during the entire ECRH phase indicating the presence of a finite size (~ 5.6 cm) q =1 surface.

- The MHD mode appears in discharges with higher density and at sufficiently low internal inductance ($l_i < 0.89$). Experiments with combined off-axis X2 (current broadening) and central X3 (current peaking) heating clearly link the sawtooth disappearance and the formation of the saturated island to the formation of a flat current profile with a small q =1 radius.

- The linear ideal kink stability and plasma shape effect are studied, in detail, with the KINX code. It is found that the destabilising effect of high elongation on the internal kink mod is compensated by the reduction in the q =1 radius and the ideal growth rate is likely to be stabilised by non-ideal effects, as also suggested by the Porcelli model in PRETOR. The modification of the central

plasma beta does not play an important role in internal kink stabilisation contrary to what was observed in the TFTR tokamak [71].

- The comparison with the Porcelli sawtooth model [63] indicates that the linear resistive kink is stabilised by the low shear on q=1.
- We suggest that the resistive kink or a tearing mode destabilised by the flat current profile enter the non-linear regime reaching the saturation. The extra transport due to this mode clumps the profile and no sawtooth crash is triggered. However, only a fully non-linear analysis may verify this scenario.

Chapter 7

MHD activity in EC-heated TCV plasmas with eITBs

In this chapter we report on the MHD activity observed in advanced TCV scenarios showing electron internal transport barrier (eITB). The eITB is created with the aid of the electron cyclotron current drive (ECCD) by producing reversed or low central magnetic shear. The phenomenology of the MHD activity is described, and mode characteristics are compared with ideal and resistive MHD modes possibly responsible for these instabilities. The performance limitations imposed by these modes are highlighted, and possible solutions are suggested.

7.1 Introduction to electron internal transport barriers

Undoubtedly the quest for improving plasma confinement has always been of major concern in tokamak experiments. Historically, tokamak reactors operating in the so-called low confinement regime (L-mode) proved to be not very attractive as nuclear fusion power plants. In L-mode, the electron diffusivity is two orders of magnitude larger than what is expected from collisions, and only very large (and expensive) devices would be able to produce energy at a reasonable price. These losses are likely to be due to turbulent transport phenomena.

The most exploited regime of improved confinement is the so-called H-mode, or high confinement mode, which is known since 1982 [76]. In this regime, a region of reduced transport close to the plasma edge is produced through mechanisms that are still not fully understood. In this region, the particle and thermal diffusivity are close to the values predicted by the collisional theory. In the past ten years, plasmas showing large internal temperature gradients have been ob-

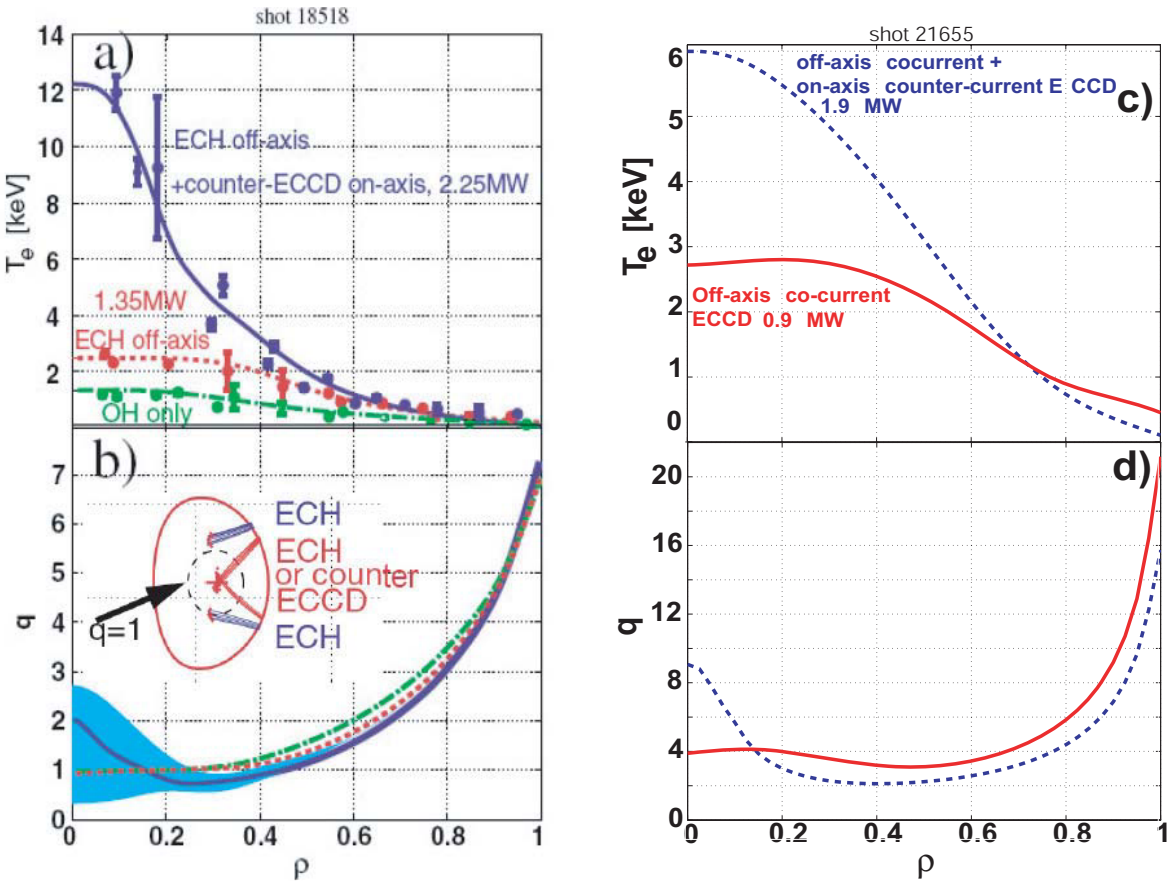

Figure 7.1: *Experimental electron temperatures (top) and simulated q-profiles (bottom). Left: Ohmic, off-axis and counter-ECCD phase for a typical ICEC plasma [82]. Right: fully non-inductive eITB plasma with and without central heating.*

tained in many devices. Some of the earliest results are reported in references [77, 78, 79], whereas a more recent review on the subject can be found in [80].

The large gradients are thought to be the result of a reduced turbulent transport. The low transport region is localised in the radial direction, and called internal transport barrier (ITB). In general, ITB plasmas are produced transiently, using fast ramps of plasma current in presence of an early pre-heat phase that slows down current diffusion to create hollow or very flat central current profiles. Strong shear in the radial electric field and/or negative shear in the q-profile are believed to be key ingredients to reduce the turbulent transport [81].

In TCV, localised electron heating and current drive by cyclotron waves (ECRH and ECCD) are used to tailor the current profile and produce inverted q-profiles. The transport barriers are clearly visible on the dominating electron transport channel and thus called electron ITB or eITB. Quasi-stationary ITB regimes, limited only by the gyrotron duty cycle or by MHD modes, are routinely obtained in TCV [82, 83, 84]. There exist essentially two regimes that have been developed at TCV:

Discharges with an inductively driven current component. The tailoring of the current density is achieved by a combination of off-axis ECRH and a strong central counter ECCD applied to an Ohmic target of fixed current in the range 120–250 kA. Heating off-axis broadens the electron temperature profile, T_e, as well as the current density profile via a change in the resistivity. The flattening of the current profile is generally observed from the variation in the plasma inductance on a resistive time scale. Subsequent power deposition in the centre, combined with counter ECCD, leads to T_e profiles which clearly reveal the formation of a transport barrier. The pre-heat phase also helps producing more stable plasmas, thus allowing the achievement of long pulses of Improved Central Electron Confinement (ICEC) discharges [82].

Discharges without an inductively driven current component. In the Fully Non-Inductive Reverse Shear (FNIRS) scenario the Ohmic current is replaced by non-inductive current driven by off axis co-ECCD [84, 83, 85] up to about 100 kA. Calculations with the Fokker-Plank code CQL3D [86] show that the off-axis co-ECCD is not sufficient to produce a hollow $j(r)$ profile. The bootstrap current, having an off-axis maximum, determines the final shape of the total current density profile [87]. Once the transport barrier is formed, it can be strengthened (weakened) by adding central counter(co)-ECCD.

The eITB plasmas resulting from the ICEC and FNIRS scenarios differ in the location of the maximum pressure gradient and in the current profile shape (figure 7.1). In ICEC plasmas, due to the strong inductive current component which tends to peak the current profile, the low or negative shear region is localised close to the magnetic axis, $\rho_{\rm ITB}$ = 0.2–0.4 with $q_{\rm min} \sim 1$. Note that there is no direct measurement of the current profile and that the calculation, and modelling of the q-profile in this scenario have been proven particularly difficult [74, 65]. This is mainly due to the fact that to obtain the total current profile one has to subtract two large and comparable contributions, namely the ECCD and the inductive current. The bootstrap current plays here an important but not crucial role. Experiments with different plasma currents showed, however, a strong link between the inferred q-profile and the eITB location [88]. In fact, it is found that at fixed power, the ITB tends to shrink at higher plasma currents. This further supports the idea that a larger region of low or negative shear corresponds to a larger $\rho_{\rm ITB}$. As a consequence, the energy fraction inside the barrier increases. When the Ohmic current is eliminated, as in the FNIRS scenario, the current profile shape can be more easily controlled, and stronger reverse shear can be obtained with an ITB located further off axis ($\rho_{\rm ITB}$ = 0.35–0.55).

Before describing the experimental results, we discuss the results of ideal MHD calculations in reverse shear scenarios with large pressure gradients [10].

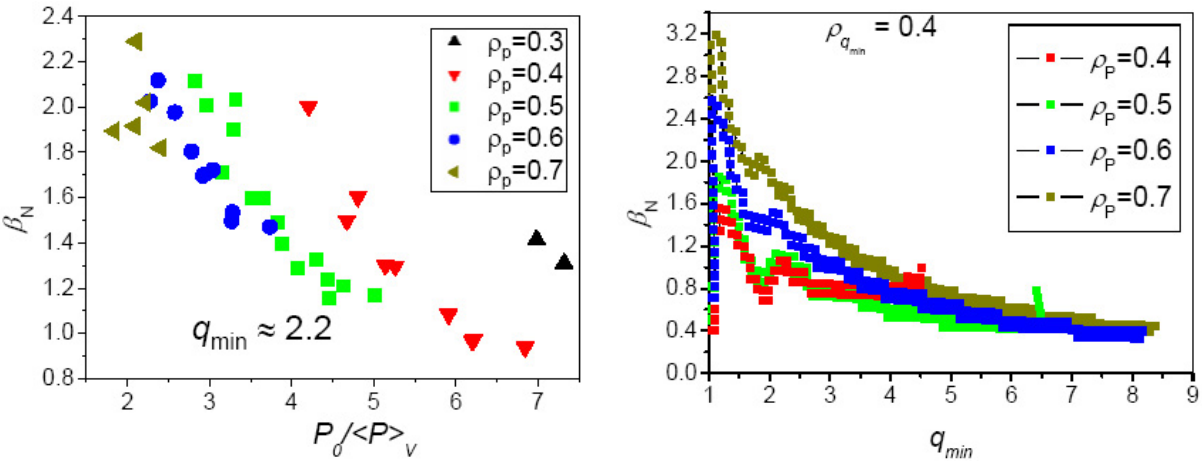

Figure 7.2: *Theoretical β limit due to global kink mode (infernal mode) in plasmas with reverse shear, calculated with the KINX code [10]. The β limit is plotted versus the pressure peaking (left) and $q_{\min}$ (right) for different positions of the ITB.*

7.2 An ideal MHD result: infernal modes in reverse shear scenario

Global, low n (typically $n = 1$) ideal instabilities in the presence of large pressure gradients and β, referred to as "infernal modes", are found to be unstable in reverse shear scenario [10]. Following the reference, we summarise a few features of the infernal modes. The main parameters used to define the infernal mode stability are the minimum safety factor $q_{\min}$ and its radial position $\rho_{q_{\min}}$, the pressure peaking, and the radius of the maximum of the pressure gradient ρ_p (often referred to as ρ_{ITB}).

The mode poloidal structure shows a strong poloidal asymmetry with larger amplitude at the LFS (sometimes called ballooning character). For q-profiles with $q_{\min}$ expected for TCV eITB plasmas, calculations show that the poloidal Fourier spectrum sharply peaks around $m = 2$ and $m = 3$. By increasing the value of $q_{\min}$ and the radial position of the maximum pressure gradient, the mode moves radially towards the positive shear region and closer to the plasma edge, changing its character into an external kink mode, a current driven mode. At values of $q_{\min} > 4$, the external kink mode character becomes dominant.

Owing to the hollow current profile and the large localised pressure gradient, the ideal β_t limit is reduced [10] in comparison to the well-known Troyon limit ($\beta_t \leq 3I_N$) [89] valid for a monotonic q-profile. The *maximum achievable β strongly decreases with the pressure peaking $p_0/ < p >_V$, and the minimum safety factor* $q_{\min}$ (see figure 7.2). On the contrary, the β_N limit increases with increasing $\rho_{q_{\min}}$ and ρ_{ITB}. Large pressure peaking ($>$ 4–5) decreases the maximum β_N also for monotonic q-profiles with similar l_i. This is important for TCV since the pressure peaking may reach very high values (up to 15) in eITB plasmas. We anticipate that the experimental β limit is strongly sensitive to the pressure peaking (see

figure 7.11) thus suggesting that the infernal modes could explain the observed disruptions and rapid internal collapses.

7.3 MHD mode in improved central electron confinement scenario

In the ICEC scenario, two main MHD activities have been observed: slowly growing magnetic islands and fast growing kink-like modes. The latter may show the signature of periodic relaxation oscillations (PROs) in the SXR signals with sawtooth-like features [90].

7.3.1 Tearing modes in ICEC plasmas

The magnetic islands cause oscillating perturbations (typically 3–6 kHz in TCV) of the magnetic field and soft X-ray emissivity. In general, the magnetic islands are associated with the destabilisation of the tearing modes (TMs), driven by current and pressure gradients. In the presented experiments, the tearing modes are localised near the $q = m/n = 2/1$ and/or $3/1$ surfaces, outside the eITB and in the region of positive magnetic shear. Neither the double tearing mode nor the $3/2$ mode have been observed.

The negative influence of TMs on global confinement is shown in figure 7.3. As an $n = 1$ mode build up at t = 0.556 s, the global confinement degrades significantly. The growth of the mode amplitude is correlated with a gradual decrease of the SXR signal, indicating that the TM is indeed responsible for the degradation of confinement and ITB strength. The confinement enhancement factor $H_{RLW} = \tau_E/\tau_{E,RLW}$ [91] drops from 3.5 to 2.5, while the eITB strength (identified by ρ_{*T}, according to Tresset [92]) decreases. As the mode amplitude further increases during the current rise (t = 1.0–1.3 s), the averaged H_{RLW} drops down to 2, and ρ_{ITB} shrinks from 0.3 to 0.2, with consequent termination of the high confinement phase.

The edge magnetic perturbations can be well reproduced by the magnetic island model (see also chapter 4), which also allows us to reconstruct the island structure (figure 7.4). In the presented discharge, the perturbation does not have a single helicity, but is composed of two coupled magnetic islands rotating together: *a* $3/1$ *island, observed predominantly in the edge magnetic signal, and a* $2/1$ *island, more clearly seen in the SXR signal*.

Note that a satisfactory modelling of the edge magnetic signal requires the presence of a $2/1$ island in the fitting procedure (section 4.4.2), whose presence is independently confirmed by the structure of the perturbed SXR signal. In the low I_p phase (figure 7.4a), the $2/1$ mode structures from the magnetics and the SXR show good agreement in the $q = 2$ resonance surface position and the island width $w_{2/1}$, indicating that the q-profile region around $q = 2$ is well reconstructed by LIUQE. More generally, the equilibrium q-profile in the positive shear region is reliably determined by the (slow) edge magnetics measurements. After the

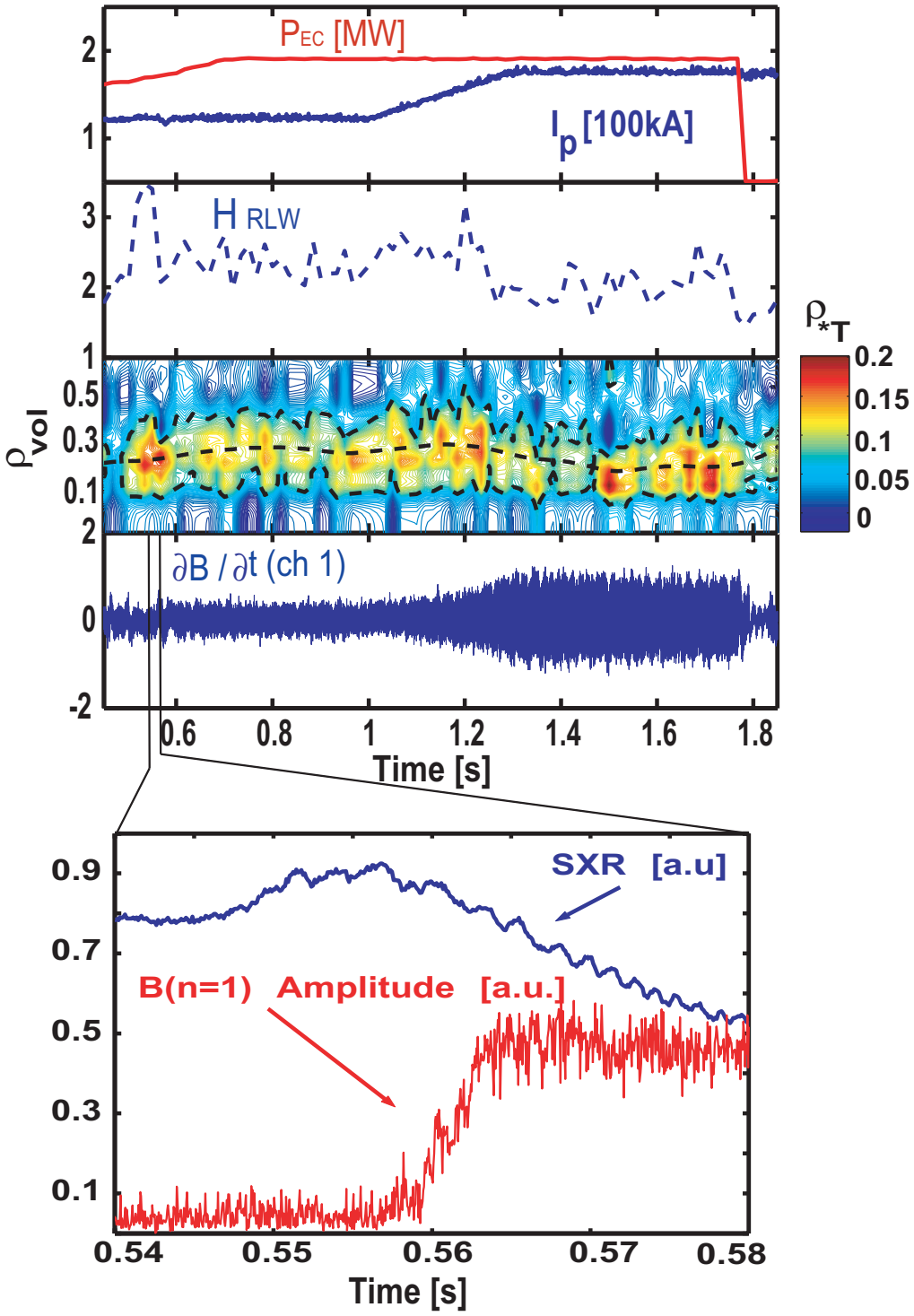

Figure 7.3: *From top to bottom: P_{EC} (solid red), I_p (solid blue), H_{RLW}, the confinement enhancement factor (dashed blue), the eITB strength ρ_{*T} (contour plot), and the mode amplitude (magnetic probe) for discharge #24139. The SXR signal and the $n = 1$ mode amplitude when H_{RLW} drops (t = 0.556 s) are also shown in the bottom plot.*

simultaneous current- and κ-ramp-up (in order to limit the q_a variation) the SXR measurements indicate a somewhat smaller $q = 2$ radius and a much larger island size than what deduced from the magnetics (figure 7.4b). However, since the SXR are line-integrated measurements, the radial structure of the perturbation amplitude is strongly influenced by the plasma geometry and by the presence of an outer mode (here the $3/1$ mode). As a result, the localisation of the mode from SXR analysis has large uncertainties.

At the mode onset, β_N ranges from 0.6 to 1.4, and the collisionality ν_{e*} from 0.003 to 0.01. For similar values of these parameters, neoclassical tearing modes NTM were previously observed in TCV plasmas without eITB [93]. A typical signature of an NTM is the linear dependence of the saturated island width on β_p [15],

$$\frac{w_{\rm sat}}{r_s} = \beta_p \frac{a_{\rm bs} - a_{\rm GGJ}}{-r_s \Delta'} \qquad (7.1)$$

where $a_{\rm bs}$ is a coefficient describing the destabilising effect of the perturbed bootstrap current, and $a_{\rm GGJ}$ describes the stabilising effect of toroidicity and shaping.

There are indications of such a β_p dependence in the ICEC tearing modes. This effect can be seen in discharges with a single $2/1$ island. As shown in figure 7.5, after a transient phase at mode onset, the saturated amplitude follow linearly the plasma β.

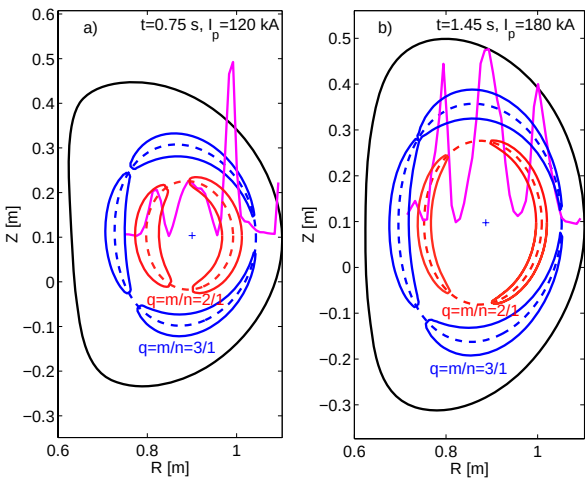

Figure 7.4: *Coupled $3/1$ (blue) and $2/1$ (red) magnetic islands reconstructed from the magnetic perturbation data in (a) early phase at low current (120 kA), and (b) later phase after current (180 kA) and κ ramp up. From discharge #24139. The radial structure of the perturbation amplitude in the SXR signal is superimposed for comparison to the $2/1$ reconstructed island.*

Despite the experimental difficulties due to mode coupling, there is evidence of the correlation between β_p and the island width also in discharges with more than one magnetic island, as in the precedent case. According to the magnetics data only (see figure 7.3), in fact, $w_{2/1}/r_s$ decreases by more than a factor of 2 (from 0.47 to 0.20) during the current rise (β_p from 1.1 to 0.6). This strongly suggests a reduction of the destabilising drive from the bootstrap current as expected for neoclassical tearing modes.

7.3.2 Pseudo sawteeth in ICEC plasmas

Fast collapses and periodic relaxation oscillations (PROs) have been observed quite frequently in ICEC plasmas. The PROs often show a sawtooth-like signature, and an associated MHD activity with $m = 2$, $n = 1$ mode numbers. The

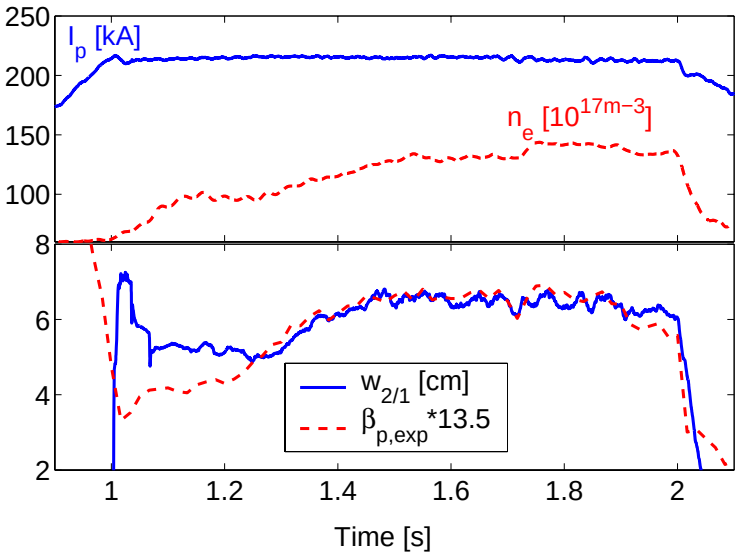

Figure 7.5: *Temporal evolution of: a) the density n_e (and therefore β_p), shown at constant I_p current; b) the island width and β_p. From an ICEC discharge with a single magnetic island (#24141).*

sawtooth period $\tau_{\rm saw}$ ranges from 5 to 20 ms depending on the plasma current. This time is considerably longer than $\tau_{\rm saw}$ in ordinary sawteeth. A paradigm of PROs is shown in figure 7.7. During the on-axis power ramp-up the plasma pressure increases steadily until an MHD event sets on, and abruptly reduces the central pressure at t=0.98 s. Subsequently the discharge undergoes several internal disruptions while a change in the plasma equilibrium occurs: the plasma elongation increases as a result of a flattening in the current profile as observed in the internal inductance. The safety factor passes from 8 to 10 at the edge. The internal relaxation phase is associated with continuous MHD activity with $2/1$ mode numbers that cease after about 150 ms (see spectrogram in figure 7.7d). The plasma β begins to rise again and after few tens of ms the PROs appear with a period of 20 ms and remain until the central EC heating power is turned off.

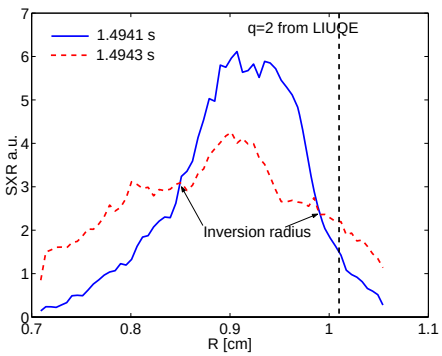

Figure 7.6: *Line-integrated soft X-ray emissivity profiles before and after the pseudo sawtooth crash. The inversion radius is located 2-3 cm inside the q=2 radius from LIUQE reconstruction.*

The regular sawtooth-like crashes are sometimes accompanied by perturbations visible in the soft X-ray signals and in the magnetics (figure 7.9). The MHD activity shows m =2, n =1 mode numbers indicating that, differently from standard sawteeth, the crashes are caused by an MHD instability resonant on q =2. The equilibrium reconstruction and q-profile modelling indicate that the q =1 surface is not present in the plasma during this phase. The pre-crash and

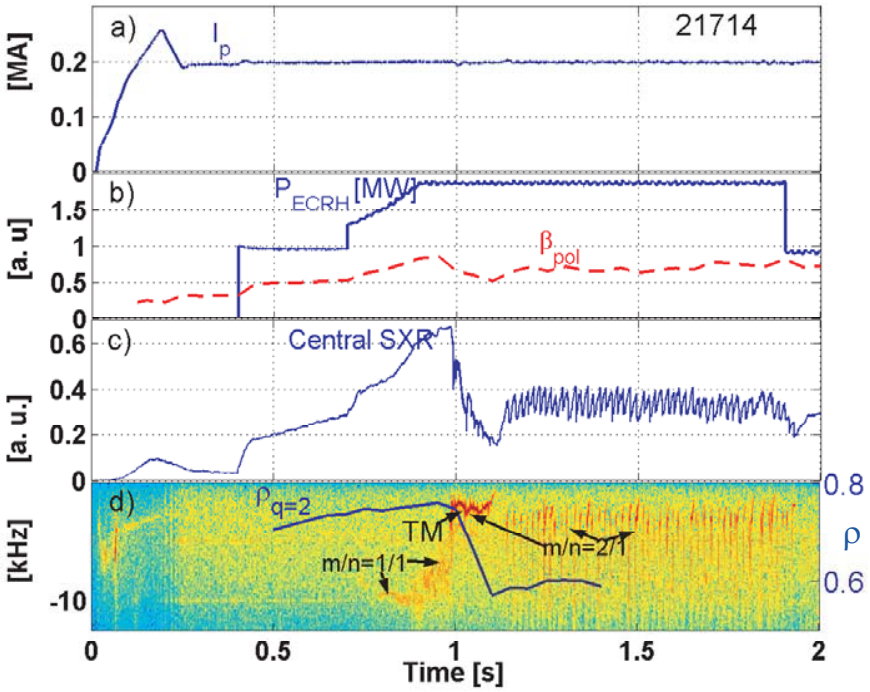

Figure 7.7: *Paradigm of pseudo sawteeth regime in ICEC discharge #21714. a) Plasma current I_p. b) ECH power and β_p. c) Central soft X-ray emissivity. d) Spectrogram of the $n = 1$ toroidal component of the magnetic signal. Negative frequencies indicate mode rotation in the electron diamagnetic drift direction. Note also the transition from continuous TM to pseudo sawteeth in correspondence of the change in $\rho_{q=2}$*

post-crash line-integrated soft X-ray profiles (figure 7.6) show an inversion radius located close but somewhat inside (about 2-3 cm) the q =2 surface as calculated by LIUQE. This discrepancy could be due to the inaccuracy of the q-profile reconstruction or to the presence of a second q =2 surface in the plasma. Consistently, in this case, the q profile should be reversed with q_{min} close to 2, corresponding to a current profile particularly unstable with respect to infernal modes (section 7.2). We may conclude that the MHD activity in ICEC plasmas, either tearing-like or sawtooth-like, is mainly originating from the most unstable q =2 resonant surface. Keeping $q_{\min} > 2$, as for FNIRS plasmas, is probably the best to produce stable eITB plasmas. It is worth noticing that the characteristic of the q =2 MHD activity, namely the continuous tearing mode or regular pseudo-sawtooth regime, appears to change from one to the other depending on the plasma parameters and, in particular, on the size of the q =2 surface. To illustrate this point it is useful to compare the discharge #21714 (figure 7.7) with the discharge #25258 (figure 7.8). Although accompanied by rapid collapses the first appearing MHD activity in #21714 is a continuous tearing mode. The subsequent changes in the equilibrium lead to a reduction of the q =2 radius with respect to the pre-MHD-activity value, passing from $\rho_{q=2}$=0.75 to $\rho_{q=2}$=0.59. With the new plasma equilibrium

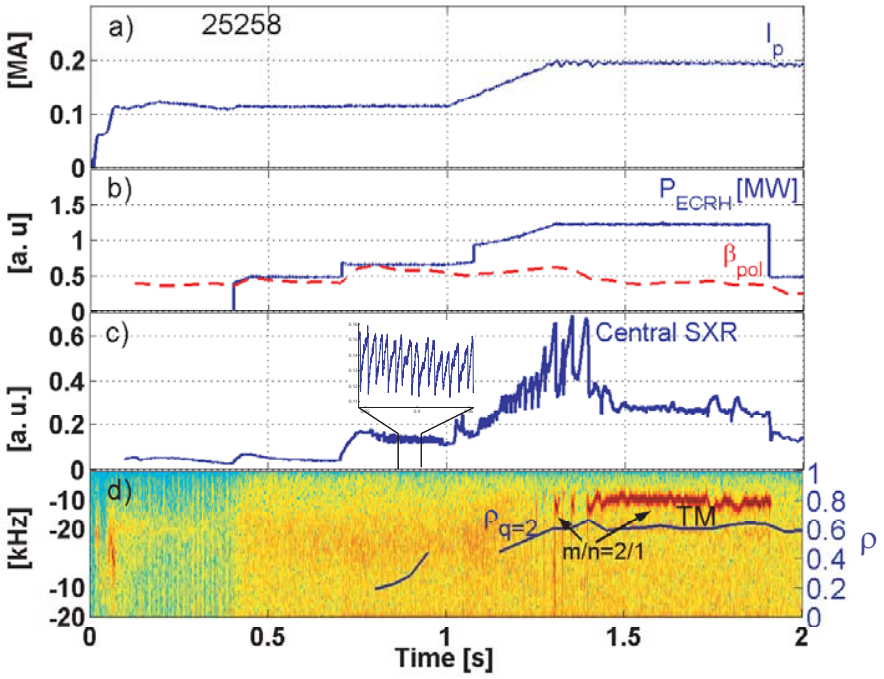

Figure 7.8: *Time evolution of several plasma parameters from discharge #25258, showing the transition from PRO regime to continuous tearing mode on q=2, as a consequence of the current rise (at constant B_t) and the larger size of the q=2 surface.*

the tearing mode stabilises (figure 7.7d) while the plasma pressure rises rapidly. After about 20 ms of stable discharge, once passed a certain threshold in pressure, the pseudo-sawteeth regime begins.

An opposite situation appears in discharge #25258 (figure 7.8). In the ICEC phase at low current (120 kA) high q_a(=15), pseudo-sawteeth develop with a small amplitude and a period of 5-7 ms. At t=1 s the plasma current is risen to 200 kA without change of the magnetic field. The relaxations become less regular and show a longer sawtooth period (up to 20 ms). After reaching the current and ECRH power flattop (figure 7.8a-b) the q =2 sawtooth-like activity is replace by a continuous m/n =2/1 mode (figure 7.8c-d), showing a tearing structure in the magnetic and SXR perturbation. During the current ramp $\rho_{q=2}$ increases from 0.2 to 0.61 (LIUQE values) while ρ_{ITB} stays substantially unvaried. This *transition from sawtooth-like to tearing mode* (and viceversa), is probably connected with the regime on the mode unstable on q =2, changing from an ideal nature close to the large pressure gradient to a resistive nature further out.

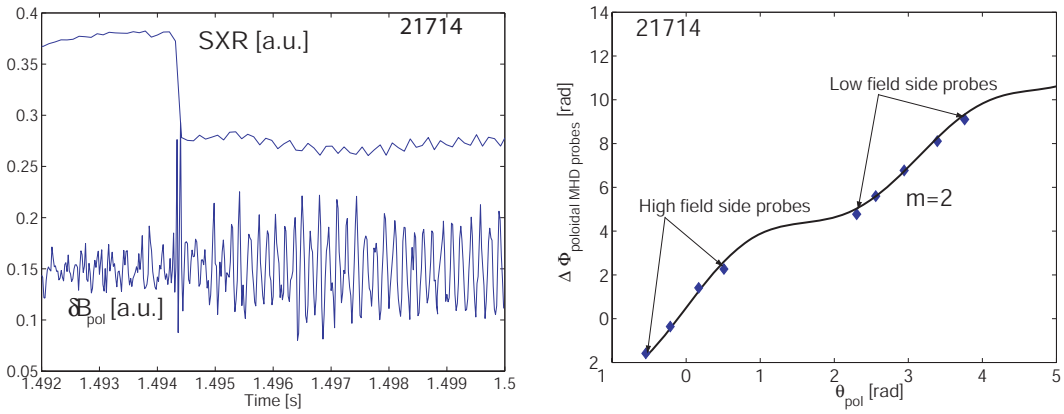

Figure 7.9: *The MHD activity during pseudo sawtooth regime. Left: sawtooth-like crash and post-cursor oscillations. Right: poloidal phase change in the magnetic signals. The high field side and low field side probes (blue diamond) are connected using the Merezhkin's model (equation 4.17) (black full line) showing an m=2 dominant poloidal number.*

7.4 MHD activity in fully non-inductive reverse shear scenario

In fully non-inductive eITB scenarios, $3/1$ or $2/1$ magnetic islands may be present when the off-axis co-current ECCD beams are too centrally aimed. In this case, the current profile becomes too peaked leading to unstable tearing modes and the transport barrier does not form. These modes can generally be avoided by widening the driven current to produce a flatter current profile. Simulations of the current profile with the ASTRA and CQL3D codes show $q_{\min} > 3$ [94], suggesting that the most TM unstable resonant surfaces are either avoided or perhaps stabilised in the proximity of $q_{\min}$.

Fast internal relaxations are observed if too much power, and consequently too much pressure, is put into the plasma. In some discharges, the plasma recovers after the rapid internal collapse and the pressure rises again, and a series of central periodic relaxations similar to the pseudo-sawteeth shown earlier take place. An example of such relaxation is shown in figure 7.10a.

In some cases, the relaxation may present some post-cursor oscillations in the magnetic field, with frequency in the 15–20 kHz range, and rotating in the electron diamagnetic drift direction. The toroidal number is easily identified as $n = 1$. The poloidal mode structure is complex and presents a marked poloidal asymmetry with a larger mode amplitude on the LFS of the torus (see figure 7.10c). This is generally interpreted as an indication of the ballooning character of the unstable mode. The poloidal number m is in the range $3 < m < 4$ ($m = 3.5$ in figure 7.10d). The soft X-ray profile collapses inside $\rho \sim 0.57$, outside ρ_{qmin} and quite close to the $q = 3$ surface (see figure 7.1d). The instability fast growth and mode numbers are consistent with those of an unstable *infernal mode* (see section 7.2), which

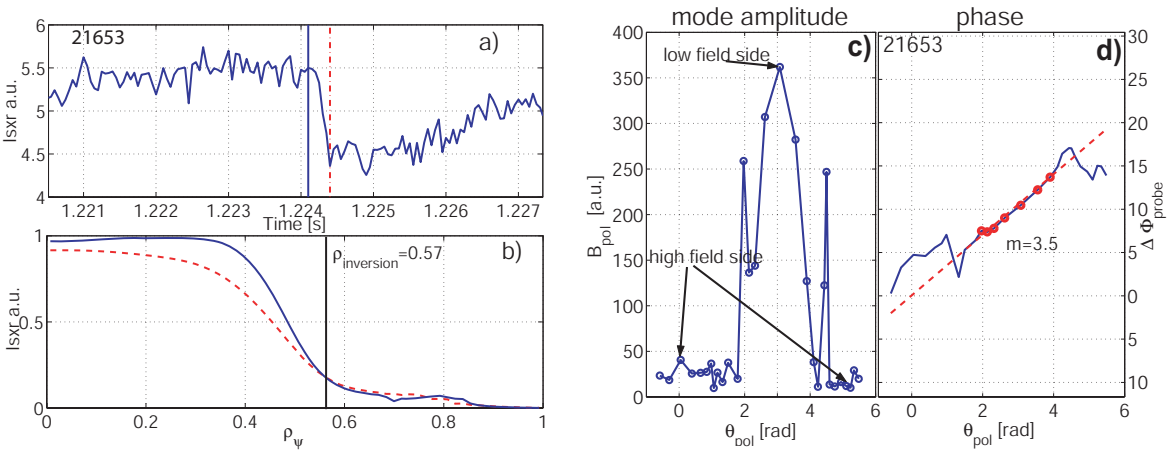

Figure 7.10: *Internal relaxation seen on the SXR emissivity (a and b), and poloidal structure from magnetic post-cursor oscillations showing the mode amplitude (c) and phase (d).*

is thus a good candidate to explain the internal collapses and the disruptions. If the thermal energy loss is dramatic, in fact, the coupling with the ECRH power is lost and the discharge disrupts. The characteristic time of disruption, $\sim$20 μs, is consistent with an ideal growth rate. Calculations with profiles approaching disruptions confirm that the ideal limit is reached [10].

7.5 Summary, further discussions and conclusions

The achievable β_N in TCV eITB discharges is limited by MHD instabilities mainly driven by very large and localised pressure gradients. Two types of MHD activity are observed in TCV plasmas with eITB: *tearing-modes* and *kink-ballooning modes*, which may lead to sawtooth-like relaxations and plasma disruptions.

The tearing modes tend to appear at a somewhat lower β than the kink-ballooning modes, and usually when the internal inductance exceeds 1.2, suggesting the presence of an unfavourable, excessively peaked, current profile. The linear dependence of the saturated island width on the poloidal beta suggests a neoclassical nature of the TMs (figure 7.5). However, some features are difficult to reconcile with the picture of an NTM. The absence of an evident trigger and the fast growth of the mode (saturation time, $\tau_{\rm tear} = 3$ ms) are not explained by the standard NTM theory (resistive time scale, $\tau_R \sim 200$ ms) based on the modified Rutherford equation (equation 2.36). The experimental growth, dw/dt, reaches up to 10 m/s, whilst the predicted growth is 1 m/s. Such a fast experimental growth could only be explained by the Rutherford equation in presence of an extremely large drive (bootstrap current, for instance), which is not easily justified by the experimental profiles.

Note that on TCV, NTMs were observed in low current ECRH discharges with a strong co-ECCD component and a very peaked current profile [23, 93]. There,

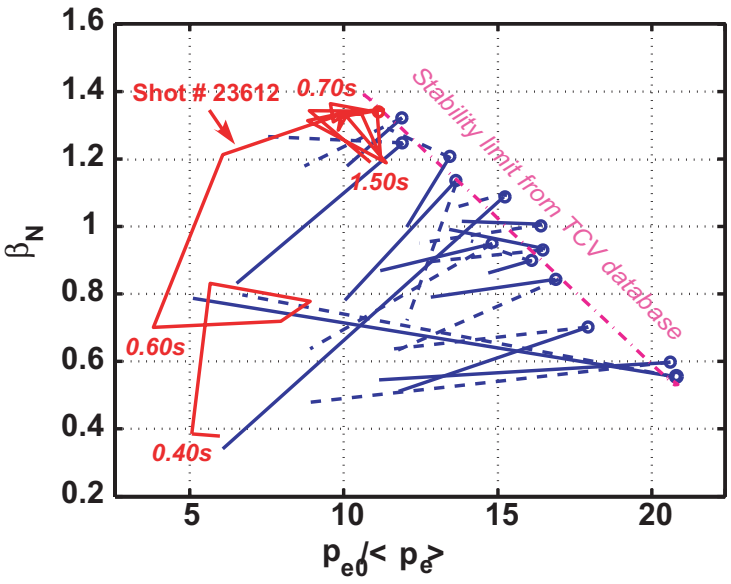

Figure 7.11: *The $\beta_N - p_{e0}/ < p_e >$ space built with several TCV eITB discharges.*

the mode evolution and saturation level are found in agreement with the modified Rutherford equation. Perhaps, the large growth rate of these modes is nothing but the sign of an ideal nature. The plasma beta at the mode onset is high β_N (see figure 7.11) and the pressure drive is very important.

This "hybrid" nature of the q=2 activity is also consistent the fact that the continuous (TM) mode changes characteristics when the resonant surface moves inward (figures 7.7 and 7.8). The mode grows faster and gives rise to rapid electron temperature and soft X-ray emissivity collapses, which may have the signature typical of the standard $q = 1$ sawtooth instability, or lead to plasma disruption. Similar crashes and disruptions generated by a fast growing mode are observed in discharges in fully non inductive scenario with more reverse shear. Interestingly, the ideal MHD theory predicts a strong destabilisation of the "infernal mode" when the maximum pressure gradient gets close to $q_{\min}$. In these experiments, the kink-ballooning mode tends to become unstable when the q=2 surface moves closer ($\rho_{q=2}$ = 0.3–0.6) to the maximum pressure gradient ($\rho_{\rm ITB}$ = 0.2–0.4). Hence it is suggested that the q=2 has a hybrid ideal-resistive nature which become more ideal when the rational surface approaches the source of the instability at $\rho_{\rm ITB}$.

The pressure gradients play an important role in stabilising eITB plasmas. In fact, the electron pressure peaking $p_{e0}/\langle p_e \rangle$ is found to be a key parameter to the stability limit (see figure 7.11).

To obtain high β_N, the pressure profile must not exceed a certain threshold in the peaking factor. Careful optimisations of the EC power level and deposition location are necessary. A particularly successful example is represented by the discharge #23612 (see figure 7.11), where off-axis ECRH is deposited slightly inside the $q = 2$ surface. At the same time (t = 0.4 s) the central counter-ECCD power is turned on, and reaches 1.5 MW at t = 0.7 s. Consequently T_e rises, but

the peaking of the pressure profiles does not exceed 12 because of the flattening effect of the off-axis heating. During the whole heating phase a small amplitude mode is present, but does not degrade the performance. The ITB radius keeps rather constant during the power ramp ($\rho_{\mathrm{ITB}} \sim 0.35$), and a good confinement ($H_{RLW} \sim$ 4–4.5) is obtained at $\beta_N = 1.4$. At t = 1.49 s the off-axis heating is switched off. The pressure exceeds the peaking limit in less than 10 ms, and at t = 1.517 s an MHD mode destroys the good confinement, decreasing the global β_N to less than 0.8, and leading to a new plasma equilibrium in the pseudo-sawtooth regime (plasma parameters close to the discharge in figure 7.7). The attempt to reach higher β_N by increasing the heating power will not be successful unless *too strong peaking of the pressure profile is avoided*. A similarly strong destabilising effect of the pressure peaking is predicted for the infernal modes by ideal MHD theory even for monotonic or flat q profiles. Note the similarity between figures 7.11 and 7.2a, in which the theoretical beta limit calculated with the code KINX is shown. The infernal mode is closely related with the observed MHD activity and may thus explain the beta limits and the pseudo-sawtooth regime in TCV eITB plasmas.

Part III

Toroidal plasma rotation and momentum transport

Chapter 8

Introduction to plasma rotation

8.1 Motivations

From the condition for plasma ignition, equation 1.17, we can see that good particle and energy confinement is required to achieve nuclear fusion. This justifies the experimental and theoretical efforts invested in the study of particle and thermal transport in magnetised plasmas in comparison to what has been performed in the study of momentum confinement. It is significant that in the ITER Physics basis report [95], the section on momentum confinement is less than four pages long compared to almost fifty pages on particle and thermal confinement. In spite of this, the issue of plasma rotation and momentum transport has recently raised renewed interest inside the fusion community, resulting in an increased number of seminars, conferences and publications on this and related subjects. Why is this so?

The study of the confinement of momentum and plasma rotation has been recognised to be of interest for several reasons. First, the plasma rotation in toroidal devices is related to several important issues, such as stability and turbulence, and it is often found to be beneficial to the plasma performance. At the DIII-D tokamak, strong plasma rotation is proven to stabilise the Resistive Wall Mode [96]; at the JET tokamak, NBI induced toroidal rotation increases the beta threshold for triggering neoclassical tearing modes (NTM) [97]; differential rotation between magnetic surfaces can decrease mode coupling enhancing the plasma stability against macro MHD modes [12] and thus increasing the achievable β. Second, the radial electric field and its associated $\vec{E} \times \vec{B}$ flow shear, intimately linked to plasma rotation, is widely believed to reduce or suppress turbulent transport through differential rotation and may result radial turbulence decorrelation. The reduced turbulence may result in regimes of enhanced confinement such as H-mode plasmas and/or plasma with internal transport barriers [98]. Third, angular momentum confinement investigations provide further insight into the general problem of confinement in tokamak plasmas. To date, several basic physical mechanisms are still poorly understood. In particular, the question of

whether the momentum transport is collisional (neoclassical) or/and turbulence driven (anomalous) is still open (see discussion in ref. [99]). In some experiments with strong momentum input from neutral beam injection (NBI), the momentum transport was found to be consistent with neoclassical theory [100] but more often the experimental momentum diffusivity χ_ϕ was found comparable with the ion heat diffusivity χ_i, which is frequently anomalous [101, 102, 103]. Neoclassical predictions of the poloidal velocity qualitatively were found to disagree with recent measurements at the DIII-D tokamak [104, 105]. The observation of rapid toroidal rotation with no external momentum input [106, 107, 108, 109, 110, 111, 112] poses the question of the origin of internal self-generated angular momentum, masked in experiments that employ strong NBI. It is important to understand and model this non-diffusive component of the radial momentum flux to estimate the expected toroidal velocity of large future experiments, such as ITER, where the planned NBI power may not be sufficient to drive strong rotation [95]. In fact, according to [95] the NBI power will drive, in standard H-mode scenario, only an angular velocity of about 1 kHz, compared with the $>$ 10 kHz of today's large experiments. The spontaneous rotation is usually observed to be comparable with or exceed the ion diamagnetic drift velocity $v_{\rm diam} = (dp_i/dr)/(eBn_i)$ and may thus be a substantial fraction, or even dominate, the ITER total toroidal rotation. A reliable scaling law for the spontaneous rotation should be assessed to model the transport level and stability in ITER plasmas.

The spontaneous toroidal rotation shows a rich and complex phenomenology varying strongly with the plasma conditions (L-mode, H-mode, limited or diverted configurations) and heating scenario (Ohmic, ECRH or ICRH) [113]. Counter-current toroidal rotation has been measured in Ohmic L-mode discharges in most tokamaks, but in some experiments co-current toroidal rotation was observed, as reported by Rice [108]. The toroidal rotation may invert in the core and the edge of a stationary discharge [114] or change sign during the temporal evolution of the plasma parameters [111]. Even the absolute rotation velocity exhibits a wide range of values from almost negligible to a significative fraction of the ion thermal velocity.

Strong toroidal acceleration in the direction of the plasma current (co-current) has been observed at the L-H transition in Alcator C-Mod in Ohmic or ICRH heated discharges. An anomalous momentum diffusivity was inferred from the temporal evolution of the rotation profile [115], and a turbulent driven edge momentum source was invoked to explain the experimental data. No rotation measurements at the edge region supporting this hypothesis were reported. In short, most of the basic physics linked with spontaneous plasma rotation remains sketchy and/or unexplained.

8.2 Aims and objectives of the TCV rotation studies

The TCV CXRS diagnostic provides high quality rotation data that allow to:

- quantify and characterise the stationary spontaneous rotation velocity along

the minor radius for various plasma shapes and TCV scenarios:

- limited or diverted Ohmic and ECH L-mode plasmas,
- diverted Ohmic and ECH H-mode plasmas,
- electron internal transport barrier plasmas;

- contribute to the determination of scaling laws to predict the level of plasma rotation in future large experiments (chapter 9);
- clarify momentum transport mechanisms (collisional or anomalous) and the nature of radial angular momentum flux and momentum sources in plasmas with no external momentum input (chapter 10);
- validate theoretical models of spontaneous rotation and momentum transport in absence of neutral beam injection (chapter 9).

The results presented in the next two chapters represent an initial effort in these directions.

Chapter 9

Stationary toroidal plasma rotation in TCV

This chapter describes the measurement of carbon impurity toroidal rotation in Ohmic L-mode limited discharges. The dependence and scaling of the toroidal velocity with plasma parameters, such as current and density, are highlighted as well as the effect of the sawtooth activity on the rotation profile. The comparison with neoclassical predictions concludes that the TCV plasma rotation is mainly driven by radial electric fields, with a negligible contribution from toroidal electric fields. The neoclassical theory of toroidal rotation in the small v_ϕ/v_{th} limit quantitatively and qualitatively disagrees with the experimental observations. An alternative empirical equation for the angular momentum flux, able to reproduce the measured stationary rotation profile outside the sawtooth inversion radius, is proposed.

9.1 Introduction

In TCV a detailed exploration of the plasma rotation in a simple scenario, characterised by stationary plasma conditions and not involving additional heating and complex edge magnetic geometry, is thought to be optimal in assessing the issue of spontaneous plasma rotation, and permits straightforward interpretation of the experimental results as well as direct comparison with the available theories.

As part of this thesis work[1], a set of experiments was performed to study systematically the dependence of the toroidal rotation on basic plasma parameters such as the plasma current, electron density and temperature. The Ohmic limited L-mode scenario was chosen as an initial step in the systematic exploration and

[1]The content of this chapter is very similar to a recent publication by A. Scarabosio et al. in "Plasma Physics and Controlled Fusion" [116].

Table 9.1: *Main parameters of the TCV Ohmic plasmas used in the rotation experiments.*

Parameter	Value
a	0.25 m
R	0.88 m
B_t	1.44 T
I_p	[–350,+320] kA
q_a	[2.4, 8.8]
V_l	[1, 2] V
$< n_e >$	[0.8, 7]·10^{19} m^{-3}
T_{e0}	[600, 1200] eV
T_{i0}	[300, 700] eV
κ	[1.3, 1.7]
δ	[–0.3, 0.65]
Z_{eff}	[1.2, 2]

characterisation of the plasma rotation in all TCV plasma conditions and scenarios. The main device and plasma parameters used for these rotation experiments are given in Table 9.1.

9.2 Experimental results

The main experimental results discussed in this section are:

1. Considerable net angular momentum is measured with central toroidal velocity up to 50 km/s in the absence of relevant external momentum input. The toroidal rotation is counter-current and inverts when reversing the direction of the plasma current (figures 9.3, 9.4 and 9.7).
2. Inside the sawtooth inversion radius, the rotation profile is flat or even hollow for low q_a, high current plasmas (figures 9.3 and 9.4).
3. Core plasma rotation scales as $v_{\phi,\max}[\text{km/s}] = -12.5 \cdot T_{i0}[\text{eV}]/I_p[\text{kA}]$, within the parameters shown in figure 9.9, with velocities up to 50 km/s.
4. Outside the inversion radius, the rotation profile decreases continuously and quasi-linearly toward the edge (fig. 9.9).
5. The edge rotation in TCV stationary plasmas is small (see figure 9.8) and perhaps slightly co-current at the plasma boundary.

9.2.1 Plasma current effects on TCV toroidal rotation profiles

This section describes the dependence of the toroidal rotation profiles on the plasma current and q-profile. The plasma current is varied from shot to shot

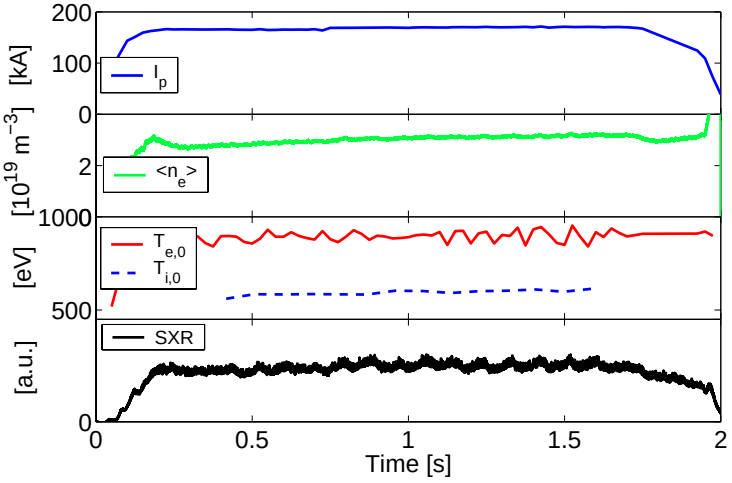

Figure 9.1: *Time evolution of discharge #27098 ($q_a \sim 6$) used for the toroidal rotation experiments with plasma current scan. The electron and ion temperatures are measured respectively by the Thomson scattering and CXRS.*

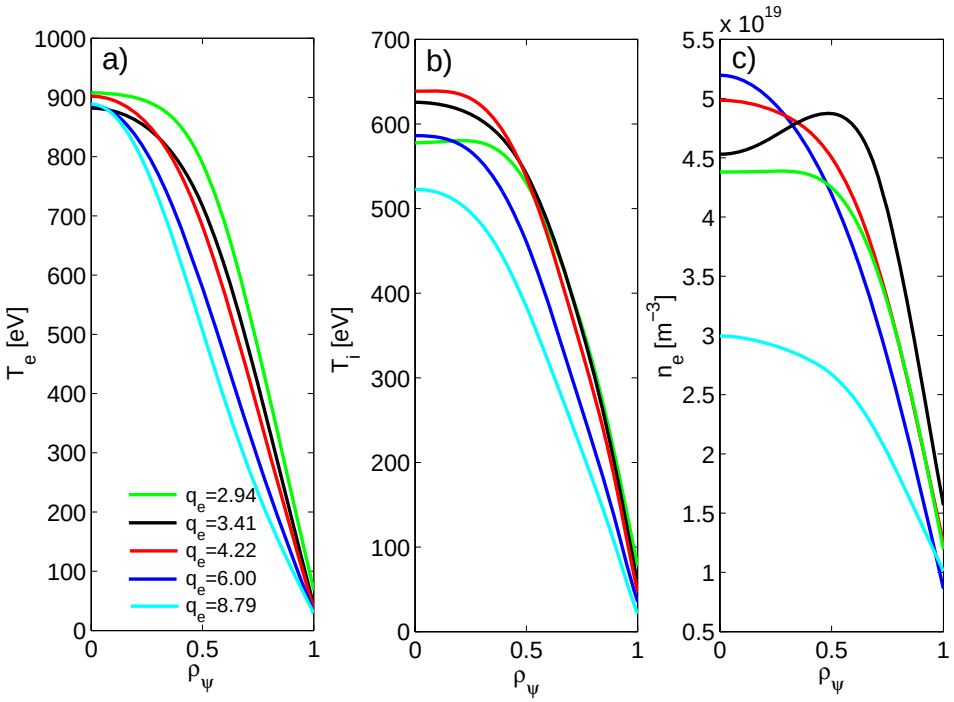

Figure 9.2: *a) Variation of the T_e, T_i, and n_e profiles in a q-scan. Time averaged electron temperature profiles from Thomson scattering. b) ion temperature from CXRS. c) electron density profiles. From discharges #27095 (green), #27494 (black), #27094 (red), #27098 (blue), #27502 (cyan).*

whilst maintaining constant, during the discharge, the plasma shape ($\kappa = 1.35$ and $\delta = 0.15$), position and averaged density ($\langle n_e \rangle \approx 3 \cdot 10^{19}$ m^{-3} for most experiments).

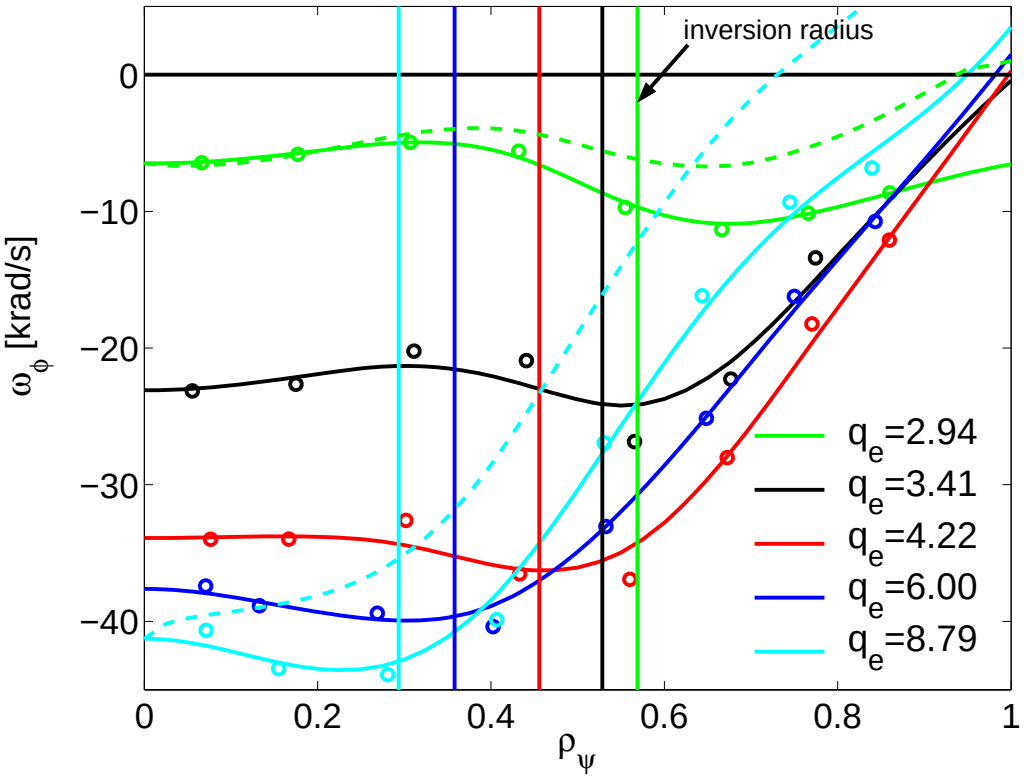

Figure 9.3: *Angular velocity for various edge safety factors with positive plasma current. The dots represent the experimental measurements, the solid lines are smoothed cubic spline curves used to extrapolate the toroidal velocity outside of the observed regions. Vertical lines indicate the measured sawtooth inversion radius obtained from the tomography inversion of the soft X-ray emissivity. The dashed lines represent the bulk plasma rotation profiles (main ion specie) predicted by neoclassical theory (equation 9.3) for high and low current discharges. From discharges #27095 (green), #27494 (black), #27094 (red), #27098 (blue), #27502 (cyan).*

The plasma parameter evolution for a typical experiment are shown in figure 9.1. The temperatures and rotation profiles are averaged over a long quasi-stationary phase where the relative variation of the plasma parameters is typically below 5%. The quasi-stationary phase is often longer than 1 s, considerably longer than the energy confinement time τ_E (of the order of 20–40 ms), and corresponds to several resistive current redistribution times ($\tau_R \approx 100$ ms). The averaged electron and ion temperatures and the electron density, from Thomson scattering and CXRS, are shown in figure 9.2 for several values of the edge safety factor q_a with positive plasma current. In figure 9.3 and 9.4 we present the rotation profiles for different q_a values with positive and negative I_p. The angular velocity $\omega_\phi = v_\phi / R$, an approximate flux function [117], is plotted versus the normalised poloidal flux

ρ_ψ. The carbon fluid is found to rotate in the electron diamagnetic toroidal drift direction, in the opposite direction to the plasma current (negative for positive I_p).

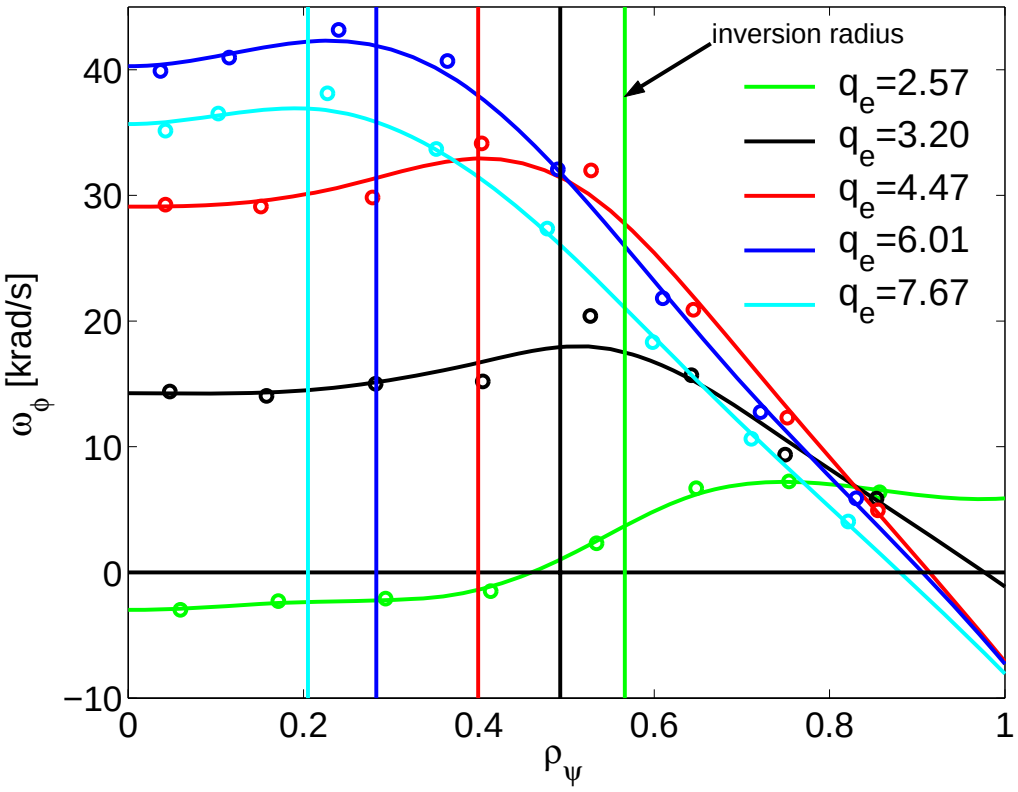

Figure 9.4: *Angular velocity for various edge safety factors with negative plasma current. Vertical lines indicate the measured sawtooth inversion radius obtained from the tomography inversion of the soft X-ray emissivity. From discharges #27478 (green), #27477 (black), #27483 (red), 27484 (blue), #27488 (cyan).*

More generally, the total impurity toroidal momentum is clearly negative (counter-current rotation) for all TCV Ohmic L-mode discharges within the plasma parameter ranges shown in table 9.1. The velocities at the plasma edge and magnetic axis are extrapolated using a smoothing cubic spline interpolation with zero first derivative on axis and zero second derivative at the plasma boundary. Interestingly, the extrapolated edge rotation has a small (<8 km/s) co-current velocity at the plasma boundary (except for the very low q_a case). This is confirmed by high spatial resolution edge rotation measurements suggesting a rotation inversion at a few centimetres inside the plasma boundary (see section 9.2.2). The velocity increases monotonically from the plasma edge reaching a maximum value $v_{\phi,\max} = v_\phi(\rho_s)$ at the location ρ_s. Inside $\rho_s(q_a)$ the profiles are hollow as most clearly shown for the higher current cases (black and green profiles). The central velocity is found to increase with the edge safety factor.

It is interesting to compare the experimental toroidal velocity with other characteristic velocities of interest such as the thermal ($v_{\rm th}$), the sound ($v_{\rm sound}$), and the diamagnetic ($v_{\rm i,diam}$) velocity for plasmas with parameters in the table 9.1. We

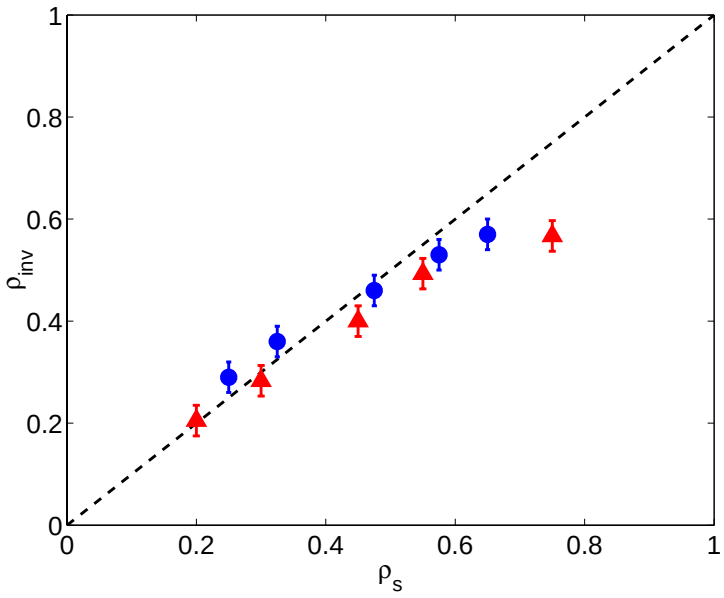

Figure 9.5: *Correlation between the radius of maximum rotation ρ_s and the sawtooth inversion radius ρ_{inv}. The blue dots refer to positive current scans, and the red squares to negative current scans. Note that $\rho_s > \rho_{inv}$ for $\rho_{inv} \geq 0.6$*

find $v_{\mathrm{sound}} \sim 2\mathrm{v}_{\mathrm{th}} \sim$ 220–450 km/s, $v_{\mathrm{i,diam}} = (dp_i/dr)/(eBn_i) =$ 4–8 km/s and $v_{\phi,\mathrm{CX}} = \omega_\phi R =$ 10–40 km/s. The measured carbon velocity is subsonic, but not a negligible fraction of the sound speed, and of the order of the diamagnetic speed. This condition is usually referred to as the small plasma rotation regime, and implies that the diamagnetic term in the momentum balance equation may not be neglected.

We now turn to the effect of the sawtooth instability on the rotation profile. The radial position of the maximum velocity, ρ_s, scales linearly with ρ_{inv} (figure 9.5), strongly suggesting that the sawtooth activity flattens, or clips, the rotation profile within the inversion radius. A further demonstration of such "clipping effect" by the sawtooth instability is provided by experiments in which the current profile is modified using the ECRH. The ECRH is used in TCV to heat and/or modify the electron temperature and current density profiles. In particular, off-axis deposition allows an increase in the off-axis electron temperature and, by keeping the total current fixed and owing to the electric conductivity dependence on T_e, to flatten the current density profile [118]. In figure 9.6 we show the temperature and rotation profiles during the Ohmic and the ECRH phase of a limited discharge. With an ECRH power deposition of 500 kW at $\rho_{\mathrm{dep}} = 0.65$, the electron temperature is flattened with no change in its central value. Consequently, the central safety factor increases, the inversion radius is observed to move inwards from 0.35 to 0.15 of the normalised radius ρ_ψ, and the central toroidal velocity increases whilst the rotation profile peaks considerably. After a transient period, shorter than the diagnostic temporal resolution, the new stationary rotation profile is found that is monotonic up to the new inversion radius of the ECRH phase, consistent with

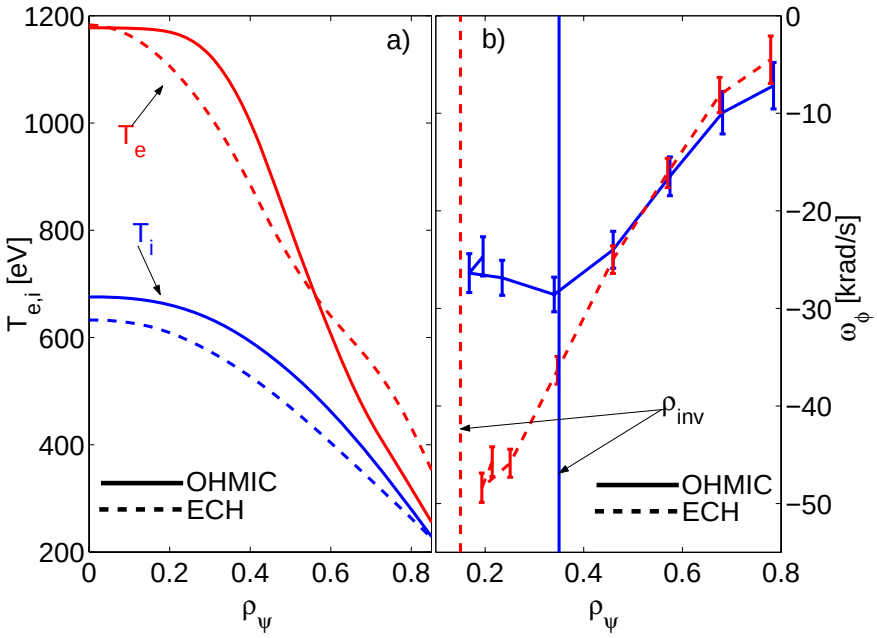

Figure 9.6: *a) Effect of 500 kW off-axis ($\rho_{\rm dep} \approx 0.65$) electron cyclotron heating on temperature profiles. The T_e (and j_ϕ) profile is flattened and the inversion radius $\rho_{\rm inv}$ moves inward from 0.35 to 0.15 in normalised radius. b) Toroidal rotation profile peaking with the reduction of the inversion radius. From discharge #27677 ($q_a \sim 6$)*

the results of the q_a scan in figures 9.3 and 9.4. This is further evidence of a core momentum transport dominated by the effect of the sawtooth instability. We observe a deviation from the linear correlation between ρ_s and $\rho_{\rm inv}$ at large $\rho_{\rm inv}$ (see figure 9.5). In fact, in the lowest q_a discharges, the rotation profile is hollow further out from the inversion radius and, in some cases, the central rotation velocity is directed co-current (as for the lowest q_a example in figure 9.4). The rotation profile hollowness increases with the plasma current and suggests the existence of some internal torque, possibly linked with the sawtooth activity, which may cause an inversion in the central rotation.

Finally, it is useful to directly compare the rotation profile from discharges with opposite plasma current directions. Attention was paid to obtain discharges with the same total current, plasma shape, temperature and electron density profiles. The toroidal rotation is found to invert when changing the direction of the plasma current as shown in detail in figure 9.7. Inside the inversion radius, the velocities are identical to within the experimental uncertainty. Note that the small, but systematic, differences observed outside $\rho_{\rm inv}$ may not be ascribed to neutral beam induced rotation. In fact, the absolute rotation velocity is larger for the case of counter-rotation (positive I_p) whereas the beam induced rotation is expected to be co-current (see section 3.2.5 and figure 9.7). Errors in the reconstructed radial position of the magnetic axis of about 1 cm or small differences in the inversion radius may explain the faster counter-rotation of the positive I_p discharge.

Summarising this section, we have shown the profiles of spontaneous toroidal

rotation in TCV Ohmic limited L-mode. The rotation velocity increases toward the centre reaching its maximum value close to the sawtooth inversion radius. Central velocities are of the order of or larger than the diamagnetic speed. The rotation velocity increases with the edge safety factor up to 50 km/s, and the rotation profiles reverse symmetrically when inverting the plasma current direction. The sawtooth activity flattens the profile inside the inversion radius.

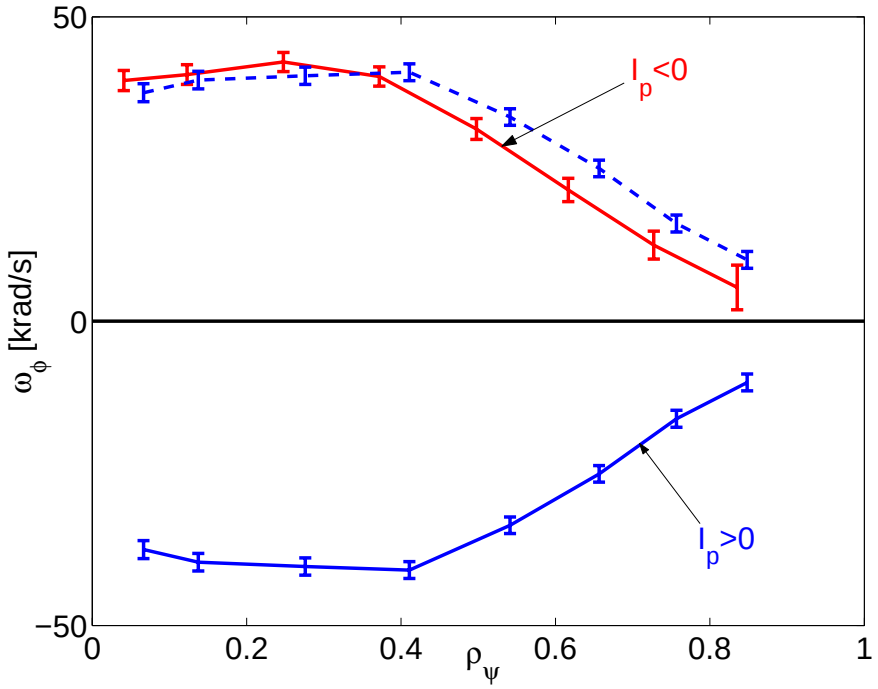

Figure 9.7: *Angular velocity profiles for positive (discharge #27098, blue) and negative (discharge #27484, red) I_p. For a closer comparison, the absolute value of the toroidal rotation in discharge #27098 is plotted (dashed blue line).*

9.2.2 Edge toroidal rotation measurements

To observe the complete rotation profile, inclusive at the plasma edge, the magnetic axis of the plasma was shifted upwards inside the TCV vessel to place the CXRS observation at the outer part of the plasma. The plasma shape and the other plasma quantities were kept constant. The rotation profiles of three discharges located at $Z_{\rm axis} \sim 0$, 15 and 25 cm, are shown in Fig. 9.8b. In figure 9.8a the observation points are graphically displaced to show the magnetic surfaces seen by the CXRS diagnostic. The profiles consistently overlap over the commonly observed region and a similar result holds for the electron and ion temperature profiles measured by Thomson scattering and CXRS respectively. The carbon impurity toroidal rotation decreases monotonically, and quasi-linearly, at the plasma periphery. The outermost measurement indicates a low, co-current toroidal rotation suggesting

a rotation inversion with respect to the majority of the plasma column close the edge.

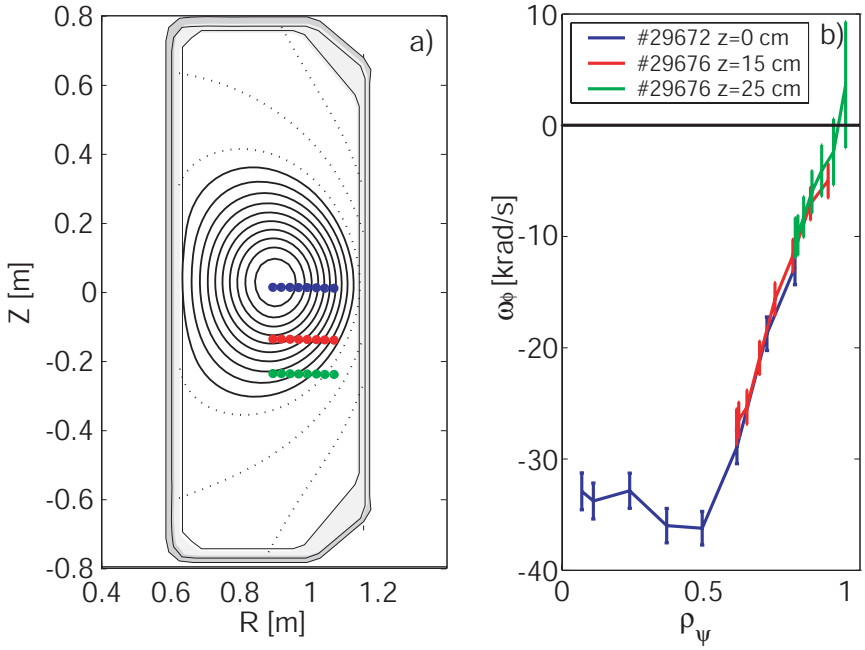

Figure 9.8: *a) Experimental view points of the CXRS system and typical poloidal cross-section of the TCV plasmas used for these investigations. Toward the plasma edge, the compression of the magnetic surfaces reduces the diagnostic's radial spatial resolution and the lower carbon density reduces the signal level. A displacement of the vertical plasma position allows the measurement of the full profile with high resolution. The observation points, with a displaced magnetic axis at* $Z_{\rm axis} \sim$ *0,15 and 25cm, are superimposed to the plasma equilibrium. From discharges #29672 (blue), #29676 (red), #29678 (green), respectively. b) Angular rotation profiles plotted as function of the normalised poloidal flux for similar plasmas with* $q_a = 4.4$ *and with different* $Z_{\rm axis}$.

Although affected by large experimental uncertainty, the small co-current rotation velocity measured at the edge is consistent with the values extrapolated from the inner part of the rotation profiles (see figures 9.3 and 9.4), as well as with other edge measurements, in particular in presence of MHD modes [119]. We notice that the total (volume integrated) plasma momentum is negative (counter-current) for all the experiments presented here.

9.2.3 Basic scaling law for the TCV toroidal rotation

In this section, we discuss the dependence of the toroidal rotation profile on the plasma total current, density and temperatures, and provide a simple scaling law for the toroidal carbon velocity.

As shown earlier (see section 9.2.1), the inner part of the profile is flat or hollow inside the inversion radius. The outer part is found to approximately vary linearly with the normalised poloidal flux coordinate, ρ_ψ, and it can be well described with a function of the type $v_{\phi,0}(1-\rho_\psi)^\alpha$ with the approximation of zero rotation at the plasma edge (see section 9.2.2), as shown in figure 9.9 (left). Thus a convenient description of the TCV rotation profile requires only the position and the value of its maximum, $v_{\phi,\max}$.

To characterise the basic dependence of $v_{\phi,\max}$ on the main plasma parameters, a database with plasma current $|I_p|$ = [100–240] kA and averaged density in the range [1.4–3.7] $\cdot 10^{19}$ m^{-3}, has been assembled. The ion temperature was varied (by approximately a factor 2) by changing the Ohmic input power (thus varying I_p), and the equipartition power through its plasma density dependence $P_{\rm equi} \sim n^2(T_e - T_i)/T_e^{3/2}$. Only discharges with a stationary phase exceeding 300 ms, and acquired electron and ion kinetic data were analysed. Discharges with strong MHD activity were also excluded from the database.

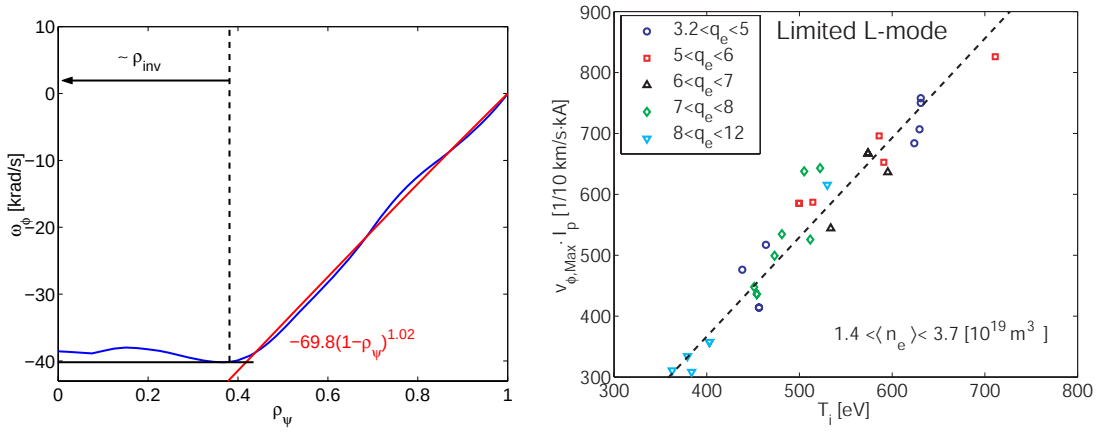

Figure 9.9: *Left: Approximate "single point" description for the rotation profile (blue) from discharge #27098, $q_a \sim 6$. The profile is approximated to flat line inside $\rho_{\rm inv}$ (black), and to a quasi-linear function $v_{\phi,0}(1-\rho_\psi)^\alpha$ outside $\rho_{\rm inv}$ (red). Right: Dependence of the product $v_{\phi,\max} \cdot I_p$ on the ion temperature. The database encompasses positive and negative plasma currents.*

When averaging over the steady state phase, a simple scaling can be extracted, as shown in figure 9.9 (right). The product $v_{\phi,\max} \cdot I_p$ is proportional to the ion central temperature, and the best linear fit (dashed line in fig. 9.9) has the scaling:

$$v_{\phi,\max}\ [\mathrm{km/s}] = -12.5 \cdot \frac{T_{i0}\ [\mathrm{eV}]}{I_p\ [\mathrm{kA}]} \tag{9.1}$$

It is worth noting that this scaling is valid not only for $v_{\phi,\max}$, but for the entire profile outside the inversion radius, reinforcing the link with ion temperature profile.

In contrast with NBI heated discharges [101], no direct dependence on plasma density is observed in these TCV experiments. The average toroidal rotation fol-

lows the ion temperature, regardless of the electron density and electron temperature evolution (see figure 9.10). In NBI discharges, the majority of the angular momentum is externally injected into the plasma. This momentum is then diffused by transport process and shared by plasma particles giving rise to a strong density dependence on the toroidal velocity. On the other hand, in the Ohmic regime, the momentum is internally generated, and there is no a priori reason for such a density dependence.

Equation (9.1) is, to our knowledge, the first experimental scaling law for Ohmic L-mode discharges using CXRS spectroscopy data. We note that this scaling is similar to that found for the central co-rotation on the C-mod tokamak [107] for ICRH and Ohmic H-mode plasmas, although, there, the toroidal velocity is proportional to the total energy content, W, rather than to the ion temperature.

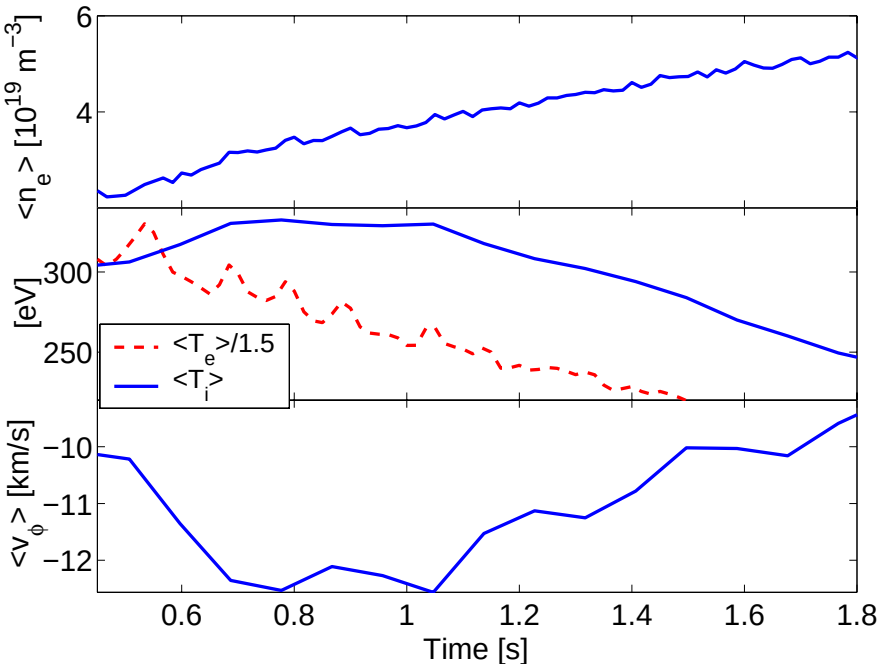

Figure 9.10: *Temporal evolution of the averaged density, temperatures, and toroidal rotation during density ramp by gas injection. The rotation velocity mimics the ion temperature evolution rather than the density and electron temperature evolution (discharge #28359).*

9.2.4 Rotation profiles with plasma triangularity

A set of experiments for a range of triangularity at fixed current and elongation was performed with the triangularity varied from $\delta = -0.3$ to $\delta = 0.65$. The plasma cross-section increases from negative to positive δ, and the edge safety factor varies accordingly from 3 to 4.8. The reconstructed q-profile differs, however, very little inside $\rho_\psi = 0.95$. Despite the fact that the preprogrammed density was the same for all discharges, the line-integrated density was found to be about 25% higher at

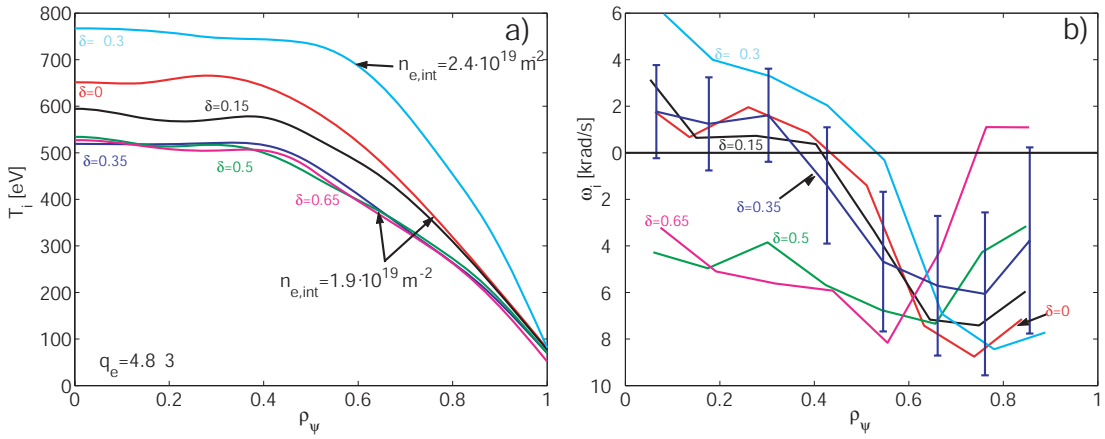

Figure 9.11: *Ion temperature (a) and rotation (b) profiles in a δ scan at fixed current (340 kA). We show for reference the experimental uncertainties on one of the profiles.*

negative δ (figure 9.11a), suggesting a better particle confinement. This can also be seen from the ion temperature increase when passing from $\delta = 0.65$ to $\delta = -0.3$. Such beneficial effect of the negative triangularity has already been observed on TCV ECRH plasmas [120], and the underlying reasons are under investigation.

For fixed triangularity, the toroidal velocity is linear with the T_i. It depends (weakly) on δ, as shown in figure 9.11b). The central rotation moves toward positive velocity (co-current) for negative plasma triangularity. However, the low values of rotation and the relatively large experimental uncertainties do not allow a clear conclusion on the triangularity dependence of the toroidal rotation. This experiment could be repeated at lower plasma current, where higher toroidal velocities are expected.

9.3 Comparison with neoclassical predictions

The experimental toroidal velocity may be readily compared with analytical expressions for the mean ion toroidal velocity derived in the framework of the neoclassical theory [121, 117]. Here, we consider the different plasma rotation drives: the thermodynamic forces, density and temperature gradients, and the radial and toroidal electric field and we quantify their effects and relative importance in the TCV case. We then compare the experimental rotation profile with the profile obtained by setting the neoclassical radial flux of angular momentum to zero.

9.3.1 Toroidal electric field contribution to impurity toroidal rotation

Kim, Diamond et al. [121], using the moment approach of Hirshman and Sigmar [122], calculate the toroidal ion flow velocities for a plasma with an impurity species, whilst neglecting the electron contributions to the viscous and friction

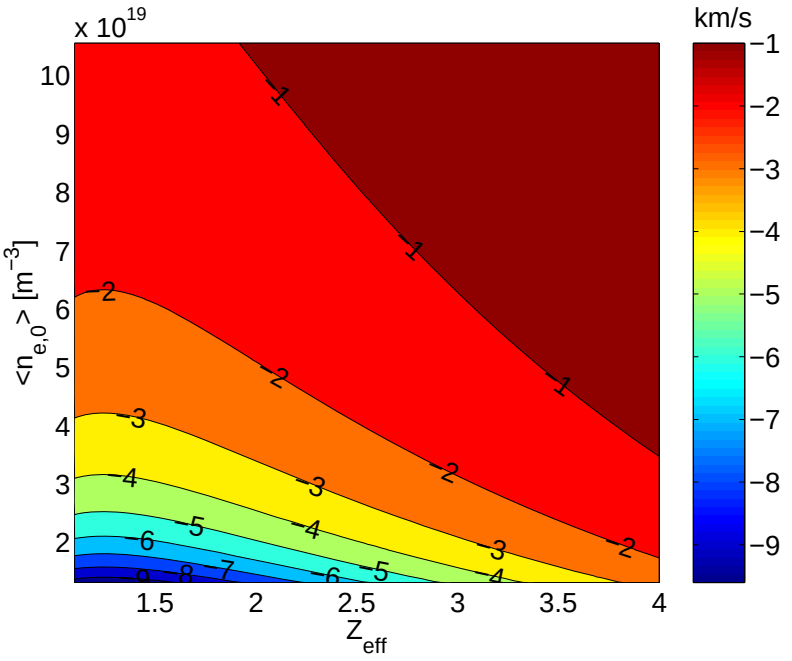

Figure 9.12: *Contour plot of the neoclassical central impurity toroidal rotation,* $v^I_{\phi,0}$ *induced by the toroidal electric field (see equation 9.2) as a function of the effective charge and central density for a* $q_a = 6$ *discharge (#27098).*

forces. The effects of the toroidal electric field are considered separately from the other drives, assuming zero total plasma momentum since an E_ϕ field cannot bring any net momentum to the plasma. The resulting main ion flow is small and co-current directed, similar to the case of an impurity free plasma. Yet, if the ion-ion collisional frequency and the impurity density are sufficiently low, a large impurity counter rotation arises balancing the co-rotation of the main ions. In TCV Ohmic plasmas, however, the E_ϕ contribution to the impurity rotation is too small to explain the measured values. In fact, the predicted counter (negative) velocity on axis is [108]:

$$v^I_{\phi,0} \quad = \quad 4.19 \cdot f(Z_{\text{eff}}) \frac{Z_i V_{\text{loop}} T^{3/2}_{I,0}}{n_{i,0}\sqrt{A_i} R_0} \tag{9.2}$$

with Z_i and A_i the main ion electric charge and mass number, V_{loop} the induced loop voltage, $T_{I,0}$ the measured central carbon temperature in keV, $n_{i,0}$ the central deuterium density, R_0 the radius of the magnetic axis, and Z_{eff} the effective charge. The factor f is close to unity. Since the largest uncertainties are in the values of the effective charge and ion density, we calculate the central carbon velocity as a function of these two quantities shown in figure 9.12. Even for very low Z_{eff} and $n_{i,0}$, the theoretical toroidal rotation is less than 10 km/s, well below the measured value. Moreover, using Z_{eff} from the soft X-ray emissivity yields $v^I_{\phi,0} \approx$ – 3 km/s, which is an order of magnitude smaller than the observed rotation velocity.

Thus, in the TCV tokamak, the toroidal electric field may only contribute a small fraction of the measured carbon toroidal rotation and its contribution will thus be neglected in the remainder of this chapter.

9.3.2 Radial electric field and diamagnetic contributions to toroidal rotation

We now turn our attention to the other rotation drives, namely the radial gradient of the electrostatic potential, the ion temperature and the plasma density, as calculated in reference [121] in the framework of the neoclassical theory. They may be expressed as:

$$v_\phi^{i,I} = \frac{E_r}{B_\theta} - \frac{T_i}{eB_\theta}\left[K_1^{i,I}(\nu_{*,i},\epsilon)\frac{1}{L_{n_i}} + K_2^{i,I}(\nu_{*,i},\epsilon)\frac{1}{L_{T_i}}\right] \tag{9.3}$$
$$1/L_T = \frac{\partial T}{\partial r}\frac{1}{T}$$
$$1/L_n = \frac{\partial n}{\partial r}\frac{1}{n}$$

where $K_1^{i,I}$ and $K_2^{i,I}$ are numerical coefficients of order unity that depend on the ion species collisionality $\nu_{*,i}$, and the inverse aspect ratio ϵ. The gradient scale lengths, L_{n_i} and L_{T_i} are negative quantities for monotonic, peaked profiles. The second and third terms in equation 9.3 depend on the ion density and temperature gradients respectively, and we will refer to them as the diamagnetic terms.

Since the coefficients $K_1^{i,I}$ and $K_2^{i,I}$ depend on the ion species, the toroidal velocity is different for deuterium and carbon ions. Such a difference between species in the rotation velocity was experimentally verified in the Doublet III-D [123], and shown to be important in JET plasmas with internal transport barrier [124]. The theoretical expression for the velocity difference,

$$\Delta v_\phi = v_\phi^I - v_\phi^i \approx \frac{3}{2}\left(\frac{3}{2}\sqrt{\frac{r}{R}}\right)\frac{1}{eB_\theta}\frac{dT_i}{dr},$$

independent of E_r according to equation 9.3, would result in the carbon impurity acquiring a counter rotation with respect to the bulk ions. Δv_ϕ is small (except near the plasma edge) for TCV high current discharges, whereas in low current plasmas it may reach values up to 10 km/s and should be taken into account for comparison with other independent measurements of the plasma toroidal velocity (see figure 9.3). The predicted difference in rotation velocities does not, however, alter the conclusions presented in this section and will be neglected in the following.

The term proportional to the radial electric field E_r in equation 9.3 arises from the combination of the parallel and perpendicular component of the velocity, and is equal for all particle species. In TCV, a direct measurement of the radial electric field is not yet available, so that a quantitative comparison with the experiment is not possible. Nevertheless, some *qualitative features* of the toroidal rotation in TCV tokamak presented in the previous sections *are consistent with equation 9.3*:

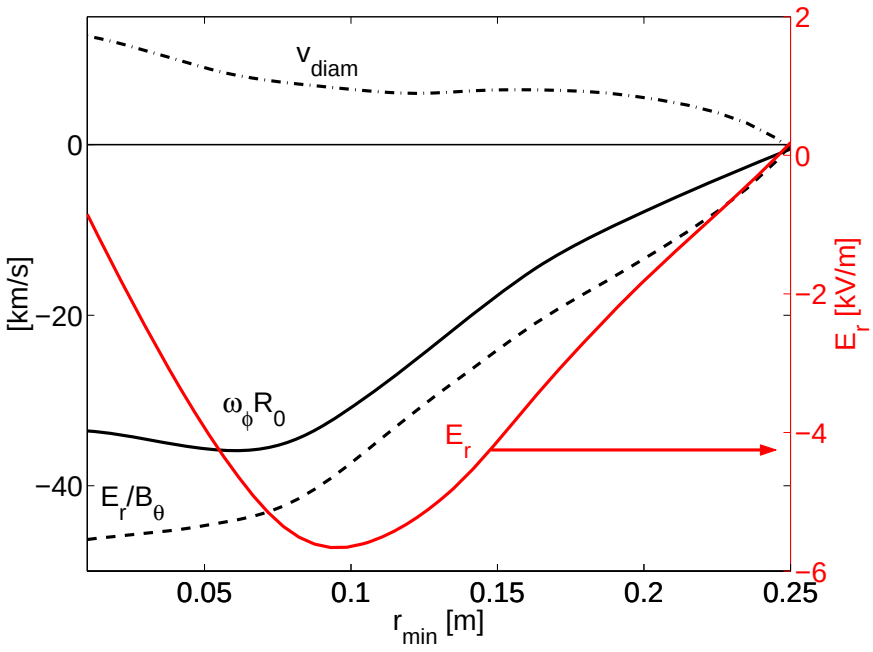

Figure 9.13: *The experimental rotation profile (full black line), the diamagnetic contributions (second and third terms in eq. 9.3) to the carbon velocity (dot-dashed black line), the E_r/B_θ inferred from eq. 9.3 (dashed black line), and the E_r profile (full red line).*

1. the ion velocity scales with the poloidal magnetic field as $1/B_\theta$, consistently with the $1/I_p$ scaling of the measured toroidal velocity and the inversion with the plasma current direction (see figure 9.7);

2. the linear dependence on T_i in the experimental scaling can be explained if the radial electric field is also proportional to T_i and/or its first derivative.

Alternatively, equation 9.3 provides an analytical expression for the evaluation of the radial electric field from the experimental toroidal rotation, density and temperature profiles together with magnetic equilibrium information without experimental knowledge of the poloidal rotation. We note that this is equivalent to estimating the radial electric field by using the radial component of the momentum balance equation with the assumption of a neoclassical poloidal rotation of the form $v_\theta = (1 - K_2^i)T_i/(eB_\phi L_{T_i})$. This assumption is not justified, a priori, but provides a zero order estimate valid in case of damped poloidal rotation.

We now evaluate the radial electric field from measured experimental profiles and compare the contribution of the various terms to the experimental toroidal velocity. It is found that, for these Ohmic discharges, the bulk ions are in the banana collisional regime (except at the plasma edge), and the impurity ions in the collisional regime. In this collisionality regime, the calculated diamagnetic toroidal velocity is co-current and of the order of 10–20 km/s (second and third term in equation 9.3). To compensate the diamagnetic contribution, the deduced E_r/B_θ term is larger than the toroidal rotation measured by CXRS (as shown in

figure 9.13). The radial electric field E_r profile presents a well close to mid radius and directed toward the plasma centre (figure 9.13), independently from the sign of the plasma current. It is thus concluded that the toroidal rotation in TCV Ohmic discharges is consistent with the dominant radial electric field as for NBI driven discharges.

9.3.3 Comparison of experimental and theoretical stationary toroidal velocity profiles

In absence of external momentum sources, the steady state rotation profile, or equivalently the radial electric field, may be explicitly evaluated by setting to zero the radial flux of toroidal angular momentum. Such calculations were performed decades ago for pure plasmas (no impurity), by Rosenbluth et al. in the banana regime [125], by Hazeltine in the collisional regime [117], and by Tsang and Frieman in the intermediate regime [126], employing the drift kinetic equation derived by Hazeltine [127]. Recently, Catto and Simakov [128] showed that Hazeltine's equation is incorrect to the order required (in the Larmor radius expansion) for the calculation of the radial momentum flux, and re-evaluated the radial electric field in the collisional regime [129]. Alternatively, Claassen et al., starting from fluid equations, developed a neoclassical theory of poloidal and toroidal rotation formally valid in the high collisional regime, which agrees with Catto's result in the $r/qR \ll 1$ limit [130]. Wong et al. [131] repeated the calculation of the small rotation version of the angular momentum flux in the banana regime finding a temperature-gradient-driven component of the flux with an equal analytical form of that in reference [125] *but with a numerical coefficient of opposite sign* (and similar absolute magnitude). In both low and high collision regimes, a component of the momentum flux, independent from the toroidal velocity (and its derivative), arises from neoclassical effects. In terms of a transport matrix, this corresponds to a coupling (off-diagonal element) between the radial gradient of the ion temperature and the toroidal velocity. This coupling term is especially important in Ohmic discharges because, acting as a source term, it determines the spontaneous stationary rotation profile.

According to most recent calculations of references [131] and [129], the stationary toroidal velocity gradient in the large aspect ratio limit may be written as,

$$\frac{dv_{\phi,\mathrm{banana}}}{dr} = 3.7\frac{1}{eB_\theta}\frac{1}{\sqrt{\varepsilon}}\left\{\frac{dT}{dr}\left[\frac{1}{2r}+\frac{2dq}{qdr}+\frac{2dn}{ndr}-\frac{dT}{2Tdr}\right]+\frac{d^2T}{dr^2}\right\} \quad (9.4)$$

$$\frac{dv_{\phi,\mathrm{PS}}}{dr} = -0.19q^2\frac{T}{eB_\theta}\left(\frac{d\ln T}{dr}\right)^2 \quad (9.5)$$

valid in the banana and in the Pfirsch-Schlüter regime respectively. $q = rB_\phi/RB_\theta$ is the safety factor, and the density and temperature refer to the main ion species.

By inspection, it is seen that for standard profiles the different terms in the square brackets of equation 9.4 are all positive except for the density-gradient

term, which is negative. The positive (negative) terms lead to negative (positive) velocity gradients, which correspond to a co-current (counter-current) toroidal rotation. When the temperature profile possesses a point of inflexion, d^2T/dr^2 changes sign from positive on the outside to negative on the inside. This term is small for typical TCV ion temperature profiles. In some cases, the density gradient term may dominate at the plasma edge, producing counter rotation. However, close to the plasma centre, the term proportional to $1/2r$ dominates, leading to a strong tendency for central co-current rotation in contrast with the TCV observations.

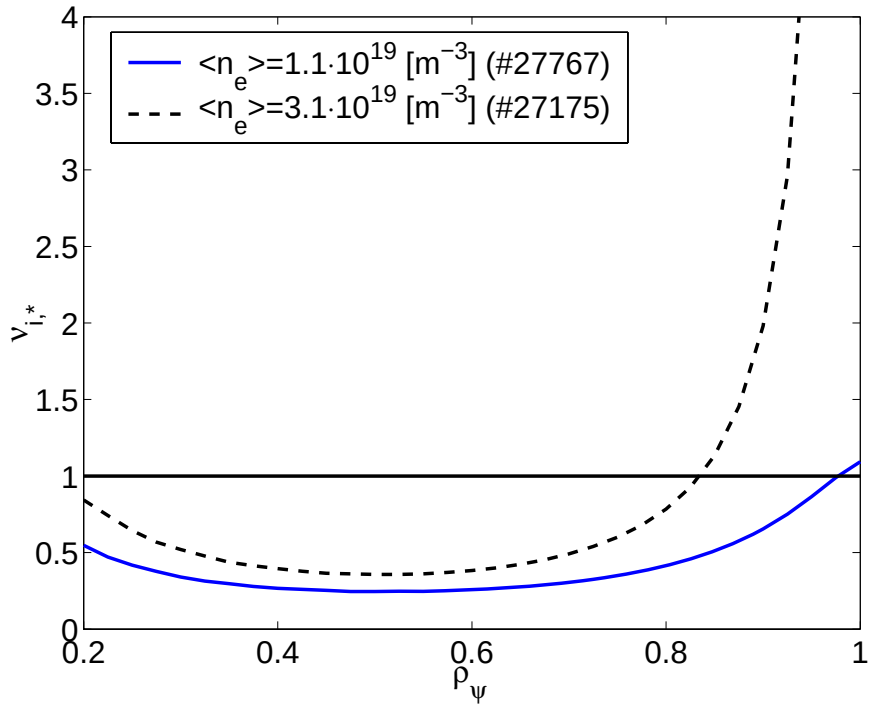

Figure 9.14: *Ion normalised collisionality $\nu_{i,*}$ for a low density ECRH discharge (solid blue) and an Ohmic discharge (dashed black) at higher density. The ions are in the banana regime except in the edge of the higher density case.*

Turning to equation 9.5, valid in the high collisional regime, we note that it has a simpler form and involves only the gradients of the ion temperature profile. The toroidal velocity is always positive, resulting in a co-current rotation everywhere in plasmas with zero rotation at the last closed flux surface. In conclusion, both the plasma edge (collisional) and the plasma centre (collisionless) are expected to co-rotate with respect to the plasma current. The predicted tendency for co-current rotation contrasts with the observations of counter-current rotation in L-mode plasmas in TCV and in other tokamaks.

Before comparing in details the neoclassical formulas (9.4) and (9.5) with the TCV experiments let us consider the ion collisionality in Ohmic TCV L-mode discharges. As anticipated in section 9.3.2, the bulk ions (deuterium) lie in the banana regime ($\nu_{*,i} < 1$) except at the plasma edge and for Ohmic plasmas at high

density (figure 9.14). The normalised ion collisionality $\nu_{*,i}$ is defined as,

$$\nu_{*,i} = \frac{qR}{\epsilon^{3/2}\tau_D v_{\mathrm{th},D}} \tag{9.6}$$

with ϵ the inverse aspect ratio, $v_{\mathrm{th},D}$ the deuterium thermal velocity, and τ_D the ion collision time.

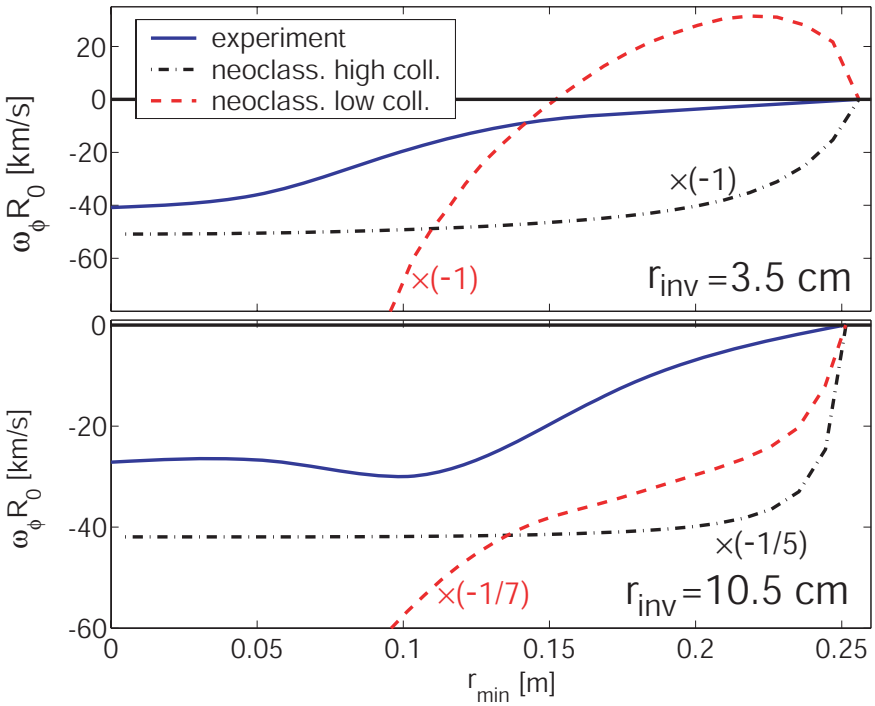

Figure 9.15: *Comparison of experimental toroidal rotation profiles with the neoclassical model. Top: discharge #27767 with $q = 6$ and $r_{\mathrm{inv}} \sim 3.5$ cm. Bottom: discharge #27175 with q=4 and $r_{\mathrm{inv}} \sim 10.5$ cm. The experimental profile (solid blue), the low (red dashed) and high (black dash-dotted) collision models are shown. The theoretical profiles have been re-scaled with numerical coefficients (shown in the picture) to allow for an easier comparison.*

We remark that the basic assumptions of small rotation and low plasma β, assumed in the calculation, are well justified for our TCV experimental conditions (see section 9.2). Although the sawtooth activity is observed to have a strong influence on the rotation profile, it is not included in the standard neoclassical theory. The comparison must be therefore limited to the region outside the inversion radius. In addition, since the models neglect the presence of plasma impurities, we assume that deuterium and carbon rotate with equal velocities.

Using the experimental profiles, we numerically integrate the R.H.S of equations 9.4 and 9.5 assuming zero rotation on the last closed flux surface, as shown in figure 9.15 for two discharges with small and large ρ_{inv}, and quite different profile peaking. The discrepancy between experimental and theoretical values is evident in the rotation direction, magnitude and profile shape. We may conclude

that, for TCV Ohmic discharges with parameters from table 9.1, not only the momentum diffusivity [119] but also the non-diffusive angular flux responsible for the observed spontaneous rotation is anomalous (non-neoclassical). It should be noted, however, that equations 9.4 and 9.5 are strictly valid only in the small aspect ratio limit of circular plasma for the high and low collisionality regimes, which does not correspond to the experimental conditions.

Finally, it is found that the simple empirical formula,

$$\frac{dv_\phi}{dr} = -\frac{\alpha}{eB_\theta r\sqrt{\varepsilon_a}}\frac{dT}{dr} \tag{9.7}$$

with $\varepsilon_a = a/R = 0.28$ and $\alpha \sim 1$, reproduces reasonably well the TCV experimental rotation profiles outside the inversion radius (see figure 9.16). Close agreement may be obtained for all profiles in figures 9.3 and 9.4, by varying α within the uncertainty for the term $\frac{1}{B_\theta r}\frac{dT_i}{dr}$ (about 30%).

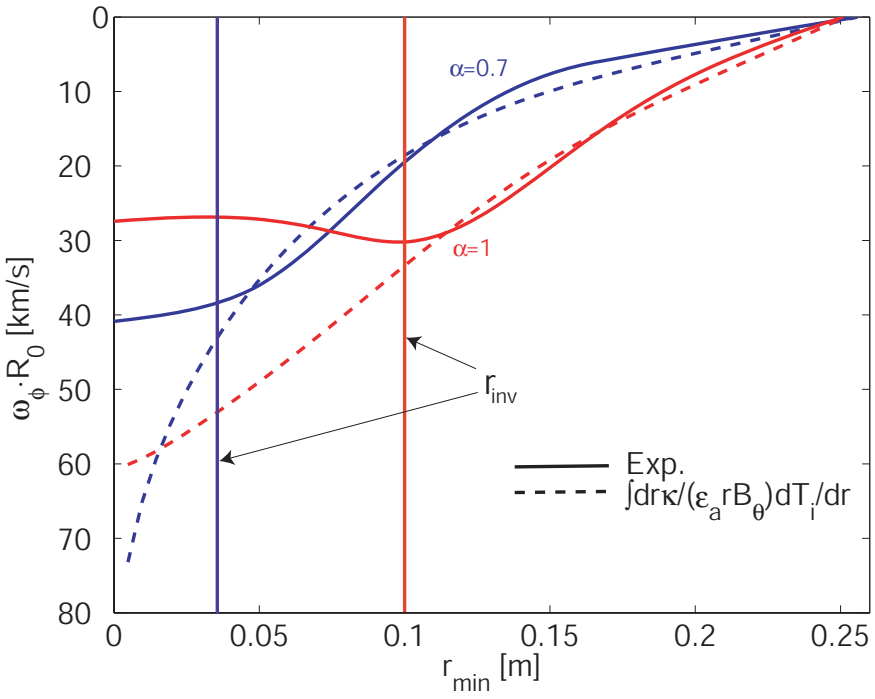

Figure 9.16: *Comparison of the experimental toroidal rotation profiles (solid lines) with the empirical model depicted by eq. 9.7 (dashed) for discharges #27767 (blue, $r_{\rm inv} \sim 3.5$ cm) and #27175 (red, $r_{\rm inv} \sim 10.5$ cm).*

9.4 Summary and conclusions

This chapter shows the first results of toroidal rotation measurement in Ohmic limited TCV plasmas. The observed carbon velocity is of the order of the deu-

terium diamagnetic drift velocity, and up to 1/5 of the deuterium thermal velocity. It is directed in the opposite direction with respect to the plasma current, and the profile reverses when reversing the plasma current. The angular velocity profile is found to be flat or hollow inside the sawtooth inversion radius, and linearly decreases towards the plasma edge. The flattening effect of the sawtooth activity was highlighted in current profile tailoring experiments using ECRH, where the rotation profile is observed to peak consistently with the modified sawtooth inversion radius. By vertically shifting the plasma magnetic axis, the plasma edge velocity was measured. Such experiments show that, close to the limiter, the asymptotic rotation is close to zero or perhaps slightly co-current, suggesting that the angular momentum cannot simply diffuse in the plasma interior from an edge source. Equivalently, these results present strong evidence for a non-diffusive component in the radial momentum flux as observed in the JFT-2M tokamak [132]. The maximum carbon velocity scales as $v_{\phi,\max}$ [km/s]=–12.5 T_i [eV]/I_p [kA] over a large range of plasma density (1.4 $< n_e <$ 3.7·10^{19} m^{-3}) and edge safety factor (3.2 $< q_a <$ 12).

We would like to emphasise here that since there is no direct toroidal momentum input, a small residual toroidal stress can modify the radial electric field and the toroidal rotation. It is therefore difficult to distinguish between the various effects, whether fluctuation induced or neoclassical. Moreover the turbulent $\vec{E} \times \vec{B}$ flow depends, in general, on the turbulent spectra [133, 134], and thus there is no comprehensive analytical formula to compare with the experiment. We therefore restrict our comparison to the neoclassical theory. Our analysis shows that the contribution to the toroidal carbon flow from the toroidal electric fields is negligible and that the diamagnetic terms act as a co-current drive and may not explain the observed counter-rotation. The TCV plasma rotation thus appears to be mainly driven by the radial electric field which has a strong potential well around mid radius. This result does not strictly depend on the validity of the neoclassical theory of equilibrium flows but relies on a sufficiently small poloidal rotation. In this case the dominant contribution to E_r comes from the toroidal rotation. A more robust measurement of the radial electric field will be soon available on TCV with the commissioning of a new vertical CXRS system able to measure the poloidal velocity along the plasma radius.

Although momentum transport is likely to be anomalous, the stationary spontaneous plasma rotation may still be partly determined by neoclassical effect under certain conditions. However we find that the TCV stationary toroidal velocity profile is not described by the neoclassical theory of small toroidal rotation recently revisited in the large aspect ratio limit [129],[131]. The neoclassical temperature-gradient-driven flux is expected to induce strong central co-current rotation, in contrast to the experimental observations of counter-current rotation. In fact, we find that the TCV stationary rotation profiles presented here are consistent with the empirical equation

$$\Gamma_{r\phi} = \frac{d\mathrm{v}_\phi}{dr} + \alpha \frac{T}{eB_\theta r\sqrt{\varepsilon_a}} \frac{d\ln T}{dr} = 0 \tag{9.8}$$

with $\alpha \sim 1$, which well reproduces the experimental rotation scaling and the pro-

file shape outside the inversion radius. Since the neoclassical expressions used for the present comparison are based on many assumptions it is possible that a more complete treatment may lead to substantially different interpretation. However we believe that a quantitative evaluation of the turbulence-driven toroidal rotation is essential for a successful explanation of the intriguing puzzle of spontaneous rotation and momentum transport in tokamak plasmas. The analysis presented here represent a first assessment and characterisation of spontaneous rotation and a starting point for future comparisons with theory. More theoretical efforts are however needed for a complete comparison with the experimental results.

Chapter 10

Angular momentum transport in TCV L-mode plasmas

In the first part of this chapter we report on the observation of a transient momentum transport that dramatically changes the toroidal rotation profile and the total plasma angular momentum. We include the observation of the toroidal rotation braking due to MHD modes, the plasma acceleration (spin-up), and the spontaneous core toroidal rotation inversion discovered in high density L-mode plasmas. In the second part we present a model of the temporal evolution of the rotation profiles during the plasma spin-up and rotation inversion.

10.1 Observations of momentum transport phenomena

In experimental conditions similar to those presented in the previous chapter, we observe transient phenomena that change dramatically the toroidal rotation. We report here on these observations.

10.1.1 Ion momentum losses with large MHD activity

As shown in chapter 5, a rotating magnetic island may couple to the conducting wall, slow down while growing to a larger size, and eventually lead to major or minor disruptions. An example of such an MHD activity is shown in figure 10.1. The rapid drop in the central soft X-ray signal (t =0.77 s) coincides with the minor disruption. After that, the discharge is stable. The magnetics and the soft X-ray measurements [135] reveal an $m/n = 2/1$ mode.

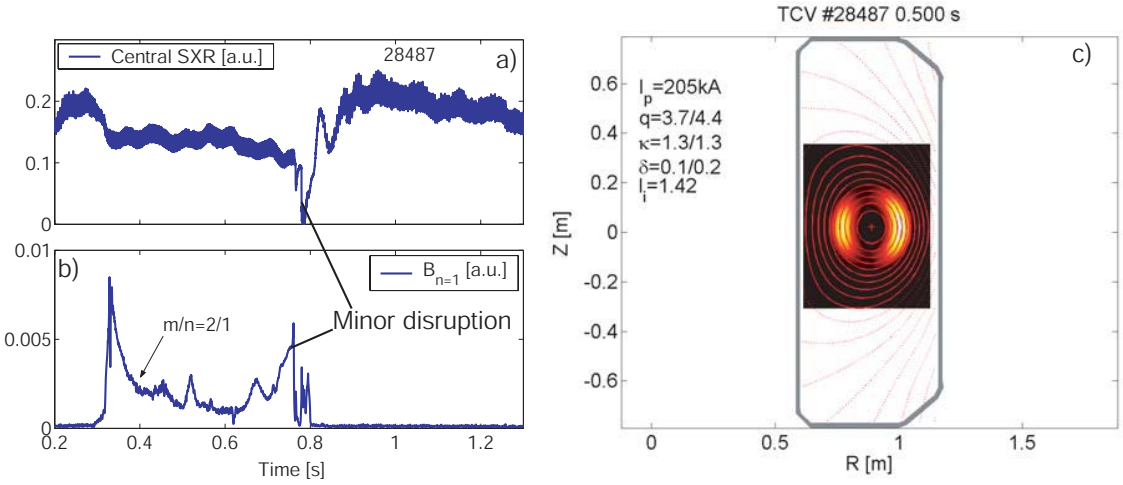

Figure 10.1: *a) Time trace of the central SXR emission. b) $n = 1$ component of the edge magnetic signal showing the mode amplitude evolution. The mode analysis reveals an $m/n = 2/1$ mode. c) The inversion of the MPX signals indicates an island width up to 7 cm.*

The large magnetic island reduces the electron and ion temperatures everywhere in the plasma (figure 10.3). During mode locking the carbon rotation frequency at the $q = 2$ rational surface agrees, within the experimental uncertainty, with the mode frequency from the Mirnov coils (figure 10.2). Thus the MHD mode forces the plasma to slow down from its natural toroidal rotation.

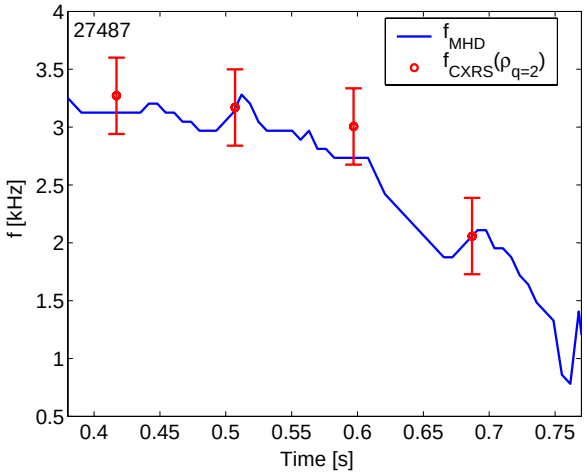

Figure 10.2: *Comparison of the carbon rotation and the MHD mode frequencies during mode locking.*

From the toroidal rotation profile shown in figure 10.4, one can see that the plasma rotates as a rigid body inside the $q = 2$ surface. While slowing down, the MHD mode drags the central ion rotation, reducing its toroidal velocity not only locally, everywhere inside the unstable flux surface.

While reducing the rotation inside the $q = 2$ surface, the presence of the MHD mode does not modify the rotation gradient outside the island rational surface (compare the profiles in figure 10.4). The instability may thus induce, for a sufficiently low mode frequency, a rotation inversion close to the plasma edge. This is clearly visible in discharges with the CXRS chord observing the plasma edge (figure 10.5). The presence of the mode induces a rotation inversion at about ρ =0.85, with an edge co-current rotation with velocities not compatible with 0. We

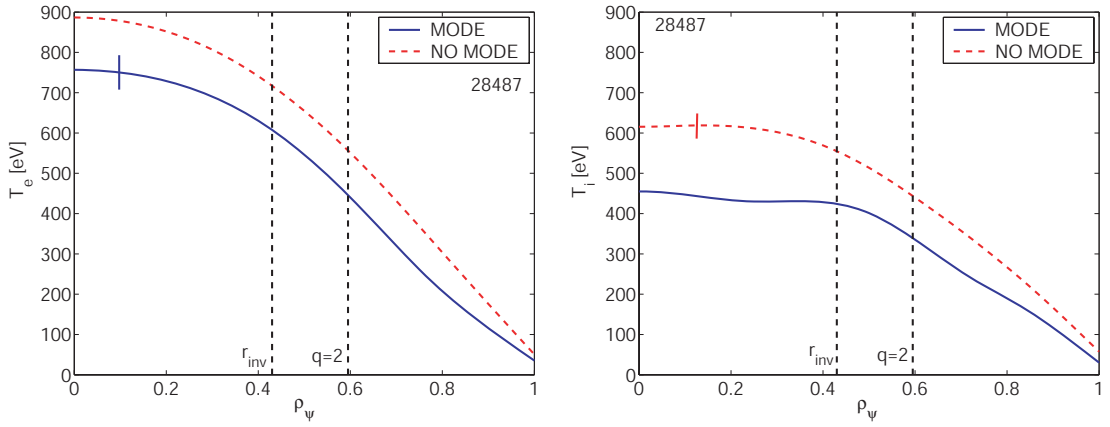

Figure 10.3: *Negative effect of the magnetic island on the temperature profiles. Electron a) and ion a) temperature profiles with and without the large magnetic island during the same discharge (#28487).*

may conclude that *the MHD mode induces a net loss of total momentum* and force a slow rigid body rotation inside the unstable flux surface, whilst it does not change the rotation gradients outside.

10.1.1.a Discussion and interpretation of the observations

Rigid-body toroidal rotation in presence of large magnetic islands has been observed at JET in NBI plasmas [136], and theoretically explained by Lazzaro et al. [137]. According to the authors, when the axisymmetry of the plasma column is broken by the helical MHD instability, an enhanced neoclassical viscosity arises. This extra viscosity is such that it flattens the rotation profile not only locally, around the magnetic island, but also in the core region inside the unstable resonant surface as observed in TCV. The inversion in the edge toroidal rotation with large co-current velocity has been, at our knowledge, observed for the first time in TCV (figure 10.5). In steady state plasmas and in absence of MHD modes, the edge carbon velocity is always found to be very small (figure 9.8). When large magnetic islands are present, however, one can not assume a small edge rotation as a natural boundary condition, despite the momentum losses with the edge neutrals and the presence of the limiter. We may reconciliate these observations by considering the following forces to play a role:

1. a spontaneous rotation drive, or torque, of unknown nature;
2. a viscous force proportional to the rotation gradient;
3. an effective viscous force due to the sawtooth activity;
4. a friction force due to the edge neutrals;
5. an electromagnetic drag and extra viscosity due to the large magnetic island.

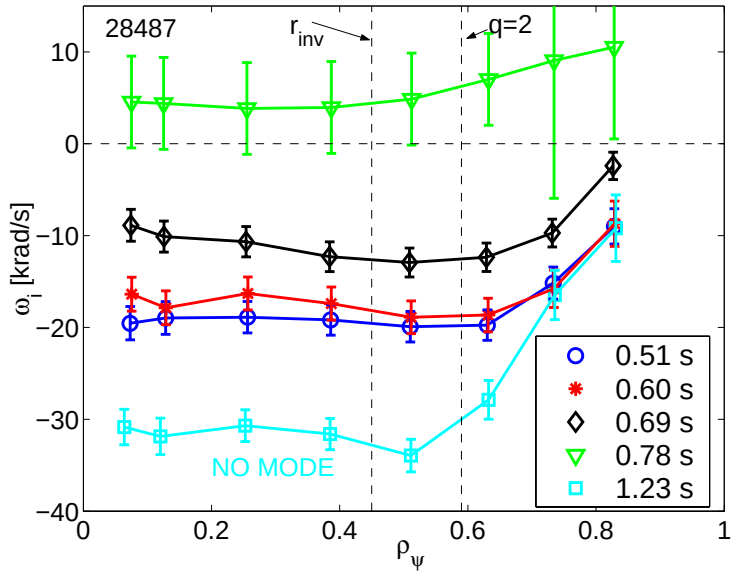

Figure 10.4: *Evolution of the toroidal rotation profile in presence of a large magnetic island. The rotation in absence of the mode is also shown for comparison (cyan).*

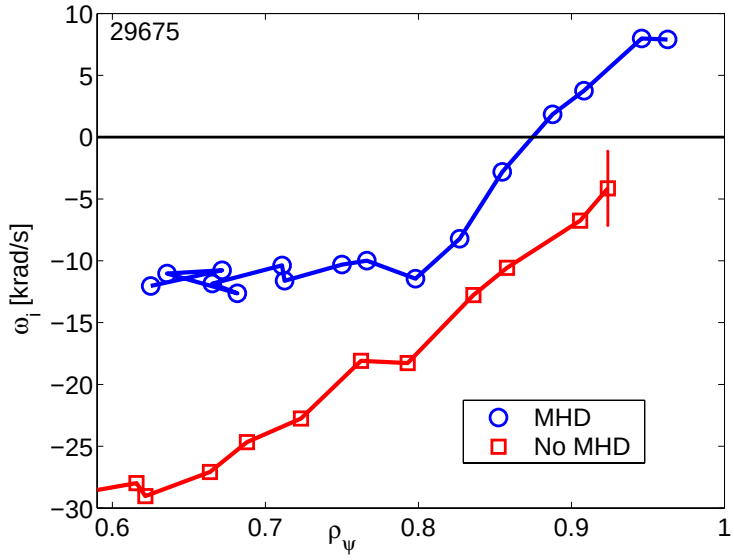

Figure 10.5: *Comparison of edge rotation profiles with and without the presence of the MHD mode.*

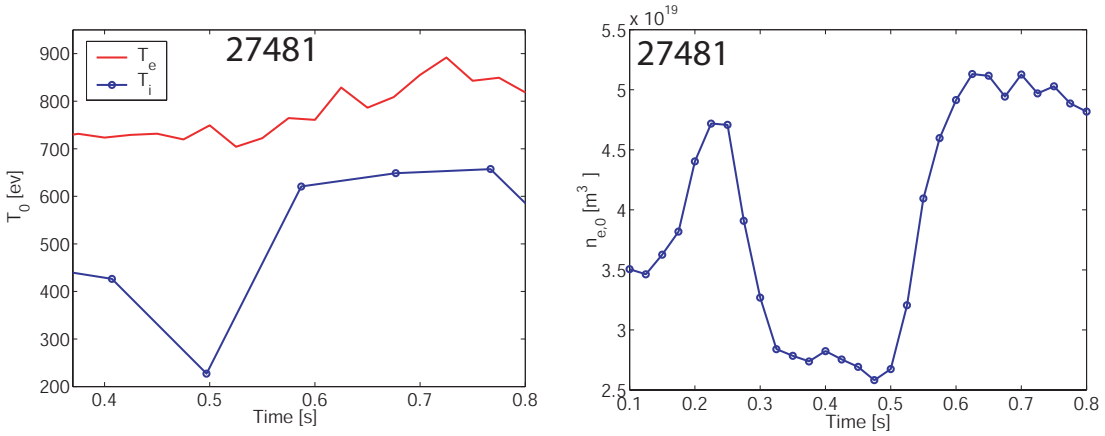

Figure 10.6: *a) Time evolution of the electron and ion temperatures (a) from TS and CXRS measurements, and of the electron density (b) after the minor disruption.*

In absence of the island, force 1, 2, and 3, which act on the gradients, balance themselves resulting in the typically observed velocity gradients (chapter 9). The plasma is essentially free to move in the toroidal direction, and even a localised friction (4) would lead to small edge velocities (without changing the gradients), in agreement with experimental observations. The extra force (5) alters the force balance. Inside the $q = 2$ surface generates a large effective viscosity that flattens the profile without changing the gradient outside. Owing to the strong "plasma-mode" coupling, the velocity on the $q = 2$ surface is forced to match the magnetic island velocity, $\omega_\phi = \omega_{\mathrm{MHD}}$. The whole plasma is then dragged by the electromagnetic interaction between the MHD mode and the conducting wall. This scheme is also consistent with the model presented at the end of this chapter.

We will now discuss the toroidal acceleration, or spin-up, following the decay of the MHD mode.

10.1.2 Plasma toroidal spin-up following large MHD event

Usually, excessively large magnetic islands lead to plasma minor disruptions. The abrupt instability almost completely brakes the plasma rotation except at the plasma edge where co-current rotation is observed (green triangles in figure 10.7, large experimental uncertainties are however present in this case).

After the minor disruption, the discharge recovers and quickly reaches a new stationary regime (note that the rotation velocity is positive because the plasma current is negative). The plasma toroidal spin-up is the restoration of the stationary rotation, at much larger timescales (200–300 ms) than for the density and temperatures ($\tau_{T_e} < 20$ ms, $\tau_{T_i} < 50$ ms, $\tau_{n_e} < 70$ ms, see figure 10.6).

The CX velocities shows a growth with a characteristic time constant, $\tau_\phi =$ 100–150 ms in the radial region outside the inversion radius (see figure 10.7b).

A rough estimate of the momentum diffusivity yields $D_\phi = a^2/\tau_\phi \approx 0.5$ m^2/s, which is of the order of the thermal diffusivity, but a hundred times larger than

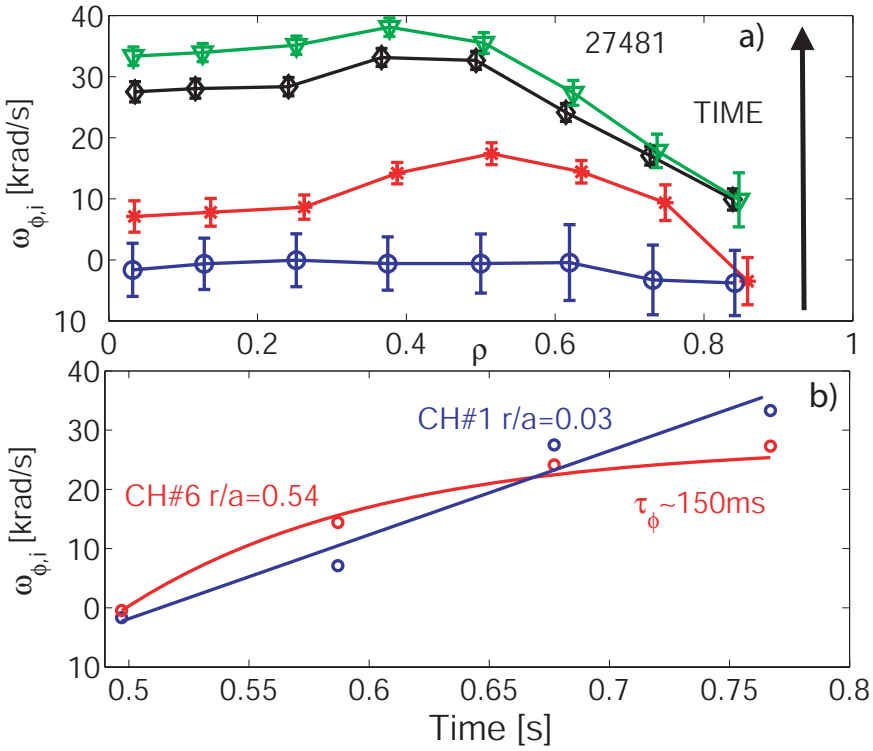

Figure 10.7: *a) Spin-up of the toroidal rotation after a minor disruption. b) Temporal evolution of signals in channels #1 and #6.*

the neoclassical prediction. From the modelling of transient profiles presented in section 10.2 we obtain a more accurate estimate of D_ϕ, obtaining a similar result: the momentum relaxation during rotation spin-up is much faster than what predicted by the neoclassical theory.

We may also note from figure 10.7a that the plasma column commences accelerating in the $0.4 < \rho < 0.8$ region, characterised by large pressure gradients but away from the edge. This will be related to the radial distribution of the momentum source in section 10.2.2).

10.1.3 Core toroidal rotation inversion at high I_p and n_e

A new rotation regime has been discovered by ramping up the plasma density. A detailed description can be found in [138], and the phenomenon is currently under investigation as part of another thesis project [139].

We present here some of the key elements of the transition, which is best observed in a slow case with $\tau_{\text{inv}} \approx 200$ ms sampled at high CXRS rate (20 Hz). An example of such a discharge is shown in figure 10.8a). The rotation profile changes in the central part of the plasma column up to $\rho \sim 0.7$ (dashed green). The subsequent profile (dotted-dashed red) indicates when the core rotation crosses $v_\phi =$ 0 km/s: the central plasma ($\rho < 0.6$) appears to accelerate rigidly in the co-current direction. The outermost CXRS chord ($\rho = 0.85$) shows a negative transient ve-

locity, $\sim$ –7 km/s, as if it is accelerated in the counter-current direction. After the inversion transient, the edge rotation recovers its pre-transition value (very close to 0).

The counter-current acceleration of the outer part of the plasma column during the early phase of the transition is confirmed by high resolution edge measurements, in discharges where the plasma axis is vertically displaced to allow the CXRS diagnostic chords to observe the plasma edge. Figure 10.8b) shows the edge toroidal rotation profile evolution for a discharge with $I_p = 340$ kA: the rotation inversion (at t = 1.15 s) affects the plasma core up to $\rho \sim 0.85$; for more external radii, the rotation for the standard (counter-) and inverted (co-current) regimes is always $\sim$ 0 km/s within the experimental uncertainty. A co-current acceleration of the plasma core > 10 km/s is accompanied by a counter-current acceleration of the plasma edge $\sim$ 7 km/s. The transient edge acceleration may be ascribed to the attempt of conserving the total momentum. Even if on a long time scale the total momentum is not conserved, it may be that on a short time ($\leq$ 50 ms) the momentum is partly conserved. We will propose a possible interpretation in section 10.2.2.b. A higher time resolution measurement is however needed to resolve the phenomenon in greater detail.

10.2 Phenomenological modelling of momentum transport

We describe the phenomenological model of momentum transport, and we apply it to the spin-up and rotation inversion experiments described in sections 10.1.2 and 10.1.3 respectively. We do not aim to a physical description of the phenomenon, but we try to estimate the momentum transport parameters.

10.2.1 Momentum transport modelling: equations and methodology

The time evolution of the velocity profiles has been simulated with a 1D momentum transport model in cylindrical geometry, which includes the conservation of the angular momentum $P_\phi = n_i m_i v_\phi$, a prescription for the radial flux of angular momentum $\Gamma_{r\phi}$, and an appropriate boundary condition,

$$\frac{\partial P}{\partial t} = \frac{1}{r}\frac{d\left(r\Gamma_{r\phi}\right)}{dr} + S_\phi \tag{10.1}$$

$$\Gamma_{r\phi} = \underbrace{D_\phi \frac{dP}{dr}}_{\text{diffusive}} + \underbrace{v_c \frac{r}{a} P}_{\text{convective}} + \underbrace{D_\phi \frac{\alpha n_i m_i}{eB_\theta}\frac{1}{\sqrt{\epsilon_a}}\frac{1}{r}\frac{dT_i}{dr}}_{\text{non-diffusive}} \tag{10.2}$$

$$P_\phi(a,t) = P_{\phi,a}(t), \quad \text{or} \quad \Gamma_{\mathrm{r}\phi}(\mathrm{a},\mathrm{t}) = \Gamma_{\mathrm{r}\phi,\mathrm{a}}(\mathrm{t}) \tag{10.3}$$

with S_ϕ being an arbitrary external momentum source, ϵ the inverse aspect ratio, a the minor radius and α a numerical constant.

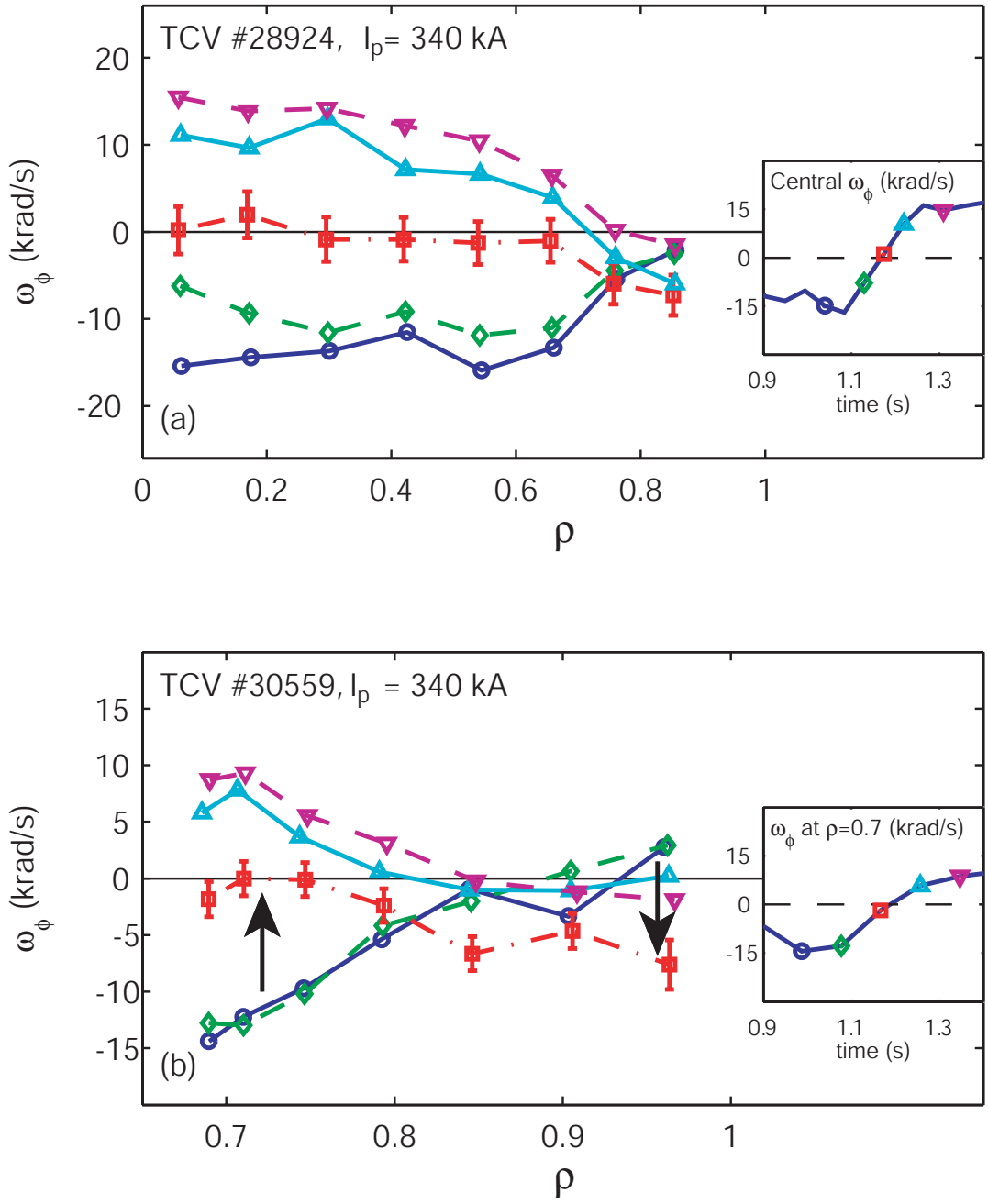

Figure 10.8: *Temporal evolution of the core (a) and edge (b) toroidal velocity profiles across a toroidal rotation inversion. The change in the rotation affects the central part of the plasma and is followed by an opposite change in the edge. After the inversion transient, v_ϕ recovers its former values for $\rho > 0.85$ [138].*

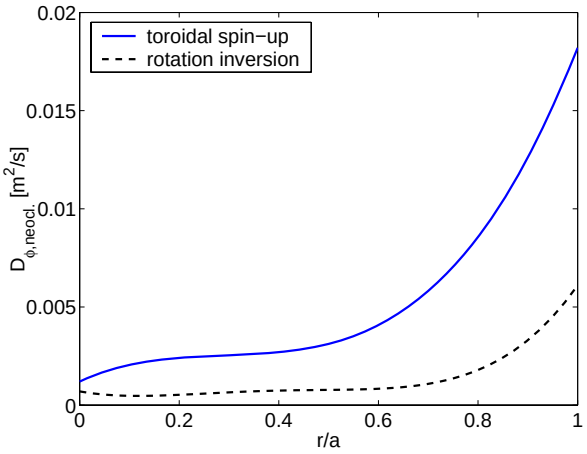

Figure 10.9: *Neoclassical momentum diffusivity profiles for the toroidal spin-up after a minor disruption (solid) and the core rotation inversion (dashed).*

The first term in equation 10.2 represents the momentum diffusion arising from the plasma viscosity, the second is a convective (pinch term) contribution to the flux, and the third is a "non-diffusive" term independent of the angular momentum P_ϕ and proportional to the ion temperature gradient. In general, non-diffusive contributions to the radial flux arise from the non-diagonal part of the transport matrix, and are held responsible for the spontaneous toroidal rotation in tokamaks. Non-diffusive flux may originate from both collisional [131, 130, 129, 125] and turbulent transport processes [133, 134]. Since there is no common agreement on the form of this term, we adopt the empirical form in equation 9.7, specifically formulated for the TCV experiments presented in chapter 9.

In pure Ohmic plasmas, there is no external momentum source S_ϕ. Nevertheless, it is instructive to model the momentum transport adopting an artificial external source and comparing with the results obtained using the third term in equation 10.2. We will drop the distinction between the external source S_ϕ and the non-diffusive part of the momentum flux unless otherwise specified.

In the following we neglect the density gradient, and in equations 10.1 and 10.2 we can replace the angular momentum density P_ϕ with the toroidal velocity v_ϕ.

We use the experimental initial conditions. The pinch velocity $\mathrm{v_c}$ is constant and the diffusion coefficient is normalised to its neoclassical value [125] $D_\phi = \beta D_{neo}$ with $D_{\mathrm{neo}} = 0.1\ q^2 \nu_{ii} \rho_L^2$, where ν_{ii} is the ion collision frequency and ρ_L the ion Larmor radius. Typically D_{neo} monotonically increases from the plasma centre to the edge, as the experimental TCV thermal and particle diffusivity coefficients [65]. D_{neo} may range from 0.0003 m/s^2 at the centre to 0.0300 m/s^2 at the edge in high density, high q discharges. Two examples of D_{neo} profile are shown in figure 10.9.

10.2.1.a External momentum source and boundary conditions

Several combinations of momentum sources and boundary conditions are possible, here we analyse a few simple cases. We use two types of momentum source S_ϕ and of boundary conditions at the plasma edge. Zero radial flux is naturally imposed at the plasma centre as a consequence of the cylindrical geometry, while the boundary condition at the edge are:

1. We fix the rotation velocity dependence, either constant in time, $v_\phi(a,t) = v_a$, or exponentially varied, $v_\phi(a,t) = v_a(1 - e^{-t/\tau_e})$. The free parameter τ_e is used to ensure stationary conditions on the characteristic experimental time of momentum confinement τ_ϕ (see section 10.1.2). The edge velocity v_a may be left as a free parameter to be fitted to the experimental data.

2. Alternatively, we fix the value of the rotation gradient $dv_\phi/dr|_a$ at the edge, or the value of the radial flux of angular momentum $\Gamma_{r\phi}(a,t)$.

The *momentum sources* S_ϕ are:

1. $S_\phi = 0$ everywhere. The spontaneous rotation is generated from the non-diffusive term in equation 10.2. Integrating equation 10.1 one finds that, in absence of an external source, the variation of the total angular momentum $P_{\phi,tot}$ is equal to the radial flux of angular momentum calculated at the plasma edge. Thus, the edge flux must be zero in steady-state condition.

2. Box-like momentum source. By varying the width, d, we can change the localisation of the momentum source. Alternatively a Gaussian shaped source can be used with very similar results. Note that when the source S_ϕ is applied in the simulation, the non-diffusive term in equation 10.2 is turned off.

Examples of source shapes used for the transport modelling are shown in figure 10.10.

10.2.1.b The effect of the sawteeth

The sawtooth activity influences the toroidal rotation by flattening the central profile and must therefore be taken into account. The diffusion term therefore dominates over the other terms in equation 10.2. The simplest method to implement this is given by considering only the diffusive part of the radial momentum flux inside r_{inv}.

10.2.1.c Implementation, tests and method of comparison

For a given set of momentum source and boundary conditions (b.c.), equation 10.1 is numerically integrated using the standard PDE solver in the *Matlab* software package. The free parameters are β, v_c, v_a and τ_e (transport properties and b.c.), or the momentum source α r_1, r_2 and S_ϕ. We look for the set of parameters that minimise,

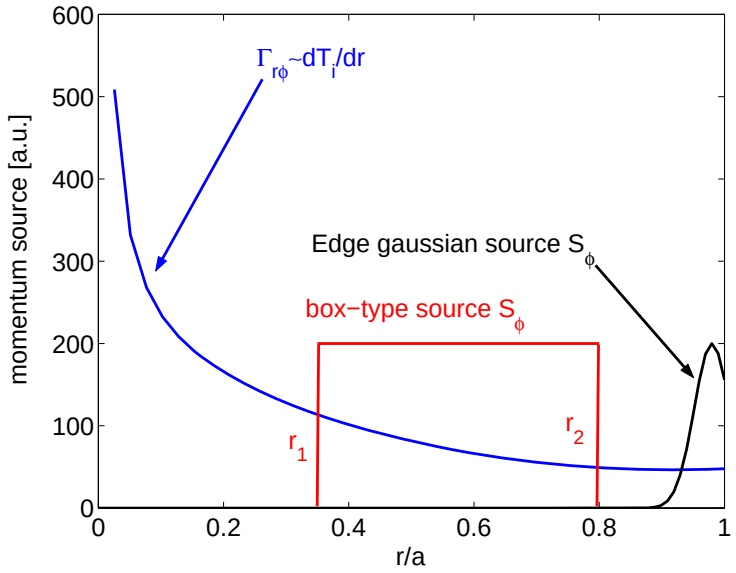

Figure 10.10: *Momentum sources used in the simulation: wide box-like and edge localised Gaussian shaped sources, and non-diffusive radial momentum flux depending on the ion temperature gradient (equation 10.2).*

$$\chi^2 = \sum_i^N (v_{\mathrm{i,exp}} - v_{\mathrm{i,sim}})^2/\sigma_i^2 \tag{10.4}$$

where $v_{\mathrm{i,exp}}$ and $v_{\mathrm{i,sim}}$ are the experimental and simulated toroidal velocity respectively, and σ_i is the uncertainty on each measurement. Typically 4–5 free parameters are used in a simulation.

For the sake of simplicity, we will admit that the torque pushing the plasma "turns on" instantaneously after the minor disruption, and remains constant thereafter. The transport parameters D_ϕ, $\mathrm{v_c}$ also do not evolve. The rotation profile will then evolve to a new steady state according to equation 10.1 and to the applied momentum source and boundary condition.

The implementation of the numerical model has been tested by comparing the numerical solutions with well-known analytical solutions available when the diffusion equation is separable. In particular we have,

$$v_\phi(r,t) = e^{-t/\tau_\phi} \cdot e^{-v_c r^2/2aD_\phi} M\left(\frac{a}{2v_c\tau_\phi}; 1; \frac{v_c r^2}{2aD_\phi}\right) \tag{10.5}$$

$$\text{if} \quad S_\phi = 0$$

$$v_\phi(r,t) = \left(1 - e^{-t/\tau_\phi}\right) \cdot e^{-v_c r^2/2aD_\phi} M\left(\frac{a}{2v_c\tau_\phi}; 1; \frac{v_c r^2}{2aD_\phi}\right) \tag{10.6}$$

$$\text{if} \quad S_\phi(r) = v_\phi(r,\infty)/\tau_\phi$$

where $M(a;b;Z)$ are the so-called Kummer functions [140]. For these solutions only the diffusive and convective terms are considered in equation 10.2, and D_ϕ

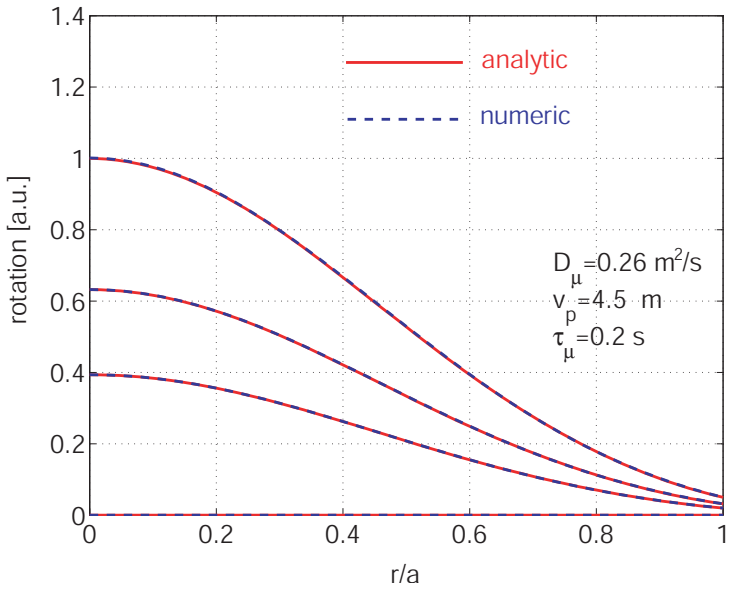

Figure 10.11: *Test of the model implementation against analytical solutions of the diffusion equation (eq. 10.5).*

and v_c are constant. The numerical solution is very accurate as seen in the example in figure 10.11.

10.2.2 Modelling of the toroidal plasma spin up and core rotation inversion

The evolution of the rotation profiles during the toroidal spin-up (figure 10.7) and rotation inversion (figure 10.8a) are modelled using equation 10.1 together with several combinations of momentum sources and boundary conditions. We attempt to address the following issues:

1. Estimation of the momentum diffusivity and comparison with neoclassical theory.

2. Estimation of the distribution of the spontaneous momentum source. In particular, is an edge localised momentum source consistent with the experiment?

3. Local and total angular momentum conservation during the transient.

The conservation of the total angular momentum may be implemented by constraining the edge radial momentum flux to match the total momentum input, $\Gamma_{r\phi}(a) = \int_V dV S_\phi$, at any time. By relaxing this condition and imposing $\Gamma_{r\phi}(a) = \int_V dV S_\phi (1 - e^{-t/\tau_e})$ the generation of total momentum is permitted.

Table 10.1: *Summary of the transport, source and boundary condition best-fit parameters of the simulations of toroidal spin-up in figure 10.12.*

source/b.c.	χ^2	$D/D_{\rm neo}$	v_c [m/s]	α;r_1	$S_\phi; r_1; r_2$	τ_e [s]
box-like/v_a	23	14	0	0	375;0.33;0.74	0.9
$dT_i/dr/v_a$	22.4	15	0	-1.1;0.4	0	0.7
$dT_i/dr/\Gamma_{r\phi}$	25.3	13.4	0	-1.22;0.4	0	0.14
edge/v_a	25.1	23	2.5	0	$3.8 \cdot 10^4$;0.4	

10.2.2.a Simulations of the toroidal spin-up

Examples of spin-up simulations are shown in figures 10.12(a-b-c-d) together with the adopted momentum source, whilst the best-fit estimates of the transport coefficients, source and boundary parameters are summarised in table 10.1. The χ^2-test at 95% confidence level is positive for all simulations.

The main results are:

- For all source types and boundary conditions, the best-fit momentum diffusivity is larger than the neoclassical value, with D_ϕ/D_{neo} ranging from 13 to 23. Therefore the momentum transport during plasma spin-up in this TCV Ohmic plasma is anomalous.

- The assumption of an edge localised momentum source is to be rejected since it directly leads to large edge velocities, 7–8 km/s for $r/a > 0.9$ (see figure 10.12d), which are inconsistent with the edge rotation measurements (see figure 9.8).

- A comparison of figures 10.12a) and 10.12b) shows that both a simple box-type momentum source and the non-diffusive flux may equally well reproduce the experimental data.

- Satisfactory results may be obtained using fixed $v(a,t) = v_0$ (figure 10.12d) or time decaying (figure 10.12a-b) $v_\phi(a,t) = v_0 e^{-t/\tau_e}$. Also a time varying boundary edge radial flux provides a good match to the experimental data. On the contrary, the exact conservation of the total angular momentum leads to large and negative edge velocities (dotted-dashed line in figure 10.12c). A dissipation, probably localised at the plasma edge, is needed to change the total angular momentum.

To summarise, the momentum radial transport during the plasma spin-up observed in TCV Ohmic L-mode plasmas is faster than what is predicted by the neoclassical theory. The toroidal torque is likely to be distributed in the outer part of the minor radius where the largest pressure gradients are present and not at the far edge. The edge friction plays an important role in determining the value of the final rotation velocities.

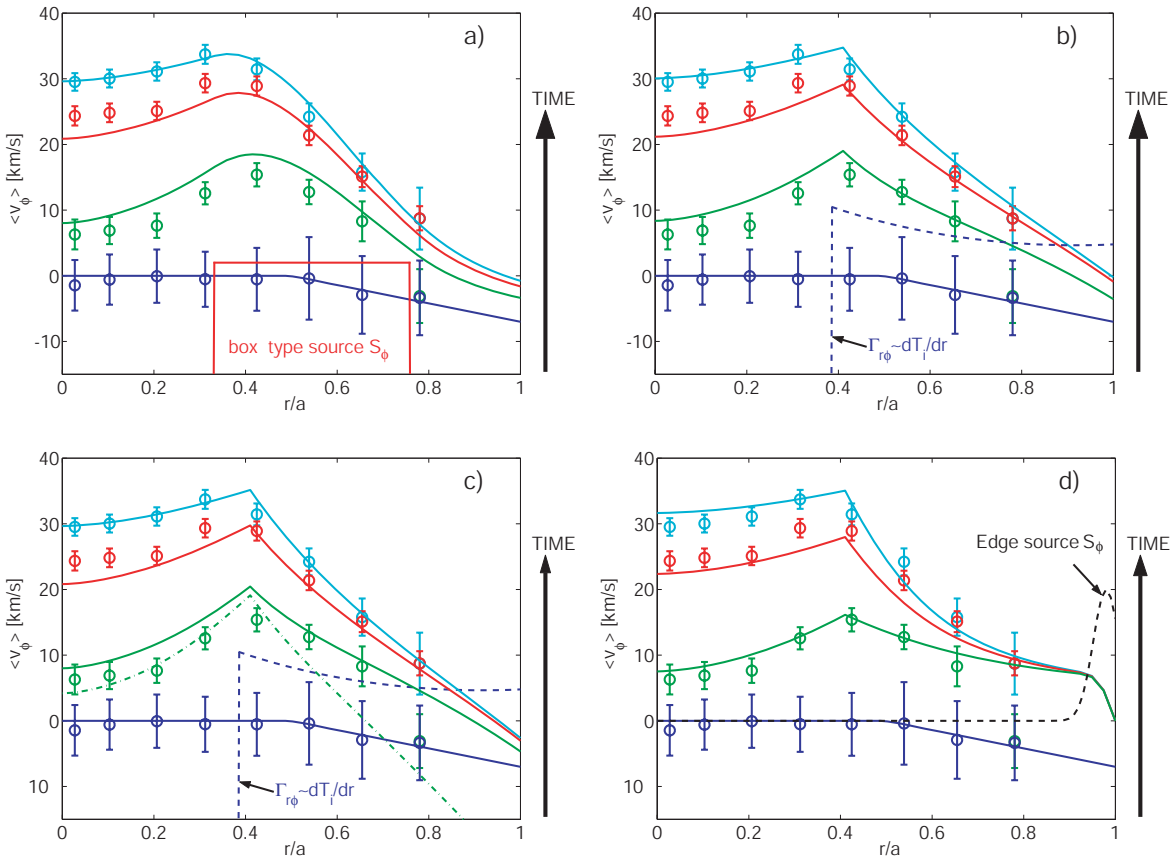

Figure 10.12: *Comparison of four simulations of the plasma spin-up. The momentum applied is indicated with a dashed line. The boundary conditions are:* $v(a,t) = v_0 e^{-t/\tau_e}$ *(a-b),* $\Gamma_{r\phi}(a) = \int_V dV S_\phi (1 - e^{-t/\tau_e})$ *(c),* $v(a,t) = v_0$ *(d).*

10.2.2.b Simulation of the core rotation inversion

To simulate the momentum variation (figure 10.8), we need to properly choose the initial condition $v_\phi(t_{\rm start})$. We estimate 1.09 s $< t_{\rm start} <$ 1.13 s. We average the two rotation profiles in this time interval, and use the result as the initial condition in the simulation.

An obvious requirements in order to simulate the edge momentum variation in $0.75 < \rho < 1$ is a freedom in the choice of the velocity at the boundary. We may however use a boundary condition of the type $\Gamma_{r\phi}(a,t) = \int_V dV S_\phi (1 - e^{-t/\tau_e})$. The stationary condition is assured by cancelling the total momentum input $\int_V dV S_\phi$ for $t \gg \tau_e$.

Alternatively we simulate the rotation inversion by including an edge friction term $F = -\nu v_\phi$ in equation 10.1, and we use the boundary condition $\Gamma_{r\phi}(a,t) = \int_V dV S_\phi$. We use as a momentum source a box-type function in $0 < \rho < 0.75$.

The simulation are shown in figure 10.13, while the best-fit transport coefficient, source and boundary condition parameters are given in table 10.2. The χ^2-test is positive at 95% confidence level.

Table 10.2: *Summary of the best-fit transport coefficient, source and boundary condition parameters for the simulation of the rotation inversion.*

source/b.c.	χ^2	D/D_{neo}	$S_\phi - r_1 - r_2$	τ_e [s]	ν [s^{-1}]
box-like/$\Gamma_{r\phi}$	21.2	77	209;0;0.75	0.1	0
box-like/$\Gamma_{r\phi}$	23.2	150	253;0;0.75	0	292

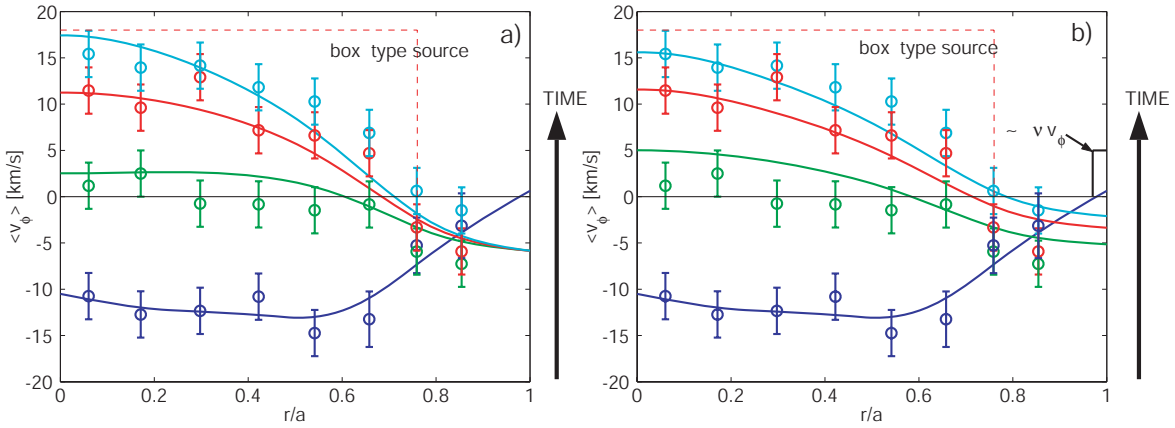

Figure 10.13: *Comparison of two rotation inversion transport models using a box-type momentum source located in* $0 < r/a < 0.75$. *a) No edge friction and boundary condition* $\Gamma_{r\phi}(a,t) = \int_V dV S_\phi(1 - e^{-t/\tau_e})$. *b) Edge friction* $F = -\nu v_\phi$ *and boundary condition* $\Gamma_{r\phi}(a,t) = \int_V dV S_\phi$.

The main results are:

- The estimated diffusivities are about two order of magnitudes larger than the neoclassical values, further supporting the anomalous nature of the momentum transport.
- The momentum source need to extend inside the inversion radius and close to the magnetic axis. The inverted rotation profile is generally slightly more peaked than in normal regime. The flattening of the sawtooth is however less effective. The peaking of the inverted profile is not understood yet, and beyond the scope of this thesis.
- The counter-current acceleration of the edge plasma is achieved by partial and total momentum conservation of the total angular momentum. However, in order to restore a small value of $v_\phi(r = a)$, some momentum loss at the plasma boundary is required.

10.3 Final remarks and conclusions

Various momentum transport phenomena have been observed in TCV Ohmic L-mode plasma. Some of them are related with the MHD activity (magnetic island)

that is observed to flatten the rotation profile up to the radius of the unstable resonant flux surface. If the magnetic island interacts with the conducting wall, the plasma close to the unstable surface rotates at the same frequency as the MHD mode. The plasma rotation appears to brake as a consequence of the rapid and dramatic loss of confinement.

Two cases of dramatic momentum variations have been analysed. In the first case, the plasma spin-up is followed by a minor disruption. In the second case, a spontaneous inversion in the core toroidal rotation is observed. Remarkably, the abrupt change in the plasma momentum is not accompanied by a similar change in the thermal or particle transport [138].

Despite their rather different features, both phenomena can be satisfactorily simulated with a phenomenological transport model that finds momentum diffusivities up to hundred times larger than the neoclassical predictions. This reveals the anomalous nature of the momentum transport. Even if many other successful

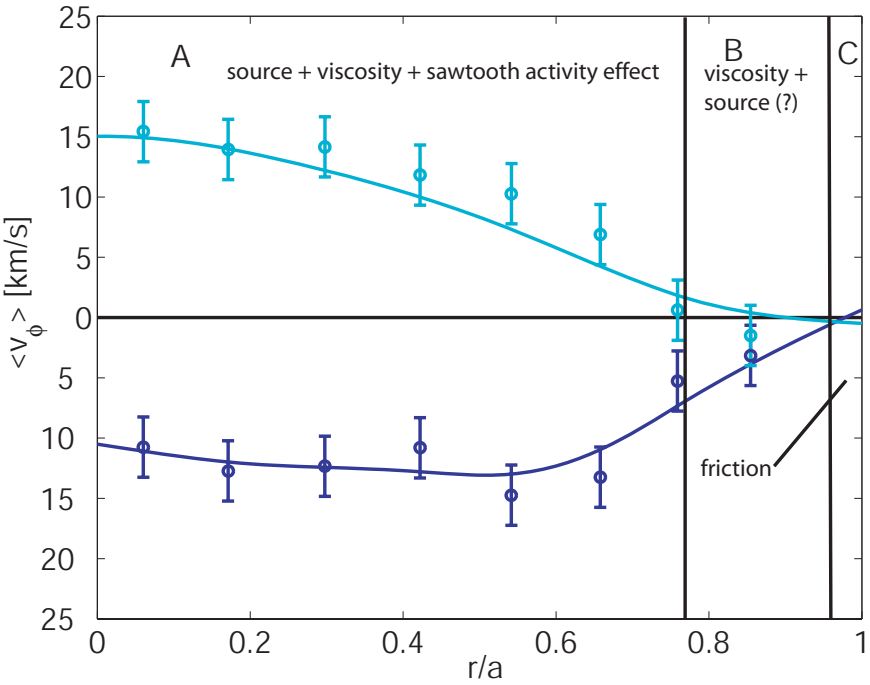

Figure 10.14: *Plasma regions characterised by different rotation properties.*

models could be thought of, with our model we are able to reproduce the experimental data with a simple scheme and a minimal number of forces acting on the plasma:

1. A momentum drive, source or sink or a non-diffusive flux of momentum. The drive acts in the core of the plasma (region A in figure 10.3). It may drive positive or negative momenta, It leads to a rotation profile characterised by $(dv_\phi/dr)/v_\phi < 0$.

2. A viscous force. The balance of the driving force and the viscous force define the stationary rotation gradients.

3. A friction which tends to reduce the edge velocity (region C) and dissipate momentum.

In region (B) the rotation velocity may invert direction, either spontaneously or forced by MHD modes. Both positive and negative $(dv_\phi/dt)/v_\phi$ are possible.

Summary and conclusions

In this thesis we explore two of the many interesting subjects in tokamak plasma physics. In the first part, we study the magnetohydrodynamic (MHD) stability for a wide range of parameters of TCV plasmas. In the second part, we report on the properties of spontaneous plasma toroidal rotation.

For the MHD stability analysis, we take advantage of TCV exceptional shaping capabilities, flexible electron heating, and current drive system to study plasmas with high elongation, high positive and negative triangularity, and unconventional current density profile. Our analysis reveals new features of instabilities commonly observed in tokamak devices. Such features may have important effects on the optimisation of future plasma performances, and are of interest for the community of experimental and theoretical fusion physicist.

The perturbations of physical quantities, such as the edge magnetic field and the soft X-ray emission, provide the information on the location and radial extent of the MHD instabilities. Techniques of numerical data analysis, such as Fast Fourier Transform and Singular Decomposition Value, are applied to extract coherent mode structures. Identifying the nature of the different modes and relating their occurrence with the plasma parameters allow us to develop strategies to modify or suppress such modes and thus improve plasma stability. TCV experiments point out that MHD instabilities strongly depend on the plasma shape as well as current density and pressure profile.

In TCV, plasma shaping is found to stabilise modes and disruptions commonly observed during the current rise in circular plasmas. With a reduced plasma shaping, bursts of low (m, n) MHD modes are observed when flux surfaces with integer q_a value (q_a =3, 4, 5) approach and cross the plasma boundary. With $q_a \sim 3$ MHD perturbations may become too large and lead to plasma disruption. However the mode structure was poorly known.

Experiments with slow plasma current rise allow us to separate the destabilising effect resulting from the transients of current profiles (skin effect) from the stability of the steady-state plasma equilibrium profiles. The evolution of the mode structure reveals a complex interaction between modes resonant at different flux surfaces. We find that the disruptions are always preceded by growing perturbations with coupled $m/n = 3/1$ and $m/n = 2/1$ modes. On the basis of the MHD

theory of coupled modes [47, 12], our calculations of the tearing stability under the TCV conditions indicate the toroidal mode coupling as the main responsible for the growth of large magnetic islands.

The toroidal mode coupling instability can be prevented by appropriate plasma shaping. Even small elongations ($\kappa \sim 1.4$) and positive or negative triangularities ($|\delta| > 0.3$) have strong beneficial effects in suppressing the perturbations and thus avoiding the disruptions. Plasma shaping induces three different mechanisms that stabilise the $2/1$ tearing mode. First, the modification of the equilibrium current density profile improves the intrinsic cylindrical Δ' plasma stability against tearing modes. Second, the conducting wall has a stabilising effect, especially effective at large plasma elongations. Third, the plasma elongation and triangularity induce the stabilising coupling respectively with the vacuum $q = 4$ and $q = 5$ resonant surfaces. Despite the impossibility to determine the relative importance of the various mechanisms, we experimentally tested the effect of the conducting wall by varying the major radius of the magnetic axis, the plasma minor radius or the vertical position of the plasma.

The strong dependence of the plasma stability on the current density is highlighted by studying the sawtooth oscillations. In presence of off-axis heating and high density, the current density profile strongly flattens creating a region of low magnetic shear around a small sized $q = 1$ surface. In highly elongated discharges with flat current profiles, the sawteeth are observed to disappear and to be replaced by a continuous MHD mode. Magnetic and soft X-ray measurements show a mode structure with three ($m/n = 1/1, 2/2, 3/3$) poloidal/toroidal Fourier harmonics resonant on the $q = 1$ surface. Linear MHD stability calculations show that the combination of the low shear and small $q = 1$ radius stabilise the ideal and resistive internal kink mode in spite of the larger plasma elongation. Assuming linear theory is applicable in this case, this would explain the sawtooth disappearance. However, the presence saturated continuous mode may indicate that the internal kink is already in the non-linear phase. Alternatively, the flat current profile may destabilise a tearing mode and inhibit the sawtooth crashes.

Pressure profiles with large and localised gradients have negative effects on the β limit in TCV eITB discharges, in which a variety of MHD modes have been observed. Again, we provide a characterisation of these modes.

Partly pressure-driven neoclassical tearing modes ($m/n = 2/1$) degrade the global confinement by destroying the internal transport barrier. Stationary $q = 2$ pseudo-sawteeth are often observed in low or weakly reversed shear plasmas. They usually limit the achievable β without destroying the transport barrier. The tearing or sawtooth-like character of the $q = 2$ MHD activity is thought to be related with the ideal or resistive regime of the instability which ultimately depends on the plasma beta. Internal localised and/or disruptive modes are observed in ITB plasma with strong reverse shear and large β_N. These modes present a fast growth rate consistent with an ideal MHD nature, and are usually avoided by reducing the heating power and hence the plasma pressure. The maximum achievable β_N is found to strongly decrease with the peaking of the electron pressure

profile, as predicted by the theoretical beta-limit in eITB plasmas [10]. This result confirms that a low n low m ideal infernal mode is the main responsible for the MHD activity in TCV eITB plasmas.

An optimal power deposition, which broadens the pressure profile, is an essential ingredient to avoid excessively large peaking in ITB plasmas and achieve stable, high β_N, discharges.

The plasma rotation is believed to have an important influence on the plasma stability and confinement. We report on the experimental study of spontaneous toroidal rotation and momentum transport properties in plasmas with negligible momentum input. Today's tokamak are strongly NBI heated, and thus present a large externally driven toroidal rotation which masks the spontaneous rotation. Future large tokamaks will however operate in a regime of low external momentum input, therefore the understanding and modelling of spontaneous rotation has recently driven a large interest in the plasma physicist community. The presented experimental represent part of the effort needed to build reliable theoretical models of spontaneous rotation.

Stationary and non-stationary toroidal rotation experiments in Ohmic L-mode plasmas have been performed. The properties of the toroidal carbon impurity rotation $v_{\phi,C}$ in limited plasmas are studied in stationary condition over a wide range of plasma parameters. The observed carbon velocity is of the order of the deuterium diamagnetic drift velocity and up to 1/5 of the deuterium thermal velocity. It is directed in opposite direction to the plasma current, and its profile reverses when reversing the plasma current. The angular velocity profile is found to be flat or hollow inside the sawtooth inversion radius and linearly decreasing toward the plasma edge. The flattening effect of the sawtooth activity is furthermore demonstrated in current profile tailoring experiments using ECRH. The rotation profile is observed to peak consistently with the modified sawtooth inversion radius. The plasma edge velocity is measured with high spatial resolution indicating that, close to the limiter, the rotation is close to zero or even slightly co-current. The experimental evidence of low edge rotation suggests that the angular momentum can not simply diffuse to the plasma interior from an edge source. We find that for quasi-circular plasmas the maximum carbon velocity scales as $v_{\phi,\max} \propto T_i/I_p$ over a significant range of plasma densities ($1.4< n_e <3.7{\cdot}10^{19}$ m^{-3}) and edge safety factors ($3.2< q_a <12$). The neoclassical theory of toroidal rotation in the low v_ϕ/v_{th} limit quantitatively and qualitatively disagrees with the experimental observation. An alternative empirical equation for the angular momentum flux, able to reproduce the measured stationary rotation profile outside the sawtooth inversion radius, is given.

The edge magnetic configuration is expected to significantly change the plasma rotation properties [141]. The characterisation of the toroidal and poloidal rotation in Ohmic and ECRH H-mode plasmas is also of fundamental importance. So far, only very preliminary rotation measurements have been obtained in these regimes. We therefore suggest a future systematic scan of basic plasma parameters in different regimes. Such measurements will hopefully provide a better

understanding of momentum generation and of the spontaneous component of toroidal rotation.

Relaxations in the toroidal velocity are commonly observed in TCV Ohmic plasmas. Large magnetic islands cause large losses of angular momentum by flattening the rotation profile and braking the plasma. The stationary angular velocity profile is restored in a typical timescale of 100–200 ms after the disappearance of the MHD mode. These observations provide experimental evidence of the spontaneous torque spinning the plasma in tokamak devices.

A phenomenological momentum transport model is employed to simulate the rotation profiles during toroidal spin-up and rotation inversion observed in Ohmic plasmas at high plasma current above a certain density threshold. The simulations well reproduce the experimental features. Transport coefficients, such as the momentum diffusivity D_ϕ are inferred and compared with neoclassical predictions. Three main results were obtained. First, it is found that the experimental D_ϕ is from 10 to more than 100 times larger that the neoclassical predictions. This result extends the observation of anomalous momentum transport found H-mode plasmas [101, 102, 115]. Second, assuming that the total angular momentum is conserved on a short time scale the simulations of the rotation inversion suggest the presence an edge friction needed to account for stationary rotation the edge. Third, the momentum source distribution must extend radially up to the core plasma and cannot be only localised at the plasma edge.

Bibliography

[1] *Energy and World Energy Production and Consumption Statistics*, http://energy.cr.usgs.gov/.

[2] *Association for the Study of Peak Oil&Gas*, http://www.peakoil.net/.

[3] *Hubbert Peak of Oil Production*, http://www.hubbertpeak.com/.

[4] J. Wesson, *Tokamaks*, International series of monograph in physics, Oxford University Press, Oxford, UK, 2004.

[5] *La fusion: une source d'énergie quasiment illimitée*, http://www-fusion-magnetique.cea.fr/.

[6] R. D. Hazeltine, J. D. Meiss, *Plasma Confinement*, Vol. 3 and 4 of *Monographs on Particle Physics, Nuclear Physics and Cosmology*, Cambridge University Press, Cambridge, UK, 1996.

[7] G. Bateman, *MHD instabilities*, MIT Press, Cambridge, Massachusetts, USA, 1978.

[8] I. H. Hutchinson, *Principles of Plasma Diagnostics*, Cambridge Univ. Press, Cambridge, 1987.

[9] M.N. Bussac et al., *Internal kink modes in toroidal plasmas with circular cross sections*, Phys. Rev. Lett. 35 (24) (1975) 1638.

[10] A. Martynov, *Ideal MHD stability limit of tokamak plasmas with moderate and low aspect ratio*, Ph.D. thesis, Ecole Polytechnique Fédérale de Lausanne, thèse EPFL n. 3218 (2005).

[11] V. D. Shafranov, Sov. Phys. Tech. Phys 15 (1970) 175.

[12] R. Fitzpatrick et al., *Stability of coupled tearing modes in tokamaks*, Nuclear Fusion 33 (10) (1993) 1533–76.

[13] P. H. Rutherford, *Nonlinear growth of the tearing mode*, Phys. Fluid 15 (11) (1973) 1903.

[14] R.B. White et al., *Saturation of the tearing mode*, Phys. Fluid 20 (5) (1977) 800.

[15] O. Sauter et al., *Beta limits in long-pulse tokamak discharges*, Phys. Plasmas 4 (1997) 1654.

[16] G. Arnoux, *Chauffage de plasma par ondes électromagnétiques à la troisème harmonique de la fréquence cyclotron des électrons dans le tokamak TCV*, Ph.D. thesis, Ecole Polytechnique Fédérale de Lausanne, thèse EPFL n. 3401 (2006).

[17] I. Furno, *Fast transient transport phenomena measured by soft X-ray emission in TCV tokamak plamas*, Ph.D. thesis, Ecole Polytechnique Fédérale de Lausanne (2001, LPR 512/01).

[18] A.N. Karpushov, *Upgrade of the diagnostic neutral beam injector for the TCV tokamak*, Fusion Eng. and Design 66-68 (2003) 899–904.

[19] P. Bosshard, *Confinement ionique dans le tokamak TCV mesuré pas spectroscopie d'échange de charge*, Ph.D. thesis, Ecole Polytechnique Fédérale de Lausanne, thèse EPFL n.2723 (2003).

[20] F. Hofmann, G. Tonetti, *Tokamak equilibrium reconstruction using Faraday rotation measurements*, Nuclear Fusion 28 (10) (1988) 1871.

[21] M. Schittenhelm, H. Zohm, *Analysis of coupled MHD modes with Mirnov probes in ASDEX Upgrade*, Nuclear Fusion 37 (9) (1997) 1255–1270.

[22] W. H. Press et al., *Numerical Recipes in Fortran: the art of scientific computing*, Cambridge University Press, Cambridge, Massachusetts, USA, 1992.

[23] H. Reimerdes, *MHD stability limit in the TCV tokamak*, Ph.D. thesis, Ecole Polytechnique Fédérale de Lausanne, thèse n.2399 (2001).

[24] O. Kluber et al., *MHD mode structure and propagation in the ASDEX tokamak*, Nuclear Fusion 31 (5) (1991) 907.

[25] V.G. Merezhkin et al., *Structure of the magnetic field perturbation in the disruptive instability in the T-6 tokamak*, Sov. J. Plasma Phys. 4 (1978) 152.

[26] D. Testa, *Diagnosis and study of Alfvén eigenmodes stability in JET*, Rev. Scient. Instr. 74 (3) (2003) 1694.

[27] J.S. Kim et al., *Phase folding of magnetic signals in tokamak plasmas*, Plasma Physics and Controlled Fusion 43 (11) (2001) 1593–1613.

[28] T. Dudok de Witt et al., *The biorthogonal decomposition as a tool for investigating fluctuations in plasmas*, Physics of Plasmas 1 (10) (1994) 3288–3300.

[29] I. Furno et al., *Understanding sawtooth activity during intense electron cyclotron heating experiments on TCV*, Nuclear Fusion 41 (2001) 403.

[30] A. Letsch et al., *Incomplete reconnection in sawtooth crashes in ASDEX Upgrade*, Nucl. Fusion 42 (2002) 1055.

[31] J.P. Meskat et al., *Analysis of the structure of neoclassical tearing modes in ASDEX Upgrade*, Plasma Physics and Controlled Fusion 43 (10) (2001) 1325–1332.

[32] P. C. de Vries et al., *Temperature profile perturbations due to magnetic islands in TEXTOR*, Plasma Physics and Controlled Fusion 39 (3) (1997) 439–451.

[33] P.C. de Vries et al., *Density profile peaking inside m/n=2/1 magnetic islands in TEXTOR-94*, Nuclear Fusion 37 (11) (1997) 1641–1646.

[34] J. A. Wesson et al., *Disruptions in JET*, Nuclear Fusion 29 (4) (1989) 641.

[35] H. P. Furth et al., Phys. of Fluids 6 (1963) 459–484.

[36] A. D. Cheetham et al., *Pre-disruption MHD activity in the LT-4 tokamak*, Nuclear Fusion 27 (5) (1987) 693.

[37] Z.A. Pietrzyk et al., *Disruptions in the TCA tokamak*, Nuclear Fusion 32 (10) (1992) 5.

[38] S. Turlur, *Etude experimentale de l'activité M.H.D. associé au mode m=2, n=1 dans le tokamak Tore Supra*, Ph.D. thesis, Université de Paris-Sud U.F.R. Scientifique D'Orsay (1996).

[39] R. Fitzpatrick, R. Hastie, T. Martin, C. Roach, *Stability of coupled tearing modes in tokamaks*, Nuclear Fusion 33 (10) (1993) 1533.

[40] C. Angioni, *Private communication* (2002).

[41] W. A. Waddell et al., *Mechanism for Major Disruptions in Tokamaks*, Phys. Rev. Lett. 41 (20) (1978) 1386–1389.

[42] R.M. Coelho et al., *Nonlinear coupling of rotating magnetic island triplets*, Physics of Plasmas 6 (4) (1999) 1194–1202.

[43] M. Nave, J. Wesson, *Mode locking in Tokamaks*, Nuclear Fusion 30 (12) (1990) 2575–2583.

[44] E. Lazzaro et al., *Dynamics of Tearing Modes during Strong Electron Cyclotron Heating on the FTU Tokamak*, Physical Review Letters 84 (26) (2000) 6038–6041.

[45] M.F.F. Nave et al., *The influence of mode coupling on the non-linear evolution of tearing modes*, Eur. Phys. J. D 8 (2000) 287.

[46] H. Reimerdes et al., *Effect of triangular and elongated plasma shape on the sawtooth stability*, Plasma Phys. Control. Fusion 42 (2000) 629–639.

[47] S.C. Cowley and R.J. Hastie, *Electron diamagnetism and toroidal coupling of tearing modes*, Phys. Fluids 31 (3) (1988) 426.

[48] A. Pletzer, A. Bondeson, R. L. Dewar, *Linear Stability of Resistive MHD Modes: Axisymmetric Toroidal Computation of the Outer Region Matching Data*, Journal of Computational Physics 115 (3) (1994) 530.

[49] Y. Camenen et al., *Electron heat transport in shaped TCV L-mode plasmas*, Plasma Phys. and Control. Fusion 47 (2005) 1971–1987.

[50] J.M. Moret et al., *Influence of Plasma Shape on Transport in the TCV tokamak*, Phys. Rev. Lett. 79 (11) (1997) 2057.

[51] L. Lao and et al., Nuclear Fusion 25 (1985) 1321.

[52] S. V. Goeler, W. Stodiek, N. Sauthoff., *Studies of internal disruption and m=1 oscillation in tokamak diascharges with soft X-ray techniques*, Phys. Rev. Lett. 33 (1974) 1201–1203.

[53] H. Weisen et al., *Effect of plasma shape on confinement and MHD behaviour in the TCV tokamak*, Nuclear Fusion 37 (12) (1997) 1741–1758.

[54] B. B. Kadomtsev, Sov. J. Plasma Phys. 1 (4) (1975) 295.

[55] P.A. Duperrex et al., *Global sawtooth instability measured by magnetic coils in the JET tokamak*, Nuclear Fusion 32 (7) (1992) 1161.

[56] F. Hofmann et al., *Experimental and Theoretical Stability Limits of Highly Elongated Tokamak Plasmas*, Phys. Rev. Lett. 81 (1998) 2918–2921.

[57] F Hohmann et al., *Stability and energy confinement of highly elongated plasmas in TCV*, Plasma Physics and Controlled Fusion 43 (12A) (2001) A161–A173.
URL `http://stacks.iop.org/0741-3335/43/A161`

[58] A. Pochelon et al., *Plasma shape effects on sawtooth/internal kink stability and plasma shaping using electron cyclotron wave current profile tailoring in TCV*, Nuclear Fusion 41 (2001) 1663–1669.

[59] Y. Camenen et al., *Current profile tailoring with far off-axis ECH power deposition in TCV elongation experiments*, in: Proc. of 12th Joint Workshop on Electron Cyclotron Emission and Electron Cyclotron Heating, Aix-en-Provence, France, 2002, p. 407.

[60] A. Pochelon et al., in: 19th IAEA FEC, Oct. 2002, Lyon, France, IAEA-CN-94/EX/P5-14, 2002.

[61] J. A. Wesson, *Snakes*, Plasma Physics and Controlled Fusion 37 (4) (1995) 337–346.

[62] G. Turri, et al., *Magnetic Reconnections in MAST*, in: 31st EPS Conference on Plasma Phys. London, 28 June - 2 July 2004 ECA Vol.28G, P-4.192 (2004), 2004.

[63] F. Porcelli, D. Boucher and M. Rosenbluth, *Model for the sawtooth period and amplitude*, Plasma Phys. Control Fusion 38 (1996) 2163.

[64] O. Sauter and al., *Sawtooth period simulationof TCV discharges*, in: E. S. J. W. Connor, J. Vaclavik (Eds.), "Theory of Fusion Plasmas", Proc. of joint Varenna-Lausanne Int. Workshop (Varenna, 1998), 1998, p. 403.

[65] C. Angioni, *Modelling of electron transport and of sawtooth activity in tokamaks*, Ph.D. thesis, Ecole Polytechnique Fédérale de Lausanne, thèse EPFL n.2479 (2001).

[66] C. Angioni et al., *Neutral beam stabilization of sawtooth oscillations in JET*, Plasma Physics and Controlled Fusion 44 (2) (2002) 205–222.

[67] D. Boucher and P.H. Rebut, in: V. . (IAEA (Ed.), Proceedings of the IAEA Technical Conference on Advances in Simulation and Modeling in Thermonuclear Plasmas, Montreal, 1992, p. 142.

[68] L. Degtyarev, A. Martynov, S. Medvedev and et al., Comput. Phys. Commun. 103 (1997) 10.

[69] S. Migliuolo, F. Pegoraro, F. Porcelli, *Stabilization of collisional drift-tearing modes at the breakdown of the constant-Psi approximation*, Physics of Fluids B: Plasma Physics 3 (6) (1991) 1338–1345.

[70] F. Pegoraro, F. Porcelli, T. J. Schep, *Internal kink modes in the ion-kinetic regime*, Physics of Fluids B: Plasma Physics 1 (2) (1989) 364–374.

[71] F.M. Levinton et al., *Stabilization and onset of sawteeth in TFTR*, Phys. Rev. Lett. 72 (1994) 2895–2898.

[72] A. Martynov, J. P. Graves, O. Sauter, *The stability of the ideal internal kink mode in realistic tokamak geometry*, Plasma Physics and Controlled Fusion 47 (10) (2005) 1743–1762.

[73] A. Martynov and O. Sauter, *Shape and Aspect Ratio Effects on the Ideal Internal Kink Mode*, in: "Theory of Fusion Plasmas", Proc. of joint Varenna-Lausanne Int. Workshop (Varenna, 2001), 2002.

[74] C. Angioni et al. , *Effects of localized electron heating and current drive on the sawtooth period*, Nuclear Fusion 43 (2003) 455–468.

[75] K. Matsuda, IEEE Trans. Plasma Sci. 17 (1989) 6.

[76] F. Wagner et al., Phys. Rev. Lett. 49 (1982) 1408.

[77] M. Hugor et al., *Shear reversal and MHD activity during pellet enhanced performance pulses in JET*, Nuclear Fusion 32 (1992) 33.

[78] F. M. Levinton et al., *Improved confinement with reverse magnetic shear in TFTR*, Phys. Rev. Lett. 75 (1995) 4417.

[79] E. J. Strait et al., *Enhanced confinement and stability in DIII-D discharges with reversed magnetic shear*, Phys. Rev. Lett. 75 (1995) 4421.

[80] R. C. Wolf, *Internal transport barrier in tokamaks plasmas*, Plasma Phys. and Control. Fusion 45 (2003) R1–R45.

[81] K. Burrell et al., Phys. Plasmas 4 (1997) 1499.

[82] Z. A. P. et al., *Long-Pulse Improved Central Electron Confinement in the TCV Tokamak with Electron Cyclotron Heating and Current Drive*, Phys. Rev. Lett. 86 (8) (2001) 1530.

[83] S. Coda et al., *High-bootstrap, noninductively sustained electron internal transport barriers in the Tokamak à Configuration Variable*, Phys. of Plasmas 12 (2005) 056124.

[84] O.Sauter and al., *Electron ITB In Fully Non-Inductive Reverse Shear Scenarios*, in: 29th EPS Conference on Plasma Phys. and Contr. Fusion Montreux, 17-21 June 2002 ECA Vol. 26B, P-2.087, 2002.

[85] T P Goodman, R Behn, Y Camenen, S Coda, E Fable, M A Henderson, P Nikkola, J Rossel, O Sauter, A Scarabosio, C Zucca, and the TCV team, *Safety factor profile requirements for electron ITB formation in TCV*, Plasma Phys. Control. Fusion 47 (2005) B107–B120.

[86] R.W. Harvey and M.G. McCoy, in: . International Atomic Energy Agency, Vienna (Ed.), Proc. IAEA TCM/Advances in Simulation and Modeling in Thermonuclear Plasmas, Montreal (1992), 1992.

[87] P. Nikkola, et al., *Modelling of the electron cyclotron current drive experiments in the TCV tokamak*, Nucl. Fusion 43 (2003) 1343–1352.

[88] R. Behn et al., *Formation of eITBs in EC-Heated TCV Plasmas with and without Inductively Driven Current Component*, in: 30th EPS Conference on Contr. Fusion and Plasma Phys., St. Petersburg, 7-11 July 2003 ECA Vol. 27A, P-3.208.

[89] F. Troyon, R. Gruber, H. Saurenmann, S. Semenzato, S. Succi, *MHD-Limits to Plasma Confinement*, Plasma Physics and Controlled Fusion 26 (1A) (1984) 209–215.

[90] G. Zhuang, A. Scarabosio, et al.., *MHD activity in EC-heated TCV plasmas with eITBs*, in: 31st EPS Conference on Plasma Phys. London, 28 June - 2 July 2004 ECA Vol.28G, P-4.192 (2004), 2004.

[91] P.H. Rebut P.P. Lallia and M.L. Watkins, in: Proceedings of the 12th International Conference on Plasma Physics and Controlled Fusion Research, Nice,1988, Vol. 2, 1989, p. 1991.

[92] G. Tresset et al., Nuclear Fusion 42 (2002) 520.

[93] H. Reimerdes et al., *From Current-Driven to Neoclassically Driven Tearing Modes*, Physical Review Letters 88 (10) (2002) 105005.

[94] E. Fable and O. Sauter, in: ISPP-21 Theory of Fusion Plasmas, Varenna, SIF, Bologna, 443, 2004.

[95] ITER Physics Expert Group on Confinement and Transport, and ITER Physics Expert Group on Confinement Modelling and Database and ITER Physics Basis Editors, *Chapter 2: Plasma confinement and transport*, Nuclear Fusion 39 (1999) 2175–2249.

[96] A. M. Garofalo, T. H. Jensen, E. J. Strait, *Analysis of stable resistive wall modes in a rotating plasma*, Physics of Plasmas 10 (12) (2003) 4776–4783.

[97] Buttery R.J. et al., *Rotation and Shape Dependence of Neoclassical Tearing Mode Thresholds on JET*, 28th Europen Physical Society Conference on Plasma Physics and controlled Fusion (Funchal, Portugal) 25A (2001) 1813–1816.

[98] R. C. Wolf, *Internal transport barriers in tokamak plasmas*, Plasma Phys. Control Fusion 45 (2003) R1–R45.

[99] J. E. Rice et al., *Toroidal rotation and momentum transport in Alcator C-Mod plasmas with no momentum input*, Physics of Plasmas 11 (5) (2004) 2427–2432.

[100] W. M. Stacey and J. Mandrekas, *Comparision of neoclassical rotation theory with experiment under a variety of conditions in DIII-D*, Physics of Plasmas 9 (5) (2002) 1622–1628.

[101] Suckewer S. et al., *Toroidal plasma rotation in the PLT tokamak with neutral-beam injection*, Nuclear Fusion 21 (10) (1981) 1301–1309.

[102] J. deGrassie et al., *Toroidal rotation in neutral beam heated discharges in DIII-D*, Nuclear Fusion 43 (2) (2003) 142–156.

[103] Synakowski E. J. et al., *Measurements of radial profiles of He2+ transport coefficients on the TFTR tokamak*, Phys. Rev. Lett. 65 (1990) 2255–2258.

[104] W. M. Solomon et al., *Neoclassical Poloidal Rotation Studies in High Temeperature Plasmas*, 32th Europen Physical Society Conference on Plasma Physics and controlled Fusion, Tarragona (Spain) 29C (2005) P–5.043.

[105] K. Crombe' et al., *Poloidal Rotation Dynamics, Radial Electric Field, and Neoclassical Theory in the Jet Internal-Transport-Barrier Region*, Phys. Rev. Lett. 95 (155003) (2005) 1.

[106] A. Romannikov et al., *Measurement of central toroidal rotation in ohmic Tore Supra plasmas*, Nuclear Fusion 40 (3) (2000) 319–324.

[107] Hutchinson I. H. et al., *Self-Acceleration of a Tokamak Plasma during Ohmic H Mode*, Phys. Rev. Lett. 84 (15) (2000) 3330–3333.

[108] J. Rice, E. Marmar, F. Bombarda, L. Qu, *X-ray observations of central toroidal rotation in ohmic Alcator C-Mod plasmas*, Nuclear Fusion 37 (3) (1997) 421–426.

[109] Bell M. G. et al., Nuclear Fusion 19 (1) (1979) 33–38.

[110] Bugarya V.I. et al., Nuclear Fusion 25 (12) (1985) 1707–1717.

[111] B. Duval, B. Joye, B. Marchal, *Behaviour of plasma rotation and radial electric field with density ramp rate in an ohmically heated tokamak*, Nuclear Fusion 32 (8) (1992) 1405–19.

[112] Peebles W.A. et al., in Plasma Physics and Controlled Nuclear Fusion Research 1990 (Proc. 13th Int. Conf. Washington, DC, 1990) 1 (IAEA, Vienna).

[113] J.S. deGrassie et al., *Toroidal rotation in DIII-D in electron cyclotron heating and Ohmic H-mode discharges*, Physics of Plasmas 11 (9) (2004) 4323–4331.

[114] J.H.F. Severo et al., *Plasma residual rotation in the TCABR tokamak*, Nuclear Fusion 43 (10) (2003) 1047–1056.

[115] J.E. Rice et al., *Observations of anomalous momentum transport in Alcator C-Mod plasmas with no momentum input*, Nuclear Fusion 44 (3) (2004) 379–386.

[116] A Scarabosio et al., *Toroidal plasma rotation in the TCV tokamak*, Plasma Physics and Controlled Fusion 48 (5) (2006) 663–683.

[117] Hazeltine R. D., Phys. Fluids 17 (5) (1974) 961–968.

[118] Pochelon A. et al., 19th IAEA FEC, Oct. 2002, Lyon, France, IAEA-CN-94/EX/P5-14.

[119] Scarabosio A. et al., 32th Europen Physical Society Conference on Plasma Physics and controlled Fusion, Tarragona (Spain) 29C (2005) P–1.049.

[120] Y Camenen et al., *Electron heat transport in shaped TCV L-mode plasmas*, Plasma Physics and Controlled Fusion 47 (11) (2005) 1971–1987.

[121] Y. B. Kim, P. H. Diamond, R. J. Groebner, *Neoclassical poloidal and toroidal rotation in tokamaks*, Physics of Fluids B: Plasma Physics 3 (8) (1991) 2050–2060.

[122] Hirshman S. and Sigmar D., *Neoclassical transport of impurities in tokamak plasmas*, Nuclear Fusion 21 (1981) 1079–1201.

[123] J. Kim, et al.,, *Rotation characteristics of main ions and impurity ions in H-mode tokamak plasma*, Phys. Rev. Lett. 72 (1994) 2199–2202.

[124] D. Testa et al., *On the measurement of toroidal rotation for the impurity and the main ion species on the Joint European Torus*, Physics of Plasmas 9 (1) (2002) 243–250.

[125] M. N. Rosenbluth et al., Plasma Physics and Controlled Nuclear Fusion Research (International Atomic Energy Agency, Vienna, 1971) 1 485.

[126] K. T. Tsang and E. A. Frieman, *Toroidal plasma rotation in axisymmetric and slightly nonaxisymmetric systems*, Phys. Fluids 19 (5) (1976) 747–756.

[127] R. D. Hazeltine and M. N. Rosenbluth, *Effect of Field Asymmetry on Neoclassical Transport in a Tokamak*, Physics of Fluids 15 (12) (1972) 2211–2217.

[128] A. N. Simakov, P. J. Catto, *Drift kinetic equation exact through second order in gyroradius expansion*, Physics of Plasmas 12 (1) (2005) 012105.

[129] Peter J. Catto and Andrei N. Simakov, *Evaluation of the neoclassical radial electric field in a collisional tokamak*, Physics of Plasmas 12 (1) (2005) 012501.

[130] H. A. Claassen, H. Gerhauser, A. Rogister and C. Yarim, *Neoclassical theory of rotation and electric field in high collisionality plasmas with steep gradients*, Physics of Plasmas 7 (9) (2000) 3699–3706.

[131] S. K. Wong, V. S. Chan, *The neoclassical angular momentum flux in the large aspect ratio limit*, Physics of Plasmas 12 (9) (2005) 092513.

[132] K. Ida et al., *Evidence for a toroidal-momentum-transport nondiffusive term from the JFT-2M tokamak*, Phys. Rev. Lett. 74 (11) (1995) 1990–1993.

[133] B. Coppi, *Accretion theory of 'spontaneous' rotation in toroidal plasmas*, Nuclear Fusion 42 (1) (2002) 1–4.

[134] K. C. Shaing, *Theory for Toroidal Momentum Pinch and Flow Reversal in Tokamaks*, Phys. Rev. Lett. 86 (4) (2001) 640.

[135] J. Rossel, *Soft X-ray emissivity profile inversion in quasi-axisymmetric equilibria*, Master's thesis, LRP-report EPFL - CRPP, Lausanne, Switzerland, CH-1015 (2005).

[136] J.A. Snipes et al., *MHD modes and toroidal rotation at JET*, Nuclear Fusion 30.

[137] E. Lazzaro et al., *Error field locked modes thresholds in rotating plasmas, anomalous braking and spin-up*, Physics of Plasmas 9 (9) (2002) 3906–3918.

[138] A. Bortolon, A. Scarabosio, B.P. Duval, A. Pochelon, *Observation of Spontaneous Toroidal Rotation Inversion in Ohmically heated Tokmak Plasmas*, submitted to Physical Review Letter.

[139] A. Bortolon, *Thesis project:*, Ph.D. thesis, Ecole Polytechnique Fédérale de Lausanne (2006).

[140] M. Abramowitz, I. A. Stegun (Eds.), *Handbook of mathematical functions*, Dover Publications, Inc., New York, 1970.

[141] B. LaBombard et al., *Transport-driven Scrape-Off-Layer flows and the boundary conditions imposed at the magnetic separatrix in a tokamak plasma*, Nuclear Fusion 44 (10) (2004) 1047–1066.

Acknowledgements

I am deeply grateful to my thesis supervisor Antoine Pochelon who has helped me a lot in accomplishing this work. Ha has always been very supportive and with his enthusiasms has often giving me the motivations especially in moments of difficulties.

I am particularly indebted with my co-supervisor Basil P. Duval, who has helped me in understanding many aspect of the tokamak physics and made my days in the control-room less miserable with his good (?British?) humour.

Thanks to Dr. Sauter and many other senior colleagues for the many useful discussions on MHD and other physics topics. I thank my younger colleagues, which were often also very good friends, for the many years of work and good time she shared together. In particular I would like to thank Alessandro Bortolon and to Sergi Ferrando.

I am grateful to Prof. R Challer, Prof. A. Fasoli, Prof. E. Lazzaro and to Dr. J. Rice who honoured me by accepting to be members of my thesis jury.

I thank Prof. M.Q. Tran and Dr K. Appert who have given me the opportunity to work in CRPP.

Special thanks go to Edith Grueter and the CRPP administrative staff foe their very efficient work that has been always of great help.

I would like to thank my parents, my brother and his family, for their support and love during these years away from home.

Finally, I would like to dedicate this thesis to my wife and true love Federica, which has not only contributed to this thesis with her support but has also had the bravery to read it and correct some of the many mistakes I have made.

This work was partly supported by the Swiss National Science Foundation.